

Resonance Testing of Asphalt Concrete

Anders Gudmarsson

Doctoral Thesis
KTH Royal Institute of Technology
School of Architecture and the Built Environment
Department of Transport Science
Division of Highway and Railway Engineering
SE-100 44 Stockholm

TRITA-TSC-PHD 14-008

ISBN 978-91-87353-50-5

© Anders Gudmarsson

Stockholm 2014

Akademisk avhandling som med tillstånd av KTH i Stockholm framlägges till offentlig granskning för avläggande av teknisk doktorsexamen måndagen den 8 december kl. 09:00 i Kollegiesalen, KTH, Brinellvägen 8, Stockholm.

Abstract

This thesis present novel non-destructive laboratory test methods to characterize asphalt concrete. The testing is based on frequency response measurements of specimens where resonance frequencies play a key role to derive material properties such as the complex modulus and complex Poisson's ratio. These material properties are directly related to pavement quality and used in thickness design of pavements.

Since conventional cyclic loading is expensive, time consuming and complicated to perform, there has been a growing interest to apply resonance and ultrasonic testing to estimate the material properties of asphalt concrete. Most of these applications have been based on analytical approximations which are limited to characterizing the complex modulus at one frequency per temperature. This is a significant limitation due to the strong frequency dependency of asphalt concrete. In this thesis, numerical methods are applied to develop a methodology based on modal testing of laboratory samples to characterize material properties over a wide frequency and temperature range (i.e. a master curve).

The resonance frequency measurements are performed by exciting the specimens using an impact hammer and through a non-contact approach using a speaker. An accelerometer is used to measure the resulting vibration of the specimen. The material properties can be derived from these measurements since resonance frequencies of a solid are a function of the stiffness, mass, dimensions and boundary conditions.

The methodology based on modal testing to characterize the material properties has been developed through the work presented in paper I and II, compared to conventional cyclic loading in paper III and IV and used to observe deviations from isotropic linear viscoelastic behavior in paper V. In paper VI, detailed measurements of resonance frequencies have been performed to study the possibility to detect damage and potential healing of asphalt concrete.

The resonance testing are performed at low strain levels ($\sim 10^{-7}$) which gives a direct link to surface wave testing of pavements in the field. This enables non-destructive quality control of pavements, since the field measurements are performed at approximately the same frequency range and strain level.

Keywords

Resonance frequencies; Modal testing; Frequency response functions; Cyclic loading; Tension-compression tests; Complex modulus; Complex Poisson's ratio

Sammanfattning

Denna avhandling presenterar nya oförstörande testmetoder för att karakterisera asfaltprovkroppars materialegenskaper. Provingen är baserad på att mäta provkroppars frekvensrespons över ett brett frekvensområde där resonansfrekvenser spelar en central roll i bestämningen av materialegenskaper som den komplexa modulen och komplexa Poisson's tal. Dessa materialegenskaper är direkt relaterade till beläggningskvaliteten och används i bärighetsdimensionering av vägar för att bestämma asfaltlagrens tjocklek.

Intresset för att använda ultraljuds- och resonansfrekvensmätningar till att bestämma materialegenskaper i asfalt har ökat på senare tid eftersom konventionella mätmetoder är dyra, tidskrävande och komplicerade att utföra. De flesta av de tidigare vägbaserade metoderna har dock använt sig av approximativa analytiska förhållanden som är begränsade till en specifik geometri och till att bestämma styvhetsmodulen för en frekvens per temperatur. Detta är en stor begränsning med tanke på asfaltens starka frekvensberoende. I denna avhandling har numeriska metoder använts för att utveckla en metodik baserad på resonansfrekvensmätningar som kan karakterisera asfaltprovkroppars materialegenskaper över ett brett frekvens- och temperaturspann (dvs. en masterkura).

Resonansfrekvensmätningar har utförts genom att excitera en provkropp via en liten hammare och genom att använda en högtalare för kontaktlös excitering. En accelerometer har använts för att mäta upp de resulterande vibrationerna i provkropparna. Materialegenskaperna kan bestämmas utifrån dessa mätningar eftersom resonansfrekvenserna av en kropp är en funktion av styvhet, massa, dimensioner och randvillkor.

Metodikerna för att karakterisera materialegenskaper genom resonansfrekvensmätningar har utvecklats i artikel I och II, jämförts mot konventionella metoder i artikel III och IV och använts för att observera avvikelser från isotropiskt linjärt viskoelastiskt materialbeteende i artikel V. Genom att använda en högtalare har detaljerade resonansfrekvensmätningar utförts för att undersöka möjligheten att detektera skador och potentiell läkning av en asfaltprovkropp i artikel VI.

Asfalten utsätts för ungefär samma töjningsnivåer och belastningsfrekvenser vid resonansfrekvensmätningar som vid oförstörande seismiska fältmätningar av beläggningar. Detta möjliggör oförstörande kvalitetskontroller av vägkonstruktioner eftersom resultaten från dessa metoder kan jämföras direkt utifrån liknande förutsättningar.

Preface

The work presented in this thesis has been carried out at Peab Asphalt AB and the division of Highway and Railway Engineering at KTH Royal Institute of Technology. I would like to express my sincere appreciation to my main supervisor Nils Ryden who has given me excellent guidance, ideas and feedback throughout the project. My supervisor Björn Birgisson is also gratefully acknowledged for his feedback and insights to this project.

I am very thankful to Lennart Holmqvist who was part of initiating this project together with Nils Ryden and Björn Birgisson.

The Swedish construction industry's organization (SBUF) and the Swedish Transport Administration (Trafikverket) are gratefully acknowledged for the financing of this project.

Thanks to all my colleagues at Peab Asphalt AB for their great support during this project.

A great appreciation is also given to the research group at Laboratories Génie Civil et Bâtiment & Tribologie et Dynamiques des Systèmes (UMR CNRS) in ENTPE, University of Lyon for all their help and hospitality during my visits to Lyon. Special thanks to Hervé Di Benedetto and Cédric Sauzéat for a great collaboration with good support and discussions.

I would also like to thank my colleagues at KTH, the participants of the Friday meeting group and the members of the reference group for valuable feedback regarding this project.

Finally, I would like to thank my family and friends for supporting and helping out during my years of studying.

Anders Gudmarsson

Stockholm, September 2014

Appended papers

This thesis is based on the following six papers which are appended at the end of the thesis.

- Paper I.** Gudmarsson, A., Ryden, N., Birgisson, B. 2012, Application of resonant acoustic spectroscopy to asphalt concrete beams for determination of the dynamic modulus, *Materials and Structures*, Vol. 45, Issue 12, 1903-1913.
- Paper II.** Gudmarsson, A., Ryden, N., Birgisson, B. 2012, Characterizing the low strain complex modulus of asphalt concrete specimens through optimization of frequency response functions, *Journal of Acoustical Society of America*, Vol. 132, Issue 4, 2304-2312.
- Paper III.** Gudmarsson, A., Ryden, N., Di Benedetto, H., Sauzéat, C., Tapsoba, N., Birgisson, B. 2014, Comparing linear viscoelastic properties of asphalt concrete measured by laboratory seismic and tension-compression tests, *Journal of Nondestructive Evaluation*, Vol. 33, Issue 4, 571-582.
- Paper IV.** Gudmarsson, A., Ryden, N., Di Benedetto, H., Sauzéat, C. 2014, Complex modulus and complex Poisson's ratio from cyclic and dynamic modal testing of asphalt concrete, submitted to *Construction and Building Materials*.
- Paper V.** Gudmarsson, A., Ryden, N., Birgisson, B. 2014, Observed deviations from isotropic linear viscoelastic behavior of asphalt concrete through modal testing, *Construction and Building Materials*, Vol. 66, 63-71.
- Paper VI.** Gudmarsson, A., Ryden, N., Birgisson, B. 2014, Non-contact excitation of fundamental resonance frequencies of an asphalt concrete specimen, accepted to The 41st Annual Review of Progress in Quantitative Nondestructive Evaluation, Boise, Idaho, *AIP Conference Proceedings*.

Related publications

Gudmarsson, A., Ryden, N., Birgisson, B., 2010, Application of resonant acoustic spectroscopy to beam shaped asphalt concrete samples, *Journal of Acoustical Society of America*, Vol. 128, Issue 4, 2453.

Gudmarsson, A., 2012, Laboratory Seismic Testing of Asphalt Concrete, Licentiate thesis, KTH Royal Institute of Technology, Stockholm, Sweden, ISBN 978-91-85539-97-0.

Gudmarsson, A., Ryden, N., Birgisson, B., 2013, Determination of the frequency dependent dynamic modulus for asphalt concrete beams using resonant acoustic spectroscopy, Nondestructive Testing of Materials and Structures, *Proceedings of NDTMS-2011*, Istanbul, Turkey, RILEM Bookseries, Vol. 6, 199-204.

Gudmarsson, A., Ryden, N., Birgisson, B., 2013, Nondestructive evaluation of the complex modulus master curve of asphalt concrete specimens, The 39th Annual Review of Progress in Quantitative Nondestructive Evaluation, Denver, Colorado, *AIP Conference Proceedings*, Vol. 1511, 1301-1308.

List of notations

E^*	Complex modulus
$ E^* $	Dynamic modulus
ν^*	Complex Poisson's ratio
G^*	Complex shear modulus
E	Storage modulus
E'	Loss modulus
Φ	Phase angle
η	Loss factor
f	Frequency
T	Temperature
T_{ref}	Reference temperature
a_T	Shift factor
$c_{1,2}$	WLF material constants
f_{red}	Reduced frequency
E_0/ν_0	Low frequency modulus/Poisson's ratio
E_∞/ν_∞	High frequency modulus/Poisson's ratio
α	Parameter governing the width of the loss factor peak
β	Parameter governing the asymmetry of the loss factor peak
τ	Relaxation time governing the position of the loss factor peak
$H(f)$	Frequency response function
$CF(f)$	Coherence function
$Y(f)$	Measured response in frequency domain
$Y^*(f)$	Complex conjugate of the response
$X(f)$	Measured load impact in frequency domain
$X^*(f)$	Complex conjugate of the load impact
i	$\sqrt{-1}$
ρ	Density
ω	Angular frequency = $2\pi f$
\mathbf{u}	Displacement
σ	Stress
ε	Strain

List of abbreviations

NDT	Non-Destructive Testing
RUS	Resonant Ultrasound Spectroscopy
RAS	Resonant Acoustic Spectroscopy
FRF(s)	Frequency Response Function(s)
FFT	Fast Fourier Transform
WLF	Williams-Landel-Ferry
HN	Havriliak-Negami
2S2P1D	2 Springs, 2 Parabolic elements, 1 Dashpot
FEM	Finite Element Method
SD	Standard Deviation
RSD	Relative Standard Deviation
NRUS	Nonlinear Resonant Ultrasound Spectroscopy

Table of Contents

Abstract.....	I
Sammanfattning.....	III
Preface.....	V
Appended papers.....	VII
Related publications.....	IX
List of notations.....	XI
List of abbreviations.....	XIII
1 Introduction.....	1
1.1 Background.....	1
1.2 Objectives	3
1.3 Limitations	3
2 Methodology	5
2.1 Resonance frequency measurements.....	7
2.2 Frequency response function measurements	10
2.3 Isotropic linear viscoelastic properties of asphalt concrete	12
2.4 Characterizing material properties through FRFs.....	14
2.5 Materials.....	16
2.6 Non-destructive quality control of pavements	16
3 Repeatability of resonance frequency testing	19
3.1 Effect of impact force and accelerometer attachment.....	19
3.2 Repeating the attachment of the accelerometer	21
3.3 Measurements performed by different operators.....	23
3.4 Position of the accelerometer and the impact	25
3.5 Summary of the repeatability studies	28
4 Summary of appended papers	29
5 Summary of results and discussion.....	33
6 Conclusions	43
7 Recommendations and future work.....	45
References	47

1 Introduction

Asphalt concrete consists mainly of stone aggregates of different sizes, bitumen and air voids. This composite material has a complex mechanical behavior that depends on loading frequency, temperature and strain level. It is known that asphalt concrete show a non-linear dependence between stress and strain above a certain degree of deformation. At these levels of deformation the material displays a viscoelastic-plastic behavior. At lower levels of deformation, asphalt concrete is assumed to have a linear viscoelastic behavior which greatly simplifies the difficult task to predict the stress-strain behavior of the material. The isotropic linear viscoelastic behavior of asphalt concrete can be governed by two constants such as the complex stiffness modulus (E^*) and complex Poisson's ratio (ν^*). These frequency and temperature dependent material properties are key parameters in thickness design of pavements.

1.1 Background

Pavement design has traditionally been based on empirical values of material properties that are applicable for the traffic and climate conditions under study. Therefore, traditional design methods are often limited for use in certain areas or countries. This approach has not helped to increase the general understanding of the fundamental mechanical behavior of pavements. Nowadays, there is an increasing interest of being able to perform more mechanically based designs of pavements to potentially optimize the cost and life length for a given road construction. Therefore, accurate characterization of the material properties of asphalt concrete is necessary to improve the design of pavements. However, the viscoelastic behavior makes asphalt concrete more complicated than many other civil engineering construction materials due to its strong temperature and frequency dependency. When other materials such as e.g. concrete and steel can be described by a constant Young's modulus, material properties of asphalt concrete need to be expressed as a function of loading frequency and temperature. A master curve describes this relation and is therefore a valuable tool for the characterization of asphalt concrete (Ceylan et al. 2009; Booshehrian et al. 2013). Any test methods used to determine the viscoelastic properties of asphalt concrete should be able to measure the response over a sufficient amount of frequencies to enable accurate estimation of master curves.

Conventional test methods to measure the linear viscoelastic properties of asphalt concrete are based on applying cyclic loading to specimens while continuously measuring the displacements. The cyclic testing is usually performed at some frequencies between 0.01 to 25 Hz and at different temperatures (Brown et al. 2009). This type of testing is associated with high costs and the accuracy of the measurements is very sensitive to the set-up of the test (Daniel et al. 2004). This makes the test complicated and extensive experience of the operator is often

2 | Introduction

required to be able to accurately perform the time consuming preparations to run the testing. Despite these issues, the cyclic loading is currently the most common and useful test to characterize a complex modulus master curve ranging from low to fairly high frequencies (Di Benedetto et al. 2007). Due to the high costs and complexity of conventional testing, predictive models have been developed to estimate the dynamic modulus of asphalt concrete. These models use information of the gradation of the aggregates, the binder, and empirical data based on conventional testing to predict the dynamic modulus of different mixtures (Bari and Witczak 2006; Christensen et al. 2003; Garcia and Thompson 2007). The use of predictive models save time and costs but is not as accurate as actual testing. In addition, most models provide an approximation of only the absolute values of the complex modulus. Recent work has been performed to also predict the phase angle of asphalt concrete, which is needed to predict a complex modulus (Yang and You 2014; Naik and Biligiri 2014)

Resonance and ultrasonic testing are interesting alternative test methods to conventional cyclic loading that have been applied to asphalt concrete specimens. These methods are economic, simple to perform and especially resonance testing has a great potential to accurately characterize the material properties. Whitmoyer and Kim (1994) used impact resonance testing to investigate if the concrete standard “ASTM C215, Test Method for Fundamental Transverse, Longitudinal, and Torsional Frequencies of Concrete Specimens” was applicable to asphalt concrete. The concrete method allows the elastic modulus to be derived for the fundamental resonance frequency by using simplified analytical formulations which are applicable to specimens with a length to diameter ratio of at least 2 (ASTM C215 2008). Although this work did not account for the viscoelasticity of asphalt concrete, the precise repeatability and reproducibility were identified as one of many advantages of resonance testing. The concrete method was further applied to asphalt concrete by Kweon and Kim (2006), where correction factors of the damping and the specimen geometry were used to increase the accuracy of the elastic modulus. The half-power bandwidth method was also used to estimate the damping, giving the phase angle and consequently the complex modulus. A large number of mixtures were tested by both impact resonance testing and conventional cyclic compression loading in this study. The comparison of the two methods showed a promising agreement. However, an important finding from this study was that shift factors were needed to be known beforehand to be able to apply the concrete standard to estimate master curves of asphalt concrete. This is due to that the ASTM C215 standard allows the elastic modulus to be determined for one (the fundamental) resonance frequency which gives only one modulus per measurement temperature. This significant limitation has been seen in most of the work applying either resonance or ultrasonic testing to asphalt concrete (cf. e.g. Lacroix et al. 2009; Nazarian et al. 2005; Di Benedetto et al. 2009; Norambuena-Contreras et al. 2010; Mounier et al. 2012; Larcher et al. 2014). An approach capable to increase the usable resonance frequencies was presented by Ryden (2011), where three-dimensional numerical calculations were applied to derive the complex moduli of asphalt concrete from resonance testing. The numerical calculations open up the possibility to estimate the complex modulus from several resonance frequencies of specimens with arbitrary dimensions. However, the measurements of the cylindrical disc-shaped specimens were limited to the fundamental longitudinal

and flexural modes of vibration in this study. This thesis continues to develop the approach of using numerical methods to derive the complex modulus and complex Poisson's ratio master curves of asphalt concrete specimens with arbitrary dimensions through resonance testing.

In addition to economic, fast and simple measurements, there are further advantages of developing accurate test methods based on resonance frequency measurements:

- The mechanical properties of asphalt concrete are, in similarity to many other materials, dependent on the magnitude of the applied stress (Airey and Rahimzadeh 2004; Nguyen et al. 2014). Conventional tests, usually performed at strain levels of around $50 \cdot 10^{-6}$, are limited to testing above the magnitude of approximately 10^{-6} . Resonance frequency testing is performed at lower strain levels (10^{-7} and below) and can therefore extend the strain level measurement range. This can be used to increase the knowledge of the strain level dependency of asphalt concrete and low strain measurements can be used for early damage detection (Van Den Abeele et al. 2000).
- The thickness and air void content of cored samples from the roads are currently used as quality control of pavements. There is a will to reduce this destructive point wise testing of pavements. Low strain laboratory resonance testing has the potential to provide the necessary link to non-destructive field measurements to enable non-destructive quality control of pavements (Ryden 2004).

1.2 Objectives

The objectives of this thesis are to develop economic and accurate non-destructive testing (NDT) methods to characterize the isotropic linear viscoelastic properties of asphalt concrete over a wide frequency range. Effects of applied strain levels, applicability to different geometries and dimensions and the possibility for early damage detection are also studied in this thesis.

1.3 Limitations

The novel NDT methods presented in this thesis have been applied to a limited number of asphalt concrete specimens of different shapes and dimensions. The appended papers present modal test results of three beam shaped asphalt concrete specimens and of three cylindrical shaped specimens. One disc-shaped asphalt concrete specimen has been tested by the non-contact excitation approach using a speaker. Concrete and PVC-U specimens have been tested in addition to the asphalt concrete specimens. The modal testing to determine frequency response functions has been performed by using an impact hammer. Other excitation methods such as e.g. a shaker remain to be applied to asphalt concrete for this purpose.

2 Methodology

The main findings presented in the appended papers of this thesis are based on resonance frequency measurements of asphalt concrete specimens with different shapes and dimensions. Resonance occurs when the frequency of a driving force equals the natural frequencies of an object. The natural frequencies of a solid with free boundary conditions are a function of the mass, the dimensions and the elastic constants. This relation has been widely used to derive elastic constants of many different materials through resonance frequency measurements. Resonant ultrasound spectroscopy (RUS) is one of the most accurate and well-known methods based on resonance frequency measurements to derive elastic constants of isotropic and anisotropic materials (Migliori and Sarrao 1997; Li and Gladden 2010). RUS is also referred to as resonant acoustic spectroscopy (RAS) in cases where the measurements are performed below the ultrasonic frequencies i.e. $< 20\,000$ Hz (Ostrovsky et al. 2001). In RUS and RAS, a large number of resonance frequencies of several modes of vibration are excited and measured by one single frequency sweep. To derive the elastic constants from these measurements the so-called forward and inverse problem need to be solved. The forward problem is solved by using numerical methods to calculate all theoretical resonance frequencies based on assumed values of the elastic constants. The following inverse problem is solved by adjusting the elastic constants so that the theoretical resonance frequencies agree with the measured resonance frequencies. The number of measured resonance frequencies is often much larger than the number of elastic constants that are to be determined. This enables very accurate estimation of the elastic constants of both isotropic and anisotropic elastic materials (Migliori and Sarrao 1997). The development of RUS is relatively new compared to e.g. wave propagation techniques, due to need of computers for efficient calculation of the forward and inverse problem. Before Holland (1967) and Demarest (1971) applied numerical approximation methods to calculate theoretical resonance frequencies, analytical calculations were limited to specific geometries as cubes or spheres. Ohno (1976) refined and extended the work performed by Demarest to determine elastic constants for further symmetries. However, RUS got widely known and applied first after work by e.g. Migliori et al. (1990), Maynard (1992) and Visscher et al. (1991) where computational algorithms were developed to enable the determination of elastic constants of samples with arbitrary geometries (Migliori et al. 1993; Maynard 1996).

Other NDT measurements based on recording the travel time of a wave propagating through a sample have been applied to asphalt concrete by e.g. Nazarian et al. (2005), Di Benedetto et al. (2009) and Norambuena-Contreras et al. (2010). The wave speed generally depend on the stiffness and the density which enable an estimation of the modulus by measuring the time of the propagating wave over a known distance. However, there are some important disadvantages related to applying ultrasonic wave propagation methods to asphalt concrete. For

6 | Methodology

example, the modulus is determined at very high frequencies (> 20 kHz) and for only one frequency at each test temperature. It is important to be able to determine the complex modulus of asphalt concrete over a wide frequency range including low frequencies, since pavements are exposed to much lower frequencies than the ultrasonic frequencies. One of the main disadvantages is although that the accuracy of the ultrasonic testing decreases when it is applied to materials that are not truly homogeneous (Bernard et al 2014). For such materials, as e.g. asphalt concrete, it is important that the wavelength is larger than the inhomogeneities in the sample to reduce diffraction and scattering effects. Inhomogeneities with similar sizes as the wavelength can cause diffraction which limits the accuracy, since wave propagation methods are usually based on the approximation of plane-waves. In addition, the waves can be scattered by the local inhomogeneities if the wavelength is shorter than the local obstructing objects. This gives a diffuse wave front and the measured wave speed becomes dependent on the fastest path of the wave inside the sample and on the placement of the sensors. At the same time the wavelength need to be much smaller than the specimen due to the plane-wave approximation. This limits the minimum size of the specimen and the measurements becomes less accurate with increasing frequencies. Resonance testing is less affected by the heterogeneous nature of asphalt concrete since measurements are performed at lower frequencies and does not rely on an approximation of plane-waves. In fact, no assumptions of idealized states of stress and strain are needed since RUS accounts for the complex vibrations of the sample. Another important advantage with RUS is that it is possible to determine the complete stiffness coefficient matrix from one single measurement. The number of measurements needed to obtain the same result using wave propagation methods is at least equal to the number of stiffness coefficients in the matrix (Leisure and Willis 1997).

The approach of measuring resonance frequencies and solving the forward and inverse problem to determine material properties has been central in the methods presented in papers I to V appended in this thesis. However, the frequency dependency of asphalt concrete does not allow the concept of RAS to be fully applied in its original form. Several discrete resonance frequencies cannot be used to increase the accuracy of a specific material property since each frequency gives a unique modulus. Therefore, there is a need to use additional information, namely the amplitude of the frequency response curve, from the resonance frequency measurements. The amplitude of the frequency response curve can be accounted for by also measuring the applied force of the impact. This force is used to normalize the amplitude of the response by dividing the response with the force. This gives a transfer function or a frequency response function (FRF) when it is expressed in frequency domain. Through the use of FRFs, the amplitude over the entire frequency range under study in addition to the resonances can be used as input to the estimation of the material properties. The additional input significantly increases the number of points that can be used to fit a theoretical curve against the measured behavior of the viscoelastic asphalt concrete. Consequently, viscoelastic material properties over a wide and fine sampled frequency range can be estimated with good accuracy by measuring and calculating FRFs. An application of RAS to asphalt concrete was applied in paper I and FRFs were measured and calculated in papers II to V. Optimization of FRFs to derive material properties have also been successfully applied to different types of frequency dependent viscoelastic materials

in other fields of engineering (Ren et al. 2011; Renault et al. 2011; Rupitsch et al. 2011; Finnveden et al. 2014).

2.1 Resonance frequency measurements

The resonance frequencies of a specimen with free boundary conditions are determined by measuring the vibrations that are generated by an excitation. The excitation can be performed by an impact giving a transient vibration of the solid over a frequency range depending on the impact contact time. The resonance frequencies can also be excited through frequency sweeps where the driving frequencies can be defined beforehand. The impact excitation has been applied in papers I to V and a frequency sweep excitation using a speaker has been used in paper VI.

The impact resonance test set-up is illustrated in Figure 1, where an impact hammer is used to apply the load and an accelerometer is used to measure the vibrations over time. The impact hammer (PCB model 086E80) and the accelerometer (PCB model 35B10) are connected to a signal conditioner (PCB model 480B21), which is shown down in the left corner of Figure 1. The signal conditioner prepares the signals for analog to digital conversion and can amplify the measurement signals if necessary. The signal conditioner is connected to the data acquisition device (NI USB-6251 M Series), shown in the right bottom corner of Figure 1, which converts the analog signals to digital signals.

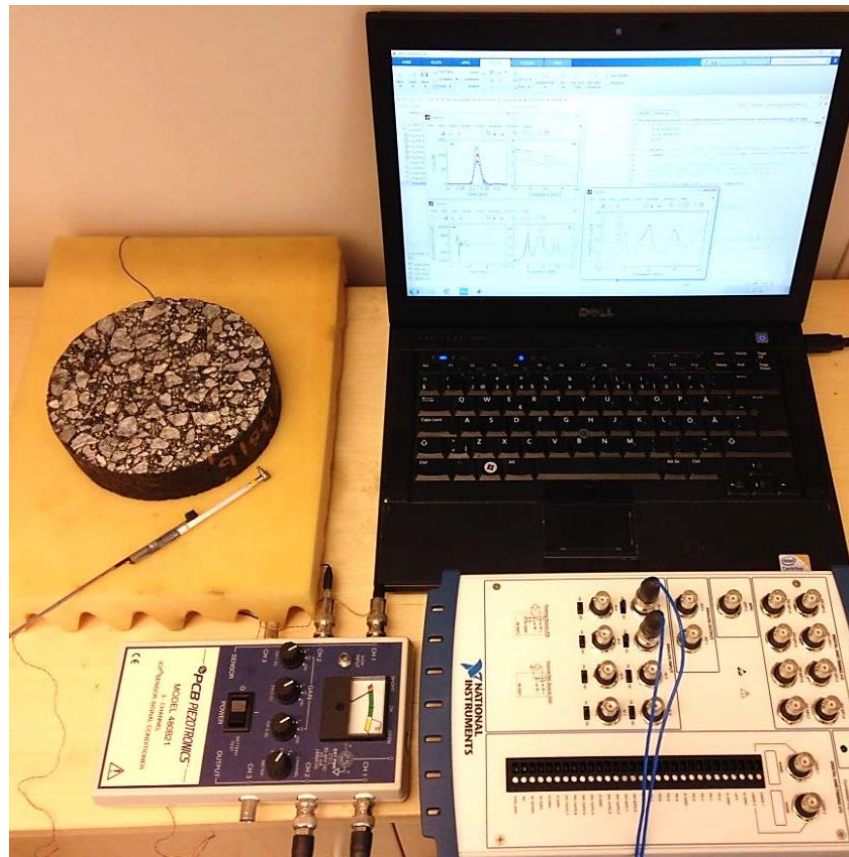


Figure 1: Equipment and test set-up for the impact hammer resonance frequency measurements

8 | Methodology

This specific data acquisition device has a sampling rate of 1.25 MHz which allows a sampling rate of 500 kHz for each of the two channels of the accelerometer and the impact hammer. The data acquisition device is connected to a computer through a USB cable. The data acquisition toolbox in MATLAB® is used to set-up the data acquisition device and to run and record the measurements. The specimen is placed on soft foam for free boundary conditions.

Figure 2 shows an example of conventional cyclic loading test set-up as a comparison to the resonance frequency test set-up. Figure 2a shows a part of the heavy load frame used to apply the cyclic loading. Additional equipment needed for this test such as hydraulics, computer systems and connections are not shown in this figure. Figure 2b shows the details of the specimen set-up where the top and bottom is glued to enable tension and compression loading. Five sensors are used in this set-up to enable accurate measurements of the axial and radial displacements. A visual comparison between Figure 1 and 2 can give an indication of the advantages in speed and simplicity of performing resonance testing compared to the conventional cyclic loading. For example, all equipment that is needed to perform resonance testing can be carried in one single bag. Note that a climate chamber, such as the rectangular box shown in Figure 2a, is necessary in both test methods to perform measurements at different temperatures.



Figure 2: Example of equipment and test set-up to perform conventional cyclic loading (a) and a detailed set-up of a specimen (b). The photos are taken at ENTPE, University of Lyon

Figure 3 shows the impact hammer and the accelerometer positioned to measure the flexural (anti-symmetric around the center of the diameter) modes of vibration of a disc-shaped asphalt concrete specimen. An impact in the center of the specimen generates the longitudinal (symmetric) modes of vibration. It is recommended to apply the impact to a stone on the surface of the specimen instead of to the binder. This is because hitting a stone often results in a shorter contact time of the impact compared to applying the impact to the binder. A shorter contact time of the impact provides energy to the specimen over a wider frequency range compared to a longer contact time of the impact. The softer binder may damp the impact which leads to a longer contact time that reduces the excitable frequency range compared to hitting a stone. The accelerometer is also recommended to be attached to a stone instead of to the binder.



Figure 3: The accelerometer attached to the specimen and the impact hammer

Figure 4 presents the measured response of the specimen due to five hammer impacts, where the acceleration is plotted over time (4a) and frequency (4b). The figure shows the response of the flexural modes of vibration of a disc-shaped specimen. The fast Fourier transform (FFT) is used to transform acceleration over time (4a) to acceleration over frequency (4b). The record time in figure 4a depends on the damping of the specimen. It is important to use a sufficiently long record time to not cut off the vibrations of the specimen before it has damped out. The record length can be reduced with increasing temperatures due to increased damping. In addition, the voltage range and amplification should be chosen so that the maximum peaks of the vibrations are not cut off. Figure 4b shows the first four flexural resonance frequencies (the peak amplitudes) excited by the impact excitation. The amplitude of the acceleration depends on the force of the impact. The resonance frequencies presented in Figure 4b can be used to apply the concept of RAS to estimate the material properties of asphalt concrete.

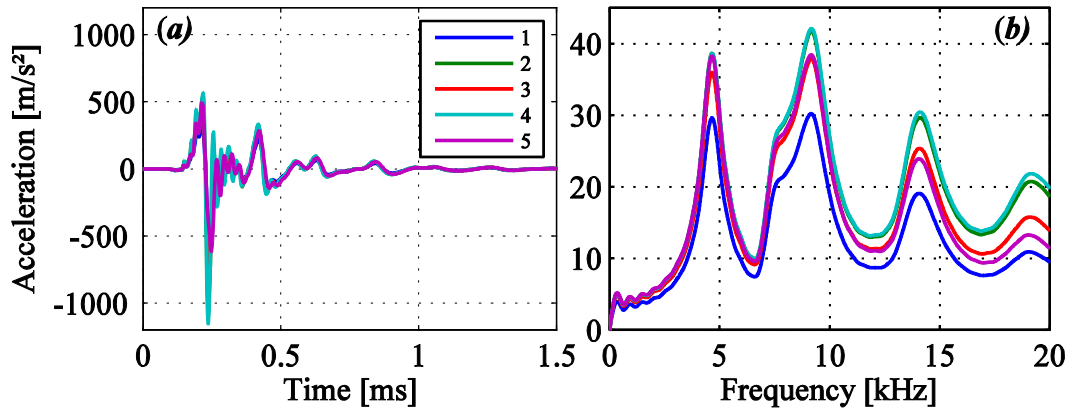


Figure 4: Measured response for an asphalt concrete specimen in time (a) and frequency domain (b) from five impacts

2.2 Frequency response function measurements

As mentioned earlier, the amplitude of the acceleration can be normalized by measuring the force of the impact. Figure 5 shows the measured force of each of the five impacts in time domain (5a) and frequency domain (5b). In similarity to the response, the FFT is used to transform the force over time to force over frequency. The recording of the measurements is initiated by using the impact of the hammer as a trigger. For this purpose a pre-trigger time is assigned to be sure to measure the complete load pulse (see Figure 5a).

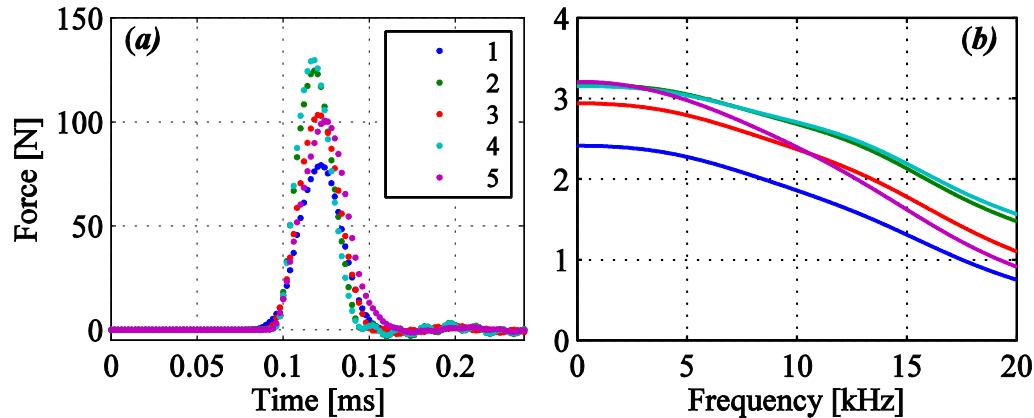


Figure 5: The applied load of five impacts in time (a) and frequency domain (b)

The amplitude of the driving force (Figure 5b) and the amplitude of the response (4b) in frequency domain are used to determine FRFs according to the following equation,

$$H(f) = \frac{Y(f) \cdot X^*(f)}{X(f) \cdot X^*(f)} \quad (1)$$

where $H(f)$ is the frequency response function, $Y(f)$ is the measured acceleration, $X(f)$ is the measured applied force and $X^*(f)$ is the complex conjugate of the

applied force. Figure 6 presents the five FRFs determined from the five measured responses and impacts (from figure 4 and 5). The five similar FRFs show the dynamic behavior of the asphalt concrete specimen independent of the applied force. Measurements of both the applied load and the resonance frequencies are often referred to as modal testing.

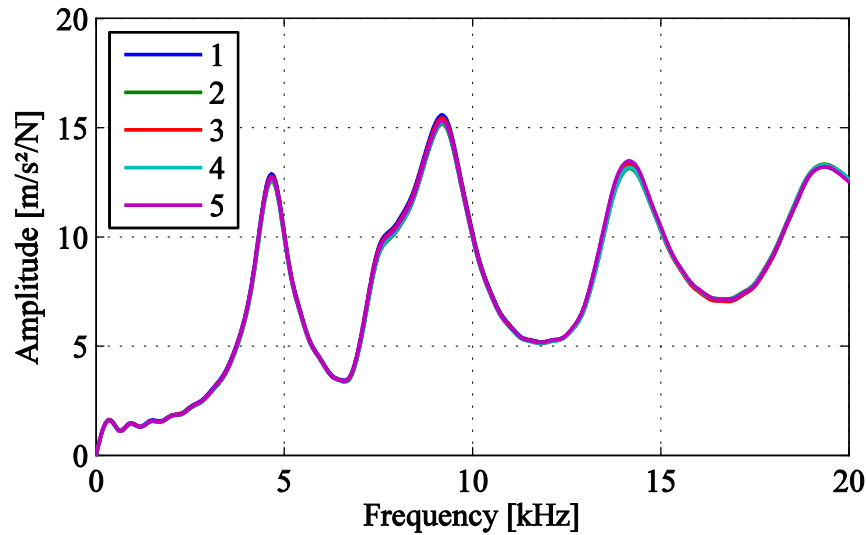


Figure 6: FRFs determined from the measured response (Figure 4b) and force (Figure 5b) of five impacts

The determination of the material properties in this thesis have been based on averaged FRFs that are calculated from n number of measurements. The averaged FRF is calculated accordingly,

$$H(f) = \left(\frac{1}{n} \sum_{k=1}^n Y_k(f) \cdot X_k^*(f) \right) / \left(\frac{1}{n} \sum_{k=1}^n X_k(f) \cdot X_k^*(f) \right) \quad (2)$$

where $n = 5$ in the example presented in this chapter and k is the index of the impact number ranging from 1 to n . The averaging of the FRFs is performed in the complex domain for each frequency. The coherence function is often used as an indication of the quality of the averaged FRF. This function is a measure of the phase difference between the different measurements at each frequency. Thus, a value of one of the coherence function means that the phase difference between input and output is constant for the five (in this example) different impacts. The coherence function is calculated accordingly,

$$CF(f) = \left(\frac{1}{n} \sum_{k=1}^n X_k^*(f) \cdot Y_k(f) \right)^2 / \left[\left(\frac{1}{n} \sum_{k=1}^n X_k(f) \cdot X_k^*(f) \right) \cdot \left(\frac{1}{n} \sum_{k=1}^n Y_k(f) \cdot Y_k^*(f) \right) \right] \quad (3)$$

where $CF(f)$ is the coherence function, $X_k^*(f) \cdot Y_k(f)$ is the cross power spectrum, $X_k(f) \cdot X_k^*(f)$ is the auto power spectrum of the impulse and $Y_k(f) \cdot Y_k^*(f)$ is the auto power

spectrum of the response. Figure 7 presents the calculated coherence function based on the five measurements presented in this chapter.

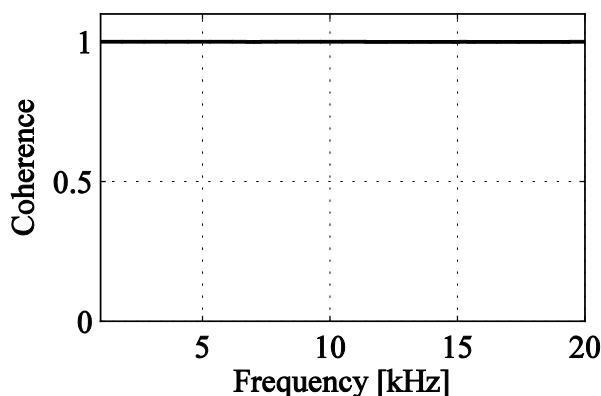


Figure 7: Coherence function determined from the measured response (Figure 4b) and force (Figure 5b) of five impacts

2.3 Isotropic linear viscoelastic properties of asphalt concrete

The isotropic linear viscoelastic behavior of asphalt concrete can be governed by two material parameters such as e.g. the complex stiffness modulus and complex Poisson's ratio. These material properties are used as input to the design of pavements and are often used to calculate the complex shear modulus for rutting predictions of pavements. The material properties are expressed as complex numbers to describe the elastic and viscous behavior of asphalt concrete, where the phase angle (ϕ) represents the relation between the viscous (imaginary part) and the elastic component (real part). The phase angle of asphalt concrete is therefore a measure of the intrinsic material damping. In conventional cyclic loading the phase angle can be quantified by the angular frequency and the measured time lag between the stresses and strains. In the case of resonance testing, the width of the resonance peaks and the amplitude of the FRFs are highly depending on the damping. The complex modulus (E^*), the dynamic modulus ($|E^*|$) and the phase angle are related according to the following relationships,

$$E^* = E' + iE'' = |E^*| \cdot e^{i\phi}, \quad (4)$$

$$\phi = \tan^{-1}\left(\frac{E''}{E'}\right), \quad (5)$$

where E' is the storage modulus representing the elastic component and E'' is the loss modulus representing the viscous component.

The material properties of asphalt concrete are frequency and temperature dependent due to the viscoelastic nature of the binder. Therefore, measurements of the material properties are performed at different temperatures and frequencies as illustrated through the dynamic modulus shown in Figure 8. The dynamic modulus

measured at 0.1 to 20 Hz and at six different temperatures is presented in this figure.

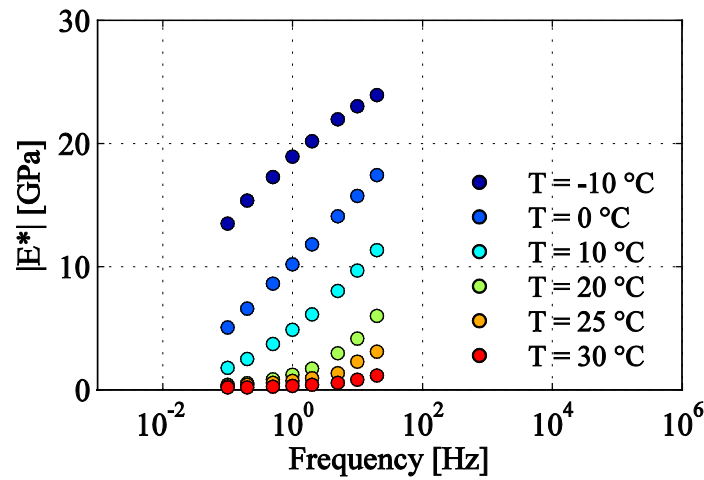


Figure 8: Temperature and frequency dependency of the dynamic modulus of asphalt concrete

Asphalt concrete is generally known to be a thermo-rheological simple material (Nguyen et al. 2009). This assumption enables shifting of the measured modulus in Figure 8 to a single curve, illustrated in Figure 9, which is valid for a specific reference temperature. The shifting is possible since a thermo-rheological simple material can have the same behavior (material properties) at low frequencies and low temperatures as at higher frequencies and higher temperatures, or vice versa. A shift factor can be calculated for each measurement temperature to shift the measured moduli so that it corresponds to performing the measurements at other frequencies at the specific reference temperature. The validity of the thermo-rheological simple assumption can be controlled by plotting the results in e.g. a Cole-Cole diagram, Black diagram or a Wicket plot which are independent of the shift factors (Levenberg 2011). Cole-Cole diagrams are presented in the appended papers for each of the estimated master curves. The Williams-Landel-Ferry (WLF) relationship can be used to calculate the shift factors (α_T) accordingly,

$$\log \alpha_T(T) = \frac{-c_1(T - T_{ref})}{c_2 + T - T_{ref}} \quad (6)$$

where c_1 and c_2 are material constants, T is the test temperature, and T_{ref} is the reference temperature (Williams et al. 1955). The shifting is performed by multiplying the shift factors with the loading frequencies (f) to obtain reduced frequencies (f_{red}) accordingly,

$$f_{red} = \alpha_T(T) f \quad (7)$$

The single curve presented in Figure 9 is the master curve, which describe the modulus over a range of frequencies and temperatures. The master curve is often

expressed by approximate relationships such as e.g. the sigmoidal function (Pellinen et al. 2003). However, there are several models that can be fitted to dynamic and complex modulus measurements to estimate master curves (Yusoff et al. 2011; Pritz 2003; Moon et al. 2013). The sigmoidal, the Havriliak-Negami (HN) and the 2S2P1D models have been applied in the appended papers in this thesis (Olard and Di Benedetto 2003; Havriliak and Negami 1966; Madigosky et al. 2006).

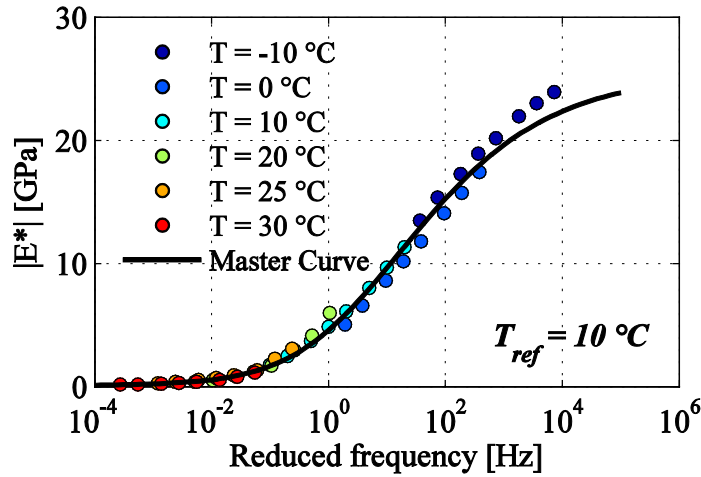


Figure 9: Shifted dynamic modulus of asphalt concrete to create a master curve at 10 °C

2.4 Characterizing material properties through FRFs

Measured FRFs, presented in chapter 2.2 and Figure 6, provide the base needed to characterize isotropic linear viscoelastic properties of asphalt concrete specimens through modal testing. In addition to measured FRFs, theoretical FRFs need to be accurately calculated to extract information of the material properties from the measurements. In this thesis, the finite element method (FEM) has been applied to perform three-dimensional calculations of FRFs using the following equation of motion,

$$-\rho\omega^2\mathbf{u}-\nabla\cdot\boldsymbol{\sigma}=F_p e^{i\phi}, \quad (8)$$

where ρ is the material density, ω is the angular frequency ($\omega = 2\pi f$), \mathbf{u} is the displacement vector, ∇ is the vector operator ($\nabla = [\partial/\partial X, \partial/\partial Y, \partial/\partial Z]$), $\boldsymbol{\sigma}$ is the Cauchy stress tensor ($\boldsymbol{\sigma} = \mathbf{C} : \boldsymbol{\varepsilon}$), F_p is a point load, ϕ is the phase of the cyclic load, $\boldsymbol{\varepsilon}$ is the strain tensor ($\boldsymbol{\varepsilon} = \frac{1}{2}[(\nabla\mathbf{u})^T + \nabla\mathbf{u}]$), \mathbf{C} is the fourth-order stiffness tensor (including E^* and ν^*) and $\nabla\mathbf{u}$ is expressed accordingly,

$$\nabla \mathbf{u} = \begin{bmatrix} \frac{\partial u}{\partial X} & \frac{\partial u}{\partial Y} & \frac{\partial u}{\partial Z} \\ \frac{\partial v}{\partial X} & \frac{\partial v}{\partial Y} & \frac{\partial v}{\partial Z} \\ \frac{\partial w}{\partial X} & \frac{\partial w}{\partial Y} & \frac{\partial w}{\partial Z} \end{bmatrix}, \quad (9)$$

where (X, Y, Z) are the constant material (reference) coordinates and (u, v, w) are the global Cartesian components of the displacement vector. Details about the finite element model such as the mesh, geometry and positions of the applied load are explained for the specific specimens in the appended papers.

Initial values of the complex modulus and complex Poisson's ratio are assumed to be able to compute FRFs that can be compared to the measured FRFs (the forward problem). Thereafter, the complex modulus and complex Poisson's ratio are adjusted iteratively until the computed FRFs match the measured ones (the inverse problem). This procedure requires the use of a model capable to account for the complex (elastic and viscous) behavior along with the temperature and frequency dependency of asphalt concrete. The following equations show the HN model including the shift factors applied to estimate the complex modulus and complex Poisson's ratio master curves,

$$E^*(\omega, T) = E_\infty + \frac{(E_0 - E_\infty)}{\left[1 + (i\omega\alpha_T(T)\tau)^\alpha\right]^\beta}, \quad (10)$$

$$v^*(\omega, T) = v_\infty + \frac{(v_0 - v_\infty)}{\left[1 + (i\omega\alpha_T(T)\tau)^\alpha\right]^\beta}. \quad (11)$$

where E_0 and v_0 are the low frequency values of the modulus and Poisson's ratio, E_∞ and v_∞ are the high frequency values of the modulus and Poisson's ratio, ω is the angular frequency, α governs the width of the loss factor peak, β governs the asymmetry of the loss factor peak, $\tau=1/\omega_0$ is the relaxation time which describes the position of the loss factor peak along the frequency axis and where ω_0 is the frequency at the loss factor peak (Hartmann et al. 1994). It is the parameter values of E_∞ , v_∞ , α , β and τ that are estimated through the optimization of the FRFs. The low frequency parameters E_0 and v_0 are assumed since realistic values of asphalt concrete do not affect the FRFs. As mentioned earlier there are several models that can be applied to accurately describe the frequency dependent complex modulus and complex Poisson's ratio (Olard and Di Benedetto 2003; Pritz 1996; Pritz 2003). However, it is of great practical advantage to limit the number of parameters that needs to be estimated in the optimization process of the computed FRFs, since this reduces the computational time and facilitates the process of finding the global minimum. The optimization has been performed by using COMSOL® LiveLink™ for MATLAB®, where COMSOL® is used to compute the FRFs and MATLAB® enable the optimization of the FRFs through the *patternsearch* function

(LiveLink™ for MATLAB® User's Guide 2013). The following objective function has been used to minimize the difference between the computed and measured FRFs.

$$Error = \sum_{i=1}^N \left(|H_{MNorm_i}| \times \left| \frac{|H_{M_i}| - |H_{T_i}|}{|H_{M_i}|} \right| \right), \quad (12)$$

where H_{MNorm} is the normalized measured FRF used to weigh the frequencies around the resonances higher, H_M is the measured FRF, H_T is the theoretical FRF, N is the number of data points and i is the index of the data point. Figure 10 shows an example of a computed FRF that has been optimized to fit the measurements.

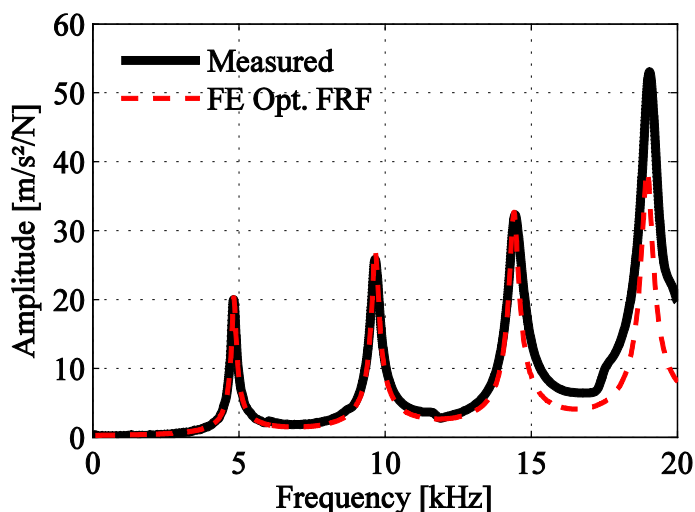


Figure 10: Example of measured and computed FRF of the longitudinal mode type of a beam shaped asphalt concrete specimen

2.5 Materials

The measurements presented in the appended papers have been performed to asphalt concrete specimens of different shapes and mixture designs. Beam shaped specimens were tested in Paper I, II and V, cylindrical specimens were tested in paper III and paper IV, and a disc-shaped specimen was tested in paper VI. Details of the materials used in this thesis are presented in each of the appended papers.

2.6 Non-destructive quality control of pavements

The above presented modal testing to estimate master curves of asphalt concrete specimens can be directly linked to surface wave testing of pavements (Ryden 2004). Surface wave testing can be used to estimate the stiffness and thickness of the different layers in a pavement construction (Nazarian 1993; Nazarian 1999; Ryden 2004). This is performed by measuring the phase velocity of dispersive guided Lamb waves generated by applying a load impulse to the surface of the pavement structure according to Figure 11. Due to the free surface and the different layers of a pavement structure, guided waves (surface waves) are formed when compression and shear waves interact at the interfaces of the different layers. The propagation of guided Lamb waves is depending on the stiffness and thickness of

the different layers making them useful for characterization of pavement structures. The guided Lamb waves are dispersive which means that the phase velocity of the propagating waves is frequency dependent. The relation between phase velocity and frequency can be described by dispersion curves. The stiffness and thickness of the layers in a pavement structure are estimated by solving the forward and inverse problem. Theoretical dispersion curves are calculated and iteratively matched against the measurements until the adjusted theoretical layer model provides dispersion curves that match the measured ones.

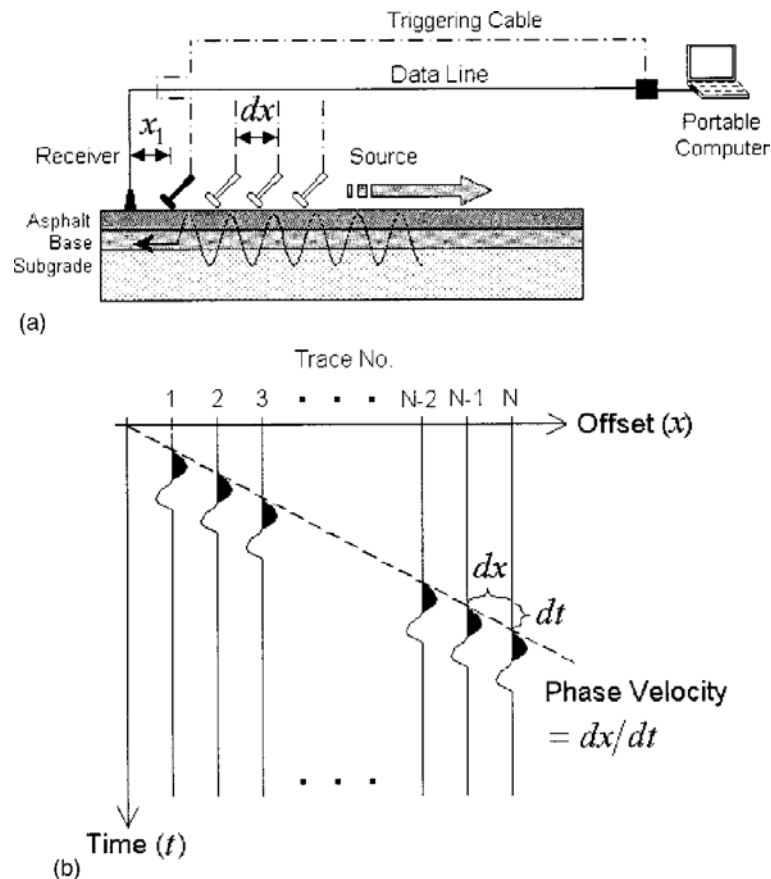


Figure 11: Surface wave testing of pavements illustrating the measurement procedure (a) and the measured phase velocity (b) (Ryden et al. 2004)

Results from non-destructive field measurements of pavements can be directly linked to laboratory modal testing since the material is subjected to approximately the same loading frequency and strain levels in both the field and laboratory measurements. As an example, a modulus measured at any temperature in the field can be directly compared to a master curve that has been estimated through modal testing of a laboratory produced specimen. This allows for non-destructive quality control and quality assurance of new and old pavement constructions. The surface wave testing of pavements has been developed by using accelerometers to measure the phase velocity. Recent work has presented an application of microphones to enable future field measurements that can be performed faster by continuously moving over the pavement (Bjurström et al. 2014).

Figure 12 illustrates the use of a master curve as a tool for quality control and quality assurance of pavements. In this example, a master curve has been determined through modal testing and upper and lower limits of the dynamic modulus are determined by the design requirements of the pavement. By performing surface wave measurements at any temperature within the presented interval and at the frequency of 500 Hz, the resulting dynamic modulus can be compared to the laboratory determined master curve and to the design requirements.

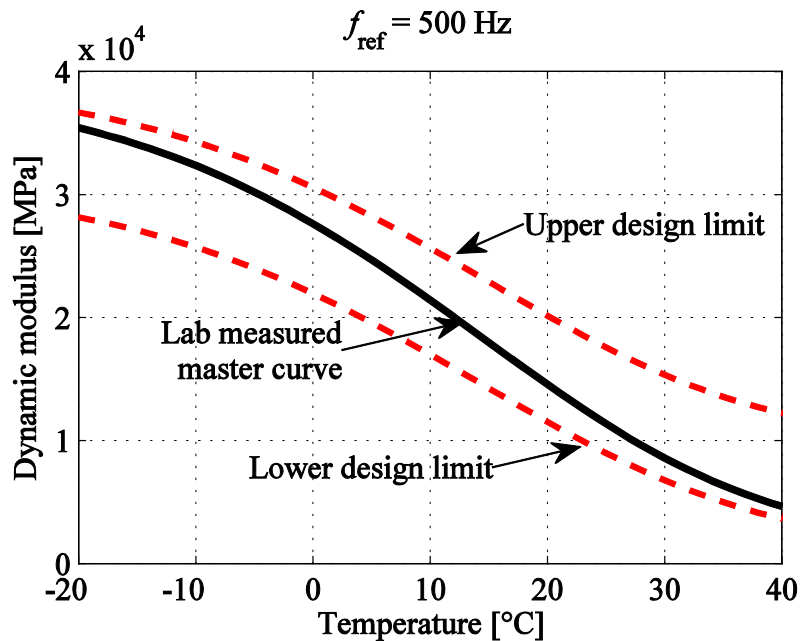


Figure 12: Non-destructive quality control of pavements through surface wave testing and laboratory modal testing

3 Repeatability of resonance frequency testing

In addition to the work presented in the appended papers, a number of measurements have been performed to investigate and demonstrate the repeatability of impact resonance testing of asphalt concrete. The findings from these measurements are aimed to facilitate the practical implementation of this testing technique by highlighting some important aspects of the test. All measurements presented in this chapter have been performed to a cylindrical disc-shaped specimen.

3.1 Effect of impact force and accelerometer attachment

A study was conducted by investigating if the force of the impact affects the amplitude and the resonance frequencies of the FRFs. The measurements were performed by applying light and hard impacts exciting the flexural modes of vibration at room temperature. Firstly, three series of five light impacts were applied, which were followed by three series of five hard impacts. Averaged FRFs were calculated for each series. Figure 13 and 14 present the magnitude of the force for one series of five light impacts and one series of five hard impacts, respectively.

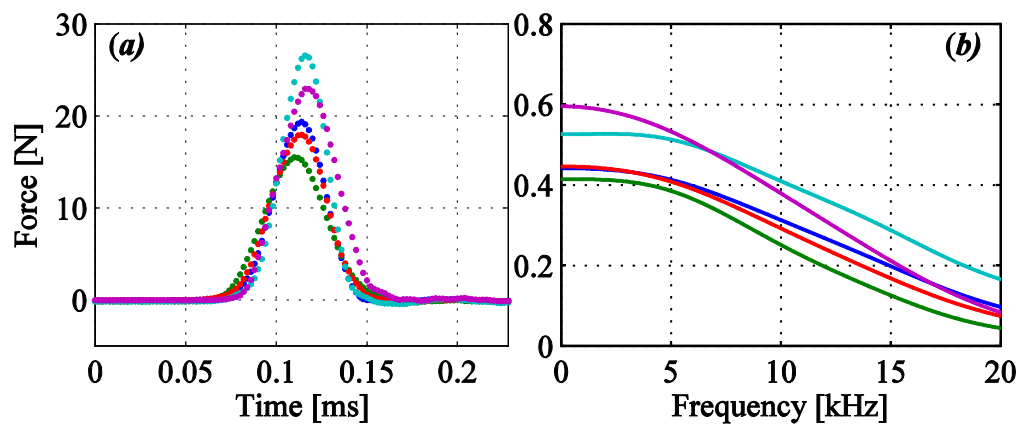


Figure 13: Magnitude of the applied force through light impacts

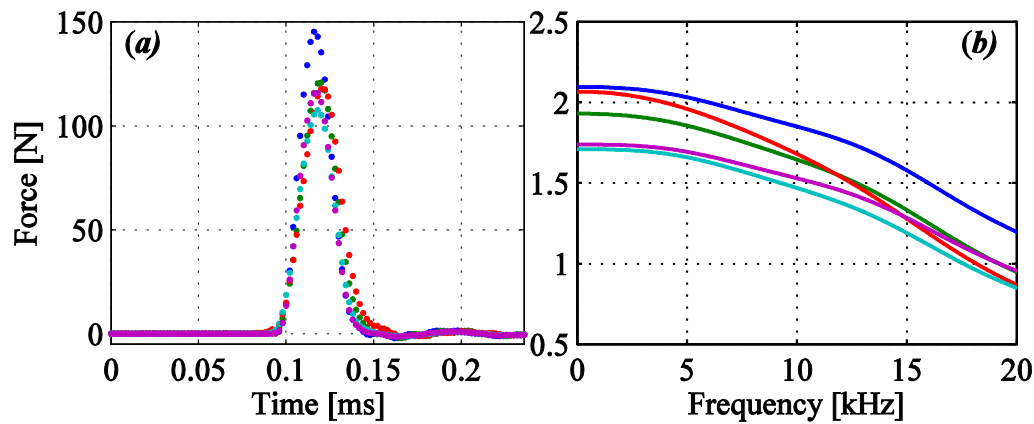


Figure 14: Magnitude of the applied force through hard impacts

The results of the six averaged FRFs presented in Figure 15 shows a good repeatability. Neither the resonance frequencies nor the amplitude seems to depend significantly on the magnitude of the applied load at the strain levels generated by these impacts. Note that the accelerometer was attached carefully once and not reattached during the measurements.

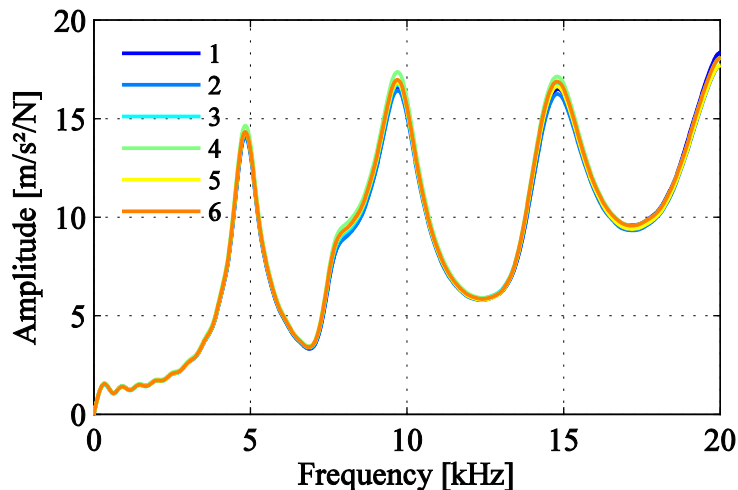


Figure 15: Effect of light (1 to 3) and hard impacts (4 to 6) to FRFs of the flexural modes of vibration

The effect of a poorly attached accelerometer was also studied. Figure 16 presents six averaged FRFs, where the accelerometer has deliberately been attached lightly and/or not perfectly aligned with the surface. Each FRF has been averaged from five impacts of the same accelerometer attachment. The figure indicates that the resonance frequencies are less affected of the poor attachment compared to the amplitude of the FRFs. Especially the two higher modes of vibration and the higher frequency range show significant variations of the amplitude. This study demonstrates that it is very important with a good bond to the specimen and to perform a proper attachment of the accelerometer. Additional results of this effect are presented in section 3.3 where measurements have been performed by different operators.

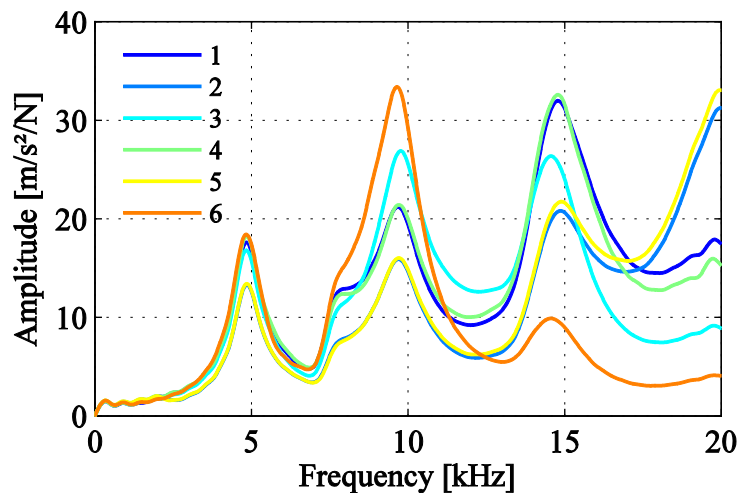


Figure 16: Effect of a poorly attached accelerometer to FRFs of the flexural modes of vibration

3.2 Repeating the attachment of the accelerometer

In this study, the accelerometer was carefully attached and removed five times to investigate if attaching and removing the accelerometer from the specimen affects the measurements. Each series, including five impacts, were followed by removing and reattaching the accelerometer before the next series. The flexural modes of vibration of a cylindrical disc-shaped asphalt concrete specimen were excited at 20 °C. The reattachments and the excitations were performed by the same operator. Table 1 shows the results of the fundamental flexural resonance frequency. The table presents the standard deviation (SD) in hertz and the relative standard deviation (RSD) in percent for each impact number and for each attachment. The SD and RSD (the absolute value of the coefficient of variation) are also calculated from the averages of the impacts and the attachments. It can be seen in Table 1 that the SD and RSD are lower for the five impacts of the same attachment compared to the SD and RSD of the five different attachments. Although it is clear that the attachment has an effect on the resonance frequency measurements, the RSD has a maximum value of 0.1 % which is still very low. It should be noted that with the sampling rate of 500 kHz (max frequency = 250 kHz) and the FFT size of 500 000 (frequency bins = 250 000), the frequency resolution becomes 1 Hz in these measurements.

Table 1: Effect of repeating the accelerometer attachment to the fundamental resonance frequency

Impact nr.	1	2	3	4	5	Average	SD (Hz)	RSD (%)
Attach. 1	4791	4791	4792	4794	4794	4792.4	1.52	0.03
Attach. 2	4779	4784	4782	4784	4783	4782.4	2.07	0.04
Attach. 3	4789	4786	4787	4788	4787	4787.4	1.14	0.02
Attach. 4	4785	4789	4788	4790	4788	4788.0	1.87	0.04
Attach. 5	4790	4791	4787	4791	4788	4789.4	1.82	0.04
Average	4786.8	4788.2	4787.2	4789.4	4788	4787.9	1.01	0.02
SD (Hz)	4.92	3.11	3.56	3.71	3.94	3.64		
RSD (%)	0.1	0.07	0.07	0.08	0.08	0.08		

Figure 17 presents the averaged FRFs measured in this study, where each averaged FRF are based on five impacts in each series. The figure shows that the amplitude of the FRFs appears to be more affected by the reattachment of the accelerometer than the resonance frequencies. Table 2 presents the values of the attachment study for the measured FRFs shown in Figure 17, where the SD and RSD of the amplitude and the resonance frequencies have been calculated for the three first flexural resonance frequencies.

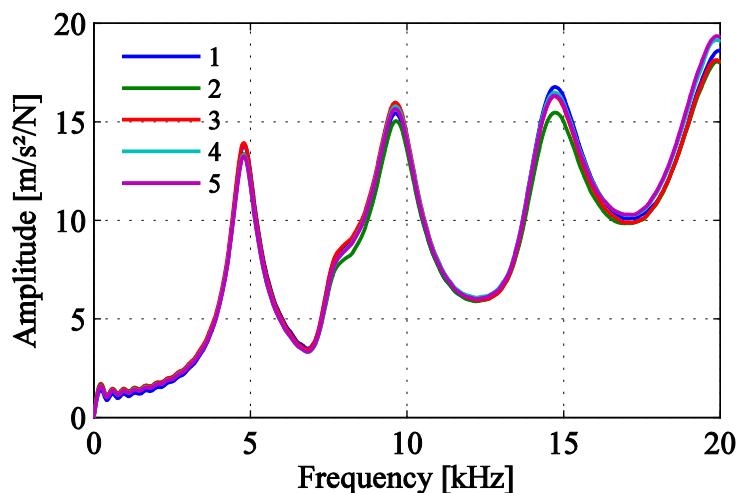


Figure 17: Averaged FRFs of five different accelerometer attachments

The RSD of the resonance frequencies of the FRFs show values in the same low magnitude as the study of the resonance frequencies of the response only. However, larger RSD values are shown for the amplitude of the FRFs.

Table 2: Effect of repeating the accelerometer attachment to FRFs

Attachment	1	2	3	4	5	Average	SD	RSD (%)
1 st resonance	4801	4783	4791	4791	4792	4791.5	6.27	0.13
1 st amplitude	13.86	13.39	13.91	13.31	13.24	13.55	0.32	2.35
2 nd resonance	9630	9652	9628	9631	9628	9633.7	10.11	0.10
2 nd amplitude	15.47	15.11	15.97	15.80	15.64	15.60	0.33	2.13
3 rd resonance	14737	14741	14712	14717	14717	14725.0	13.48	0.09
3 rd amplitude	16.91	15.55	16.30	16.55	16.31	16.32	0.50	3.04

3.3 Measurements performed by different operators

The effect of different operators was investigated by letting people with no earlier experience of resonance frequency measurements perform the measurements. After a brief (~5 minutes) introduction and demonstration by the author, the unexperienced operators were supposed to attach the accelerometer to the specimen and apply five impacts each. The resulting FRFs from the five operators are shown in Figure 18. There are clear differences between the different operators regarding the amplitude of the second and third resonance frequency. The resonance frequencies showed a good agreement between the operators with one exception for the third resonance frequency.

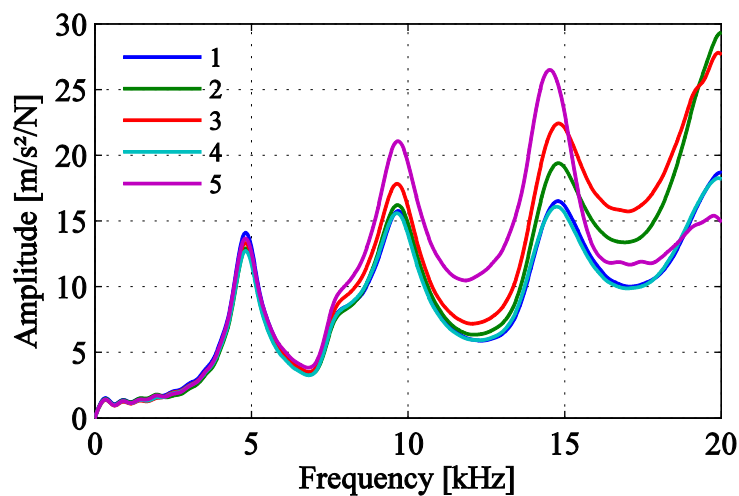


Figure 18: Averaged FRFs of the five operators. Each operator attached the accelerometer before applying five impacts

24 | Repeatability of resonance frequency testing

Table 3 present the measured values of the frequencies and amplitudes for the three first flexural resonance frequencies. The RSD of the resonance frequencies show that the third resonance stands out from the others. The RSD of the amplitudes increases considerably with increasing frequencies.

Table 3: Results of five different operators attaching and applying five impacts to excite the flexural modes of vibration of the disc-shaped asphalt concrete specimen

Operator	1	2	3	4	5	Average	SD	RSD (%)
1 st resonance	4816	4826	4811	4815	4811	4816	6.18	0.13
1 st amplitude	14.08	12.94	13.31	12.71	13.70	13.35	0.55	4.14
2 nd resonance	9687	9666	9648	9644	9678	9665	18.48	0.19
2 nd amplitude	15.72	16.24	17.76	15.59	21.14	17.29	2.32	13.42
3 rd resonance	14792	14802	14809	14747	14527	14735	119	0.81
3 rd amplitude	16.49	19.39	22.26	16.13	26.65	20.18	4.38	21.71

Based on the earlier results of the effect of a poorly attached accelerometer it was identified that this might be an influence to the deviations shown in Figure 18 and Table 3. Therefore, another study was performed by carefully attaching the accelerometer once, which was followed by five different operators applying five impacts each to the specimen. These results are presented in Figure 19 and show a better agreement between the operators.

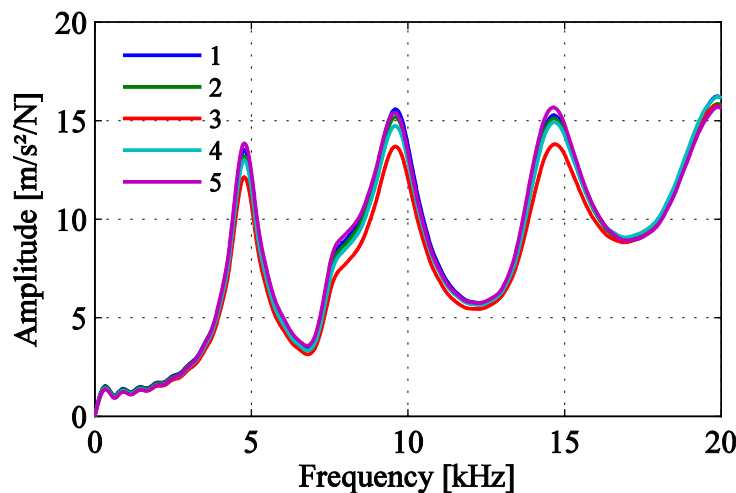


Figure 19: Averaged FRFs of the five operators. The author attached the accelerometer and each operator applied five impacts without changing the position of the accelerometer

Table 4 presents the averages, the SD and the RSD of the frequencies and amplitudes of the three first flexural resonance frequencies. The second and the third resonance frequency show an improved repeatability for both resonances and amplitudes of the FRFs compared to the results in Table 3. As mentioned earlier it is important with a proper attachment of the accelerometer when performing these kinds of measurements. Therefore some training of attaching the accelerometer is recommended for new operators that will perform this kind of testing. However, the most essential aspect to avoid errors is to simply be careful when attaching the accelerometer and to control that the accelerometer is properly attached.

Table 4: Results of five different operators applying five impacts to excite the flexural modes of vibration of the disc-shaped asphalt concrete specimen

Operator	1	2	3	4	5	Average	SD	RSD (%)
1 st resonance	4784	4778	4776	4777	4779	4779	3.11	0.07
1 st amplitude	13.51	13.19	12.24	13.00	13.94	13.18	0.63	4.80
2 nd resonance	9605	9593	9600	9594	9571	9593	13.26	0.14
2 nd amplitude	15.58	15.18	13.84	14.75	15.38	14.95	0.69	4.60
3 rd resonance	14660	14665	14696	14674	14643	14668	19.48	0.13
3 rd amplitude	15.27	15.11	13.96	14.96	15.95	15.05	0.71	4.74

3.4 Position of the accelerometer and the impact

The effect of the position of the accelerometer and the impact on a cylindrical disc-shaped asphalt concrete specimen was investigated for the flexural and longitudinal modes of vibration. Small variations in geometry and possible inhomogeneity within the specimen may introduce differences to these resonance frequency measurements. The different positions of the accelerometer are illustrated in Figure 20. The excitation of the flexural modes of vibration was performed by applying the impact to the opposite position of the accelerometer, e.g. an impact in position 5 for accelerometer position 1 and so on. The longitudinal modes of vibration were excited in the middle of the specimen while moving the accelerometer around the eight different positions.

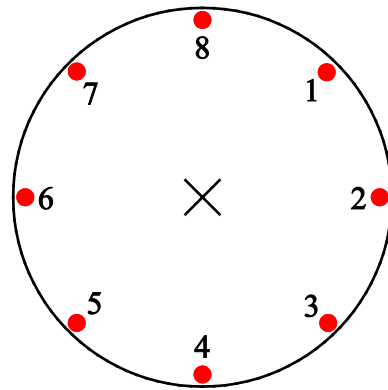


Figure 20: Positions of the accelerometer on the cylindrical specimen

Figure 21 shows the measured FRFs of the flexural modes of vibration measured at eight different positions. The resonance frequencies seem to be less affected by the position compared to the amplitude in this figure. Table 5 shows the values of the frequencies and amplitudes of the three first resonances frequencies. Also in this study there are higher values of the RSD for the amplitude compared to the resonance frequencies.

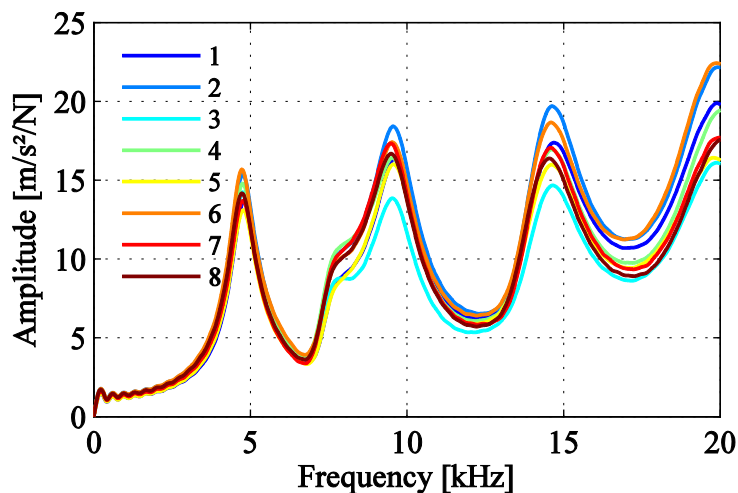


Figure 21: FRFs of the flexural modes of vibration due to eight different positions of the accelerometer

The results presented in Figure 21 and Table 5 can be compared to the study of repeating the accelerometer attachment in chapter 3.2 (Figure 17 and Table 1 and 2). Such a comparison indicates how much the reattachments of the accelerometer contribute to the variations and how much the position of the measurements affects the variations.

Table 5: Different position of the accelerometer and the impacts of the flexural modes of vibration

Position	1	2	3	4	5	6	7	8	Average	SD	RSD (%)
1 st resonance	4796	4755	4754	4755	4772	4730	4760	4732	4757	21.2	0.45
1 st amplitude	13.63	15.39	14.24	14.79	13.12	15.63	13.69	14.20	14.34	0.88	6.12
2 nd resonance	9621	9558	9529	9522	9571	9527	9466	9478	9534	50.0	0.52
2 nd amplitude	16.33	18.45	13.79	16.37	16.01	17.24	17.36	16.71	16.53	1.35	8.16
3 rd resonance	14709	14649	14668	14631	14630	14613	14574	14530	14626	55.24	0.38
3 rd amplitude	17.39	19.82	14.66	16.91	16.08	18.52	17.24	16.41	17.13	1.56	9.01

Figure 22 shows the results of the different accelerometer positions of the longitudinal modes of vibration and Table 6 present the frequency and amplitude for the fundamental resonance frequency. Also in this case, the amplitude of the FRFs is more affected by the different positions than the frequency of the fundamental longitudinal mode of vibration.

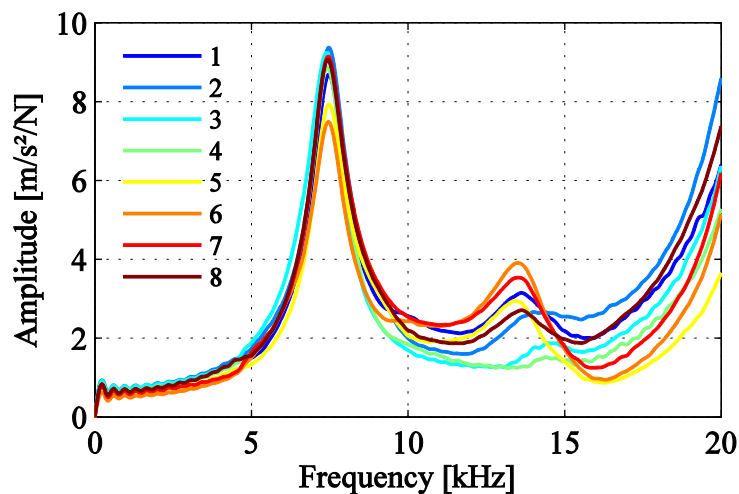


Figure 22: FRFs of the longitudinal modes of vibration due to eight different positions of the accelerometer

Table 6: Different position of the accelerometer and the impacts of the longitudinal modes of vibration

Position	1	2	3	4	5	6	7	8	Average	SD	RSD
Frequency	7474	7472	7393	7423	7474	7456	7450	7438	7448	28.6	0.38
Amplitude	8.69	9.38	9.24	8.87	7.94	7.49	9.15	9.09	8.73	0.67	7.70

3.5 Summary of the repeatability studies

The resonance frequencies show low values of the RSD throughout all of the repeatability studies. However, the amplitude is consequently showing higher values of the RSD for the different studies. The dominating elastic component (storage modulus) of the complex modulus is mostly depending on the resonance frequencies while the smaller viscous component (loss modulus) is governed by the amplitude. The accuracy of the dynamic modulus is therefore reflected by the good repeatability of the resonance frequencies while the loss modulus (e.g. phase angle and damping) is more sensitive to the factors showed to affect the amplitude. To conclude, measurements of resonance frequencies measurements can be performed by unexperienced operators and still provide repeatable values of the dynamic modulus. To obtain a high repeatability of the phase angle, care must be taken when attaching the accelerometer and the position of the impact and accelerometer may affect these results. Studies as presented in chapter 3.2 and 3.4 may be used in the future to estimate a magnitude of the error that comes from measuring an actual specimen (heterogeneous to some degree) in comparison to a truly homogenous modelled specimen.

4 Summary of appended papers

This thesis is based on six papers which are presented in an order reflecting the steps taken to develop and apply the resonance and modal testing to characterize asphalt concrete. This chapter presents a brief summary of each appended paper while the following chapter 5 summarizes the key figures and findings of the six papers appended in this thesis.

Paper I: *Application of resonant acoustic spectroscopy to asphalt concrete beams for determination of the dynamic modulus*

In this paper, resonant ultrasound spectroscopy was applied to asphalt concrete to study the potential to determine the complex modulus for several measured resonance frequencies. Resonance frequency measurements were performed by measuring the responding vibration of the specimens due to a hammer impact. Numerical calculations based on minimizing the Lagrangian and the Rayleigh-Ritz approximation is applied to solve the forward problem of calculating the natural frequencies. This is followed by the inverse problem where the elastic constants are adjusted iteratively until a good match between calculated and measured resonance frequencies are obtained. The complex modulus was derived for three resonance frequencies per temperature and mode type for the studied beam shaped specimens. Although this was an improvement to earlier reported resonance frequency measurements, binder shift factors were still needed to accurately determine the master curves due to the limited temperature and frequency range covered in these tests.

Paper II: *Characterizing the low strain complex modulus of asphalt concrete specimens through optimization of frequency response functions*

The gained knowledge from paper I showed that the complex modulus needed to be characterized over a wider frequency range at each measurement temperature. For this purpose, frequency response functions (FRFs) were determined by measuring both the applied impact force and the responding vibration of the specimen. The FRFs adds an additional input to the complex moduli characterization in terms of the amplitude of the measured frequency response. The finite element method was used to compute theoretical FRFs that were optimized against the amplitudes and frequencies of the measured FRFs to derive the complex modulus and Poisson's ratio over a wide frequency range. The fitting of the amplitude gives a direct estimation of the damping properties (hence the complex moduli) in contrast to only matching resonance frequencies. The approach of optimizing FRFs was compared to the application of RAS used in paper I. The developed method based on FRFs showed an improved accuracy of estimating the damping compared to the application of RAS to asphalt concrete. Furthermore, master curves of the complex modulus were determined by only applying modal testing to the specimen.

Paper III: *Comparing linear viscoelastic properties of asphalt concrete measured by laboratory seismic and tension-compression tests*

In this paper the modal test method presented in paper II and conventional tension-compression test were performed to a cylindrical asphalt concrete specimen. The complex moduli and the complex Poisson's ratio determined from the two test methods were compared. The master curves of the complex moduli and complex Poisson's ratio are determined at lower strain levels in the modal test method (maximum $\sim 10^{-7}$) compared to the tension-compression testing ($50 \cdot 10^{-6}$). As expected, the modal testing resulted in a slightly higher dynamic modulus where the strain level dependency of the asphalt concrete was seen to increase with increasing temperatures. However, the complex Poisson's ratio of the two test methods showed large differences that could not be explained except for that the tension-compression determined complex Poisson's ratio could not match the measured FRFs.

Paper IV: *Complex modulus and complex Poisson's ratio from cyclic and dynamic modal testing of asphalt concrete*

Due to the observed differences between the Poisson's ratio of the modal and the conventional tension-compression testing presented in paper III, further comparisons between the two methods and Poisson's ratio were performed in this paper. This comparison was extended to include eight different specimens of two different mixes including the mix tested in paper III. Modal testing was performed to two cylindrical specimens of different mixes and compared to previously tension-compression tested specimens. Hence, the comparison between the two testing methods is based on results from different specimens in this paper. The complex modulus and complex Poisson's ratio that were characterized through the modal test showed consistent results to the previous measurements presented in paper III. However, the new tension-compression results showed different values of the complex Poisson's ratio compared to the tension-compression measurements performed in paper III. The new tension-compression determined Poisson's ratio agreed well with the modal testing determined complex Poisson's ratio. It was concluded that the modal testing and tension-compression measurements results in similar values of the complex Poisson's ratio while the dynamic modulus of the modal test becomes slightly higher than the conventional testing due to the strain level dependency of asphalt concrete.

Paper V: *Observed deviations from isotropic linear viscoelastic behavior of asphalt concrete through modal testing*

The modal testing developed in paper II was used to measure E^* , ν^* and G^* of a beam shaped asphalt concrete specimen by exciting the longitudinal, flexural and torsional modes of vibration. The measurements were performed to the same specimen to investigate the validity of isotropic linear viscoelastic theory to asphalt concrete. Unlike previous conventional testing of E^* and G^* performed to asphalt concrete, the modal testing does not introduce any differences in the test conditions (such as e.g. boundary conditions, set-up, and specimens) between the characterization of E^* and G^* . This enables a direct study of the different material

behavior without a need to account for possible differences in the test equipment as in the case of the conventional testing. The results indicated that the asphalt concrete specimen agreed with the isotropic linear viscoelastic assumption at low temperatures and high frequencies (>10 kHz at 0 °C). However, at higher temperatures and lower frequencies, deviations from the isotropic linear viscoelastic behavior were observed. An overestimation of the dynamic shear modulus and Poisson's ratio values above 0.5 were obtained at the low frequency and high temperature range when these material properties were calculated according to isotropic linear viscoelastic theory.

Paper VI: *Non-contact excitation of fundamental resonance frequencies of an asphalt concrete specimen*

In this paper, the possibility to excite an asphalt concrete specimen through non-contact excitation was studied. The fundamental longitudinal resonance frequency of a disc-shaped asphalt concrete specimen was measured by using a speaker to perform the non-contact excitation. The non-contact excitation enabled automated measurements at different strain amplitudes without disturbing the temperature of the asphalt concrete. The effect of damage to the fundamental resonance frequency of an asphalt concrete specimen could therefore be investigated. Neither the undamaged nor the damaged asphalt concrete specimen showed any strain level dependency at the applied strain levels (maximum ~0.26 micro-strains). However, the damaged specimen showed a drop in resonance frequency compared to the resonance frequency of the undamaged state. Continuous measurements over time of the damaged specimen revealed a recovery (healing) of the resonance frequency towards the frequency of the undamaged state. The results of this non-contact approach demonstrated an accuracy which opens up the possibility for future studies of damage, fatigue, and healing with a precision that has not been possible before.

5 Summary of results and discussion

Paper I shows that an application of RAS can be used to characterize the complex modulus of asphalt concrete. However, RAS only provide a sparse amount of data at each temperature since the derivation of the modulus is limited to the first few resonance frequencies. Furthermore, the damping properties need to be estimated by an additional approach such as e.g. the half-power bandwidth method, which may reduce the accuracy of the complex modulus in the case of high intrinsic damping. The optimization of FRFs developed in Paper II overcomes these problems and can provide accurate values of the complex modulus (including damping) over a wide and fine sampled frequency range. Figure 23 presents the key results of Paper I and Paper II, where the RAS and FRFs characterized complex moduli at different measurement temperatures are compared. The presented master curve is determined through the FRF optimization approach.

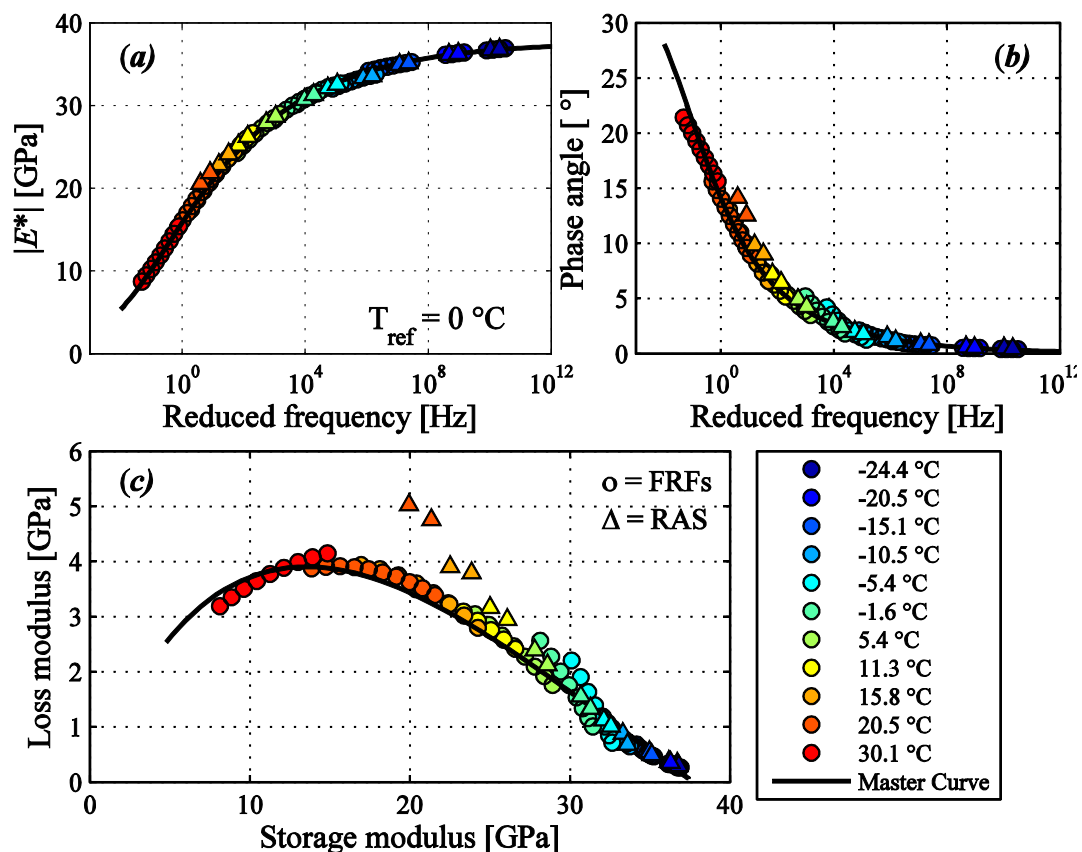


Figure 23: Complex modulus of a beam shaped asphalt concrete specimen determined through RAS (paper I) and optimization of FRFs (paper II)

Figure 23a show that the two approaches results in very similar dynamic moduli, while the phase angle presented in Figure 23b indicate small differences between the RAS and FRF determined moduli at higher temperatures and lower frequencies. The differences between the two approaches are more clearly shown in the Cole-Cole diagram presented in Figure 23c, where results from the low frequency and high temperature range are emphasized. The Cole-Cole diagram show that the loss moduli estimated through RAS deviates from the FRF estimated loss moduli when the intrinsic damping increases due to increasing temperatures. The half-power bandwidth method applied in the application of RAS has been shown to be sufficiently accurate only as long as the damping ratio is below approximately 0.1, corresponding to a phase angle of approximately 11° (Wang et al. 2012). In this case, the complex moduli of the two approaches start to deviate at a phase angle of approximately 10° , which indicates a reduced accuracy of the half-power bandwidth method. The Cole-Cole diagram presented in Figure 23c is an indication of the accuracy of the estimated master curve due to that it is independent of the calculated shift factors. Therefore, a unique curve is expected for the complex moduli determined for each temperature if the assumption of a thermo-rheological simple material holds. The estimated loss and storage moduli (complex moduli) at each temperature follow the unique master curve in Figure 23c.

The modal testing and optimization of FRFs are compared to conventional tension-compression testing in paper III and IV. Figure 24 shows the results of the complex moduli measured and presented in these papers for one of the mixtures. The tension-compression results of three different specimens show consistent results in all three subplots which include the dynamic moduli (Figure 24a), the phase angle (Figure 24b) and a Cole-Cole diagram presenting the loss and storage moduli (Figure 24c). Also, the modal testing of two measured specimens show consistent results in all three subplots. Note that the specimen GB3 (s.3) has been tested by both tension-compression and modal testing. The master curves enable a detailed comparison of the two test methods over a wide frequency range even though the modal testing is performed at higher frequencies compared to the tension-compression tests. The difference between the dynamic moduli and phase angle (Figure 24a and 24b) of the two test methods is believed to be due to the strain level dependency of asphalt concrete. This difference was seen to be smaller at high frequencies and low temperatures and to increase with increasing temperatures and decreasing frequencies

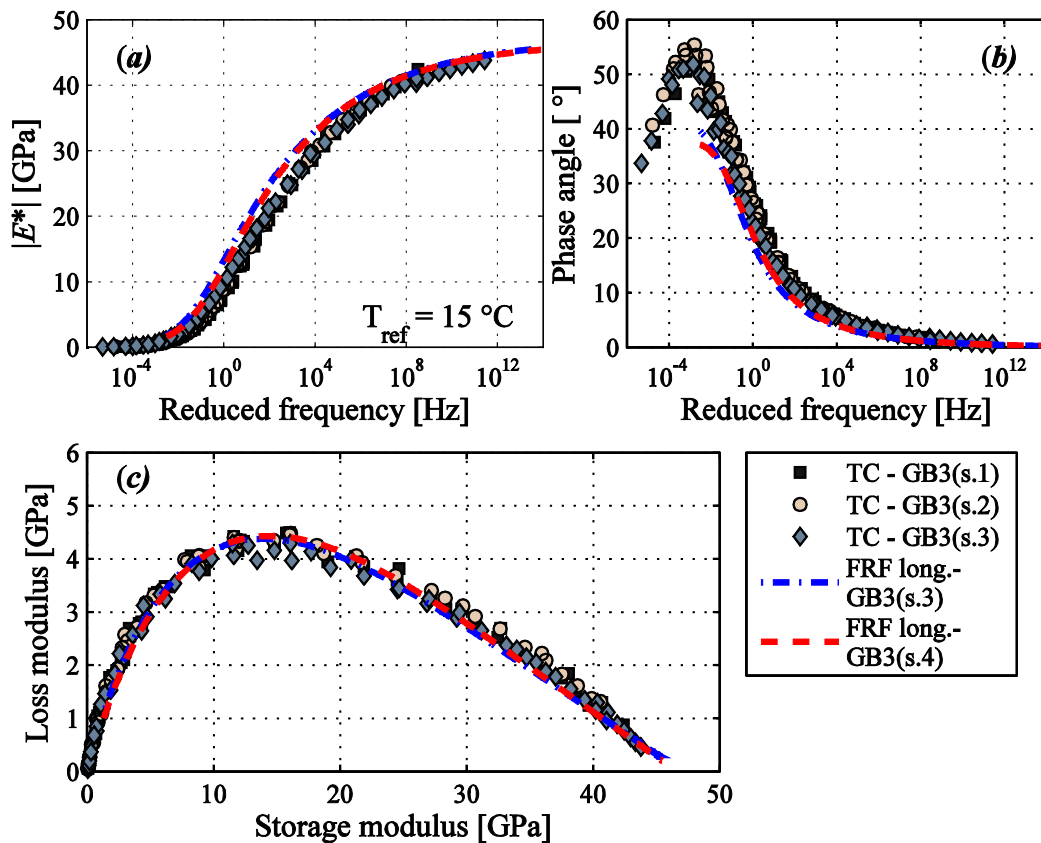


Figure 24: Complex modulus determined through modal and tension-compression testing of cylindrical asphalt concrete specimens

Figure 25 shows the modal and tension-compression determined complex Poisson's ratio of the same specimens as presented in Figure 24. It is clear that the tension-compression determined Poisson's ratio of the specimen labeled TC-GB3 (s.3) differs from all other tension-compression and modal test results of the complex Poisson's ratio. The most likely reason for this is that there have been some measurement errors in this conventional test. The deviation is an example of the sensitivity of the conventional test set-up. Very small measurement errors have a relatively large effect on the Poisson's ratio. For example, a $\sim 0.4\mu\text{m}$ change of the specimen diameter corresponds to a change of Poisson's ratio with ~ 0.1 , which is approximately the difference shown in Figure 25a. The difference between the Poisson's ratio of the two specimens characterized through modal testing comes from that different amount of parameters in the applied HN model were optimized to match the theoretical and measured FRFs. In the case of the specimen measured in paper III (GB3 (s.3)), the estimated parameters (α , β and τ) of the complex modulus were also applied to the complex Poisson's ratio. However, it was observed in paper IV that a different value of the relaxation time (τ) for Poisson's ratio may in some cases improve the fit between measured and theoretical FRFs as the temperatures increases. The complex Poisson's ratio of the specimen labeled FRF long. – GB3 (s.3) in Figure 25 has been estimated using the τ of the complex modulus, while the specimen labeled FRF long. – GB3 (s.4) has been estimated with a different value of τ for Poisson's ratio in the HN model. The characterized complex Poisson's ratio of the modal testing using a specific value of τ for Poisson's

ratio show a good agreement with the Poisson's ratio determined through the tension-compression testing.

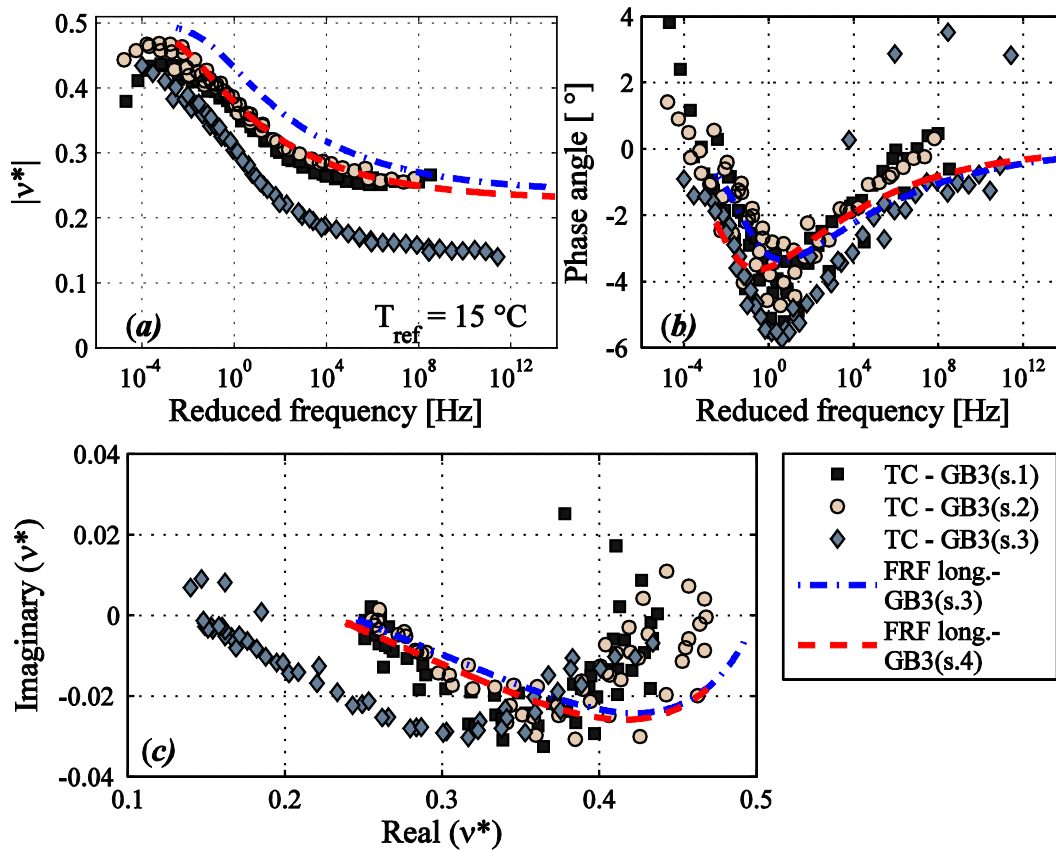


Figure 25: Complex Poisson's ratio determined through modal and tension-compression testing of cylindrical asphalt concrete specimens

The developed modal testing provides new opportunities to accurately study the behavior of asphalt concrete. Therefore, the modal testing was applied to a beam-shaped specimen in Paper V to study if the commonly assumed isotropic linear viscoelastic behavior of asphalt concrete is valid over a wide frequency range. Previous measurements to investigate the validity of this relation have shown discrepancies from isotropic linear viscoelastic behavior. However, different specimens for the shear and Young's modulus measurements have been required in most of these different conventional tests (Christensen et al. 2003; Saadeh et al. 2003). The complex shear modulus determined through the torsional modal testing is presented in Figure 26 along with the complex shear moduli calculated from the measured complex Young's moduli and Poisson's ratio. The results in Figure 26 show that the isotropic linear viscoelastic behavior is valid at higher frequencies and lower temperatures but not at higher temperatures and lower frequencies. Figure 26 also shows that a dynamic shear modulus calculated according to linear viscoelastic theory from the measured complex Young's modulus and Poisson's ratio is overestimated at temperatures and frequencies that pavements normally are exposed to.

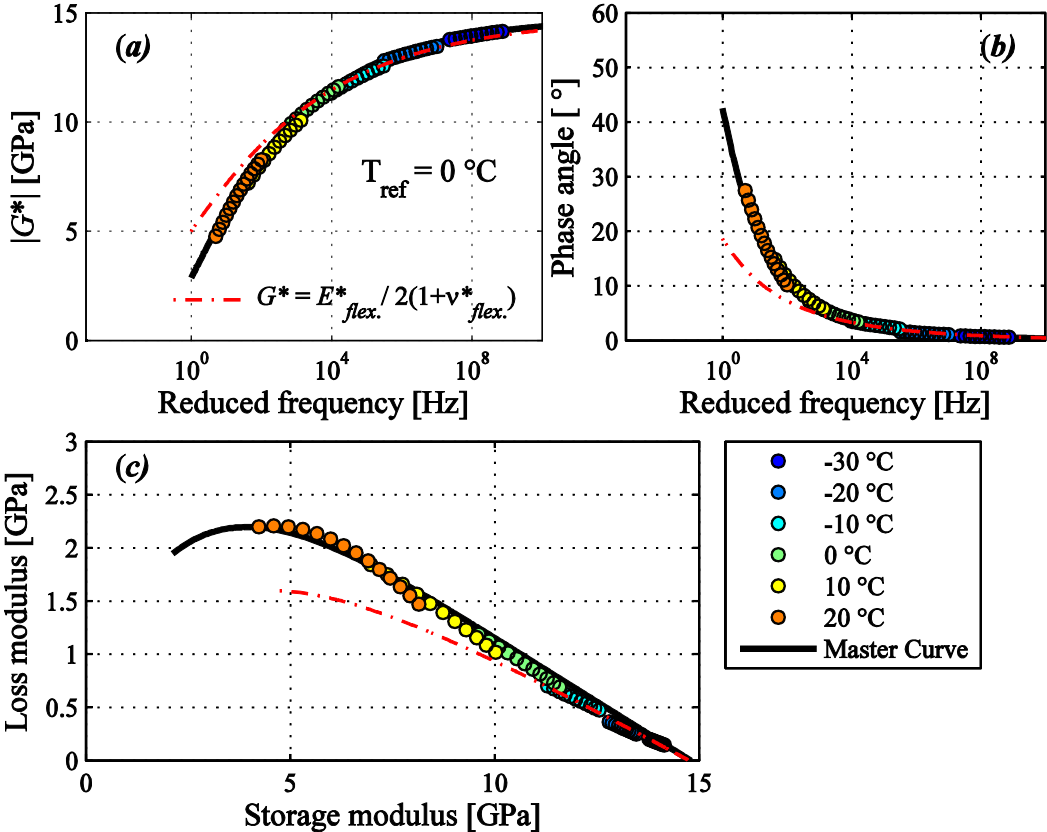


Figure 26: Measured and calculated complex shear modulus of a beam-shaped asphalt concrete specimen

Figure 27 show a similar discrepancy between the measured and calculated complex Poisson’s ratio. The calculated Poisson’s ratio based on the measured Young’s and shear moduli agrees with the measured Poisson’s ratio at higher frequencies. However, at lower frequencies the Poisson’s ratio deviates from the measurements and eventually exceeds 0.5. These results of the discrepancy from isotropic linear viscoelastic theory presented here confirm the results of earlier conventional testing.

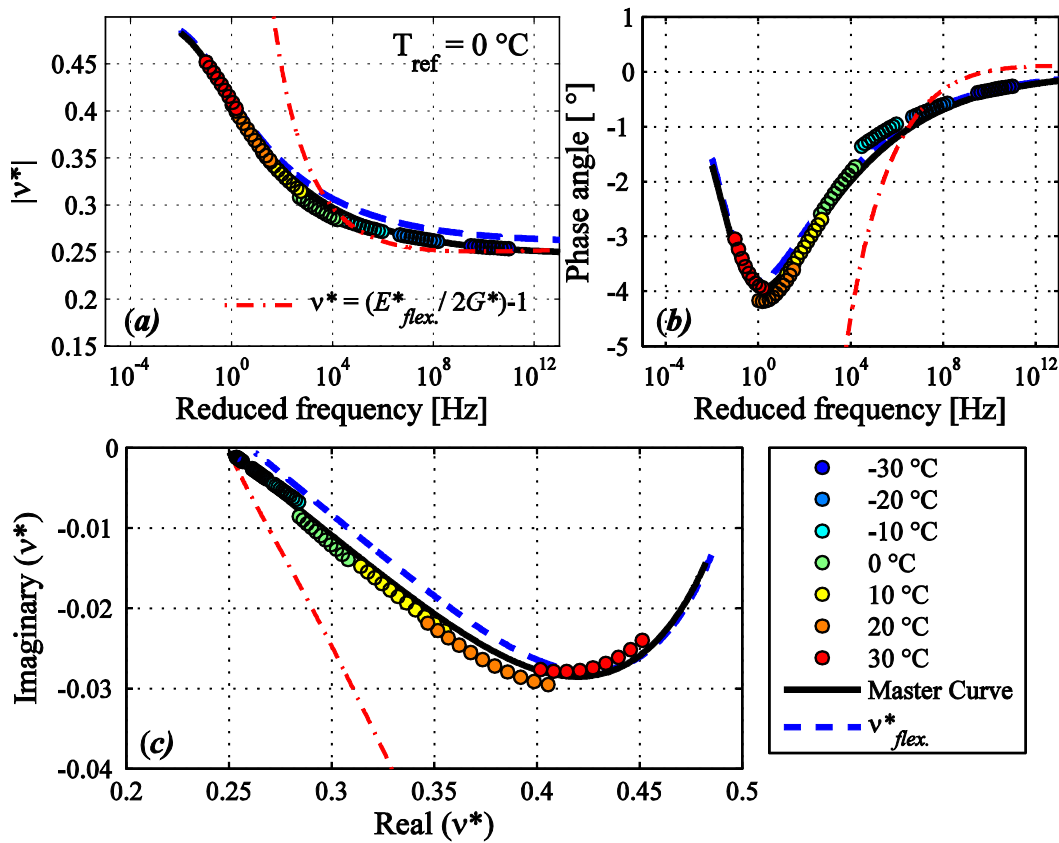


Figure 27: Measured and calculated complex Poisson's ratio of a beam-shaped asphalt concrete specimen

Figure 28 presents the normalized complex Young's moduli determined from the longitudinal and flexural modes of vibration measurements. The normalized complex shear moduli determined from the torsional modes of vibration are also presented in this figure. Figure 28 shows that the phase angle and the damping of the shear moduli are higher than the Young's moduli at the lower frequency range and higher temperatures. The increasing deviation between the complex shear and complex Young's moduli as the frequencies decreases seems to be a reason to the discrepancies from isotropic linear viscoelastic behavior.

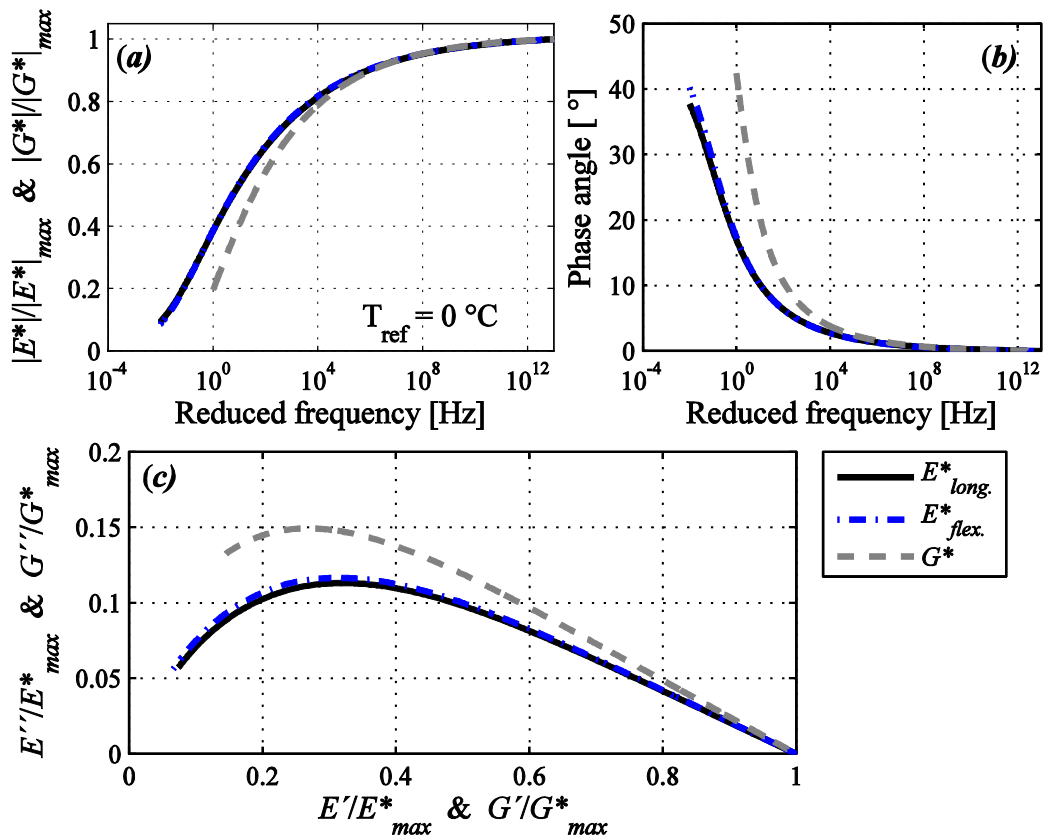


Figure 28: Normalized complex modulus master curves of the flexural, longitudinal and torsional modes of vibration

Measurements of resonance frequencies can also be applied to study nonlinear properties such as damage, healing and fast and slow dynamics (Payan et al. 2014). Nonlinear resonant ultrasound spectroscopy (NRUS) was therefore applied to a disc-shaped asphalt concrete specimen in Paper VI. Figure 29 presents the fundamental longitudinal resonance frequency of the specimen excited by both an impact hammer and by a speaker. The use of the speaker enabled non-contact excitation of the specimen at different automatically controlled drive levels and the measurements could be performed without opening the door to the climate chamber. This eliminated any disturbances to the temperature when measuring small possible changes of the resonance frequency due to nonlinear effects. Figure 29 show that both the hammer and speaker excitation of an undamaged asphalt concrete specimen resulted in the same resonance frequency. Also, the resonance frequency of the undamaged specimen did not change with increasing drive amplitudes. Consequently, a linear behavior was observed at these strain levels where the maximum strain level was approximated to ~ 0.26 micro-strains.

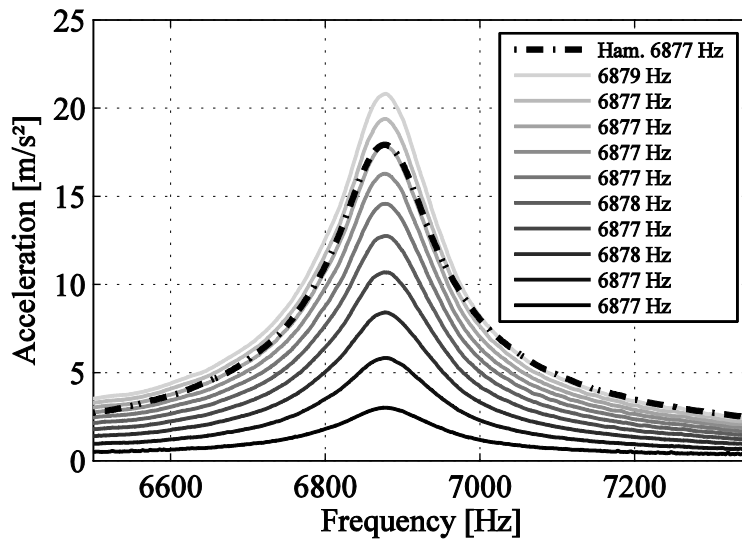


Figure 29: The fundamental longitudinal resonance frequency excited at different strain amplitudes before damage

Figure 30 show results of measurements performed after a small damage was induced by applying several hard impacts with a ~0.055 kg hex key to the asphalt concrete specimen. The damage caused a drop in the resonance frequency (compare to Figure 29) but no strain level dependency was seen from the speaker excitation at different drive amplitudes. However, a small difference between the resonance frequency excited by the hammer and speaker can be observed in this figure which may indicate nonlinearity.

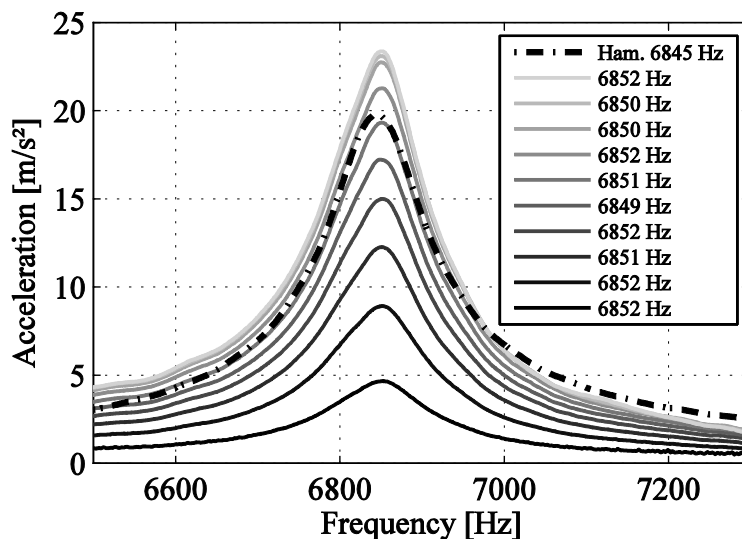


Figure 30: The fundamental longitudinal resonance frequency excited at different strain amplitudes after damage

Potential healing or slow dynamics effects were studied by repeating the speaker frequency sweeps at several different times after the damage was induced. These measurements showed a systematic recovery of the resonance frequencies towards the initial resonance with increasing time. Figure 31 presents the resonance

frequency measured before damage and at four different times after the damage was induced. The measured recovery may be due to healing of the asphalt concrete specimen or due to slow dynamics, where the recovery to the equilibrium state may last for days. However, since the degree of damage was not measured it is difficult to separate these effects. A comparison of these presented results of the asphalt concrete specimen can be made to rubber, where measurements showed large slow dynamics effects while no strain level dependency was observed (Haller and Hedberg 2006). This novel application of a speaker demonstrates the accuracy and truly non-destructive nature of non-contact resonance testing, which enables studies of nonlinear parameters such as e.g. damage, healing, aging and slow dynamics with a new level of precision.

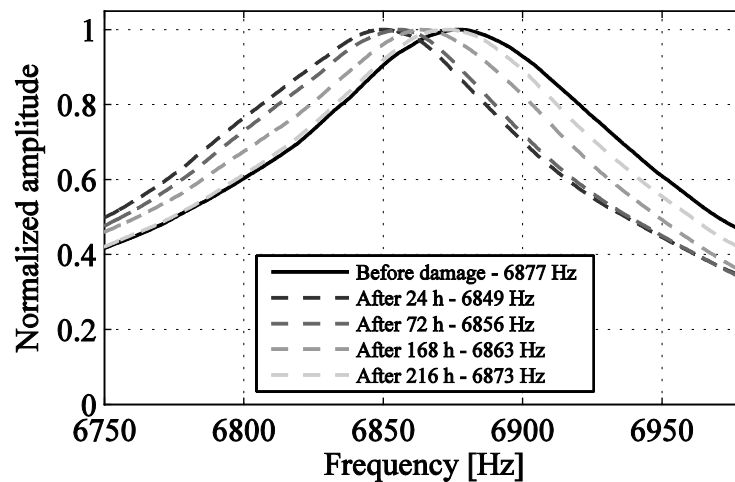


Figure 31: Recovery of the fundamental longitudinal resonance frequency excited by a speaker

6 Conclusions

The resonance frequencies of asphalt concrete specimens can be measured with very good repeatability. Therefore, resonance and modal testing can be used to characterize material properties of asphalt concrete with high accuracy. However, care should be taken when attaching the accelerometer so that a good bond to the sample is obtained. A poor bond between the accelerometer and the sample can affect the accuracy of the measured amplitude of the FRFs.

The application of RAS to asphalt concrete beams has shown that the complex modulus can be characterized for multiple modes of vibration at each testing temperature. However, by optimizing FRFs an increased accuracy of the complex moduli is obtained due to the improved estimation of the damping. In addition, measuring and calculating FRFs enable material characterization over a sufficiently wide frequency range to determine master curves by only applying modal testing.

The comparison between the modal testing and the conventional cyclic loading show that the lower strain levels applied in the modal testing gives higher dynamic moduli and lower phase angle than the conventional measurements. The strain level does not seem to have a significant effect on the complex Poisson's ratio since the two test methods results in similar values. However, it was observed that an accurate characterization of the complex Poisson's ratio is more challenging than determining the moduli. Modal testing in combination with conventional tests can be used to extend the material characterization over a wider range of frequencies and strain levels. This may increase the knowledge of the nonlinear behavior of asphalt concrete. Although, the modal testing have several advantages compared to the conventional testing such as cost and time, it may not be possible to characterize the material properties at the lowest frequencies of the conventional testing. The modal testing is also performed at lower strain levels compared to what an actual pavement are exposed to.

The results of the discrepancy from isotropic linear viscoelastic theory confirmed results of earlier measurements. However, the modal testing does not introduce any differences in the test conditions between the complex Young's modulus and complex shear modulus unlike some of the previous conventional measurements performed to asphalt concrete. Therefore, the comparison can be focused only on different material behavior instead of accounting for possible differences in the test equipment. In addition, the measurements are performed to the same specimen. The differences in the damping properties between the complex Young's moduli and complex shear moduli at higher temperatures and lower frequencies may be a reason to the observed deviations from isotropic linear viscoelastic theory. An overestimation of the dynamic shear modulus is made for the asphalt concrete specimen at high temperatures when calculated from the measured Young's modulus and Poisson's ratio.

44 | Conclusions

Non-contact excitation of the resonance frequencies of asphalt concrete specimens can be performed through the use of a speaker. Impact and speaker excited resonance frequencies at different strain amplitudes were shown to give similar results for the undamaged asphalt concrete specimen. Damage in the asphalt concrete specimen was identified by a drop of the resonance frequency, but no nonlinear fast dynamics was observed. However, a recovery of the resonance frequency was measured over time for the damaged asphalt concrete specimen. This recovery may be due to healing or slow dynamics. These results demonstrate the possibility for new truly non-destructive applications to monitor damage and healing of asphalt concrete.

To conclude, resonance frequency measurements are in contrast to conventional cyclic loading economic and simple to perform. Resonance and modal testing can provide an improved accuracy to the characterization of asphalt concrete which may lead to a better understanding of the mechanical material properties at low strain levels. The modal testing provide a link to surface wave testing of pavements which enable non-destructive quality control of new and old pavement constructions.

7 Recommendations and future work

It is recommended to measure specimens with other gradations, binder, shapes and dimensions than those presented in this thesis. Such a study may help to find geometries that can be excited over extended frequency ranges to include more resonance frequencies which can simplify accurate estimation of the complex modulus and especially the complex Poisson's ratio. In addition, the possibility to estimate and account for the magnitude of the error that comes from measuring an actual (heterogeneous) specimen in comparison to a truly homogenous modelled specimen could be further studied.

Further studies of nonlinear measurements to asphalt concrete are of interest. The work presented in paper VI show that non-contact measurements of resonance frequencies is a promising method to detect damage and to study healing. This method can be further used to study healing of samples with a known degree of damage. These types of measurements are needed to be able to account for possible healing in future design procedures.

The methodology presented in this thesis can be implemented for practical use in any laboratory aiming at testing asphalt concrete. The testing is easily performed and does not require expensive or heavy equipment. The main challenge for a successful implementation may be to compute and optimize the FRFs. However, measurements of FRFs performed in a laboratory could be combined with an application developed specifically to compute and optimize FRFs. The development of such an application could be a focus of future work to facilitate the implementation of the presented method.

References

- Airey, G. D., Rahimzadeh, B. (2004) "Combined bituminous binder and mixture linear rheological properties," *Constr. Build. Mater.*, Vol. 18, 535–548
- ASTM (2008), C215-08, *Standard Test Method for Fundamental Transverse, Longitudinal, and Torsional Frequencies of Concrete Specimens* (American Society for Testing and Materials, West Conshohocken, PA)
- Bari, J., Witczak, M. (2006) "Development of a New Revised Version of the Witczak E* Predictive Model for Hot Mix Asphalt Mixtures," *J. of AAPT*, Vol. 75, 381-423
- Bernard, S., Grimal, Q., Laugier, P. (2014). "Resonant ultrasound spectroscopy for viscoelastic characterization of anisotropic attenuative solid materials," *J. Acoust. Soc. Am.*, Vol. 135, Issue 5, 2601-2613
- Bjurström, H., Ryden, N. and Birgisson, B., (2014), "Non-contact surface wave testing of pavements: comparing a rolling microphone array with accelerometer measurements," accepted for publication in the special issue on *Advanced Sensing Technologies for NDE and SHM of Civil Infrastructures, Smart Structures and Systems*.
- Booshehrian A., Mogawer, W. S., Bonaquist, R. (2013) "How to Construct an Asphalt Binder Master Curve and Assess the Degree of Blending between RAP and Virgin Binders", *J. Mater. Civ. Eng.*, Vol. 25, No. 12
- Brown, E. R., Kandhal, P. S., Roberts, F. L., Kim, Y. R., Lee, D. Y., Kennedy, T. W. (2009). *Hot Mix Asphalt Materials, Mixture Design and Construction* (NAPA Research and Education Foundation, Lanham, MD)
- Ceylan, H., Gopalakrishnan, K., and Kim, S. (2009) "Looking to the future: the next-generation hot mix asphalt dynamic modulus prediction models", *Int. J. Pavement Eng.*, 10(5), 341 – 352
- Christensen Jr, D. W., Pellinen, T., Bonaquist, R. F. (2003). "Hirsch model for estimating the modulus of asphalt concrete," *J. of AAPT*, Vol. 72, 97-121.
- Comsol Mutliphysics 4.3b, LiveLink™ for MATLAB® User's Guide, © Comsol (2009-2011)
- Daniel, J., Chehab, G., Kim, Y. R. (2004). "Issues Affecting Measurement of the Complex Modulus of Asphalt Concrete." *J. Mater. Civ. Eng.* 16, Special Issue: Strengthening of Concrete Structures with Advanced Composite Materials-Prospects and Problems, 469–476.

- Demarest, H. H. (1971) "Cube-resonance method to determine the elastic constants of solids", *J. Acoust. Soc. Am.* 49, 768-775
- Di Benedetto, H., Delaporte, B., Sauzéat, C. (2007) "Three-Dimensional Linear Behavior of Bituminous Materials: Experiments and Modeling," *Int. J. Geomech.*, Vol. 7, No. 2, 149-157.
- Di Benedetto, H., Sauzéat, C., Sohm, J. (2009) "Stiffness of Bituminous Mixtures Using Ultrasonic Wave Propagation", *Road Mater. Pavement*, 10(4), 789-814
- Finnveden, S., Hörlin, N.-E., Barbagallo, M. (2014) "Dynamic characterization of viscoelastic porous foams used in vehicles based on an inverse finite element method," *J. Acoust. Soc. Am.*, Vol. 135(4), 1834-1843
- Garcia, G., Thompson, M. (2007) "HMA Dynamic Modulus Predictive Models– A Review, "Research Report FHWA-ICT-07-005, Illinois Center for Transportation
- K. C. E. Haller and C. M. Hedberg, "Three Nonlinear NDE Techniques On Three Diverse Objects," in *Innovations in Nonlinear Acoustics: 17th International Symposium on Nonlinear Acoustics*, AIP Conference Proceedings 838, edited by A. A. Atchley et al. (American Institute of Physics, State College, Pennsylvania, 2006), pp. 87-90.
- Hartmann B, Lee G.F., Lee J.D. (1994) "Loss factor height and width limits for polymer relaxations," *J. Acoust. Soc. Am.* Vol.95, 226–33.
- Havriliak, S., and Negami, S. (1966). "A complex plane analysis of α -dispersions in some polymer systems," *J. Polym. Sci. C*, Vol. 14, 99–117.
- Holland, R. (1968) "Resonant properties of piezoelectric ceramic rectangular parallelepipeds", *J. Acoust. Soc. Am.* 43, 988-997.
- Kweon, G., and Kim, Y. R. (2006). "Determination of the complex modulus of asphalt concrete using the impact resonance test", *J. Transp. Res. Board* 1970, 151–160.
- Lacroix, A., Kim, Y. R., and Far, M. S. S. (2009). "Constructing the dynamic modulus mastercurve using impact resonance testing", *Assoc. Asph. Paving Technol.* 78, 67–102.
- Larcher, N., Takarli, M., Angellier, N., Petit, N., Sebbah, H. (2014) "Towards a viscoelastic mechanical characterization of asphalt materials by ultrasonic measurements," *Mater. Struct.*, DOI 10.1617/s11527-013-0240-0
- Leisure, R. G., Willis, F. A. (1997). "Resonant Ultrasound Spectroscopy" *J. Phys.: Condens. Matter* 9, 6001-6029.
- Levenberg, E. (2011). "Smoothing Asphalt Concrete Complex Modulus Test Data." *J. Mater. Civ. Eng.*, 23(5), 606–611.

- Li, G., Gladden, J.R. (2010) "High Temperature Resonant Ultrasound Spectroscopy: A Review", *Int. J. Spectroscopy*, doi:10.1155/2010/206362.
- Madigosky, W. M., Lee, G. F., and Niemiec, J. M. (2006). "A method for modeling polymer viscoelastic data and the temperature shift function," *J. Acoust. Soc. Am.*, Vol. 119, 3760–3765.
- Maynard, J., (1996) "Resonant Ultrasound Spectroscopy," *Phys. Today* 49, 26-31
- Maynard, J. D. (1992) "The use of piezoelectric film and ultrasound resonance to determine the complete elastic tensor in one measurement," *J. Acoust. Soc. Am.* Vol. 91(3), 1754-1762
- Migliori, A., Sarrao, J. L. (1997). *Resonant Ultrasound Spectroscopy – Applications to Physics, Materials Measurements and Nondestructive Evaluation* (Wiley – Interscience Publication, New York)
- Migliori, A., Sarrao, J. L., Visscher, W. M., Bell, T. M., Lei, M., Fisk, Z., Leisure, R.G. (1993) "Resonant ultrasound spectroscopic techniques for measurement of the elastic moduli of solids", *Physica B* 183, 1-24
- Migliori, A., Visscher, W. M., Brown, S. E., Fisk, Z., Cheong, S. W., Alten, B., Ahrens, E. T., Kubat-Martin K. A., Maynard, J. D., Huang, Y., Kirk, D. R., Gillis, K. A., Kim, H. K., Chan, M. H. W. (1990) "Elastic constants and specific-heat measurements on single crystals of La_2CuO_4 ," *Phys. Rev. B*, Vol. 41, 2098-2102
- Moon, K. H., Cannone Falchetto, A., Marasteanu M. O. (2013). "Rheological modelling of asphalt materials properties at low temperatures: from time domain to frequency domain," *Road Materials and Pavement Design*, Vol. 14, Issue 4, pp. 810-830, DOI:10.1080/14680629.2013.817351
- Mounier, D., Di Benedetto, H., Sauzéat, C., (2012). "Determination of bituminous mixtures linear properties using ultrasonic wave propagation," *Constr. Build. Mater.*, Vol. 36, 638-647
- Naik, A. and Biligiri, K. (2014). "Predictive Models to Estimate Phase Angle of Asphalt Mixtures." *J. Mater. Civ. Eng.*, 10.1061/(ASCE)MT.1943-5533.0001197 , 04014235.
- Nazarian, S., Desai, M. R. (1993). "Automated Surface Wave Method: Field Testing", *J. Geotech. Engrg.* ASCE 119(7), 1094-1111
- Nazarian, S., Tandon, V., Yuan, D. (2005). "Mechanistic Quality Management of Hot Mix Asphalt Layers with Seismic Methods", *J. ASTM Int.* 2(9)
- Nazarian, S., Yuan, D., Tandon, V. (1999). "Structural Field Testing of Flexible Pavement Layers with Seismic Methods for Quality Control" *J. Transp. Res. Board* 1654, 50-60

Norambuena-Contreras, J., Castro-Fresno, D., Vega-Zamanillo, A., Celaya, M., Lombillo-Vozmediano, I., (2010) "Dynamic modulus of asphalt mixture by ultrasonic direct test", *NDT&E Int.* 43, 629-634.

Nguyen, Q. T., Di Benedetto, H., Sauzéat, C. (2014) "Linear and nonlinear viscoelastic behaviour of bituminous mixtures," *Mater. Struct.*, DOI: 10.1617/s11527-014-0316-5.

Nguyen, H. M., Pouget, S., Di Benedetto, H., Sauzéat, C. (2009) Time-temperature superposition principle for bituminous mixtures, *Eur. J. Environ. Civ. Eng.*, 13:9,1095-1107

Ohno, I. (1976) "Free vibration of a rectangular parallelepiped crystal and its application to determination of elastic constants of orthorhombic crystals", *J. Phys. Earth* 24(4), 355-379.

Olard, F., Di Benedetto, H. (2003). "General "2S2P1D" Model and Relation Between the Linear Viscoelastic Behaviours of Bituminous Binders and Mixes," *Road Mater. Pavement*, Vol. 4, No. 2, 185-224.

Ostrovsky, L., Lebedev, A., Matveyev, A., Potapov, A., Sutin, A., Soustova, I., Johnson, P. (2001). "Application of three-dimensional resonant acoustic spectroscopy method to rock and building materials", *J. Acoust. Soc. Am.* 110(4), 1770-1777.

Payan, C., Ulrich, T.J., Le Bas, P. Y., Saleh, T., Guimaraes, M. (2014) "Quantitative linear and nonlinear resonance inspection techniques and analysis for material characterization: Application to concrete thermal damage," *J. Acoust. Soc. Am.* 136 (2), 537-546

Pellinen, T. K., Witczak, M. W., Bonaquist, R. F. (2003) "Asphalt Mix Master Curve Construction Using Sigmoidal Fitting Function with Non-Linear Least Squares Optimization," *Recent Advances in Materials Characterization and Modeling of Pavement Systems*: pp. 83-101. doi: 10.1061/40709(257)6, Edited by Erol Tutumluer; Yacoub M. Najjar; and Eyad Masad, 15th Engineering Mechanics Division Conference Columbia University, New York, United States

Pritz, T. (1996) "Analysis of four-parameter fractional derivative model of real solid materials," *J. Sound Vib.*, Vol. 195(1), 103-115

Pritz, T. (2003) "Five-parameter fractional derivative model for polymeric damping materials," *J. Sound Vib.*, Vol. 265(1), 935-952

Ren, Z., Atalla, N., Ghinet, S. (2011) "Optimization Based Identification of the Dynamic Properties of Linearly Viscoelastic Materials Using Vibrating Beam Technique", *ASME J. Vib. Acoust.* 133(4), 041012 1-12.

Renault, A., Jaouen, L., Sgard, F. (2011) "Characterization of elastic parameters of acoustical porous materials from beam bending vibrations", *J. Sound Vib.* 330, 1950-1963.

- Rupitsch, S. J., Ilg, J., Sutor, A., Lerch, R., Döllinger, M. (2011) "Simulation based estimation of dynamic mechanical properties for viscoelastic materials used for vocal fold models", *J. Sound Vib.* 330, 4447-4459.
- Ryden, N. "Surface Wave Testing of Pavements," Doctoral Thesis, Department of Engineering Geology Lund Institute of Technology, Lund University, ISBN 91-973406-4-2, 2004.
- Ryden, N. (2011). "Resonant frequency testing of cylindrical asphalt samples," *Eur. J. Environ. Civ. Eng.*, Vol. 15, 587-600.
- Ryden, N., Park, C., Ulriksen, P., and Miller, R. (2004). "Multimodal Approach to Seismic Pavement Testing." *J. Geotech. Geoenviron. Eng.*, 130(6), 636–645.
- Saadeh, S., Masad, E., Stuart, K., Abbas, A., Papagainnakis, T., Al-Khateeb, G. (2003). "Comparative analysis of axial and shear moduli of asphalt mixes," *J. of AAPT*, Vol. 72, 122-153.
- Van Den Abeele, K. E.-A., Carmeliet, J., Ten Cate, J. A., Johnson, P. A. (2000) "Nonlinear Elastic Wave Spectroscopy (NEWS) Techniques to Discern Material Damage, Part II: Single-Mode Nonlinear Resonance Acoustic Spectroscopy," *Res. Nondestr. Eval.* 12, 31–42 (2000)
- Visscher, W. M., Migliori, A., Bell, T. M., Reinert, R. A. (1991) "On the normal modes of free vibration of inhomogeneous and anisotropic elastic objects", *J. Acoust. Soc. Am.* 90(4), 2154-2162.
- Wang, J.- T., Jin, F., Zhang, C.- H. (2012) "Estimation error of the half-power bandwidth method in identifying damping for multi-DOF systems", *Soil Dyn. Earthquake Eng.* 39, 138-142.
- Whitmoyer, S. L., and Kim, Y. R. (1994). "Determining asphalt concrete properties via the impact resonant method", *J. Test. Eval.* 22(2), 139–148.
- Williams, M. L., Landel, R. F., Ferry, J. D. (1955) "The temperature dependence of relaxation mechanisms in amorphous polymers and other glass-forming liquids", *J. Am. Chem. Soc.* 77, 3701.
- Yang, X., You, Z. (2014). "New Predictive Equations for Dynamic Modulus and Phase Angle Using a Nonlinear Least-Squares Regression Model." *J. Mater. Civ. Eng.*, 10.1061/(ASCE)MT.1943-5533.0001070, 04014131.
- Yusoff, N. I. Md., Shaw, M. T., and Airey, G. D. (2011). "Modelling the linear viscoelastic rheological properties of bituminous binders," *Constr. Build. Mater.* 25(5), 2171–2189.

Paper I

Application of resonant acoustic spectroscopy to asphalt concrete beams for determination of the dynamic modulus

ANDERS GUDMARSSON
NILS RYDEN
BJÖRN BIRGISSON

Published in
Materials and Structures 45 (12)
1903–1913



Application of resonant acoustic spectroscopy to asphalt concrete beams for determination of the dynamic modulus

A. Gudmarsson · N. Ryden · B. Birgisson

Received: 11 April 2011 / Accepted: 21 May 2012 / Published online: 15 June 2012
© RILEM 2012

Abstract In this paper, a new application of resonant acoustic spectroscopy (RAS) is examined for constructing asphalt concrete mastercurves from seismic testing. The frequency-dependent material properties can be characterized from multiple modes of vibration through the use of RAS. Beam-shaped asphalt specimens are tested at multiple temperatures to determine the resonance frequencies of the specimens. The resonance frequencies are estimated by applying a small load impulse and measuring the resulting acceleration through the specimens. Using RAS, the material properties of the specimens are determined numerically using the measured resonance frequencies. The results presented show that the frequency-dependent dynamic modulus of the asphalt concrete specimens can be characterized using several modes of vibration at each testing temperature.

Keywords Resonant acoustic spectroscopy · Resonance frequency · Dynamic modulus · Mastercurve

A. Gudmarsson (✉) · B. Birgisson
Highway and Railway Engineering, Royal Institute of Technology, Brinellvägen 23, 100 44 Stockholm, Sweden
e-mail: anders.gudmarsson@abe.kth.se

N. Ryden
Engineering Geology, Faculty of Engineering,
Lund University, Box 118, 221 00 Lund, Sweden

1 Introduction

The dynamic modulus mastercurve describes the material behavior as a function of temperature and frequency and is therefore a key parameter in modern pavement design and management. Traditional methods to determine the dynamic modulus mastercurve for asphalt concrete are based on cyclic loading over a range of frequencies (0.1–25 Hz) at different temperatures [1]. These tests are time consuming and require expensive equipment and are therefore inappropriate for control during construction. It is also important that the testing is truly non-destructive so that the properties of the specimen do not change during the test.

Resonance frequencies depend on the geometry, mass, boundary conditions and the material properties of a solid and can therefore be used to calculate the dynamic modulus. Measurements based on exciting the resonance frequencies of elastic or viscoelastic objects to determine the material properties are widely known as resonant ultrasound spectroscopy (RUS). Within the civil engineering field the method is also known as free–free resonant column test or impact resonance test. However, it should be noted that traditional RUS is usually based on multiple modes of vibration while applications in civil engineering have so far mostly been restricted to the fundamental modes of vibration.

Previous papers reporting the use of seismic testing applied to asphalt concrete specimens have been based on wave propagation techniques [6, 9], free–free



resonant column test [16] and ultrasonic direct test [17]. The material properties presented in these papers have all been determined from the fundamental modes of vibration. In RUS, unlike in the other methods, the evaluation of the data is always based on numerical methods to obtain the elastic properties of the material, since a complete analytical solution of the problem does not exist today. In fact the efficient and accurate calculation of resonance frequencies of a solid is a central requirement for the application of RUS [15]. Since the development of computer data processing, the use of RUS within different applications has been increasing and it is now a well-established method in many fields for determination of material properties [12, 18].

For measurements that are not only in the ultrasound frequency range (>20 kHz), it has been suggested that the method should be called resonant acoustic spectroscopy (RAS) [18]. Since material properties of asphalt concrete at lower frequencies are of key importance to pavement response analysis, RAS is used in this paper.

Fundamental single mode testing on asphalt concrete has previously been investigated using ASTM C215, which is a standard test method for concrete specimens where the fundamental frequency of the transverse, longitudinal and torsional modes can be determined [2]. A wide range of asphalt mixtures have been tested with the ASTM C215 method and a good agreement with traditional methods has been shown [10, 11, 22]. Limitations with the ASTM standard include that it should only be applied to specimens with a Length (L) to Diameter (D) ratio of $L/D > 2$ and that only the first resonant frequency from each mode type can be used in the evaluation [2]. In order to construct the mastercurve from measurements of the fundamental frequency, shift factors from the binder have been used as representative of the mixture shift factors [11]. Previous research has shown that this assumption is a good approximation [5, 7].

However, RAS based on variational methods, such as the Rayleigh–Ritz algorithm allows for using several frequencies from the same temperature in the evaluation. The damping characteristic of the material forces a limit for how many resonance frequencies can be used in the evaluation. When the damping is too high it will no longer be possible to determine the resonances. In traditional applications of RUS and RAS multiple modes are measured and used in the

evaluation of isotropic or anisotropic Young's modulus (E) and Poisson's ratio (ν) to increase the accuracy of the estimated parameters. In the case of a viscoelastic material, multiple modes facilitate the interpretation of the frequency dependent material properties, which is necessary in the construction of a mastercurve directly from RAS [14]. Another important advantage with RAS is that it is applicable to objects of arbitrary geometries [15].

Results from RAS applied to cylindrical disc-shaped asphalt concrete specimens evaluated with the Rayleigh–Ritz method have shown good correlation with mastercurves from the Witczak dynamic modulus predictive model in the high modulus range of the mastercurve [19]. However, the measurements reported were limited to the fundamental flexural mode and the fundamental longitudinal mode. Therefore, there is a need to explore the possibility of using multiple modes of vibration to determine the material properties of asphalt concrete.

The objective of this paper is to investigate the use of RAS applied to beam-shaped asphalt concrete specimens to determine the material properties of asphalt concrete from several flexural and longitudinal resonant modes. This method opens the possibility to determine the high frequency (or low temperature) part of the dynamic modulus mastercurve.

In this paper it is shown that by applying RAS to beam shaped asphalt concrete specimens, the dynamic modulus can be characterized for several resonance modes at each testing temperature.

2 The dynamic modulus mastercurve

The dynamic modulus, $|E^*|$, is the absolute value of the complex modulus, E^* , which is defined as:

$$E^* = E' + iE'' = |E^*|e^{i\phi} \quad (1)$$

where E' is the storage modulus, E'' is the loss modulus and ϕ is the phase angle between those.

In traditional dynamic modulus testing of asphalt concrete, sinusoidal loads are applied to a specimen while measuring its deformation:

$$|E^*| = \frac{\sigma_0}{\varepsilon_0}, \quad (2)$$

where σ_0 is the peak-to-peak stress amplitude and ε_0 is the peak-to-peak strain amplitude.



To consider the temperature and frequency dependence of asphalt concrete, this testing is performed at several different temperatures over a limited frequency range (0.1–25 Hz). Assuming a thermorheologically simple material, these measurements are equivalent to measurements made at a specific temperature over a wider range of frequencies. According to the time–temperature superposition principle, a temperature-dependent shift function is used to shift the test results along the frequency axis to a single mastercurve. The following equations are commonly used in the determination of the mastercurve. Reduced frequencies are calculated to shift the data along the frequency axis,

$$f_{\text{red}} = \alpha_T f \quad (3)$$

where the shift factors, α_T can be calculated with the Williams–Landel–Ferry equation [23],

$$\log \alpha_T = \frac{-c_1(T - T_{\text{ref}})}{c_2 + T - T_{\text{ref}}} \quad (4)$$

The coefficients c_1 and c_2 are unknown constants that are estimated along with δ , α , β and γ (the unknown constants in the sigmoidal function),

$$\log |E^*| = \delta + \frac{\alpha}{1 + e^{(\beta - \gamma \log(f_{\text{red}}))}} \quad (5)$$

by fitting the calculated dynamic modulus with the measured dynamic modulus.

3 Resonant acoustic spectroscopy

The computation of the elastic parameters in RUS is based on two parts. First, the so-called forward problem is solved where an approximation of the elastic parameters is made in order to calculate the theoretical natural frequencies. Secondly, the inverse problem is solved where the theoretically calculated natural frequencies are fitted to the measured natural frequencies iteratively, by adjusting the approximated elastic parameters until the best least-square fit is obtained.

Through history, two general approaches have been used to determine resonance frequencies of solids non-analytically. One of the approaches is the finite element method, in which the solid is divided into elements and the governing physical equations for each element are solved separately, under the condition that there is continuity across the element boundaries. The

theoretical development of RUS is instead based on the approach of energy minimization techniques that search only for the minimum energy configuration of the body, ensuring that none of the vibrational modes are excluded [15].

The algorithm for calculating the eigenfrequencies of a body has been described in work by Migliori and Sarrao [15]. Here we present only the concept of the energy minimization techniques and how we apply it to beam-shaped asphalt concrete specimens.

From classical mechanics it can be shown that the free vibration of a body is exactly the same as the solution of Lagrangian mechanics for a 3D linear elastic body of arbitrary shape,

$$L = \int_V (KE - PE) dV, \quad (6)$$

where L is the Lagrangian, KE is the kinetic energy and PE is the potential energy of the body with the volume V . By assuming simple harmonic motion, the equilibrium configuration of the system can be found and the displacements that fulfill this state correspond perfectly to the normal modes of the system. In order to evaluate the displacements numerically, the Rayleigh–Ritz method is used to expand each displacement component (u_i) in terms of basis functions (ϕ_λ):

$$u_i = \sum_\lambda a_{i\lambda} \phi_\lambda, \quad (7)$$

where the coefficients $a_{i\lambda}$ are constants and $\lambda = (p, q, r)$, which are positive integers.

Different types of basis functions for the displacements can be used depending on the geometry of the sample. However, by using powers of Cartesian coordinates a solution can be found for samples with different types of geometry. This is also the chosen basis function in this paper:

$$\phi_\lambda = x^p y^q z^r \quad (8)$$

Now substituting the displacement function into the Lagrangian gives the following matrix equation:

$$L = \frac{1}{2} \omega^2 \vec{a}^T \overleftrightarrow{E} \vec{a} - \frac{1}{2} \vec{a}^T \overleftrightarrow{\Gamma} \vec{a} \quad (9)$$

where \overleftrightarrow{E} denotes the E matrix, $\overleftrightarrow{\Gamma}$ denotes the Γ matrix, \vec{a} the eigenvectors and ω^2 the eigenvalues.

This matrix equation (Eq. 9) is the complete solution of the system when $N \rightarrow \infty$, where N is an



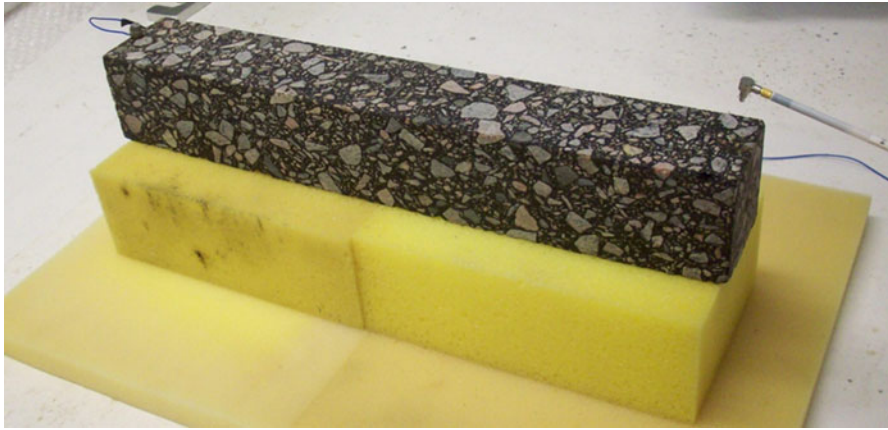


Fig. 1 The test set-up for resonance testing with free boundary conditions

arbitrarily chosen upper limit (usually $N = 10$) to balance the computational time against the number of resonance frequencies needed to determine the elastic parameters with certain accuracy [15]. This is commonly done by:

$$p + q + r \leq N \quad (10)$$

The final eigenvalue equation is obtained considering that the Lagrangian is stationary for the natural frequencies. Therefore the solutions to the problem can be found when the derivatives $\partial L / \partial a_{i\lambda}$ are equal to zero, which gives:

$$\omega^2 \vec{E} \vec{a} = \vec{\Gamma} \vec{a} \quad (11)$$

For rectangular parallelepiped samples with the length of the sides of $2d_1$, $2d_2$ and $2d_3$ the calculations of the Γ and E matrices can be reduced by calculating the following analytical formulation [15],

$$f(p, q, r) = \frac{8d_1^{p+1}d_2^{q+1}d_3^{r+1}}{(p+1)(q+1)(r+1)} \quad (12)$$

Now solving the Lagrangian with the Rayleigh–Ritz approximation, the displacements that give the minimum (stationary) solution can be found (from the eigenvectors \vec{a}) and the natural frequencies without losses can be determined (from the eigenvalues ω^2).

3.1 Test procedure and analysis

The theory behind RAS requires that the specimen have free boundary conditions. By using pads of soft foam it is assumed that the specimen is floating with free boundary conditions [22]. To excite the normal

modes of vibration, a small hammer is used to manually apply a small load impulse to the specimen. An accelerometer (PCB model 352B10) with the weight of 1.5 g, attached to the specimen by wax, is used to transform the resulting vibrations in the specimen into electrical signals. The miniature accelerometer is assumed to have no influence on the resonance frequencies of the beam. Figure 1 presents the set-up used for the resonance testing.

Each 10 ms long signal is stored in a computer by the PC-CARD DAS 16/16-AO from Measurement Computing and by using the Fast Fourier Transform (FFT) the signals are transformed from time domain to frequency domain. Figure 2a shows the measured data in time domain and Fig. 2b the transformed data in frequency domain, where each peak is a resonance mode. Figure 3 illustrates the displacements of the beam for the first three flexural and longitudinal modes.

The test procedure has been repeated for each testing temperature (-10 , 0 , 10 , 20 , 25 and 30 °C). At each temperature, three different excitation directions were used to extract as many modes of vibration as possible. For each mode type, ten load impulses were applied to the specimen and the average resonance frequencies from these load impulses were used in the determination of the dynamic modulus. The coefficient of variation for the fundamental resonant frequencies from the ten load impulses was calculated to analyze the repeatability of the measurements. The repeatability is presented in Fig. 4 for the fundamental flexural mode of the different specimens. The good repeatability is a known advantage of resonance

Fig. 2 Data from resonance testing in time domain (a) and in frequency domain (b)

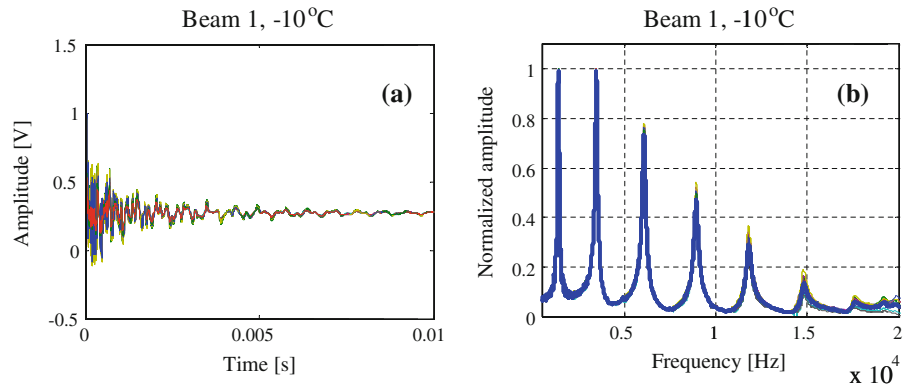
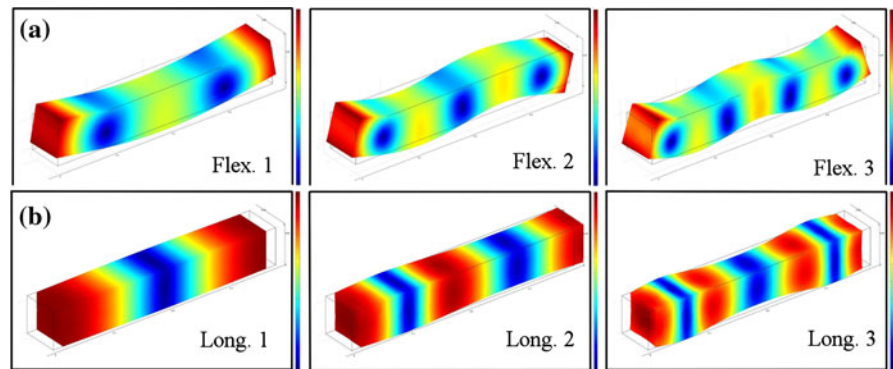


Fig. 3 Illustration of the 3 first flexural modes (a) and the 3 first longitudinal modes (b)



testing [6, 10, 11, 22]. The three different excitation directions are illustrated in Fig. 5, along with the direction of the beams in the compacted slab.

The measured resonance frequencies from this procedure are the damped natural frequencies of the specimen. These measured resonance frequencies must therefore be converted to natural frequencies before comparison with the theoretically calculated natural frequencies. This is done according to:

$$f_n = \frac{f_d}{\sqrt{1 - \zeta^2}} \tag{13}$$

where f_n is the natural frequency, f_d is the damped natural frequency and ζ is the damping ratio. The damping ratio is determined according to the half-power bandwidth method,

$$\zeta = \frac{\Delta f}{2f_d} \tag{14}$$

where Δf is the width of the frequency response curve at 0.707 (half-power) of the maximum amplitude of

the curve. The damping ratio is also used to determine the phase angle, ϕ ,

$$\phi = \arctan(2\zeta) \tag{15}$$

This procedure of estimating damping is applicable as long as the damping ratio does not exceed approximately 0.5 (half of the critical damping) and the recorded length of the signal is longer than the inverse of the bandwidth (Δf) [22].

To find the elastic modulus, knowledge about Poisson’s ratio (ν) is needed. At this point Poisson’s ratio has been estimated iteratively from the dynamic modulus with the relationship used in the NCHRP Guide for Mechanistic-Empirical Design [8],

$$\nu = 0.15 + \frac{0.35}{1 + e^{(a+b \times \log(E))}} \tag{16}$$

To account for the energy losses in the material that have been excluded so far, the phase angle is used to determine the dynamic modulus,

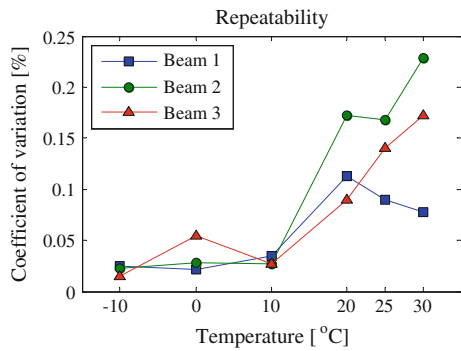


Fig. 4 The repeatability of resonance testing for the fundamental flexural modes in z-direction

$$|E^*| = \frac{E'}{\cos(\phi)} \tag{17}$$

where E' is the storage modulus.

In the application of RUS, it has been suggested that the number of resonance frequencies to accurately fit the elastic parameters should be at least five times the number of unknown parameters to be determined. This requirement has been developed from the experience of the RUS users through history. Due to the visco-elasticity in asphalt concrete each frequency results in different elastic parameters and this requirement can therefore not be fulfilled in this application. Considering that RUS aims to determine a relative accuracy of 10^{-6} and the traditional standards within the pavement industry accepts variations of 10 % this requirement may not be necessary to successfully apply RAS to asphalt concrete [15, 20].

Fig. 5 Measured modes of vibrations (a) and the direction of the beams in the slab (b)

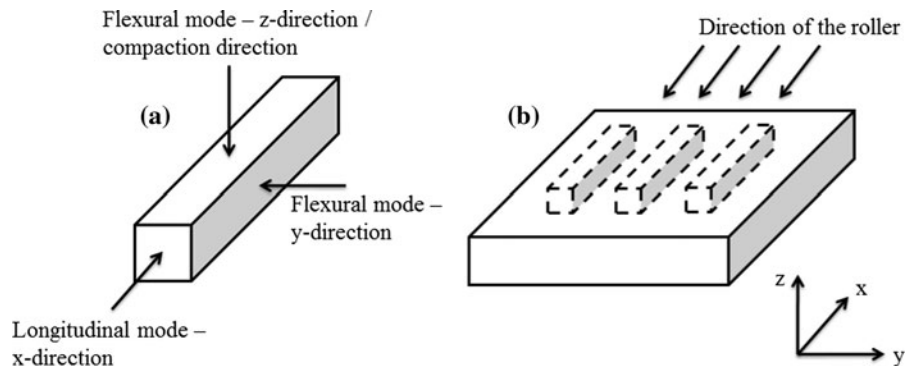
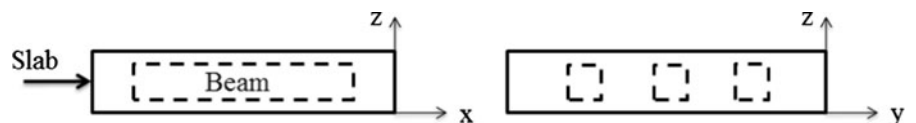


Fig. 6 The cut out beams position in the compacted slab



4 Materials

A common mixture used in Swedish pavements, with an accepted range of air voids between 1.5–3.5 % and a minimum binder content of 6.0 % by weight, called ABT 16 70/100 has been tested in this study [21]. Granite aggregates from the Bjärsgård quarry in Skåne with the nominal aggregate size of 16 mm and binder with penetration grade 70/100 from Nynas AB were used in the mixture. The mixing of the asphalt concrete was made in a laboratory mixer with an electrical heating function and a thermometer monitoring the mixing temperature. The mixture was compacted into a slab with the dimensions of 500*560*80 mm (x, y, z) in a laboratory with a roller (see Fig. 5). From the slab, rectangular parallelepiped specimens were sawn along all sides. The positions of the beams related to the slab are presented in Fig. 6 and the dimensions of the three beams are presented in Table 1. Using RAS

Table 1 Specimen data

	Beam 1	Beam 2	Beam 3
Width (y-dir.) (mm)	58.74	58.74	58.65
Height (z-dir.) (mm)	58.87	58.94	58.88
Length (x-dir.) (mm)	382.0	382.0	382.0
Mass (g)	3133	3120	3126
Density (g/cm ³)	2.372	2.359	2.370
Air voids (%)	2.2	2.7	2.3



Table 2 Gradation of the mix

Sieve size (mm)	0.063	0.125	0.25	0.5	1	2	4	5.6	8	11.2	16	22.4
Passing (%)	8.9	12	16	21	28	39	50	58	70	81	98	100
Upper limit (%)	9	–	–	30	–	47	–	–	73	88	100	100
Lower limit (%)	6	–	–	13	–	26	–	–	57	71	90	100

the measured dimensions are equally important as the measured resonance frequencies.

These dimensions were chosen according to the test standard SS-EN 12697-26:2004, where it is stated that the width and the height should be at least three times the maximum grain size. The length should also be six times the highest value of the height or the width [20]. The temperature during mixing and compaction of the mixture was 150 °C. Table 2 presents the gradation of the mix and the gradation limits. The binder content of the mix was determined to 6.3 % by weight.

A temperature chamber was used for the temperature conditioning of the specimens during the test. The actual temperature of the specimens was controlled using a separate “dummy” specimen with thermometers attached to the center and the edge of the specimen. The test was performed during less than half a minute outside the temperature chamber applying 10 impacts on three different sides of the specimen.

5 Results and discussion

In this paper RAS is compared with the test method, ASTM E 1876-99 Standard test method for dynamic Young’s modulus, shear modulus, and Poisson’s ratio by impulse excitation of vibration. With ASTM E 1876-99 it is possible to determine the fundamental resonant frequency of each type of vibrational mode by exciting the resonance frequencies from a single impulse. The material is assumed to be elastic, homogeneous and isotropic [3].

The dynamic modulus has been characterized for three resonance frequencies for each type of vibration at the testing temperatures between –10 to 10 °C by using RAS. At the higher temperatures (20 °C to 30 °C), increased damping has limited the number of available resonance frequencies for successful characterization of the dynamic modulus. At this point it was not possible to evaluate the longitudinal modes at 30 °C.

Figures 7, 8 and 9 present the dynamic modulus for each type of vibration calculated from the ASTM E 1876-99 standard and from RAS. The results are presented as an average of the three different samples (Beam 1 to Beam 3). The highest coefficient of variation for the dynamic modulus between the different specimens (over the tested temperature interval) is 4.5- %, 5.3 % and 2.0 % for the flexural modes in *z*-direction, flexural modes in *y*-direction and the longitudinal modes (*x*-direction) respectively.

In the comparison between the two methods (RAS and ASTM E 1876-99) a mastercurve is presented for each method. As seen in Figs. 7, 8 and 9, the evaluated data was not enough to create an overlap of the dynamic modulus between the testing temperatures, which is necessary in order to apply the time–temperature superposition. Binder shift factors have therefore been used to construct the mastercurve. The binder shift factors presented in Table 3 have been determined from frequency sweep dynamic shear rheometer measurements.

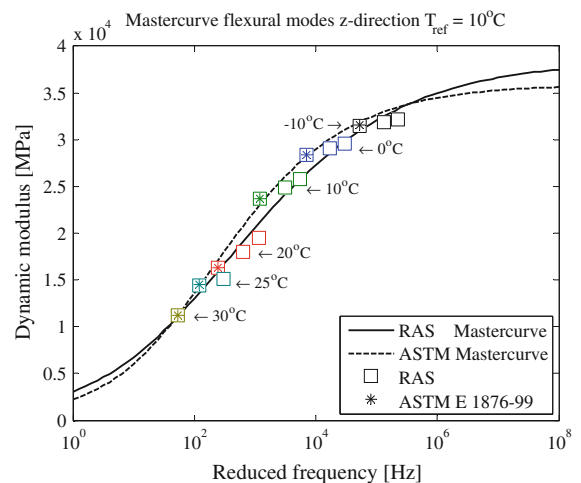


Fig. 7 The average dynamic modulus mastercurve of Beams 1–3 for the flexural modes in the *z*-direction calculated from both the ASTM E 1876-99 standard and RAS. The mastercurves are constructed from binder shift factors

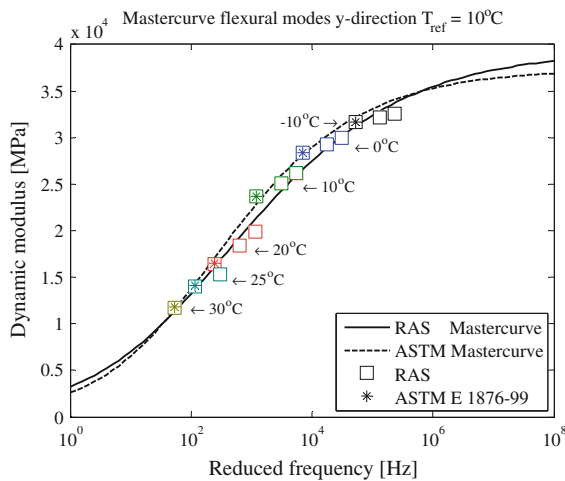


Fig. 8 The average dynamic modulus mastercurve of Beams 1–3 for the flexural modes in the y-direction calculated from both the ASTM E 1876-99 standard and RAS. The mastercurves are constructed from binder shift factors

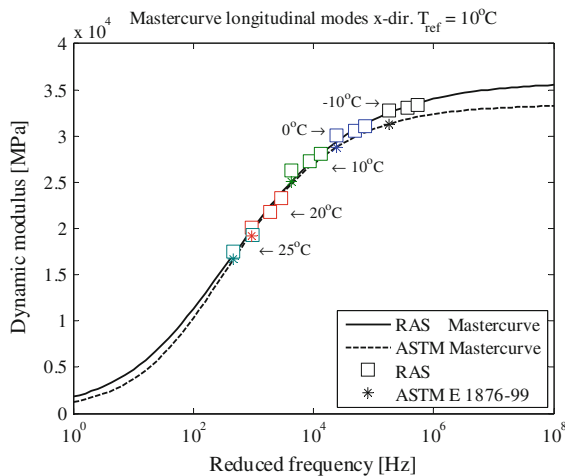


Fig. 9 The average dynamic modulus mastercurve of Beams 1–3 for the longitudinal modes (x-direction) calculated from both the ASTM E 1876-99 standard and RAS. The mastercurves are constructed from binder shift factors

It can be seen that there is a perfect match between the two methods for the fundamental flexural modes (Figs. 7, 8). However, the match for the fundamental longitudinal mode is not as precise (Fig. 9). This

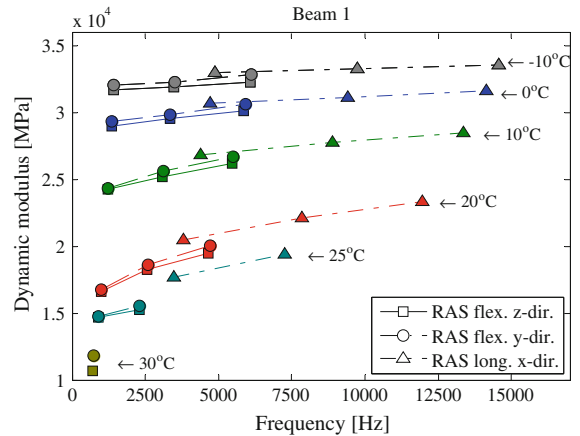


Fig. 10 The dynamic modulus of Beam 1 for the different modes of vibration at the testing temperatures –10, 0, 10, 20, 25 and 30 °C

indicates that for the longitudinal modes of vibration the approximate formulation in the standard test method does not provide precise results for the geometry investigated in this paper. It can also be seen that the shape of the mastercurves differs between the two methods for all mode types (Figs. 7, 8, 9). This fact highlights the importance of characterizing the dynamic modulus using multiple modes of vibration.

Looking more closely to the evaluated dynamic modulus from RAS for the different beams, it can be seen in Figs. 10, 11 and 12 that there is a systematic difference in the dynamic modulus for the different mode types. The most noticeable difference is between the flexural modes of vibration and the longitudinal modes of vibration, where the longitudinal mode type has higher dynamic modulus especially at high temperatures. However, there is also a small difference in the dynamic modulus between the flexural modes in z-direction and the flexural modes in the y-direction. Here the y-direction in general has a slightly higher dynamic modulus than the z-direction.

These specific results of the anisotropy, where the modulus is higher in the y-direction than in the z-direction, have also been seen by Di Benedetto et al. [6] for rolling wheel compacted asphalt concrete. One reason for this could be that the aggregates tend to

Table 3 Binder shift factors

Temperature (°C)	–10	0	10	20	25	30
Log(a_T)	1.5733	0.7163	0	–0.6077	–0.8782	–1.1296



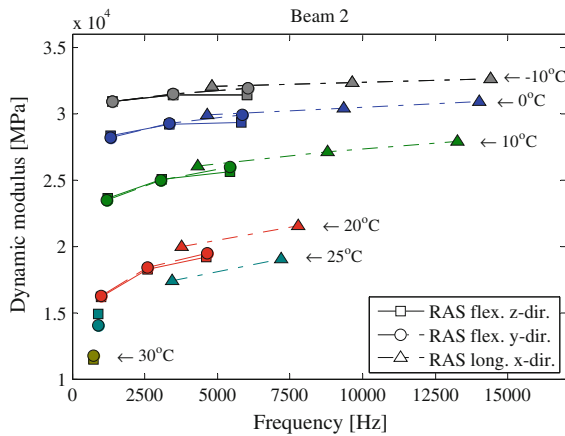


Fig. 11 The dynamic modulus of Beam 2 for the different modes of vibration at the testing temperatures $-10, 0, 10, 20, 25$ and 30°C

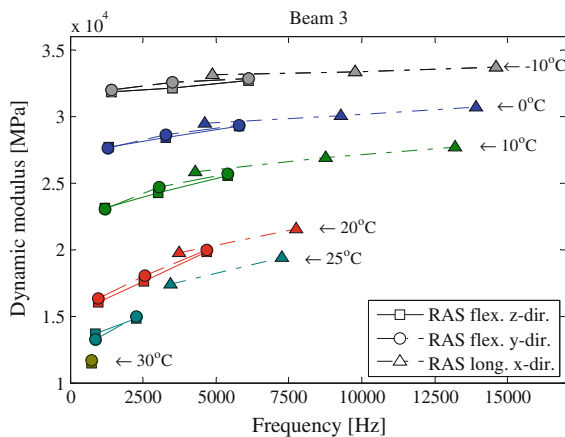


Fig. 12 The dynamic modulus of Beam 3 for the different modes of vibration at the testing temperatures $-10, 0, 10, 20, 25$ and 30°C

orient themselves with the longest axis horizontally during this type of compaction, leading to a stiffer response in the horizontal direction (y -direction). These results agree with research showing that the stiffness in the direction of the longest axis is significantly higher than the stiffness in the direction of the aggregates short axis [4]. It can also be seen that the longitudinal horizontal direction gives a higher modulus than both of the flexural mode types. In previous research it has been seen that a stiffening effect is observed when asphalt concrete is subjected to compression [13]. These results of the anisotropy are systematic for the tested specimens and agree well

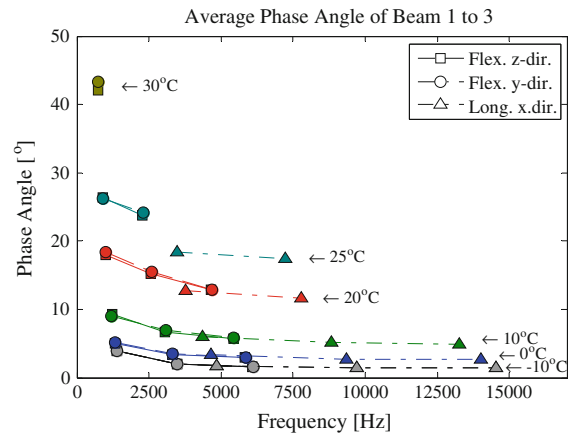


Fig. 13 The measured average phase angle of Beams 1–3 at the testing temperatures $-10, 0, 10, 20, 25$ and 30°C

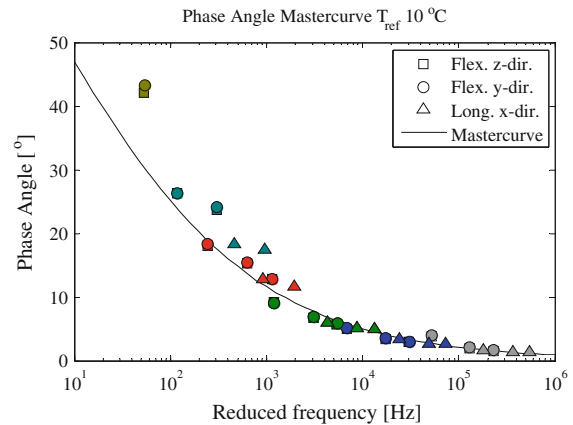


Fig. 14 The measured average phase angle mastercurve

with previous research of anisotropy in asphalt concrete.

Figure 13 shows the result of the measured phase angle as an average of Beam 1 to 3. Using resonance testing, no correction are needed for obtaining the phase angle.

The average phase angle is also presented as a mastercurve in Fig. 14, where the mastercurve was determined from the fitted storage and loss modulus and by using the binder shift factors.

The influence of the air voids on the dynamic modulus is presented in Fig. 15. The specimen with the highest air voids (Beam 2) has the lowest dynamic modulus at 10 kHz and 10°C . The dynamic modulus at this specific frequency and temperature are calculated from the RAS mastercurve.

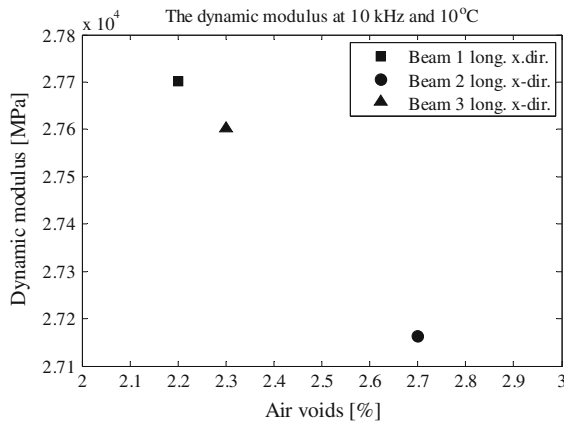


Fig. 15 The dynamic modulus dependency of the air voids at 10 kHz and 10 °C

Table 4 The dynamic modulus at 10 kHz and 10 °C

	Beam 1	Beam 2	Beam 3
Air voids (%)	2.2	2.7	2.3
Flex. z-dir. (MPa)	27,539	27,057	27,156
Flex. y-dir. (MPa)	27,957	27,249	27,540
Long. x-dir. (MPa)	27,702	27,163	27,603

Table 4 presents the dynamic modulus at 10 kHz and 10 °C for the three different mode types. It can be seen that the results in Fig. 15 are typical for all mode types. Also here the dynamic modulus is calculated from the RAS mastercurve.

The coefficients in the equation of Poisson's ratio (Eq. 16) were chosen so that the dynamic modulus increases with increasing mode number (frequency). Figure 16 presents the dynamic modulus dependency of mode number and Poisson's ratio at -10 °C. As shown in Fig. 16 the expected increase in the dynamic modulus with frequency requires a Poisson's ratio above approximately 0.2 at this temperature. The coefficients in Eq. 16 were set to $a = -19$ and $b = 2.95$ based on these results.

The approximation of Poisson's ratio is an uncertainty, but to the authors knowledge there is no other relationship that is known to be more correct in order to describe the frequency dependency of Poisson's ratio. The empirical relation in Eq. 16 is here treated as a first approximation to be further evaluated in future studies using RAS.

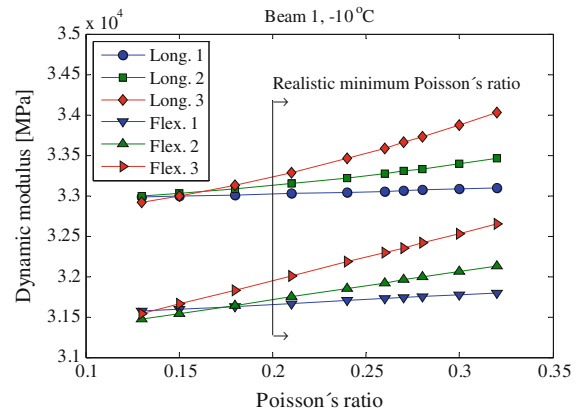


Fig. 16 The dynamic modulus dependency of Poisson's ratio for different modes of vibration

6 Conclusions

The application of RAS to asphalt concrete beams has been investigated in this paper. The results show that the material properties can be characterized for multiple modes of vibration at each testing temperature. Therefore, the dynamic modulus can be characterized for a wider frequency range by using RAS compared to the traditional methods. Since the standard test methods used today to determine the dynamic modulus are limited to testing at maximum 25 Hz (AASHTO 2007), RAS holds the promise of being able to provide more knowledge about asphalt concrete at low temperatures and higher stiffness. The results were also compared to the ASTM E 1876-99 method. The comparison indicated that the approximate formulation (ASTM E 1876-99) for the longitudinal modes of vibration did not provide precise results for the geometry investigated in this paper. The results throughout this paper show a good repeatability of the method.

Importantly, RAS can be used for testing over extended frequency ranges, thus providing increased accuracy in future comparisons with other standard test methods for the dynamic modulus. This knowledge can be used to develop even more accurate and precise theoretical models for asphalt concrete.

Acknowledgments The authors would like to thank the Swedish Transport Administration (Trafikverket) and the Swedish construction industry's organization (SBUF) for their financial support. A great appreciation is also given to Olof Åkesson and Viktor Petterson at Peab Asfalt's laboratory in Helsingborg for their support in producing and testing the specimens.



References

- American Association of State Highway and Transportation Officials (AASHTO) (2007) Standard method of test for determining dynamic modulus of hot-mix asphalt mixtures. AASHTO Designation: TP 62, Washington
- ASTM C215-08 Standard Test Method for Fundamental transverse, longitudinal, and torsional frequencies of concrete specimens. American Society for Testing and Materials (ASTM), New York
- ASTM E 1876-99, Standard test method for dynamic Young's modulus, shear modulus, and Poisson's ratio by impulse excitation of vibration. American Society for Testing and Materials (ASTM), New York
- Chen J, Pan T, Huang X (2011) Numerical investigation into the stiffness anisotropy of asphalt concrete from a microstructural perspective. *Constr Build Mater*. doi:10.1016/j.conbuildmat.2011.01.002
- Di Benedetto H, Des Croix P (1996) Binder-mix rheology: limits of linear domain, non linear behavior. In: *Eurasphalt & Eurobitume congress*, Strasbourg, 7–10 May 1996
- Di Benedetto H, Sauzéat C, Sohm J (2009) Stiffness of bituminous mixtures using ultrasonic wave propagation. *Road Mater Pavement Des* 10(4):789–814
- Dongre R, Myers L, D'Angelo J, Paugh C, Gudimettla J (2005) Field evaluation of Witczak and Hirsch models for predicting dynamic modulus of hot-mix asphalt, vol 74, pp 381–442. Association of Asphalt Paving Technologists, Long Beach
- NCHRP Guide for Mechanistic-Empirical Design (2004) Final Report, Part 2. Design inputs, chap 2. Material Characterization, NCHRP, March 2004
- Hochuli AS, Sayir MB, Poulikakos LD, Partl MN (2001) Measuring the complex modulus of asphalt mixtures by structural wave propagation. Association of Asphalt Paving Technologists (AAPT), Clearwater Beach, 19–21 March 2001
- Kweon G, Kim YR (2006) Determination of the complex modulus of asphalt concrete using the impact resonance test. *J Transp Res Board* 1970:151–160
- Lacroix A, Kim YR, Far MSS (2009) Constructing the dynamic modulus mastercurve using impact resonance testing. Association of Asphalt Paving Technologists (AAPT)
- Lebedev AV, Ostrovskii LA, Sutin AM, Soustova IA, Johnson PA (2003) Resonant acoustic spectroscopy at low Q factors. *Acoust Phys* 49(1):81–87
- Levenberg E (2006) Constitutive Modeling of asphalt-aggregate mixes with damage and healing. PhD dissertation, Technion, Israel Institute of Technology
- Madigosky WM, Lee GF (1979) Automated dynamic Young's modulus and loss factor measurements. Naval Surface weapons Center, White Oak, Silver Spring
- Migliori A, Sarrao JL (1997) Resonant ultrasound spectroscopy—applications to physics, materials measurements and nondestructive evaluation. Wiley-Interscience, New York, ISBN 0-471-12360-9
- Nazarian S, Yuan D, Tandon V, Arellano M (2005) Quality management of flexible pavement layers with seismic methods. Center for Transportation Infrastructure Systems, Research Report 0-1735-3, The University of Texas at El Paso
- Norambuena-Conteras J, Catsro-Fresno D, Vega-Zamamilla A, Celaya M, Lombillo-Vozmediano I (2010) Dynamic modulus of asphalt mixture by ultrasonic direct test. *NDT&E Int* 43:629–634
- Ostrovsky L, Lebedev A, Matveyev A, Potapov A, Sutin A, Soustova I, Johnson P (2001) Application of three-dimensional resonant acoustic spectroscopy method to rock and building materials. *Acoust Soc Am* 110:1770–1777
- Ryden N (2011) Resonant frequency testing of cylindrical asphalt samples. *Eur J Environ Civ Eng* 15:587–600
- SS-EN 12697-26:2004, Bituminous mixtures—test methods for hot mix asphalt—part 26: Stiffness, ICS 93.080.20
- VVTBT (2009) Bitumenbundna lager 09, Publikation 2009:140, Vägverket
- Whitmoyer SL, Kim YR (1994) Determining asphalt concrete properties via the impact resonant method. *J Test Eval* 22(2):139–148
- Williams ML, Landel RF, Ferry JD (1955) The temperature dependence of relaxation mechanisms in amorphous polymers and other glass-forming liquids. *J Am Chem Soc* 77:3701–3707

Paper II

Characterizing the low strain complex modulus of asphalt concrete specimens through optimization of frequency response functions

ANDERS GUDMARSSON
NILS RYDEN
BJÖRN BIRGISSON

Published in
Journal of Acoustical Society of America 132 (4)
2304-2312



Characterizing the low strain complex modulus of asphalt concrete specimens through optimization of frequency response functions

Anders Gudmarsson,^{a)} Nils Ryden, and Björn Birgisson

Highway and Railway Engineering, KTH Royal Institute of Technology, Brinellvägen 23,
100 44 Stockholm, Sweden

(Received 18 May 2012; revised 12 July 2012; accepted 1 August 2012)

Measured and finite element simulated frequency response functions are used to characterize the low strain ($\sim 10^{-7}$) complex moduli of an asphalt concrete specimen. The frequency response functions of the specimen are measured at different temperatures by using an instrumented hammer to apply a load and an accelerometer to measure the dynamic response. Theoretical frequency response functions are determined by modeling the specimen as a three-dimensional (3D) linear isotropic viscoelastic material in a finite element program. The complex moduli are characterized by optimizing the theoretical frequency response functions against the measured ones. The method is shown to provide a good fit between the frequency response functions, giving an estimation of the complex modulus between minimum 500 Hz and maximum 18000 Hz depending on the temperature. Furthermore, the optimization method is shown to give a good estimation of the complex modulus master curve.

© 2012 Acoustical Society of America. [<http://dx.doi.org/10.1121/1.4747016>]

PACS number(s): 43.40.At, 43.40.Le, 43.60.Pt, 43.40.Cw [DAB]

Pages: 2304–2312

I. INTRODUCTION

Non-destructive testing (NDT) is of great importance for future quality control and quality assurance of new and old pavement constructions. NDT offers a fast, economic, and truly non-destructive method of linking low strain measurements of asphalt concrete from field and laboratory together. Using seismic testing, measurements of specimens in the laboratory are performed at approximately the same strain level as seismic measurements in the field. This allows for a direct comparison between the strain level dependent material properties determined in field and laboratory. Today there are three different standard test methods available to measure the dynamic modulus of asphalt concrete specimens (Brown *et al.*, 2009). The dynamic modulus can be measured at minimum 0.01 Hz and maximum 25 Hz through these methods. However, there is no non-destructive measurement technique in the field that can be linked to the results from these methods. In addition, the traditional methods require expensive equipment and are not completely non-destructive. They may also be considered as too time consuming to be used in the daily production.

A general problem with NDT applied to asphalt concrete specimens has been to evaluate the complex modulus at several frequencies at each testing temperature. Previous resonance frequency measurements applied to asphalt concrete specimens have for example been based on the ASTM C215 standard (Whitmoyer and Kim, 1994; Kweon and Kim, 2006; Lacroix *et al.*, 2009) and resonant ultrasound spectroscopy (RUS) (Ryden, 2011; Gudmarsson *et al.*, 2012). The ASTM C215 standard is limited to determination

of the complex modulus to the fundamental modes of vibration (ASTM, 2008), while RUS offers a possibility to determine the complex modulus at more than one resonance frequency (Leisure and Willis, 1997; Migliori and Sarrao, 1997). However, using only the resonances of a specimen for a viscoelastic material usually limits the determination of the modulus to a few numbers of frequencies at a specific temperature (Buchanan, 1987). Ryden (2011) applied resonant acoustic spectroscopy (RAS) (Ostrovsky *et al.*, 2001) to cylindrical asphalt concrete disks, characterizing the dynamic modulus for two different fundamental modes of vibration at different temperatures. Gudmarsson *et al.* (2012) characterized the dynamic modulus at most three resonance frequencies per temperature by applying RAS to beam shaped asphalt concrete specimens. In common for all these results applying resonance testing to asphalt concrete is the limitation of not being able to construct master curves using only NDT. So far the construction of the master curve has been based on binder shift factors obtained from measurements of the binder in a lower frequency range (Kweon and Kim, 2006; Lacroix *et al.*, 2009; Gudmarsson *et al.*, 2012). Therefore the number of measurement points (frequency range) from each temperature needs to be increased to be able to determine master curves using only NDT. Also, the applicability of the time-temperature superposition principle to results obtained from high frequency measurements of asphalt mixtures needs to be further investigated.

Through the use of frequency response functions (FRFs), it is possible to characterize the material properties at a wider range of frequencies and not only at the resonances of a specimen (Buchanan, 1987). Therefore the finite element method is applied in this paper to perform frequency response simulations of a beam shaped asphalt concrete specimen to determine the theoretical frequency response.

^{a)}Author to whom correspondence should be addressed. Electronic mail: andgud@kth.se

TABLE I. Gradation of the mix (Gudmarsson *et al.*, 2012).

Sieve size (mm)	0.063	0.125	0.25	0.5	1	2	4	5.6	8	11.2	16	22.4
Passing (%)	8.9	12	16	21	28	39	50	58	70	81	98	100
Upper limit (%)	9	-	-	30	-	47	-	-	73	88	100	100
Lower limit (%)	6	-	-	13	-	26	-	-	57	71	90	100

Using this approach, the material properties of a specimen can be determined iteratively over a wide frequency range by fitting theoretical FRFs with measured FRFs. Optimization of FRFs for determination of the material properties of specimens is commonly used in other fields of application. For example, Guo and Brown (2000) and Renault *et al.* (2011) matched measured and analytical determined FRFs of frequency dependent materials to characterize their material properties. Ren *et al.* (2011) evaluated seven parameters describing the temperature and frequency dependent material properties by optimizing FRFs of metal polymer sandwich beams. Rupitsch *et al.* (2011) determined the dynamic complex Young's modulus and Poisson's ratio of a viscoelastic material used for vocal fold models through the use of FRFs. Advantages using FRFs compared to only the resonance frequencies are not only the increased usable frequency range. The procedure of matching the measured resonance frequency with the corresponding theoretical resonance frequency is not always straight forward. This is due to the fact that the computation of the theoretical resonance frequencies gives results of resonance frequencies for all modes of vibration of the solid. Therefore the theoretical resonance frequencies that correspond to the measured mode of vibration must be identified. This is generally rather simple for the first two or three resonance frequencies but may be more problematic for higher resonances, where the resonance frequencies of different modes of vibration may be difficult to differentiate.

The aim of this paper is to expand the frequency range and number of measurement points, from which the complex modulus of asphalt concrete specimens can be characterized through NDT. Moreover, the possibility of constructing asphalt concrete master curves through optimization of FRFs is studied.

II. METHODOLOGY

A. Materials

Measurements have been performed to an asphalt concrete beam and to an unplasticized polyvinyl chloride (PVC-U) beam. The PVC-U beam (398.6 mm × 63.66 mm × 50.08 mm) with the density of 1.374 g/cm³ has been tested to investigate the applicability of the method.

The asphalt concrete specimen has a nominal aggregate size of 16 mm, and the recipe of the mix follows the criteria of an ABT 16 mixture with 70/100 Nynas bitumen and granite aggregates (Trafikverket, 2009). The mixing of the asphalt concrete was performed in a laboratory mixer at 150 °C, giving a binder content of 6.3% and the gradation according to Table I (Gudmarsson *et al.*, 2012). The asphalt

mix was compacted with a roller in a laboratory to a slab (500, 560, 80 mm), from which the specimen was sawn out to the dimensions of 382 mm × 58.74 mm × 59.94 mm (x, y, z) according to Fig. 1. The density of the measured specimen is 2.359 g/cm³, and the air void content of the specimen is 2.7%.

B. Experimental determination of the frequency response function

The test setup used for measuring the FRFs of the beam shaped asphalt concrete specimen is illustrated in Fig. 1. The soft foam is assumed to provide free boundary conditions to the specimen (Whitmoyer and Kim, 1994). The measurements can be applied to specimens with arbitrary geometry.

An impact hammer (PCB model 086E80) is used to apply a load impulse, and an accelerometer (PCB model 352B10) is used to measure the response. The accelerometer is attached to the specimen by soft wax. Note that the accelerometer is very light (0.7 g) and is assumed to have no effect on the response of the system. The impact hammer and the accelerometer are connected to a signal conditioner (PCB model 480B21), which is further connected to a data acquisition device (NI USB-6251 M Series) for analog to digital conversion. The Data Acquisition Toolbox in MATLAB has been used to set up the data acquisition device and to perform the measurements. The data collected from this testing are stored in a computer.

The load impulse in time domain of a measurement at -1.6 °C of the asphalt concrete specimen and the fast Fourier estimation the recorded signals are presented in Figs. 2(a) and 2(b), respectively. The sampling frequency was set to 500 kHz when using the NI USB-6251 M Series device. Figure 3(a) shows the response of the measurement in time domain, and Fig. 3(b) shows the fast Fourier transform of the response in frequency domain. The record lengths of the response were chosen depending on the temperature (damping) of the specimen. At this temperature, 0.008 s was chosen.

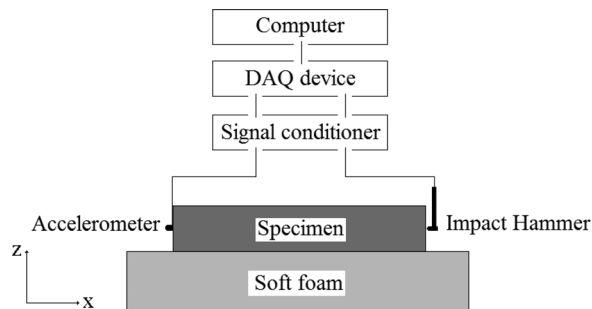


FIG. 1. Illustration of the experimental setup.

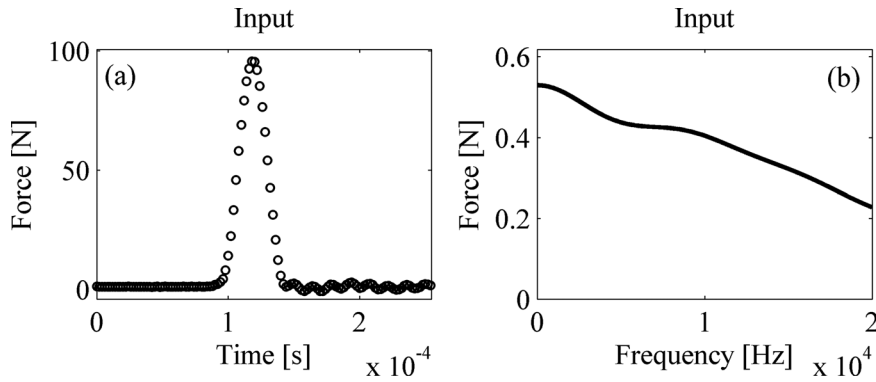


FIG. 2. The load impulse in time domain (a) and frequency domain (b).

A frequency response function (H) can be calculated according to Eq. (1), where Y is the Fourier transform of the measured response (output) and X is the Fourier transform of the load impulse (input),

$$H(f) = \frac{Y(f)}{X(f)}. \quad (1)$$

To reduce measurement noise when determining FRFs, the ratio between the cross power spectrum and the power spectrum [Eq. (2)] is usually used in practice (Halvorsen and Brown, 1977). This equation is also used in this paper to determine the FRFs,

$$H(f) = \frac{X^*(f) \times Y(f)}{X^*(f) \times X(f)}, \quad (2)$$

where $X^*(f)$ = the complex conjugate of $X(f)$.

A FRF of the longitudinal vibration modes (x direction) has been determined for each testing temperature (-24.4°C , -20.5°C , -15.1°C , -10.5°C , -5.4°C , -1.6°C , 5.4°C , 11.3°C , 15.8°C , 20.5°C , and 30.1°C). Figure 4(a) presents the absolute value of the measured FRFs for five of the tested temperatures, and Fig. 4(b) presents the unwrapped phase angle of the same temperatures. The FRFs at different temperatures are calculated from an average of five individual measurements at each temperature. The maximum strains applied to the specimen through these tests have been approximated to 0.12 micro-strains. The maximum strains occur at the first resonance frequency and have been approximated by Eq. (3) (Pasqualini, 2006), where ε is the strain, $Y(f)$ is the measured acceleration, L is the length of the specimen, and f is the frequency,

$$\varepsilon = \frac{Y(f)}{4\pi L f^2}. \quad (3)$$

The coherence function presented in Fig. 5 is an indication of the quality of the FRF measurements. A value of zero means no correlation between the impulse signal and the response. A value of one indicates that the response is completely explained by the impulse signal and that there is no other interference. The coherence function is determined from the average of five individual FRF measurements at each temperature. Based on the coherence function, a minimum limit of the usable frequency range to characterize the complex modulus is set to 500 Hz for all temperatures except -20.5°C and -24.4°C . At these temperatures, there is some interference up to approximately 4000 Hz, which is set as a minimum limit for these temperatures. The coherence function (CF) is calculated according to Eq. (4),

$$CF = \frac{\left| \overline{X^*(f) \times Y(f)} \right|^2}{\left(\overline{X^*(f) \times X(f)} \right) \times \left(\overline{Y^*(f) \times Y(f)} \right)}, \quad (4)$$

where $\overline{X^*(f) \times Y(f)}$ = averaged cross power spectrum, $\overline{X^*(f) \times X(f)}$ = averaged auto power spectrum (impulse), and $\overline{Y^*(f) \times Y(f)}$ = averaged auto power spectrum (response).

C. Theoretical determination of the frequency response function

The theoretical frequency response analysis of the specimen was performed by using a finite element program (COMSOL MULTIPHYSICS 4.2, 1998), where the specimen was

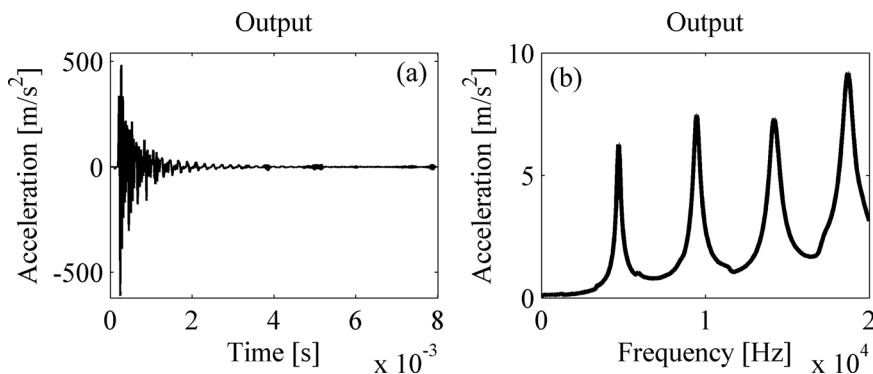


FIG. 3. The measured response of the specimen in time domain (a) and frequency domain (b).

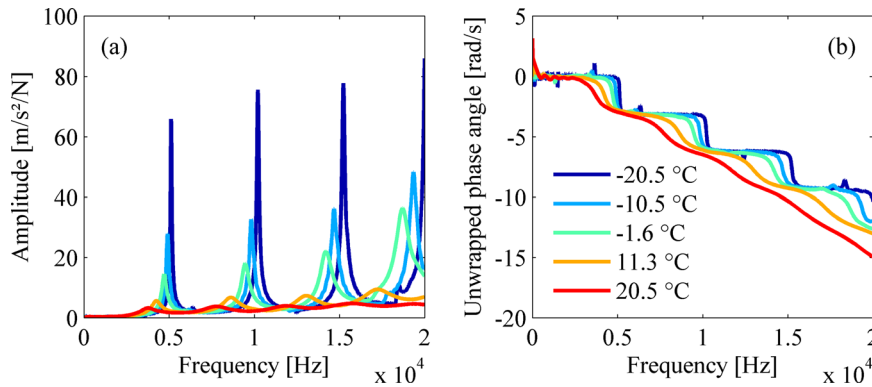


FIG. 4. (Color online) Measured FRFs of the longitudinal vibration modes (a) and the unwrapped phase angle of the measured FRFs (b).

modeled as a 3D linear isotropic viscoelastic material. The viscoelastic parameters of the material are described using the Havriliak–Negami model according to Eq. (5) (Havriliak and Negami, 1966) and the relationship of Poisson’s ratio [Eq. (6)] from the National Cooperative Highway Research Project’s *Guide for Mechanistic-Empirical Design* (NCHRP, 2004),

$$E^* = E_\infty + \frac{(E_0 - E_\infty)}{[1 + (i\omega\tau)^\alpha]^\beta}, \quad (5)$$

where E_0 is the low frequency modulus (Pa), E_∞ is the high frequency modulus (Pa), α governs the frequency dependency, β governs the asymmetry of the loss peak, τ is the relaxation time (s), i is the complex number, and $\omega = 2\pi f$ where f is the frequency (Hz);

$$\nu = 0.15 + \frac{0.35}{1 + e^{(a+b \times \log(|E^*|))}}, \quad (6)$$

where a and b are material constants.

The Havriliak–Negami model has been chosen instead of the sigmoidal function, commonly applied to asphalt concrete (Brown *et al.*, 2009), due to the model’s ability to characterize the complex modulus. The sigmoidal function describes only the dynamic modulus and is therefore not able to characterize the complete viscoelastic behavior of the material (Yusoff *et al.*, 2011). Furthermore, the Havriliak–Negami model can account for an asymmetrical loss peak and has proven to be very accurate in modeling the behavior of viscoelastic materials (Hartmann *et al.*, 1994; Madigosky *et al.*, 2006). Another important advantage with the Havriliak–Negami model is that it has relatively few parameters to estimate in an optimization

process compared to other models commonly applied to asphalt concrete (Yusoff *et al.*, 2011).

A convergence study of the finite element model was performed to determine a sufficient maximum element size for good accuracy and to minimize the computational time. Figure 6 presents the finite element simulation of different mesh sizes for the fourth resonance frequency of the longitudinal vibration mode. The fourth resonance is presented because it is more sensitive to the mesh size than the lower resonance frequencies. In Fig. 6, it can be seen that results converges at a mesh size of 2 cm (2455 number of elements). The mesh of the finite element model (shown in Fig. 7) was built up by tetrahedral elements with quadratic shape functions.

The frequency response simulation of the specimen was performed by applying a unit force (1 N) in the x direction (see Fig. 7) at the center point of the y - z plane (0, 29.37, 29.47 mm). The force was applied over a frequency range of 100–20 000 Hz in steps of 20 Hz. The response of the simulation was obtained from the center point 382, 29.37, 29.47 mm. These points of the specimen correspond to the real load impulse and where the accelerometer was attached in the real measurements.

D. Optimization of the frequency response functions

The time-temperature superposition principle (TTSP) allows results from measurements at different temperatures and frequencies to be shifted to a single master curve expressed at a specific reference temperature or reference frequency (Brown *et al.*, 2009). Materials to which the TTSP can be applied are classified as thermorheological simple materials. In the Havriliak–Negami model, it is assumed that

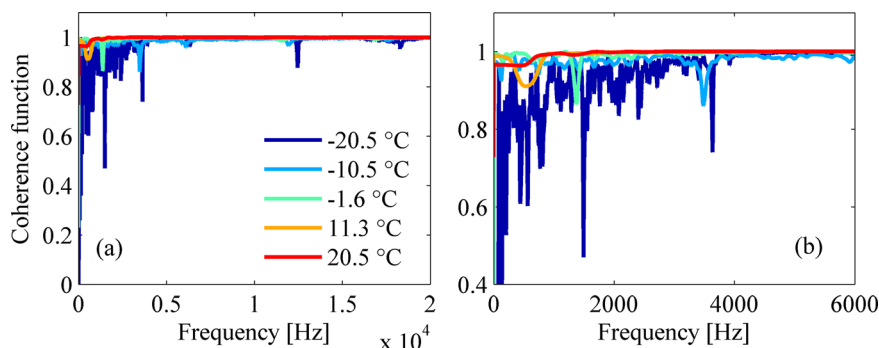


FIG. 5. (Color online) The coherence function of the measured FRFs (a) and a zoom of the lower frequency area (b).

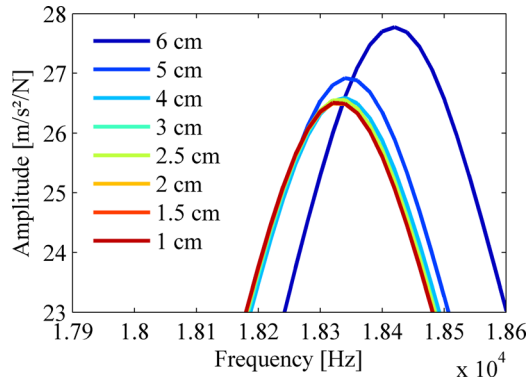


FIG. 6. (Color online) Convergence study of the finite element mesh.

the relaxation time (τ) is the only temperature dependent parameter (Madigosky *et al.*, 2006). This means that if the material is thermorheologically simple, the relaxation time is the only parameter that needs to be determined uniquely for each tested temperature. All other parameters in the Havriliak–Negami model should be able to be estimated to the same value for each temperature if the TTSP is applicable. Therefore theoretical FRFs are optimized against all measured FRFs simultaneously to estimate the complex modulus master curve through one single simulation. This is performed by substituting the Williams–Landel–Ferry equation [Eq. (7)] into the Havriliak–Negami model [see Eq. (8)]. By this, the shift factors allow the relaxation time (τ) to be unique for each temperature while all other parameters take the same values for all temperatures. A similar approach has been applied by Ren *et al.* (2011),

$$\log \alpha_T(T) = \frac{-c_1(T - T_{ref})}{c_2 + T - T_{ref}}, \quad (7)$$

where $\alpha_T(T)$ is the shift factor, T is the test temperature, T_{ref} is the reference temperature, and c_1 and c_2 are material constants (Williams *et al.*, 1955),

$$E^* = E_\infty + \frac{(E_0 - E_\infty)}{[1 + (i\omega\alpha_T(T)\tau)^{\alpha\beta}]^\beta}. \quad (8)$$

The FRF optimized complex modulus master curve is in this paper also compared to complex moduli results obtained through optimizing the FRFs separately by estimating the

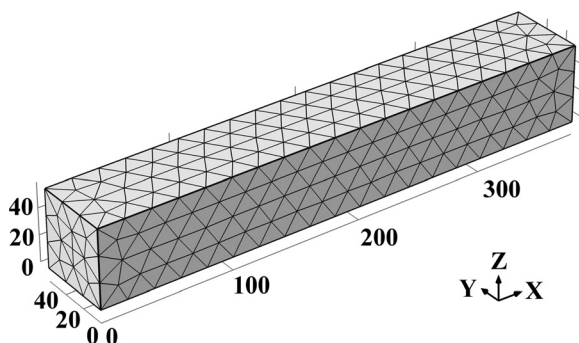


FIG. 7. The mesh of the finite element model.

four parameters E_∞ , α , β , and τ for each test temperature [using Eq. (5)]. This comparison is performed to investigate the accuracy of the estimated master curve against results of the best possible matches of measured and theoretical FRFs.

MATLAB and the finite element program COMSOL MULTIPHYSICS 4.2 were used to perform the optimization of the FRFs. The frequency response simulations in the finite element program were combined with the *patternsearch* function in MATLAB, allowing an update of the model parameters by minimizing the error between the measured and theoretical FRFs. The *patternsearch* function has been found to be efficient in finding the global minimum for optimization of FRFs (Ren *et al.*, 2011). The following objective function [Eq. (9)] was used for the optimization of the FRFs, where the normalized measured FRF were used to weigh frequencies around the resonance peaks of the specimen higher. Other objective functions were also tested for the optimization process leading to similar results. The error was calculated for 60 points (frequencies) distributed over the three first resonance frequencies of the FRFs,

$$\text{Error} = \sum_{i=1}^N \left(|H_{MNorm_i}| \times \left| \frac{|H_{M_i}| - |H_{T_i}|}{|H_{M_i}|} \right| \right), \quad (9)$$

where H_{MNorm} = normalized measured frequency response function, H_M = measured frequency response function, H_T = theoretical frequency response function, N = number of data points, and i = index of the data point.

III. RESULTS AND DISCUSSIONS

A. Validation of the FEM optimization method

The method of optimizing FRFs was first applied to a PVC-U beam for measurements performed at a temperature of 21 °C. The reason for using a PVC-U specimen as validation of the method is that the material is homogenous with a relatively small frequency dependency. The specimen was modeled by the following simple relationship,

$$E^* = E_1(1 + \eta i) \quad (10)$$

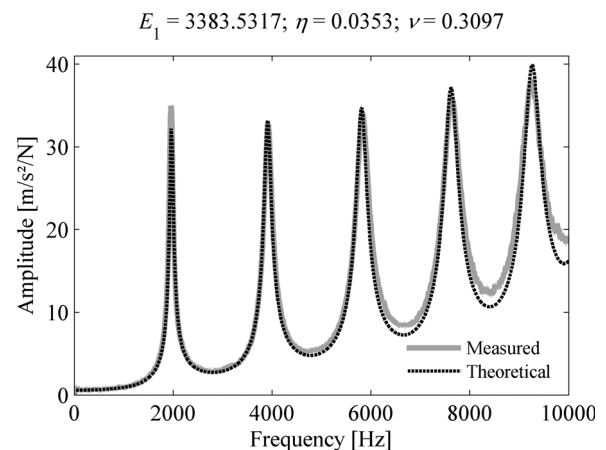


FIG. 8. The measured and fitted theoretical FRF of the beam shaped PVC-U specimen.

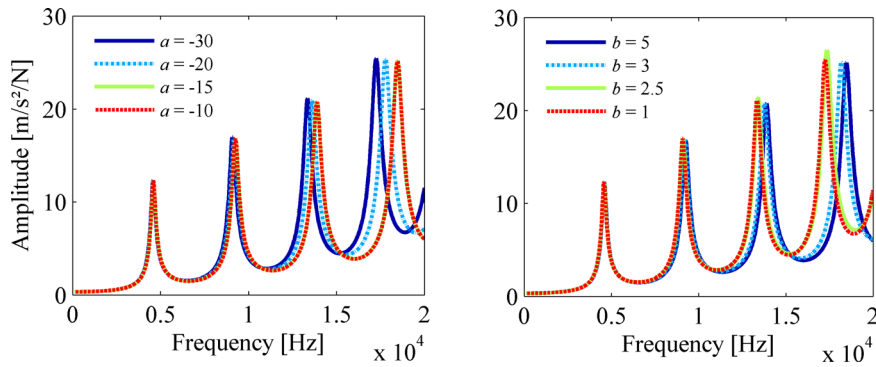


FIG. 9. (Color online) The influence of the parameters a and b in the relationship of Poisson's ratio [Eq. (6)] to the FRFs.

Values of the storage modulus (E_1), the loss factor (η), and Poisson's ratio (ν), giving the best possible match between the FRFs, were estimated in the optimization process. The match of the theoretical FRF of the PVC-U specimen to the measured FRF is presented in Fig. 8. The optimization of the FRF resulted in a dynamic modulus (E^*) of 3385.53 MPa and a Poisson's ratio of 0.31. This result is comparable to statically determined elastic moduli of PVC-U material reported in literature to be in the range of 2600 to 3300 MPa (Motavalli *et al.*, 1993).

B. Parameter analysis

Figure 9 presents a parameter analysis of Poisson's ratio where it can be seen that the FRFs at the lower half of the frequency range are not so sensitive to the coefficients a and b in the used Poisson's ratio relationship [Eq. (6)]. This may aggravate an accurate estimation of Poisson's ratio if a wider frequency range is not used to match the FRFs.

A parameter study of the low frequency modulus (E_0) showed that this parameter has a negligible influence of the FRFs for reasonable values of asphalt concrete. The low frequency modulus was therefore set to a fixed value of 100 MPa. This specific value is based on falling weight deflectometer measurements performed by Ullidtz *et al.*

(2006), where the measurements resulted in a dynamic modulus higher than 100 MPa for all tested temperatures in field.

C. Results of the complex modulus and Poisson's ratio

Frequency ranges covering the three first resonance frequencies have been used to estimate the complex moduli at the different temperatures. However, the parameter study of the influence of Poisson's ratio to the FRFs showed that Poisson's ratio has a larger influence on higher resonance frequencies (Fig. 9). Thus using the three first longitudinal resonance frequencies was shown to not be enough to accurately evaluate the coefficients a and b in Eq. (6). These coefficients were therefore chosen to values of $a = -19$ and $b = 2.95$ (Gudmarsson *et al.*, 2012). These values might not provide the best possible match of the FRFs, but they give a reasonable estimation of Poisson's ratio. Moreover these fixed values still contribute to a good match between theoretical and measured FRFs (Fig. 10), which supports the previous approximation of the material constants a and b for this specimen.

Figure 10 shows the match of the optimized FRFs to the measured FRFs for four test temperatures. The figure presents the results of the directly estimated master curve through optimization of all FRFs simultaneously [Eq. (8)] as well as results of the FRFs optimized for each temperature separately [Eq. (5)]. A good match is seen especially for the individual optimized FRFs [Eq. (5)] but also the optimization of all FRFs simultaneously (Eq. (8)) shows a satisfying match. These results show that the optimization method can accurately describe the frequency dependent dynamic properties of an asphalt concrete specimen. Table II presents the resulting parameter values of the FRF optimized master curve using Eq. (8).

The resulting dynamic moduli (the absolute value of the complex moduli) based on optimizing the FRFs for each temperature separately [Eq. (5)] is presented in Fig. 11 along with the dynamic moduli determined using

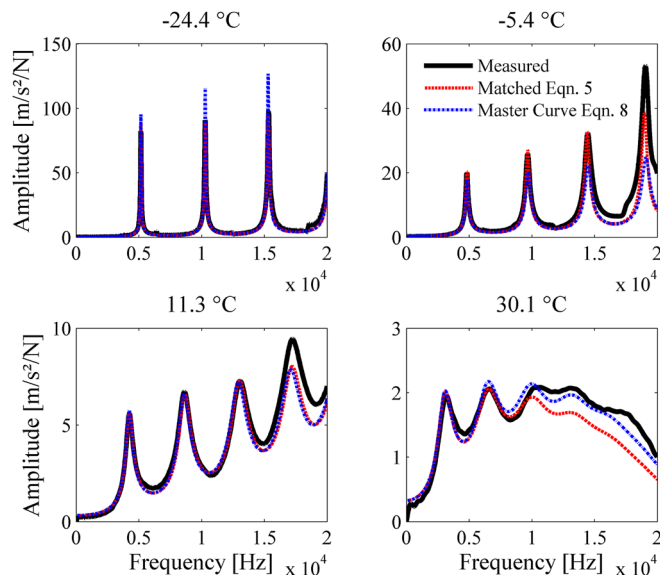


FIG. 10. (Color online) Measured and matched theoretical FRFs.

TABLE II. Estimated master curve parameters through optimization of all FRFs simultaneously (where $E_0 = 100$ MPa, $a = 19$, $b = 2.95$ and $T_{ref} = 0^\circ\text{C}$).

Parameter	E_∞	α	β	τ	c_1	c_2
Value	37723e6	0.4239	0.3163	4.5072	14.9947	82.4206

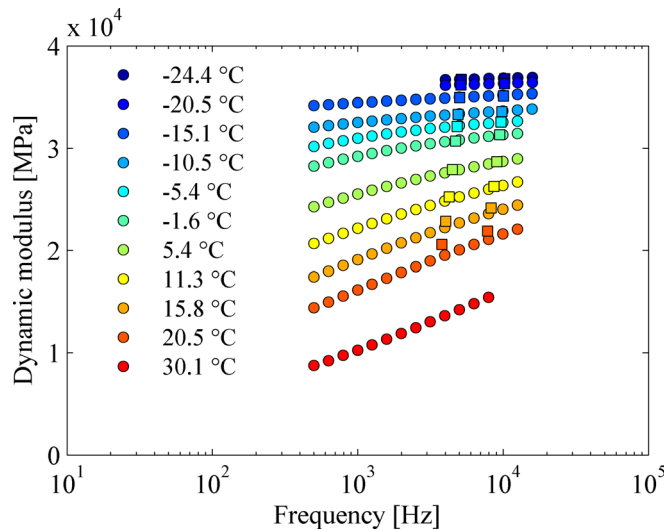


FIG. 11. (Color online) The results of the dynamic modulus using FRFs (○) and RAS (□).

RAS (Gudmarsson *et al.*, 2012). The FRFs optimized moduli are estimated over a frequency range of minimum 500 Hz to maximum 181000 Hz through the separately matched FRFs. Table III presents values of the dynamic modulus for some intermediate frequencies. A good agreement between optimization of FRFs and RAS are seen at lower temperatures. However, at higher temperatures, the agreement is worse. A reason for the difference between the methods at the higher temperatures could be due to limitations with the half-power bandwidth method. This method has been used to estimate the damping when applying RAS to a viscoelastic material (Gudmarsson *et al.*, 2012). Recent work by Wang *et al.* (2012) has showed that the half-power bandwidth method may overestimate the damping for multi-DOF systems. An overestimation of the damping leads to a higher modulus as can be seen in this case at the higher temperatures. Furthermore, Wang (2011) showed that the half-power bandwidth method is quite accurate for damping ratios less than 0.1 but that the accuracy of the method decreases with increasing damping ratios. Therefore the accuracy of the RAS determined moduli may decrease when the damping in the specimen increases with increasing tem-

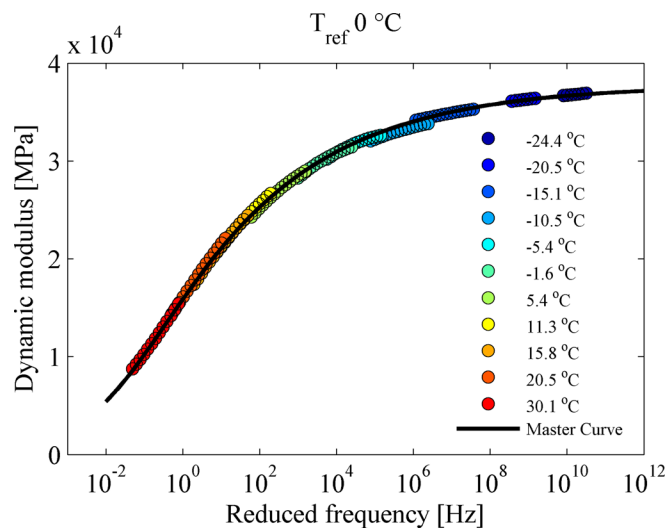


FIG. 12. (Color online) The dynamic modulus master curve determined through optimization of all FRFs simultaneously and the shifted dynamic moduli determined using optimization of the FRFs for each temperature separately.

peratures. At the highest test temperature (30.1 °C), it was not possible to estimate the complex moduli using RAS due to the high damping in the material.

Figures 12 and 13 present the master curve determined by optimizing all FRFs at different temperatures simultaneously using Eq. (8) as well as the estimated moduli for each set of temperatures using Eq. (5) plotted against the reduced frequency. The master curve has been expressed over a frequency range of 10^{-2} to 10^{12} Hz. The dynamic modulus is shown in Fig. 12, and Fig. 13 shows the phase angle, which is defined as \tan^{-1} of the ratio between the loss and storage modulus. A small deviation between the two optimization approaches can be seen in the two figures. This indicates that the asphalt concrete specimen has some degree of deviance from a complete thermorheologically simple behavior. However, the fit may be considered well enough for engineering applications in pavement management and design.

The Cole-Cole diagram (Fig. 14) emphasizes any differences between the two optimization methods because

TABLE III. The dynamic modulus (in MPa) for different frequencies and temperatures determined through optimization of each FRF separately.

f (kHz) T (°C)	-24.4	-20.5	-15.1	-10.5	-5.4	-1.6	5.4	11.3	15.8	20.5	30.1
0.5	-	-	34177	32071	30183	28254	24262	20670	17392	14387	8729
1	-	-	34443	32524	30973	29218	25506	22160	19105	16129	10246
2	-	-	34685	32917	31595	30010	26618	23552	20730	17855	11886
3	-	-	34818	33124	31893	30404	27208	24316	21628	18841	12893
4	36687	36135	34909	33263	32080	30655	27602	24834	22237	19525	13626
6	36756	36219	35034	33446	32311	30973	28123	25530	23054	20462	14679
8	36805	36278	35120	33570	32456	31175	28468	26000	23604	21105	15436
10	36843	36324	35186	33662	32557	31321	28724	26350	24012	21590	-
12	36874	36362	35239	33736	32634	31432	28924	26628	24334	21978	-
14	36900	36394	35283	33796	32695	31521	29088	26857	24597	-	-
16	36923	36421	35322	33848	-	-	-	-	-	-	-
18	36923	36445	-	-	-	-	-	-	-	-	-

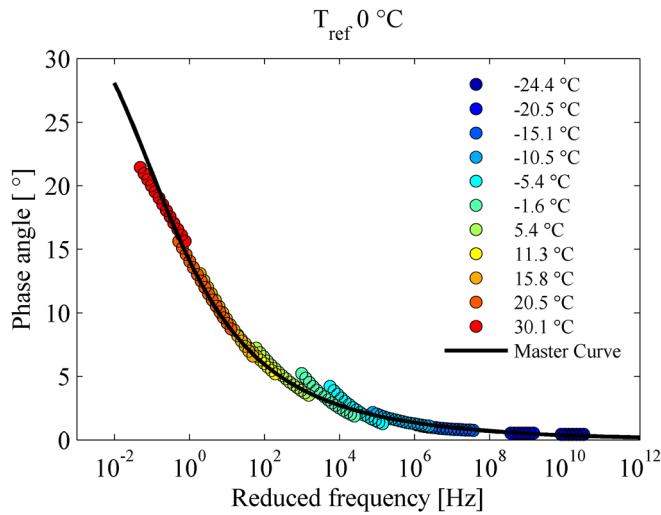


FIG. 13. (Color online) The phase angle master curve determined through optimization of all FRFs simultaneously and the shifted phase angle determined using optimization of the FRFs for each temperature separately.

this diagram is independent of any shift factors [Eq. (7)]. The results of the complex modulus at different frequencies and temperatures should all form a single curve in the Cole–Cole diagram if the material is thermorheologically simple (Cole and Cole, 1941; Levenberg, 2011). The Cole–Cole diagram of the complex moduli is a further indication of that constructing master curves using FRFs is a promising approach due to the relatively small deviation of the separately optimized FRFs to the FRF optimized master curve. The Cole–Cole figure also presents the results obtained by applying RAS to the same specimen. The difference (previously shown in Fig. 11) between the FRF optimization methods and RAS is highlighted in this figure. These results support the theory of the half-power bandwidth method being the reason for the deviation at higher temperatures between RAS and optimization of FRFs.

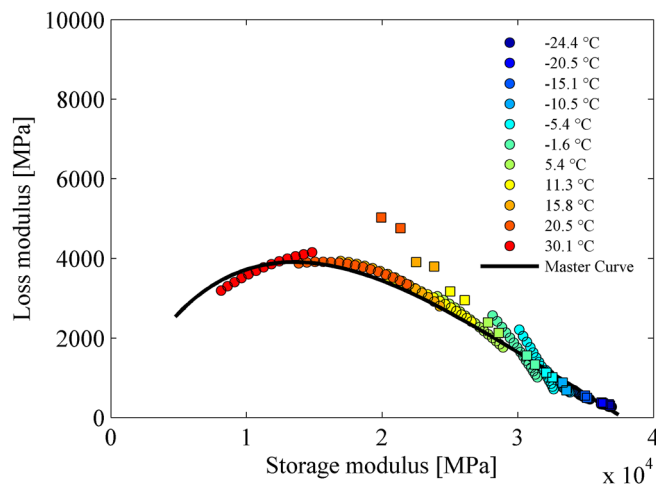


FIG. 14. (Color online) Cole–Cole diagram of the complex moduli determined for each temperature by optimizing the FRFs separately (○), determined by RAS (□), and by optimization all FRFs simultaneously (master curve).

IV. CONCLUSIONS

The method of optimizing FRFs is shown to be able to give a good fit between theoretical and measured FRFs and thereby accurately characterize the frequency dependent dynamic properties of an asphalt concrete specimen. The low strain complex modulus has been estimated over a frequency range of minimum 500 Hz to maximum 18000 Hz through the separately optimized FRFs. The FRF optimized master curve expresses the complex modulus over a wider frequency range, approximately between 10^{-2} and 10^{12} Hz. The separately estimated complex moduli are shown to have a relatively small deviation from a unique curve in the Cole–Cole space; this indicates that the method is promising in characterizing the master curve of an asphalt concrete specimen. The fixed values of the material constants of Poisson's ratio are an approximation that may be improved, although these values are shown to contribute to a good fit of the FRFs. An important benefit with the proposed FRF method is that it can be automated without any need for individual mode identification and also extend the frequency range used compared to the ASTM C215 standard and RAS.

ACKNOWLEDGMENTS

The Swedish transport administration and Swedish construction industry's organization (SBUF) are gratefully acknowledged for their financial support.

- ASTM (2008). C215-08, *Standard Test Method for Fundamental Transverse, Longitudinal, and Torsional Frequencies of Concrete Specimens* (American Society for Testing and Materials, West Conshohocken, PA).
- Brown, E. R., Kandhal, P. S., Roberts, F. L., Kim, Y. R., Lee, D. Y., and Kennedy, T. W. (2009). *Hot Mix Asphalt Materials, Mixture Design and Construction* (NAPA Research and Education Foundation, Lanham, MD).
- Buchanan, J. L. (1987). "Numerical solution for the dynamic moduli of a viscoelastic bar," *J. Acoust. Soc. Am.* **81**, 1775–1786.
- Cole, K. S., and Cole, R. H. (1941). "Dispersion and absorption in dielectrics. I. Alternating current characteristics," *J. Chem. Phys.* **9**, 341–351.
- COMSOL MULTIPHYSICS (1998). Version 4.2.
- Gudmarsson, A., Ryden, N., and Birgisson, B. (2012). "Application of resonant acoustic spectroscopy to asphalt concrete beams for determination of the dynamic modulus," *Mater. Struct.*, DOI:10.1617/s11527-012-9877-3.
- Guo, Q., and Brown, D. A. (2000). "Determination of the dynamic elastic moduli and internal friction using thin resonant bars," *J. Acoust. Soc. Am.* **108**(1), 167–174.
- Halvorsen, W. G., and Brown, D. L. (1977). "Impulse technique for structural frequency response testing," *J. Sound Vib. Nov. 1977*, pp. 8–21.
- Hartmann, B., Lee, G. F., and Lee, J. D. (1994). "Loss factor height and width limits for polymer relaxations," *J. Acoust. Soc. Am.* **95**, 226–233.
- Havriliak, S., and Negami, S. (1966). "A complex plane analysis of α -dispersions in some polymer systems," *J. Polym. Sci. C* **14**, 99–117.
- Kweon, G., and Kim, Y. R. (2006). "Determination of the complex modulus of asphalt concrete using the impact resonance test," *J. Transp. Res. Board* **1970**, 151–160.
- Lacroix, A., Kim, Y. R., and Far, M. S. S. (2009). "Constructing the dynamic modulus mastercurve using impact resonance testing," *Assoc. Asph. Paving Technol.* **78**, 67–102.
- Leisure, R. G., and Willis, F. A. (1997). "Resonant ultrasound spectroscopy," *J. Phys.: Condens. Matter* **9**, 6001–6029.
- Levenberg, E. (2011). "Smoothing asphalt concrete complex modulus test data," *ASCE J. Mater. Civ. Eng.* **23**(5), 606–611.
- Madigosky, W. M., Lee, G. F., and Niemiec, J. M. (2006). "A method for modeling polymer viscoelastic data and the temperature shift function," *J. Acoust. Soc. Am.* **119**, 3760–3765.
- Migliori, A., and Sarrao, J. L. (1997). *Resonant Ultrasound Spectroscopy—Applications to Physics, Materials Measurements and Nondestructive Evaluation* (Wiley–Interscience Publication, New York).

- Motavalli, M., Farshad, M., and Flüeler, P. (1993). "Buckling of polymer pipes under internal pressure." *Mater. Struct.* **26**, 348–354.
- NCHRP (2004). "Material characterization," in *Guide for Mechanistic-Empirical Design, Final Report. Part 2. Design Inputs* (National Cooperative Highway Research Project, St. Paul, MN), Chap. 2.
- Ostrovsky, L., Lebedev, A., Matveyev, A., Potapov, A., Sutin, A., Soustova, I., and Johnson, P. (2001). "Application of three-dimensional resonant acoustic spectroscopy method to rock and building materials," *J. Acoust. Soc. Am.* **110**(4), 1770–1777.
- Pasqualini, D. (2006). "Intrinsic nonlinearity in geomaterials: Elastic properties of rocks at low strain," in *Universality of Nonclassical Nonlinearity Applications to Non-Destructive Evaluations and Ultrasonic*, edited by P. P. Delsanto (Springer Science and Business Media, New York), pp. 417–423.
- Ren, Z., Atalla, N., and Ghinet, S. (2011). "Optimization based identification of the dynamic properties of linearly viscoelastic materials using vibrating beam technique," *ASME J. Vib. Acoust.* **133**(4), 041012.
- Renault, A., Jaouen, L., and Sgard, F. (2011). "Characterization of elastic parameters of acoustical porous materials from beam bending vibrations," *J. Sound Vib.* **330**, 1950–1963.
- Rupitsch, S. J., Ilg, J., Sutor, A., Lerch, R., and Döllinger, M. (2011). "Simulation based estimation of dynamic mechanical properties for viscoelastic materials used for vocal fold models," *J. Sound Vib.* **330**, 4447–4459.
- Ryden, N. (2011). "Resonant frequency testing of cylindrical asphalt samples," *Eur. J. Environ. Civ. Eng.* **15**, 587–600.
- Trafikverket (2009). "VVTBT Bitumenbundna lager 09" ("VVTBT Bituminous layers 09"), Publication 2009:140, Borlänge, Sweden.
- Ullidtz, P., Harvey, J., Tsai, B.-W., and Monismith, C. (2006). "Calibration of CalME models using WesTrack performance data," Report No. UCPRC-RR-2006-14 (Pavement Research Center, University of California, Berkeley, CA).
- Wang, I. (2011). "An analysis of higher order effects in the half power method for calculating damping," *J. Appl. Mech.* **78**, 014501.
- Wang, J.-T., Jin, F., and Zhang, C.-H. (2012). "Estimation error of the half-power bandwidth method in identifying damping for multi-DOF systems," *Soil Dyn. Earthquake Eng.* **39**, 138–142.
- Whitmoyer, S. L., and Kim, Y. R. (1994). "Determining asphalt concrete properties via the impact resonant method," *J. Test. Eval.* **22**(2), 139–148.
- Williams, M. L., Landel, R. F., and Ferry, J. D. (1955). "The temperature dependence of relaxation mechanisms in amorphous polymers and other glass-forming liquids," *J. Am. Chem. Soc.* **77**, 3701.
- Yusoff, N. I. Md., Shaw, M. T., and Airey, G. D. (2011). "Modelling the linear viscoelastic rheological properties of bituminous binders," *J. Constr. Build. Mater.* **25**(5), 2171–2189.

Paper III

Comparing Linear Viscoelastic Properties of Asphalt Concrete Measured by Laboratory Seismic and Tension– Compression Tests

ANDERS GUDMARSSON
NILS RYDEN
HERVÉ DI BENEDETTO
CÉDRIC SAUZÉAT
NOUFFOU TAPSOBA
BJÖRN BIRGISSON

Published in
Journal of Nondestructive Evaluation 33 (4)
571-582



Comparing Linear Viscoelastic Properties of Asphalt Concrete Measured by Laboratory Seismic and Tension–Compression Tests

Anders Gudmarsson · Nils Ryden · Hervé Di Benedetto ·
Cédric Sauzéat · Nouffou Tapsoba · Björn Birgisson

Received: 24 January 2014 / Accepted: 30 June 2014 / Published online: 16 July 2014
© Springer Science+Business Media New York 2014

Abstract Seismic measurements and conventional cyclic loading have been applied to a cylindrical asphalt concrete specimen to compare the complex modulus and complex Poisson's ratio between the two testing methods. The seismic moduli and Poisson's ratio have been characterized by optimizing finite element calculated frequency response functions to measurements performed at different temperatures. An impact hammer and an accelerometer were used to measure the frequency response functions of the specimen which was placed on soft foam for free boundary conditions. The cyclic loading was performed by applying both tension and compression to the specimen while measuring the displacements in the axial and radial direction. The Havriliak–Negami and the 2S2P1D model have been used to estimate master curves of the complex modulus and complex Poisson's ratio from the seismic and the tension–compression tests. The seismic measurements performed at a lower strain level than the tension–compression test give a higher absolute value of the complex moduli (e.g. $\sim 12\%$ at 100 Hz) and a lower phase angle compared to the tension–compression results.

Keywords Asphalt concrete · Complex modulus · Complex Poisson's ratio · Seismic measurements · Frequency response functions · Conventional cyclic loading

1 Introduction

The complex modulus of asphalt concrete is a fundamental parameter in pavement design. It is therefore important with an economic and accurate test method to measure the temperature and frequency dependent complex modulus of asphalt concrete. The high cost and complexity of performing conventional testing based on cyclic loading introduces a need for alternative methods that are more economical. Nondestructive seismic measurements are economic, simple to perform and well known for accurate characterization of materials properties in many different applications [1]. Furthermore, laboratory seismic testing can be directly compared to seismic field measurements, which enables nondestructive quality control of pavements [2].

Laboratory seismic testing of asphalt concrete to determine the complex moduli have been performed through wave propagation measurements [3–5] and by measurements of the asphalt concrete specimens fundamental resonance frequencies [6–8]. In these tests, simplified approximate formulations have been used to determine a complex modulus for each measurement temperature and mode type [9]. A wide range of mixtures have been tested and the results have shown a promising agreement to conventional cyclic loading test results of the Young's modulus, expressed over a wide frequency and temperature range (i.e. the master curve). However, seismic complex modulus determined only at one loading frequency per measurement temperature has been compared to conventional determined master curves. This sparse amount of seismic data points is a limitation of applying the simplified approximate fundamental mode formulations. Therefore, master curves cannot be estimated through these applications of seismic testing without additional test methods. Other seismic testing of asphalt concrete has applied three-dimensional numerical methods

A. Gudmarsson (✉) · N. Ryden · B. Birgisson
Highway and Railway Engineering, KTH Royal Institute
of Technology, Brinellvägen 23, 100 44 Stockholm, Sweden
e-mail: andgud@kth.se

H. Di Benedetto · C. Sauzéat · N. Tapsoba
Departement Génie Civil et Bâtiment, University of Lyon/Ecole
Nationale des Travaux Publics de l'Etat (ENTPE), Rue Maurice Audin,
69518 Vaulx-en-Velin, France

(resonant acoustic spectroscopy) to calculate resonance frequencies for different mode types of cylindrical discs and beams [10,11]. Although, resonant acoustic spectroscopy makes it possible to determine the complex modulus at several resonance frequencies per temperature, it may still not provide enough information to estimate a master curve for viscoelastic materials. Through the use of frequency response functions (FRFs) it has been shown that other viscoelastic materials can be characterized over a wide and fine sampled frequency range [12–14]. Therefore, the master curve estimation of asphalt concrete can be facilitated through FRF measurements of a specimen since the determination of the complex modulus is not limited to the resonance frequencies. Laboratory FRF measurements of asphalt concrete have shown to be a promising method to determine the complex modulus master curve [15]. The application of FRFs enables a detailed comparison between seismic and conventional measurements over a wider frequency range, where possible effects of different applied strain levels may be studied. This is interesting since e.g. Doubbaneh [16] showed that there is a reduction of the dynamic modulus with increasing strain levels between 30 and 800 micro-strains. These effects can be further studied down to strain levels around approximately 0.1 micro-strains [15] through the combination of seismic and tension–compression tests. However, a master curve of asphalt concrete based only on seismic measurements has previously not been compared to conventional cyclic loading test results. The combination of conventional and seismic testing has previously shown to be useful to improve the characterization of other materials as for example different types of sands [17,18].

In this paper, linear viscoelastic properties (complex modulus and complex Poisson's ratio) of an asphalt concrete specimen are determined through seismic measurements and conventional cyclic loading. The applied seismic test method includes measurements of FRFs at different temperatures and optimization of calculated FRFs against the measured FRFs to characterize the material properties. The cyclic test is performed by applying both tension and compression loading while measuring the axial and radial displacements of the specimen. Master curves of the complex modulus and complex Poisson's ratio estimated from both methods are then compared.

2 Methodology

The tests presented in this paper have been performed at the University of Lyon, Ecole Nationale des Travaux Publics

de l'Etat (ENTPE) in the laboratory of Departement Génie Civil et Bâtiment. The seismic testing was performed before the tension–compression test since the seismic measurements is completely nondestructive. The tension–compression test requires gluing of the top and bottom of the specimen, which disables further types of testing to the specimen without changing the dimensions of the specimen. The details of the materials and the two test procedures are presented in the following sections.

2.1 Materials

Seismic and tension–compression tests have been applied to a cylindrical shaped specimen with a height of 122.63 mm, diameter of 74.09 mm and a density of 2,607 kg/m³. The specimen was cored from a slab that was compacted by a French Roller Compactor at *Eiffage Travaux Publics* in France. The dimensions of the compacted slab were 600(122.63) × 400 × 120(74.09) mm, where the values in the parentheses shows the direction of the cored specimen within the slab. The roller moved over the slab in the direction of the longest side (600 mm)—hence the horizontal rolling direction was along the height of the specimen. The compacted asphalt mixture consists of aggregates with a gradation according to Table 1 and pure bitumen with penetration grade of 35–50. The binder content of the mix is 4.45 % by weight. The specific specimen has been a part of a round robin test organized by the RILEM technical committee 237-SIB: *Testing and characterization of sustainable innovative bituminous materials and systems*, where a number of different groups has performed complex modulus tests of specimens cored from roller compacted slabs of the same asphalt mixture (labeled GB3) [19].

2.2 Seismic Measurements

The applied method to characterize linear viscoelastic properties through seismic testing includes three parts; measurements of the FRFs, finite element calculations of FRFs and an optimization procedure to match calculated and measured FRFs.

2.2.1 Measuring FRFs

The test set-up of the seismic measurements is illustrated in Fig. 1. An impact hammer (PCB model 086E80) is used to manually apply a load impulse to the specimen and an accelerometer (PCB model 352B10), attached by wax, is

Table 1 Gradation of the asphalt concrete mixture (GB3)

Sieve size (mm)	0.063	0.125	0.25	0.5	1	2	3.15	4	5	6.3	10	12.5	14	16	20
% Passing	7.5	11	14	20	26	36	42	45	48	53	65	86	94	99	100

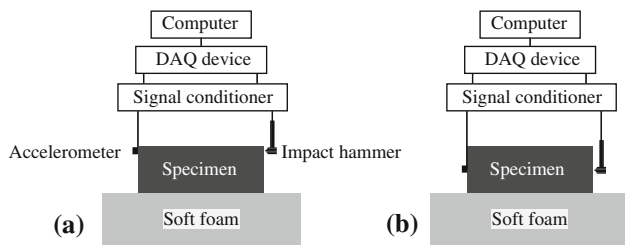


Fig. 1 Illustration of the seismic test set-up of the flexural (a) and longitudinal modes of vibration (b)

used to measure the standing wave modes. The weight of the accelerometer is 0.7 g and is assumed to not affect the response of the specimen. The specimen is placed on soft foam to achieve free boundary conditions [6]. A signal conditioner (PCB model 480B21), a data acquisition device (NIDAQPad-6015) and a computer are connected to the hammer and the accelerometer according to Fig. 1. The sampling frequency, which is depending on the data acquisition device, was in these measurements set to 90 kHz.

The measurements were performed at the temperatures of -21.0 , -1.0 , 14.5 , 19.2 , 29.2 and 39.3 °C while the specimen was located inside a temperature chamber. The door to the chamber was opened to manually apply the load. This caused a small change of the temperature inside the chamber but it is assumed that the temperature of the specimen was not changed during the short time of the measurements (~ 10 to 20 s). The flexural mode of vibration was measured by placing the accelerometer at the edge of one of the two short sides of the specimen while hitting the opposite point on the other short side with the hammer (see Fig. 1a). For the longitudinal mode the impact and the measurement point were positioned opposite to each other in the middle of the two

short sides (illustrated by Fig. 1b). The flexural and the longitudinal modes of vibration of the cylindrical specimen were excited by five impacts each and a FRF has been calculated from the average of these five impacts for each measurement temperature. Figure 2a shows the measured acceleration in time domain at -21.0 °C for the flexural and the longitudinal mode of vibration. Note in Fig. 2a that the record length of the response is chosen depending on the temperature due to the increasing damping for increasing temperatures of asphalt concrete. Figure 2b shows the measured FRF and Fig. 2c the coherence function where a value of one means that the response is completely explained by the load impulse. The main deviations from one in the coherence function presented in Fig. 2c coincide with amplitude minimum in the measured FRF at frequencies where there is little amount of energy. The FRFs of the specimen at each temperature were calculated according to Eq. 1,

$$H(f) = \left(\overline{Y(f) \cdot X^*(f)} \right) / \left(\overline{X(f) \cdot X^*(f)} \right), \tag{1}$$

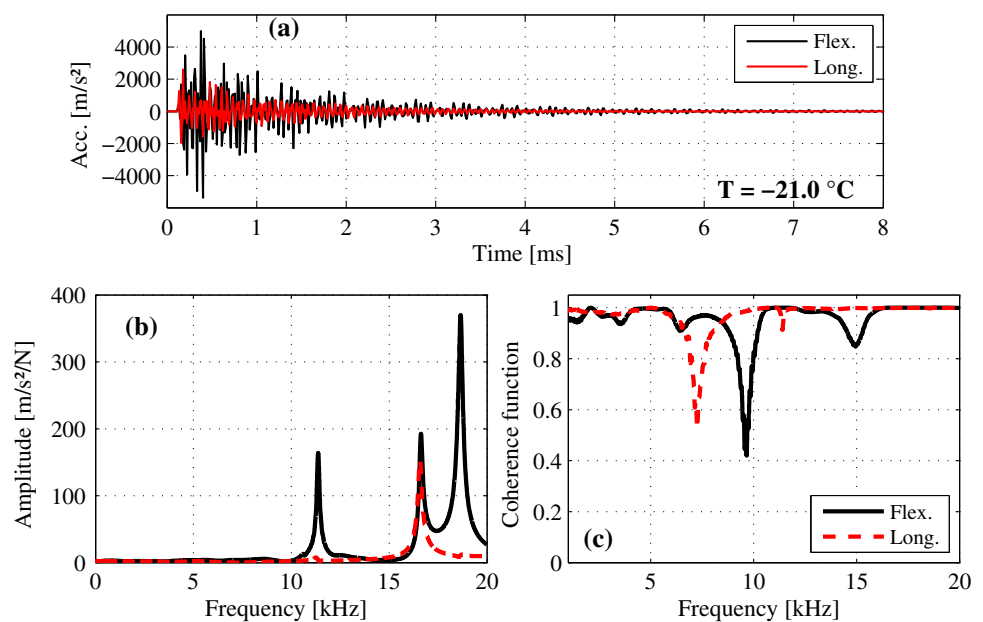
where $H(f)$ is the FRF, $Y(f)$ is the measured acceleration, $X(f)$ is the measured applied force, $X^*(f)$ is the complex conjugate of the applied force and the bar above represents the arithmetic mean.

2.2.2 Calculating Theoretical FRFs

Theoretical FRFs have been calculated through the finite element method, using the following three-dimensional equation of motion in frequency domain [20],

$$-\rho\omega^2 \mathbf{u} - \nabla \cdot \boldsymbol{\sigma} = F_p e^{i\phi}, \tag{2}$$

Fig. 2 The measured dynamic response of the asphalt concrete specimen in time domain (a), the frequency response function (b) and the coherence function (c) at -21.0 °C



where ρ is the density, ω is the angular frequency ($\omega = 2\pi f$), \mathbf{u} is the displacement vector, ∇ is the vector operator ($\nabla = [\partial/\partial X, \partial/\partial Y, \partial/\partial Z]$), i is the square root of -1 and σ is the Cauchy stress tensor according to Eq. 3;

$$\begin{aligned} \sigma &= \mathbf{C} : \varepsilon \\ \varepsilon &= \frac{1}{2} [(\nabla \mathbf{u})^T + \nabla \mathbf{u}], \\ \nabla \mathbf{u} &= \begin{bmatrix} \frac{\partial u}{\partial X} & \frac{\partial u}{\partial Y} & \frac{\partial u}{\partial Z} \\ \frac{\partial v}{\partial X} & \frac{\partial v}{\partial Y} & \frac{\partial v}{\partial Z} \\ \frac{\partial w}{\partial X} & \frac{\partial w}{\partial Y} & \frac{\partial w}{\partial Z} \end{bmatrix} \end{aligned} \quad (3)$$

where \mathbf{C} is the fourth-order stiffness tensor built up by the complex modulus (E^*) and complex Poisson's ratio (v^*), ε is the strain tensor, the “:” is the double contraction operator [21], (X, Y, Z) are the constant material (reference) coordinates and (u, v, w) are the global Cartesian components of the displacement vector \mathbf{u} . F_p is a point load equal to 1 N and ϕ is the phase of the cyclic load [20].

The point load in the model has been applied to the corresponding points of the hammer impact in the measurements of the flexural and longitudinal modes of vibration. Similarly, the response has been determined at the points corresponding to the actual placement of the accelerometer. The computation of the model was performed in steps of 20 Hz in a frequency range of 100–20,000 Hz. The mesh consists of tetrahedral elements with a maximum element size of 2 cm and quadratic shape functions. The maximum element size was determined through a convergence study.

2.2.3 Optimizing FRFs

The complex modulus and complex Poisson's ratio are estimated by optimizing the finite element calculated FRFs against the measured FRFs. For this purpose any appropriate model to characterize the linear viscoelastic properties of asphalt concrete can be used [22]. In this paper, the complex modulus and complex Poisson's ratio is expressed by the 2S2P1D model [23] and the Havriliak–Negami (HN) model [24] to include a comparison between these models capability to characterize the behavior of asphalt concrete. This is interesting since fewer parameters in the models reduce the computational time which gives a practical advantage when optimizing FRFs. The HN and 2S2P1D models consist of five and seven parameters, respectively.

The 2S2P1D model has shown to be able to match cyclic tension–compression measured complex modulus and complex Poisson's ratio of asphalt concrete with good accuracy [23, 25, 26]. 2S2P1D stands for two springs, two parabolic elements and one dashpot and the complex modulus (E^*) is expressed according to Eq. 4, as it was presented by Olard and Di Benedetto [23]:

$$E^*(\omega) = E_0 + \frac{(E_\infty - E_0)}{1 + \delta(i\omega\tau)^{-k} + (i\omega\tau)^{-h} + (i\omega\beta_\eta\tau)^{-1}}, \quad (4)$$

where E_0 is the static/low frequency modulus when $\omega \rightarrow 0$, E_∞ is the high frequency modulus when $\omega \rightarrow \infty$, δ is a constant, k and h are exponents according to $0 < k < h < 1$, β_η is dimensionless giving the Newtonian viscosity (η) according to $\eta = (E_0 - E_\infty)\beta_\eta\tau$, and τ is characteristic time depending only on the temperature.

Di Benedetto et al. [26] extended the 2S2P1D model to characterize complex Poisson's ratio (v^*) giving Eq. 5,

$$v^*(\omega) = v_0 + \frac{(v_\infty - v_0)}{1 + \delta(i\omega\tau_v)^{-k} + (i\omega\tau_v)^{-h} + (i\omega\beta_\eta\tau_v)^{-1}}, \quad (5)$$

where v_0 is the low frequency Poisson's ratio when $\omega \rightarrow 0$ and v_∞ is the high frequency Poisson's ratio when $\omega \rightarrow \infty$. Note that the same value of the parameters δ, k, h , and β_η are used to determine both the complex modulus and complex Poisson's ratio in the 2S2P1D model [26], while τ is determined uniquely for Poisson's ratio and is therefore labeled here as τ_v .

The HN model is known to accurately model viscoelastic materials [24, 27, 28], and has previously been applied to characterize the complex modulus of asphalt concrete through seismic testing [15]. The HN model has also been applied to match conventional complex moduli measurements [29]. Equation 6 presents the formulation of the HN model applied in this paper,

$$E^*(\omega) = E_\infty + \frac{(E_0 - E_\infty)}{[1 + (i\omega\tau)^\alpha]^\beta}, \quad (6)$$

where α describes the frequency dependency, β governs the asymmetry of the loss factor peak, and τ is the relaxation time.

The empirical HN model is here also formulated to characterize a complex Poisson's ratio according to Eq. 7,

$$v^*(\omega) = v_\infty + \frac{(v_0 - v_\infty)}{[1 + (i\omega\tau_v)^{\alpha_v}]^{\beta_v}}, \quad (7)$$

where α_v, β_v and τ_v governs the same factors as in Eq. 6, but for complex Poisson's ratio instead of the complex modulus.

Through the Eqs. 4–7, the complex modulus and complex Poisson's ratio can be estimated so that calculated FRFs matches the measured FRFs for each measurement temperature. Similarly, master curves can be directly optimized by adding temperature dependent shift factors to the Eqs. 4–7. This operation is based on the assumption that the material is thermo-rheological simple, which is often true for asphalt concrete [15, 23, 25, 26, 30]. Thermo-rheological simple means that the material properties measured at a low temperature and low frequency are the same at a higher temperature and higher frequency, or vice versa. Thus, measurements at different temperatures or frequencies can be shifted to a single continuous curve (i.e the master curve). This means that all of the FRFs measured at different temperatures can be used simultaneously to directly estimate the master curves.

Equation 8 presents the complex modulus of the HN model where the Williams–Landel–Ferry shift factors (α_T) have been substituted to Eq. 6 to include the temperature dependency of the material,

$$E^*(\omega, T) = E_\infty + \frac{(E_0 - E_\infty)}{[1 + (i\omega\alpha_T(T)\tau)^\alpha]^\beta}. \tag{8}$$

The same approach has been applied to the HN model of complex Poisson’s ratio (Eq. 7) and to the 2S2P1D model for both complex modulus (Eq. 4) and complex Poisson’s ratio (Eq. 5). Equation 9 presents the Williams-Landel-Ferry equation used to calculate the shift factors,

$$\log \alpha_T(T) = \frac{-c_1(T - T_{ref})}{c_2 + T - T_{ref}}, \tag{9}$$

where T is the test temperature, T_{ref} is the reference temperature and c_1 and c_2 are material constants [31].

COMSOL Multiphysics 4.3 and MATLAB were used to perform the optimization of the FRFs. The theoretical FRFs were calculated in COMSOL and the *pattnsearch* function in MATLAB was applied to automatically and objectively minimize the difference between the measured and calculated FRFs. The following objective function was used to minimize the error between the FRFs,

$$Error = \sum_{i=1}^N \left(\left| H_{MNorm_i} \right| \times \left| \frac{|H_{M_i}| - |H_{T_i}|}{|H_{M_i}|} \right| \right), \tag{10}$$

where H_{MNorm} is the normalized measured FRF, H_M is the measured FRF, H_T is the theoretical FRF, N is the number of data points and i is the index of the data point. 40 frequencies were used to calculate the error and normalized measured FRFs were used to weigh the frequencies around the resonances higher.

2.3 Tension–Compression Measurements

Figure 3 show the set-up for the cyclic (sinusoidal) loading test to determine the complex modulus and complex Poisson’s ratio. The top and bottom of the specimen is glued so both tension and compression loading can be applied. The axial stresses ($\sigma_1^* = \sigma_1 \cdot e^{i(\omega t + \phi_E)}$) are determined from a load cell and the axial strains ($\varepsilon_1^* = \varepsilon_1 \cdot e^{i\omega t}$) are determined from the average of three extensometers placed in the middle part of the specimen, measuring the displacements in the vertical direction. The extensometers have a length of 75 mm and are positioned around the specimen with a 120° distance between each other. Two non-contact sensors placed horizontally measures the radial strains ($\varepsilon_2^* = -\varepsilon_2 \cdot e^{i(\omega t + \phi_v)}$). The complex modulus at different loading frequencies and temperatures are calculated according to Eq. 11,

$$E^*(\omega) = \frac{\sigma_1^*}{\varepsilon_1^*} = |E^*(\omega)| e^{i\phi_E}, \tag{11}$$



Fig. 3 Test set-up of the tension–compression complex modulus and complex Poisson’s ratio measurements

and complex Poisson’s ratio according to Eq. 12,

$$v^*(\omega) = -\frac{\varepsilon_2^*}{\varepsilon_1^*} = |v^*(\omega)| e^{i\phi_v}, \tag{12}$$

where ϕ_E and ϕ_v is the phase angle of the complex modulus and complex Poisson’s ratio, respectively [19,26]. The tension–compression test was performed by controlling the strain amplitude to 50 $\mu\text{m/m}$.

The tension–compression test was performed at nine temperatures between -30 and 40 °C and at seven loading frequencies (0.01, 0.03, 0.1, 0.3, 1, 3 and 10 Hz). From these tests, the 2S2P1D and the HN model were used to determine the master curves of the complex modulus and complex Poisson’s ratio.

3 Results and Discussion

3.1 Tension–Compression Test Results

The tension–compression determined complex moduli and complex Poisson’s ratio is presented in Figs. 4 and 5, respectively. The nine measurements temperatures enabled the complex moduli to be determined over a wide frequency range. The Cole–Cole diagram (Fig. 4c) shows a good continuity of the measurements performed at different temperatures, which indicates a good accuracy of the test. In Fig. 5b and c there is some scatter visible in the measured complex Poisson’s ratio, where all the deviating points are the results

Fig. 4 Tension–compression complex modulus test results, where the 2S2P1D model and the Havriliak–Negami model have been fitted to the measurements. **a** presents the master curve of the absolute value of the complex modulus, **b** the phase angle master curve and **c** the Cole–Cole diagram of the complex modulus

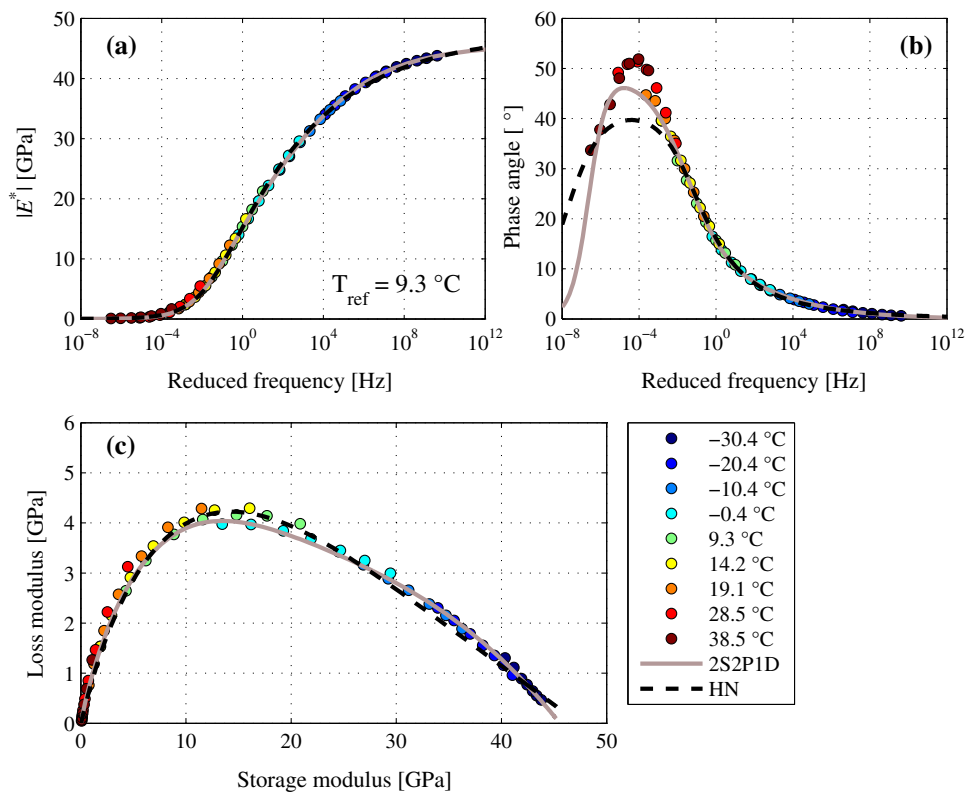
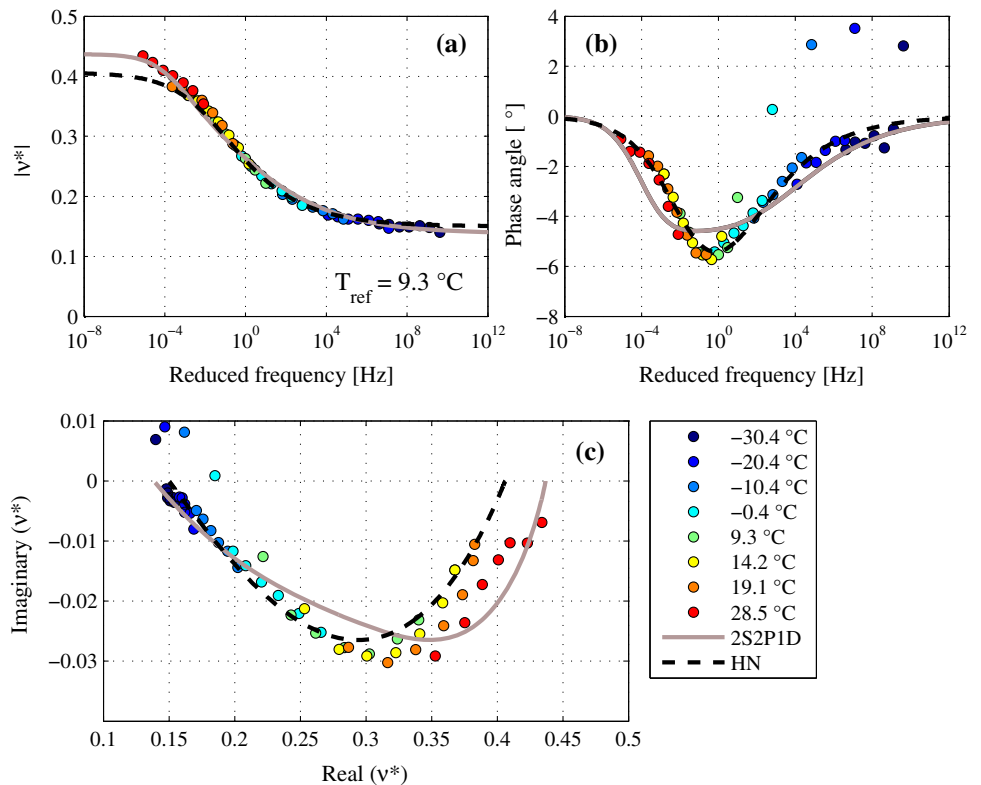


Fig. 5 Tension–compression complex Poisson’s ratio test results, where the 2S2P1D model and the Havriliak–Negami model have been fitted to the measurements. **a**) presents the master curve of the absolute value of complex Poisson’s ratio, **b** the phase angle master curve and **c** the Cole–Cole diagram of complex Poisson’s ratio



from measurements at 10 Hz. These points have not been considered in the fit of the HN and 2S2P1D master curves. Both of the applied models (HN and 2S2P1D) provide a good fit of the master curve to the absolute values of the complex mod-

ulus as can be seen in Fig. 4a. The models also give a similar fit in the Cole–Cole diagram (Fig. 4c). Regarding the phase angle presented in Fig. 4b, there is a noticeable difference of the models ability to match the phase angle at lower

Table 2 Estimated parameter values of the HN model to match the tension–compression measurements

Model	E_0 (MPa)	E_∞ (MPa)	ν_0	ν_∞	α	β	τ (s)	c_1	c_2
HN (E^*)	11.31	47377	–	–	0.463	0.212	4.50	37.0	210.3
HN (ν^*)	–	–	0.406	0.150	0.316	0.578	7.02	37.0	210.3

Table 3 Estimated parameter values of the 2S2P1D model to match the tension–compression measurements

Model	E_0 (MPa)	E_∞ (MPa)	ν_0	ν_∞	δ	k	h	β_η	τ (s)	c_1	c_2
2S2P1D (E^*)	23.17	45556	–	–	1.95	0.164	0.534	777.9	1.59	37.0	210.3
2S2P1D (ν^*)	–	–	0.432	0.138	1.95	0.164	0.534	777.9	284.6	37.0	210.3

frequencies. This may be a consequence of the two extra parameters h and β_η in the 2S2P1D model compared to the HN model. The differences between the HN and 2S2P1D model seen in Fig. 5b and c of complex Poisson’s ratio is most likely due to that the HN model was applied with unique parameters for Poisson’s ratio while the 2S2P1D model was applied with the already estimated complex modulus parameters (except for τ) according to Di Benedetto et al. [26].

The estimated values of the unknown coefficients in the HN model are presented in Table 2 and the values for the 2S2P1D model are presented in Table 3. In total 12 unknown parameters have been estimated to match the HN model to the tension–compression measurements (five for the complex

modulus, five for complex Poisson’s ratio and two for the shift factors). 12 unknown parameters are also to be estimated when applying the 2S2P1D model (seven for the complex modulus, three for complex Poisson’s ratio and two for the shift factors). However, since the shift factors should be the same independent of the two models, the estimated shift factors from the HN model were applied to the 2S2P1D model reducing the unknown parameters to ten.

3.2 Seismic Test Results

Figure 6 show the measured and finite element calculated FRFs, where the theoretical FRFs have been calculated for

Fig. 6 Measured and finite element calculated FRFs of the flexural and the longitudinal modes of vibration

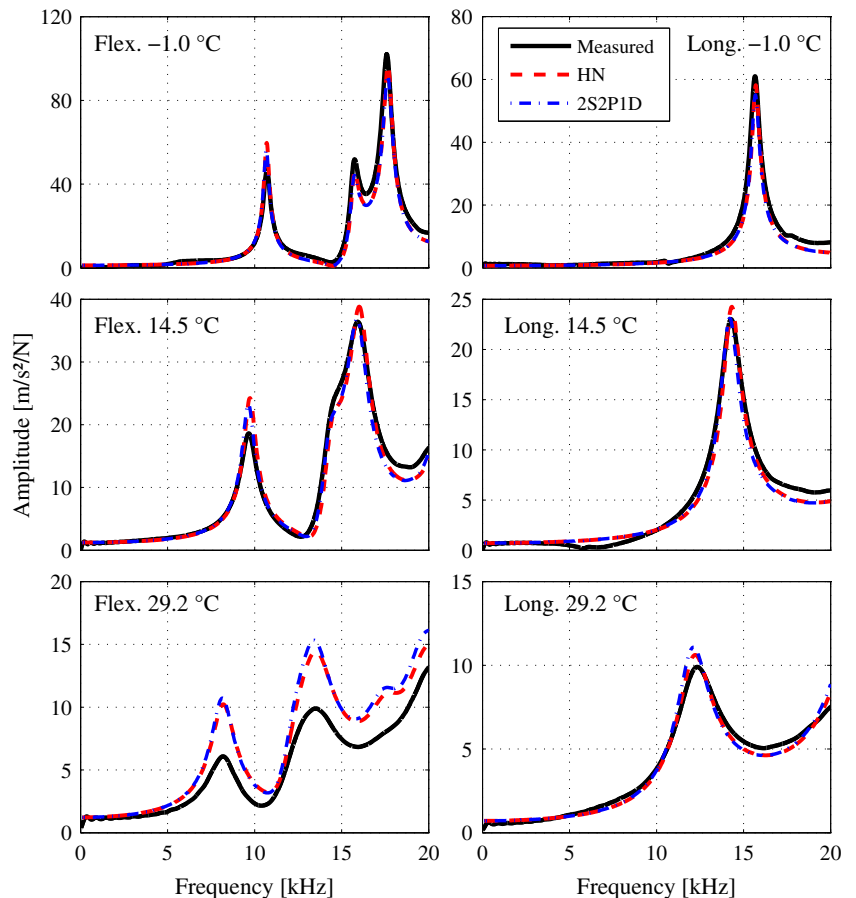


Table 4 Optimized parameter values of the HN master curve model to match the seismic measurements

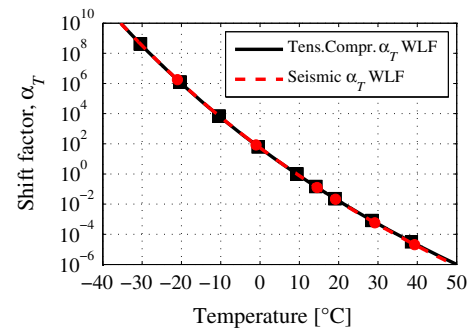
Model	E_0 (MPa)	E_∞ (MPa)	ν_0	ν_∞	α	β	τ (s)	c_1	c_2
HN	11.31	47058	0.5	0.239	0.492	0.205	20.26	36.6	207.4

Table 5 Optimized parameter values of the 2S2P1D master curve model to match the seismic measurements

Model	E_0 (MPa)	E_∞ (MPa)	ν_0	ν_∞	δ	k	h	β_η	τ (s)	c_1	c_2
2S2P1D	17.56	46148	0.5	0.239	1.516	0.142	0.545	554.8	1.158	36.6	207.4

each model (HN and 2S2P1D). The presented calculated FRFs are the results of the master curve optimization. One set of parameters for the HN and 2S2P1D models have been estimated together with the shift factors. The values of the estimated parameters are presented in Tables 4 and 5 for the HN and 2S2P1D model, respectively. In total seven parameters of the HN model were needed to be evaluated to obtain a good fit of the calculated FRFs to the measured FRFs. The seven parameters optimized for this purpose were: the high frequency modulus (E_∞), the high frequency Poisson's ratio (ν_∞), α , β , τ and the shift factors c_1 and c_2 . In contrast to the tension–compression test, the same values of the parameters α , β and τ were used in both the complex modulus relationship (Eq. 6) and Poisson's ratio relationship (Eq. 7). This simplification saved calculation time and still provided a good match of the FRFs for each temperature. Furthermore, the low frequency asymptotic parameters E_0 and ν_0 have a very small influence on the FRFs for reasonable values of asphalt concrete. Therefore, the low frequency parameters can be assumed to common values of asphalt concrete [15]. In this case, the parameter E_0 was assumed to same value as determined by the tension–compression test and ν_0 was assumed to 0.5. Both of these assumptions were able to provide a good match of HN calculated and measured FRFs. There are nine parameters to estimate for the 2S2P1D model (E_∞ , ν_∞ , δ , k , h , τ , β_η , c_1 and c_2) when applying the same approach as the HN model. However, by using the shift factors determined from the HN model the number of parameters needed to provide a good match of the FRFs can be reduced to seven for the 2S2P1D model. Figure 7 presents the shift factors determined through the master curve estimation of the tension–compression test and through the seismic master curves optimization of FRFs.

The measured FRFs of both the flexural and longitudinal modes of vibration have been used as input in the optimization of the calculated theoretical FRFs at four of the six temperatures (−21.0 to 19.2 °C). At the two highest temperatures (29.2 and 39.3 °C) only the longitudinal modes of vibration have been used as input to the optimization. This is due to the mismatch in amplitude between the calculated and measured flexural FRF that can be seen in Fig. 6 at 29.2 °C. A good fit of the resonance frequencies as well as the amplitude was obtained for the longitudinal mode of vibration at these two

**Fig. 7** Shift factors determined from the tension–compression test and from the seismic test method

higher temperatures, while only the resonances matched for the flexural mode of vibration for the same parameter estimation. An attempt to adapt the calculated FRFs to the amplitude of the measured flexural mode of vibration resulted in too low amplitude of the longitudinal mode and in an unrealistic high loss modulus compared to both the previous analyzed temperatures and the tension–compression test results. However, this lower amplitude did not have a significant effect on the resulting dynamic modulus.

The current seismic results of this specimen show a higher damping ratio of the flexural mode of vibration compared to the longitudinal mode at the two highest temperatures. This may, for asphalt concrete, indicate that there are differences in the damping ratio/phase angle due to different mode types. Previous seismic measurements investigating possible anisotropy of a beam shaped asphalt concrete specimen gave close results of the flexural modes of vibration in two different directions [11]. However, the longitudinal mode of vibration gave a larger difference than the shown anisotropy of the different directions. Clec'h et al. [32] reported results of anisotropy that showed differences of the moduli at higher frequencies but similar moduli at lower frequencies. Furthermore, a similar phase angle was measured of the different directions [32]. Therefore, it is possible that different mode types may have a higher influence to the complex behavior than the anisotropy in different directions. However, at this stage further seismic measurements of different modes of vibration are needed to clarify the different response of asphalt concrete to compression, bending and shear loading.

3.3 Comparing Seismic and Tension–Compression Test Results

Figure 8 presents the absolute value of the complex modulus for the tension–compression and the seismic test. The figure shows the clear difference of the applicable frequency ranges of the seismic and tension–compression tests, where the seismic moduli have been characterized in the range of 500–17,000 Hz for each measurement temperature. Although, the moduli are presented at two different frequency ranges, it is noticeable that the seismic method seems to give little higher moduli at some temperatures that can not only

be explained by the higher frequencies. This indicates that the lower applied strain level in the seismic test results in a higher absolute value of the complex moduli compared to the tension–compression test. Note also in Fig. 8 that the two models (HN and 2S2P1D) applied to determine the seismic moduli give very similar results.

The higher seismic moduli are shown more clearly in Fig. 9, where the master curves of the tension–compression and seismic test are compared. This figure shows that the seismic test method results in a higher absolute value of the complex modulus (Fig. 9a) and in a lower phase angle (Fig. 9b) compared to the tension–compression test. At the

Fig. 8 Seismic modulus compared to the tension–compression modulus at the measurement temperatures and frequencies

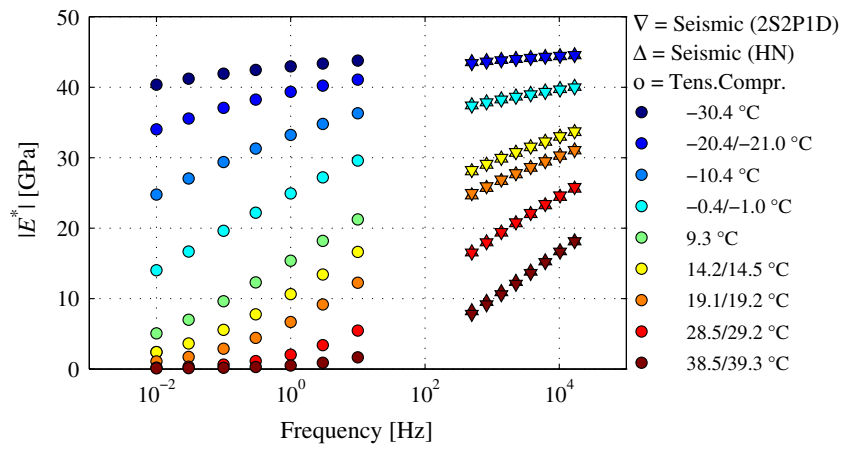


Fig. 9 Comparison of the complex modulus determined by the seismic and tension–compression test, including the absolute value (a), the phase angle (b), and loss and storage modulus (c)

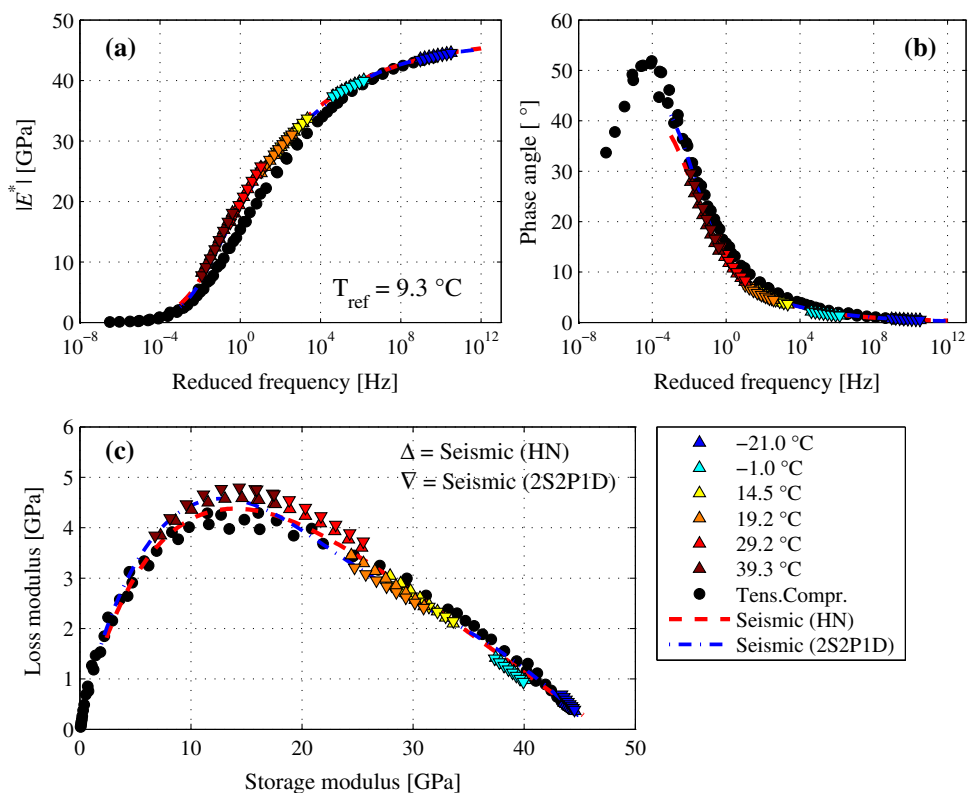
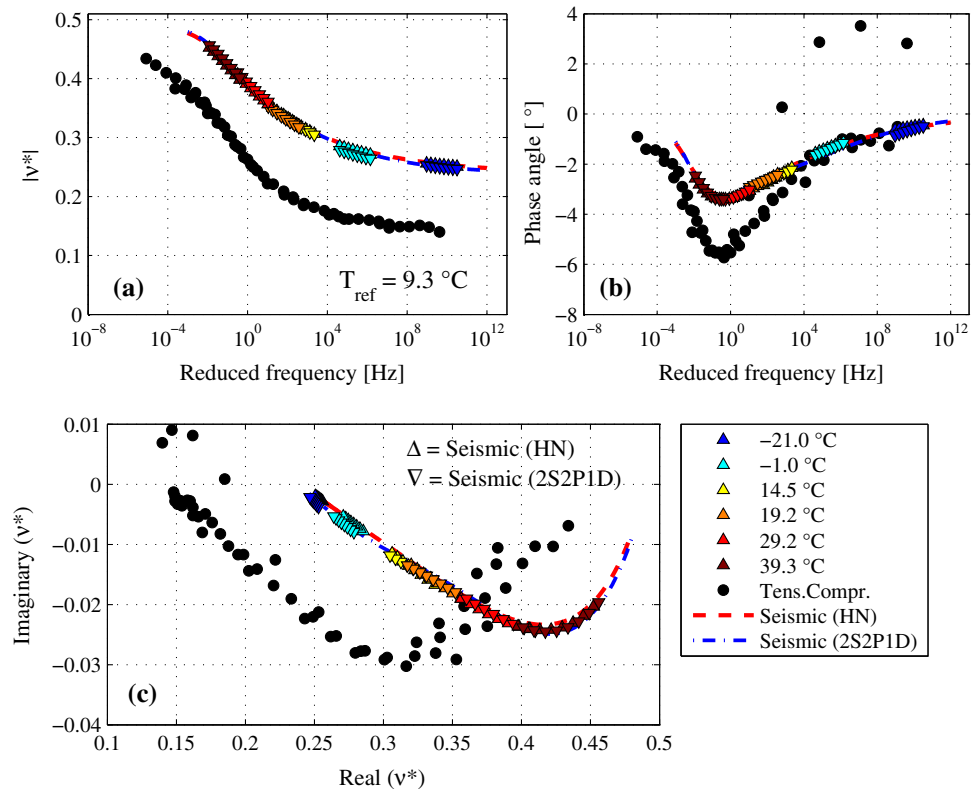


Table 6 Comparison of the absolute values of the complex modulus master curve at $T_{ref}=9.3\text{ }^{\circ}\text{C}$ determined through seismic (HN model) and tension–compression testing

f (Hz)	0.1	1	10	100	1000	10000	100000	1000000
$ E^* _{seismic}$ (MPa)	13133	19342	24802	29311	32947	35852	38165	40003
$ E^* _{TC}$ (MPa)	9199.7	15212	21085	26171	30369	33768	36500	38689
$ E^* _{seismic}/ E^* _{TC}$ (%)	42.8	27.2	17.6	12	8.5	6.2	4.6	3.4

Fig. 10 Comparison of complex Poisson's ratio determined by the seismic and tension–compression test, including the absolute value (a), the phase angle (b), and the imaginary and real part of complex Poisson's ratio (c)



same time, the complex moduli expressed in the Cole–Cole space (Fig. 9c) show a good agreement between the seismic and the tension–compression master curves, even if the loss moduli at 29.2 and 39.3 °C are slightly higher for the seismic determined complex moduli. Table 6 presents the seismic (HN model) and the tension–compression absolute values of the complex modulus. Note that the difference between the seismic and the tension–compression $|E^*|$ master curves corresponds approximately to a temperature change of 3.1 °C. For example, expressing the seismic master curve at a reference temperature of 12.4 °C gives a better agreement to the tension–compression master curve.

Results presented by Rollins et al. [33] gives that a unique curve independent of the strain level is obtained in the Cole–Cole diagram for non-viscous materials as gravels. For viscous materials as asphalt concrete, a unique curve is obtained independently of loading frequency and temperature if the material is thermo-rheological simple. However, for asphalt concrete it is not clarified if different strain levels affects the loss factor (=loss modulus/storage modulus) in the same

direction for different frequencies and temperatures in the Cole–Cole space. Due to the viscoelasticity of asphalt concrete the direction of the loss factor change due to different strain levels may depend on the temperature and loading frequency. Since a lower strain level results in a higher absolute value of the modulus and in a lower phase angle, the loss factor should be lower for the seismic modulus compared to a modulus at the same frequency and temperature determined from the tension–compression test. When comparing Figs. 4c and 9c it can be seen that the seismic test gives a lower loss factor compared to the tension–compression results measured at the same temperature. The seismic results are therefore located to the right of the tension–compression results measured at the same temperature, closely along a unique curve in the Cole–Cole space. However, this shift to the right along the curve is mainly due to the higher loading frequencies applied in the seismic tests compared to the tension–compression test, and a much smaller part is due to the lower applied strain levels.

The results presented in Fig. 10 show that complex Poisson's ratio differs between the two methods. The values

of complex Poisson's ratio determined by the tension–compression test could not contribute to an optimum fit of the calculated FRFs to the measured FRFs. Complex Poisson's ratio measured by the tension–compression test led to a mismatch of the distance between the first and second resonance frequency for the calculated resonance frequencies compared to the measured resonances. The match of the FRFs shown in Fig. 6 was only possible with the seismic Poisson's ratio presented in Fig. 10. The biggest difference of the absolute value of Poisson's ratio between the two methods is approximately 0.1, which corresponds to a change in the specimen diameter of $\sim 0.4 \mu\text{m}$ when measuring Poisson's ratio through the tension–compression test.

4 Conclusions

The comparison of the two test methods show that the seismic test gives a higher absolute value of the complex modulus and a lower phase angle than the tension–compression test. Since the seismic test is performed at a lower strain level than the tension–compression test, these are expected results and agree with previous research of the strain level dependency of asphalt concrete as well as for other materials. The study shows that seismic measurements in combination with conventional tests are useful to increase the knowledge of the nonlinear behavior of asphalt concrete.

The seismic measurements show that the HN and the 2S2PID model give very similar results of the complex modulus and complex Poisson's ratio when they are applied to calculate frequency response functions through the finite element method. The fit of the models to the tension–compression test resulted in almost the same master curve of the absolute value of the complex modulus. Looking more closely at the damping properties there are some differences between the models which is most likely due to the extra number of parameters in the 2S2PID model.

The seismic test indicates that there are differences in the damping properties of the asphalt concrete specimen at higher temperatures that may depend on different modes of vibration. However, these results need further investigation.

The results of complex Poisson's ratio differ between the seismic and tension–compression test method, since an optimum fit of the FRFs could not be obtained with the tension–compression measured Poisson's ratio.

Acknowledgments The Swedish transport administration (Trafikverket) and the Swedish construction industry's organization (SBUF) are acknowledged for their financial support. A great appreciation is also given to the research group at Departement Génie Civil et Bâtiment in ENTPE at the University of Lyon for all their help and hospitality.

References

- Migliori, A., Sarrao, J.L.: Resonant Ultrasound Spectroscopy: Applications to Physics, Materials Measurements and Nondestructive Evaluation. Wiley, New York (1997). ISBN 0-471-12360-9
- Ryden, N., Park, C.H.: Fast simulated annealing inversion of surface waves on pavement using phase–velocity spectra. *Geophysics* **71**(4), R49–58 (2006)
- Di Benedetto, H., Sauzéat, C., Sohm, J.: Stiffness of bituminous mixtures using ultrasonic wave propagation. *RMPD* **10**(4), 789–814 (2009)
- Norambuena-Contreras, J., Castro-Fresno, D., Vega-Zamanillo, A., Celaya, M., Lombillo-Vozmediano, I.: Dynamic modulus of asphalt mixture by ultrasonic direct test. *NDT & E Int.* **43**, 629–634 (2010)
- Mounier, D., Di Benedetto, H., Sauzéat, C.: Determination of bituminous mixtures linear properties using ultrasonic wave propagation. *Constr. Build. Mater.* **36**, 638–647 (2012)
- Whitmoyer, S.L., Kim, Y.R.: Determining asphalt concrete properties via the impact resonant method. *J. Test. Eval.* **22**(2), 139–148 (1994)
- Kweon, G., Kim, Y.R.: Determination of the complex modulus of asphalt concrete using the impact resonance test. *J. Transp. Res. Board* **1970**, 151–160 (2006)
- Lacroix, A., Kim, Y.R., Far, M.S.S.: Constructing the dynamic modulus mastercurve using impact resonance testing. *Assoc. Asph. Paving Technol.* **78**, 67–102 (2009)
- ASTM: C215–08, Standard Test Method for Fundamental Transverse, Longitudinal, and Torsional Frequencies of Concrete Specimens. American Society for Testing and Materials, West Conshohocken (2008)
- Ryden, N.: Resonant frequency testing of cylindrical asphalt samples. *Eur. J. Environ. Civ. Eng.* **15**, 587–600 (2011)
- Gudmarsson, A., Ryden, N., Birgisson, B.: Application of resonant acoustic spectroscopy to asphalt concrete beams for determination of the dynamic modulus. *Mater. Struct.* **45**, 1903–1913 (2012)
- Ren, Z., Atalla, N., Ghinet, S.: Optimization based identification of the dynamic properties of linearly viscoelastic materials using vibrating beam technique. *ASME J. Vib. Acoust.* **133**(4), 1–12 (2011)
- Rupitsch, S.J., Ilg, J., Sutor, A., Lerch, R., Döllinger, M.: Simulation based estimation of dynamic mechanical properties for viscoelastic materials used for vocal fold models. *J. Sound Vib.* **330**, 4447–4459 (2011)
- Renault, A., Jaouen, L., Sgard, F.: Characterization of elastic parameters of acoustical porous materials from beam bending vibrations. *J. Sound Vib.* **330**, 1950–1963 (2011)
- Gudmarsson, A., Ryden, N., Birgisson, B.: Characterizing the low strain complex modulus of asphalt concrete specimens through optimization of frequency response functions. *J. Acoust. Soc. Am.* **132**(4), 2304–2312 (2012)
- Doubbaneh, E.: Comportement mécanique des enrobés bitumineux des petits aux grandes déformations. Ph.D. dissertation, Institut National des Sciences Appliquées, ENTPE, Lyon (1995)
- Duttine, A., Di Benedetto, H., Ezaoui, A.: Anisotropic small strain elastic properties of sands and mixture of sand–clay measured by dynamic and static methods. *Soils Found.* **47**(3), 457–472 (2007). doi:10.3208/sandf.47.457
- Ezaoui, A., Di Benedetto, H.: Experimental measurements of the global anisotropic elastic behaviour of dry Hostun sand during triaxial tests, and effect of sample preparation. *Géotechnique* **59**(7), 621–635 (2009). doi:10.1680/geot.7.00042
- Nguyen, Q.T., Di Benedetto, H., Sauzéat, C.: Prediction of linear viscoelastic behaviour of asphalt mixes from binder properties and reversal. In: Kringos, N., Birgisson, B., Frost, D., Wang, L. (eds.)

- Multi-Scale Modeling and Characterization of Infrastructure Materials, vol. 8, pp. 237–248. Springer, Netherlands (2013)
20. COMSOL Multiphysics: Version 4.3b. Structural Mechanics Module User's Guide (2013)
 21. Neeman, A.G., Brannon, R., Jeremić, B., Van Gelder, A., Pang, A.: Decomposition and visualization of fourth-order elastic-plastic tensors. In: Hege, H.-C., Laidlaw, D., Pajarola, R., Stadt, O. (eds.) IEEE/EG Symposium on Volume and Point-Based Graphics, pp. 121–128 (2008)
 22. Yusoff, N.I.M., Shaw, M.T., Airey, G.D.: Modelling the linear viscoelastic rheological properties of bituminous binders. *J. Constr. Build. Mater.* **25**(5), 2171–2189 (2011)
 23. Olard, F., Di Benedetto, H.: General “2S2P1D” model and relation between the linear viscoelastic behaviours of bituminous binders and mixes. *RMPD* **4**(2), 185–224 (2003)
 24. Havriliak, S., Negami, S.: A complex plane analysis of α -dispersions in some polymer systems. *J. Polym. Sci. C* **14**, 99–117 (1996)
 25. Di Benedetto, H., Olard, F., Sauzéat, C., Delaporte, B.: Linear viscoelastic behaviour of bituminous materials: from binders to mixes. *Road Mater. Pavement Des.* **5**(sup1), 163–202 (2004)
 26. Di Benedetto, H., Delaporte, B., Sauzéat, C.: Three-dimensional linear behavior of bituminous materials: experiments and modeling. *Int. J. Geomech.* **7**(2), 149–157 (2007)
 27. Hartmann, B., Lee, G.F., Lee, J.D.: Loss factor height and width limits for polymer relaxations. *J. Acoust. Soc. Am.* **95**, 226–233 (1994)
 28. Madigosky, W.M., Lee, G.F., Niemiec, J.M.: A method for modeling polymer viscoelastic data and the temperature shift function. *J. Acoust. Soc. Am.* **119**, 3760–3765 (2006)
 29. Zhao, Y., Liu, H., Bai, L., Tan, Y.: Characterization of linear viscoelastic behavior of asphalt concrete using complex modulus model. *J. Mater. Civ. Eng.* **25**(10), 1543–1548 (2013)
 30. Nguyen, H.M., Pouget, S., Di Benedetto, H., Sauzéat, C.: Time-temperature superposition principle for bituminous mixtures. *Eur. J. Environ. Civ. Eng.* **13**(9), 1095–1107 (2009)
 31. Williams, M.L., Landel, R.F., Ferry, J.D.: The temperature dependence of relaxation mechanisms in amorphous polymers and other glass-forming liquids. *J. Am. Chem. Soc.* **77**, 3701 (1955)
 32. Clec'h, P., Sauzéat, C., Di Benedetto, H.: Linear viscoelastic behaviour and anisotropy of bituminous mixture compacted with a French wheel compactor. *Paving Mater. Pavement Anal.*, 103–115 (2010). doi:10.1061/41104(377)14
 33. Rollins, K.M., Evans, M.D., Diehl, N.B., Daily III, W.D.: Shear modulus and damping relationships for gravels. *J. Geotech. Geoenviron. Eng.* **124**(5), 396–405 (1998)

Paper IV

Complex modulus and complex Poisson's ratio from cyclic and dynamic modal testing of asphalt concrete

ANDERS GUDMARSSON
NILS RYDEN
HERVÉ DI BENEDETTO
CÉDRIC SAUZÉAT

Submitted to
Construction and Building Materials

Complex modulus and complex Poisson's ratio from cyclic and dynamic modal testing of asphalt concrete

Anders Gudmarsson¹, Nils Ryden¹, Hervé Di Benedetto², Cédric Sauzéat²

¹ KTH Royal Institute of Technology, Highway and Railway Engineering, Brinellvägen 23, 100 44 Stockholm, Sweden

² University of Lyon/Ecole Nationale des Travaux Publics de l'Etat (ENTPE), Laboratoire Génie Civil et Bâtiment & Tribologie et Dynamiques des Systèmes (UMR CNRS), Rue Maurice Audin, 69518 Vaulx-en-Velin, France

Abstract. The complex moduli and complex Poisson's ratio of two cylindrical asphalt concrete specimens have been determined through modal testing in this paper. These results have been compared to cyclic tension-compression measured complex moduli and complex Poisson's ratio of asphalt concrete specimens with different dimensions. The modal testing has been performed by measuring frequency response functions of the specimens using an impact hammer and an accelerometer. The material properties have been characterized by matching finite element computed frequency response functions to the measurements. The results of the different specimens show that the modal test systematically give a slightly higher absolute value of the complex moduli compared to the cyclic testing. The differences are most likely a result of the different strain levels applied in the two test methods. However, the modal and cyclic tension-compression testing resulted in similar values of the complex Poisson's ratio for the two different asphalt concrete mixtures despite the different applied strain levels.

Keywords: Asphalt concrete; complex modulus; complex Poisson's ratio; modal testing; cyclic testing; frequency response functions

E-mail: andgud@kth.se

1 Introduction

There is a need for simple and economic test methods to measure the linear viscoelastic material properties of asphalt concrete. Modal testing is widely known to be economic, accurate and simple to perform which makes it advantageous compared to costly conventional cyclic loading test methods to measure the complex moduli (Di Benedetto et al. 2001). Nondestructive test methods based on impact modal testing have shown great potential in characterizing the temperature and frequency dependent complex moduli of asphalt concrete (Ryden 2011; Gudmarsson et al. 2012a; Gudmarsson et al. 2012b; Gudmarsson et al. 2014a; Gudmarsson et al. 2014b). In addition, wave-based measurements can be used for nondestructive quality control and quality assurance of pavement materials by e.g. comparing laboratory and field measured complex moduli (Whitmoyer and Kim 1994; Ryden and Park 2006).

Alternative test methods to conventional testing have measured fundamental resonance frequencies of asphalt concrete specimens and applied simplified analytical formulations to derive a complex modulus at different temperatures (Whitmoyer and Kim 1994; Kweon and Kim 2006; Lacroix et al. 2009). Limitations of this approach are that the analytical approximate formulations are valid only for certain specimen geometries and that the complex modulus can be determined for only one frequency per temperature. Ultrasonic test methods applied to asphalt concrete has also been based on simplified analytical formulations and suffers therefore from the same limitations (Nazarian et al. 2005; Di Benedetto et al. 2009; Norambuena-Contreras et al. 2010; Mounier et al. 2012; Larcher et al. 2014). These alternative test methods to conventional testing have not been able to characterize the frequency dependency of asphalt concrete. However, through measurements of frequency response functions (FRFs) it has been possible to determine master curves of asphalt concrete that describe the viscoelastic material properties as a function of frequency and temperature (Gudmarsson et al. 2012b; Gudmarsson et al. 2014a; Gudmarsson et al. 2014b). FRFs are determined by dividing the measured response with the measured applied force in frequency domain. The characterization of the frequency dependency of the asphalt concrete through modal testing has been enabled by combining numerical computations with measured FRFs (Gudmarsson et al. 2012b). This approach was developed for a beam shaped asphalt concrete specimen in Gudmarsson et al. (2012b) and further applied to a cylindrical specimen to compare the method to conventional cyclic tension-compression tests in Gudmarsson et al. (2014a). As expected, the comparison between the two test methods showed small differences of the complex moduli due to the known nonlinearity of asphalt concrete and because different strain levels are applied in the two test methods (cf. e.g. Airey and Rahimzadeh 2004; Nguyen et al. 2014; Doubbaneh 1995). However, the results showed large differences between the two methods regarding the complex Poisson's ratio. Although, the reasons for the different results of complex Poisson's ratio could not be fully determined, it was seen that the tension-compression measured complex Poisson's ratio did not agree with the measured FRFs. Therefore, further comparisons of complex Poisson's ratio of

asphalt concrete determined through modal and tension-compression measurements are needed. It is also of interest to further apply the modal test to specimens with different dimensions and to quantify the applied strain levels at different temperatures.

In this paper, modal testing of two asphalt concrete specimens have been performed to enable further comparisons of the complex moduli and complex Poisson's ratio to cyclic tension-compression test results. The linear viscoelastic properties of specimens with different dimensions are compared. The results presented show that the modal and tension-compression test methods are able to give similar complex Poisson's ratio.

2 Methodology

The applied methodology to determine the material properties of the asphalt concrete specimens includes modal testing to measure FRFs and numerical computations of FRFs that are optimized to match the measurements. The modal testing has been performed to two cylindrical specimens from two different asphalt mixes called GB3 and GB5[®] (Olard 2012). These measurements have been compared to results of conventional cyclic tension-compression testing performed to cylindrical specimens of the same mixes but with different dimensions. The modal and tension-compression measurements have been performed at the *University of Lyon, Ecole Nationale des Travaux Publics de l'Etat (ENTPE), Laboratoire Génie Civil et Bâtiment*. Results from a total of eight different specimens are presented here, where two specimens have been tested through modal testing, five specimens through tension-compression measurements and one specimen have been tested by both modal and cyclic tension-compression measurements (Gudmarsson et al. 2014a). The specimens have been produced at the same time at *Eiffage Travaux Publics* in France but tested at different times. Therefore, there may be small differences in the material properties of the specimens due to aging of the binder. However, research has shown that even if aged binders show significant physical hardening effects, the asphalt mixtures are less affected by the aged binder (Falchetto and Marasteanu 2011). The mixes have been part of a round robin test (RILEM technical committee 237-SIB: *Testing and characterization of sustainable innovative bituminous materials and systems*), where the three-dimensional linear viscoelastic behavior of the specimens have been characterized. The tension-compression test method is thoroughly described in work by e.g. Di Benedetto et al. (2007), Nguyen et al. (2013a) and Nguyen et al. (2013c).

2.1 Materials

Table 1 presents details of the eight different specimens from which results are reported. Note that the modal and tension-compression measurements have been performed to different specimens except for the specimen GB3 (s.3). To this specimen both modal and tension-compression testing have been performed and reported by Gudmarsson et al. (2014a). Results of the tension-compression tested specimens have previously been presented by e.g. Nguyen et al. (2013b). The GB5[®]

mix has a higher content of large aggregates than the GB3 mix as shown by the gradation curves in Fig. 1 and presented by Table 2 and 3. Otherwise, the two mixes contain the same binder with the penetration grade of 35/50 and a binder content of 4.5 percent by weight.

TABLE 1. Details of the specimens from which results are reported.

Specimen	Test date	Test method	Test ID	Mass (g)	Height (mm)	Diameter (mm)	Density (kg/m³)
GB3 (s.1)	Aug. 2012	Tension-compression	TC – GB3 (s.1)	1572	140.9	73.8	2609.7
GB3 (s.2)	Aug. 2012	Tension-compression	TC – GB3 (s.2)	1564	140.1	73.7	2613.6
GB3 (s.3)	May 2013	Tension-compression and FRFs	TC – GB3 (s.3)	1378	122.6	74.1	2606.8
			FRF flex.-GB3 (s.3)				
			FRF long.-GB3 (s.3)				
GB3 (s.4)	Feb. 2014	FRFs	FRF flex.-GB3 (s.4)	1198	140.7	64.6	2586.0
			FRF long.-GB3 (s.4)				
GB5 (s.1)	Sep. 2012	Tension-compression	TC – GB5 (s.1)	1616	142.3	74.1	2635.9
GB5 (s.2)	Aug. 2012	Tension-compression	TC – GB5 (s.2)	1595	140.4	73.9	2647.7
GB5 (s.3)	Aug. 2012	Tension-compression	TC – GB5 (s.3)	1596	140.7	73.9	2641.3
GB5 (s.4)	Feb. 2014	FRFs	FRF flex.-GB5 (s.4)	1209	140.2	64.6	2630.9
			FRF long.-GB5 (s.4)				

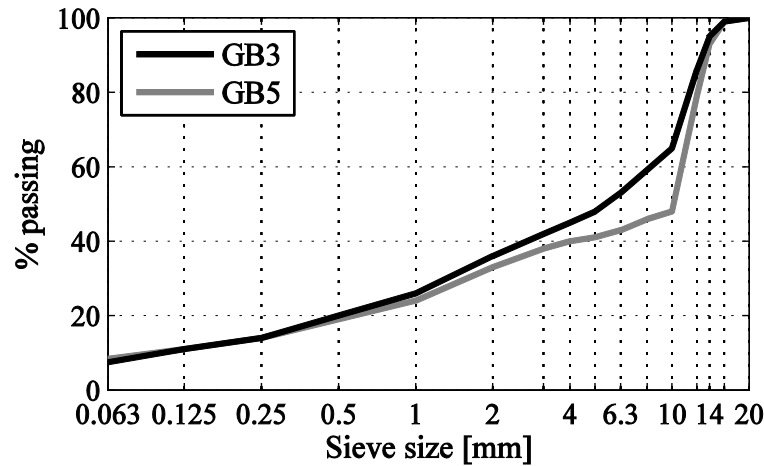


Figure. 1 Gradation curves of GB3 and GB5®.

TABLE 2. Gradation of GB3.

Sieve size [mm]	0.063	0.125	0.25	0.5	1	2	3.15	4	5	6.3	10	12.5	14	16	20
% passing	7.5	11	14	20	26	36	42	45	48	53	65	86	95	99	100

TABLE 3. Gradation of GB5®.

Sieve size [mm]	0.063	0.125	0.25	0.5	1	2	3.15	4	5	6.3	8	10	12.5	14	16	20
% passing	8.4	11	14	19	24	33	38	40	41	43	46	48	79	93	99	100

2.2 Impact hammer modal testing

Waves in a solid generated from an external input can interfere and create standing waves if the input provides energy to the frequencies that corresponds to the solids natural frequencies. The condition of when the input frequencies equal the natural frequencies of a solid is known as resonance. Any system or solid in which standing waves can form have a large number of natural frequencies which depend on the elastic constants, the geometry, the boundary conditions and the density. The elastic constants can therefore be determined with great accuracy by measuring a complete set of resonance frequencies below some upper limit (Migliori and Sarrao 1997). Since a large number of resonance frequencies of different mode types can be measured by one single excitation, all elastic constants of a solid with free boundary conditions can be determined by one single measurement of an isotropic or anisotropic elastic material if the solids dimensions and density are known (Leisure and Willis 1997). This is a great advantage compared to methods measuring the velocity of propagating waves, where measurements needs to be performed in several directions to obtain the same information. Furthermore, no assumptions of idealized states of stress and strain are needed since the numerical methods to derive elastic constants from resonance frequency measurements account for the complex vibrations of a solid (Bernard et al. 2014). In the case of viscoelastic materials as asphalt concrete, each frequency are related to a unique material property which means that several resonance frequencies cannot be used to increase the accuracy of

a specific material property. However, several resonance frequencies can enable the characterization of the frequency dependency of the material properties (Gudmarsson et al. 2012a), and by using FRFs the amplitudes over the entire studied frequency range provides additional input to the resonances to accurately characterize the viscoelastic material properties (Gudmarsson et al. 2012b).

2.2.1 Measuring FRFs

To measure the FRFs at different temperatures an instrumented impact hammer (PCB model 086E80) was used to excite the specimen, which was placed on soft foam for free boundary conditions, and an accelerometer (PCB model 352B10) attached by wax was used to measure the response. The accelerometer has a weight of 0.7 g and is assumed to not affect the response of the specimen. The hammer and the accelerometer were connected to a signal conditioner (PCB model 480B21), which was connected to a data acquisition device (NI USB-6251 M Series), which in turn was connected to a computer. The measurements were recorded with a sampling frequency of 500 kHz and performed by using the data acquisition toolbox in MATLAB. The FRFs at different temperatures were determined from the measured input and output based on averaging five measurements ($n = 5$) in the complex domain at each frequency according to Eqn. 1,

$$H(f) = \left(\frac{1}{n} \sum_{k=1}^n Y_k(f) \cdot X_k^*(f) \right) / \left(\frac{1}{n} \sum_{k=1}^n X_k(f) \cdot X_k^*(f) \right), \quad (1)$$

where $H(f)$ is the frequency response function, $Y(f)$ is the measured acceleration, $X(f)$ is the measured applied force and $X^*(f)$ is the complex conjugate of the applied force. FRFs of the longitudinal and flexural modes of vibrations have been measured for both mixes. The positions of the impact excitation for the flexural and longitudinal modes of vibration are illustrated in Fig. 2.

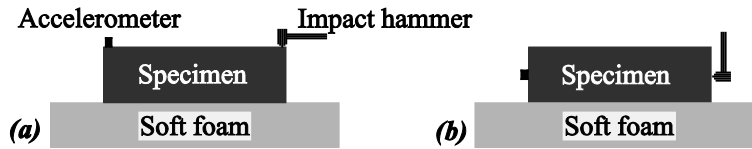


Fig. 2 Positions of the accelerometer and the impact excitation for the flexural (a) and longitudinal (b) modes of vibration

Figure 3 present the measured response of the specimens over time (Fig. 3a), the measured FRFs (Fig. 3b) and the measured coherence functions (Fig. 3c) at 14.2 °C. The coherence function is a measure of the phase difference between the input and output where a value of one means that this difference is constant for the five different impacts. The coherence function is calculated accordingly,

$$CF(f) = \left(\left| \frac{1}{n} \sum_{k=1}^n X_k^*(f) \cdot Y_k(f) \right| \right)^2 / \left[\left(\frac{1}{n} \sum_{k=1}^n X_k(f) \cdot X_k^*(f) \right) \cdot \left(\frac{1}{n} \sum_{k=1}^n Y_k(f) \cdot Y_k^*(f) \right) \right], \quad (2)$$

where $CF(f)$ is the coherence function, $X^*(f) \cdot Y(f)$ is the cross power spectrum, $X(f) \cdot X^*(f)$ is the auto power spectrum of the impulse and $Y(f) \cdot Y^*(f)$ is the auto power spectrum of the response.

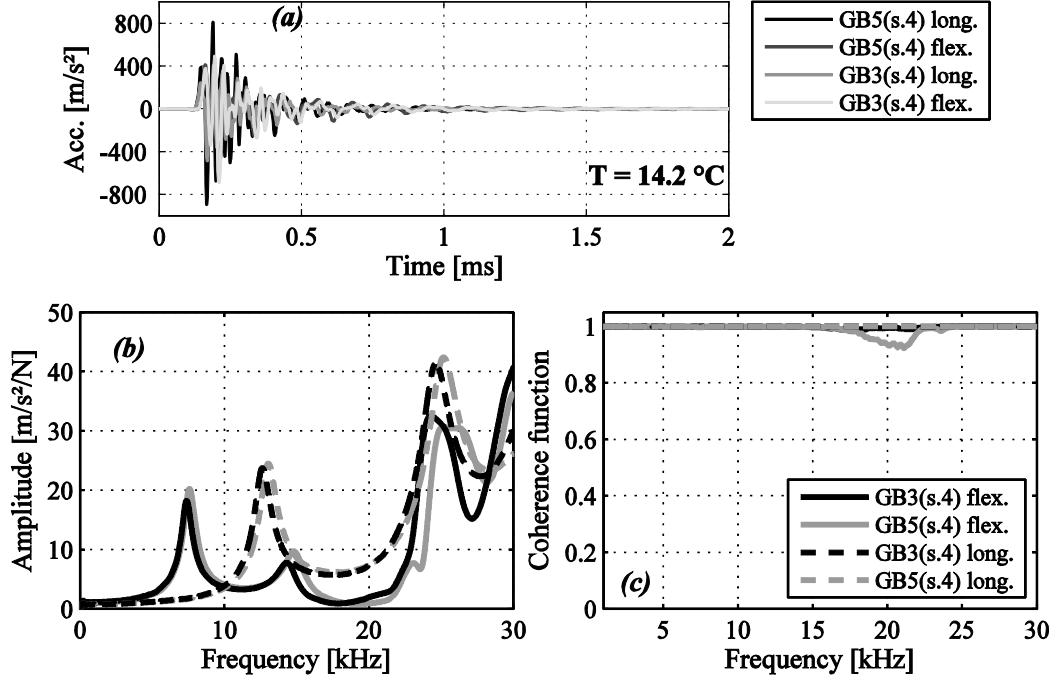


Fig. 3 The measured dynamic response of the asphalt concrete specimen in time domain (a), the frequency response function (b) and the coherence function (c) at $14.2 \text{ }^\circ\text{C}$

2.2.2 Calculating and optimizing theoretical FRFs

The numerical computations were performed through the finite element method (FEM) in a three-dimensional space using the following equation of motion,

$$-\rho\omega^2\mathbf{u} - \nabla \cdot \boldsymbol{\sigma} = F_p e^{i\phi}, \quad (3)$$

where ρ is the density, ω is the angular frequency ($\omega = 2\pi f$), \mathbf{u} is the displacement vector, ∇ is the vector operator ($\nabla = [\partial/\partial X, \partial/\partial Y, \partial/\partial Z]$), $\boldsymbol{\sigma}$ is the Cauchy stress tensor ($\boldsymbol{\sigma} = \mathbf{C} : \boldsymbol{\varepsilon}$), F_p is a point load, ϕ is the phase of the cyclic load, $\boldsymbol{\varepsilon}$ is the strain tensor ($\boldsymbol{\varepsilon} = \frac{1}{2}[(\nabla\mathbf{u})^T + \nabla\mathbf{u}]$), \mathbf{C} is the fourth-order stiffness tensor (including E^* and ν^*) and $\nabla\mathbf{u}$ is expressed accordingly

$$\nabla\mathbf{u} = \begin{bmatrix} \frac{\partial u}{\partial X} & \frac{\partial u}{\partial Y} & \frac{\partial u}{\partial Z} \\ \frac{\partial v}{\partial X} & \frac{\partial v}{\partial Y} & \frac{\partial v}{\partial Z} \\ \frac{\partial w}{\partial X} & \frac{\partial w}{\partial Y} & \frac{\partial w}{\partial Z} \end{bmatrix}, \quad (4)$$

where (X, Y, Z) are the constant material (reference) coordinates and (u, v, w) are the global Cartesian components of the displacement vector. The computations were performed over a frequency range of 100 to 30 000 Hz with the increment of 20 Hz. The point load in the model of 1 N was applied to points corresponding to the points of the actual hammer impacts during the measurements of the longitudinal and flexural modes of vibration (see Fig. 2). The response in the model was also determined in the points corresponding to the accelerometer placements during the measurements. The mesh of the model consists of tetrahedral elements with quadratic shape functions. A suitable mesh size for good accuracy and to limit the computational time was determined through a convergence study to a maximum element size of 2 cm.

Initial values of the complex moduli (E^*) and complex Poisson's ratio (ν^*) are assumed to be able to compute FRFs that can be compared to the measured FRFs. Thereafter, E^* and ν^* are adjusted iteratively until the computed FRFs match the measured FRFs. The viscoelasticity of the asphalt concrete are accounted for by the use of a suitable model that can express E^* and ν^* as a function of frequency. There are different models that are capable of expressing $E^*(\omega)$ and $\nu^*(\omega)$ of asphalt concrete accurately (Olard and Di Benedetto 2003; Yusoff et al. 2011; Gudmarsson et al. 2014a). For example, the 2S2P1D model has been commonly applied to bituminous materials and can accurately characterize the complex behavior of both asphalt binders and mixtures (Olard and Di Benedetto 2004; Di Benedetto et al. 2007; Tiouajni et al. 2011). The Havriliak-Negami (HN) model has been widely used to characterize viscoelastic materials and has also been successfully applied to asphalt concrete (Havriliak and Negami 1966; Hartmann et al. 1994; Madigosky et al. 2006; Gudmarsson et al. 2012b; Gudmarsson et al. 2014a, Zhao et al. 2013). A comparison of the HN and the 2S2P1D models performed by Gudmarsson et al. (2014a) showed that these two models provide similar results of $E^*(\omega)$ and $\nu^*(\omega)$ when applied to the optimization of FRFs of asphalt concrete specimens. The comparison also showed that the 2S2P1D model may be advantageous for the approximation of the phase angle at low frequencies and/or high temperatures when applied to cyclic tension-compression testing. However, this advantage of the 2S2P1D model that comes from the extra number of model parameters is difficult to utilize for the modal testing, since this test is performed at higher frequencies compared to the cyclic testing. Instead, it is of great practical advantage to limit the number of parameters that needs to be estimated in the optimization process of FRFs, since this reduces the computational time and facilitates the process of finding the global minimum. Therefore, $E^*(\omega)$ and $\nu^*(\omega)$ have been expressed by the HN model according to Eqn. 5 and 6,

$$E^*(\omega) = E_\infty + \frac{(E_0 - E_\infty)}{[1 + (i\omega\tau)^\alpha]^\beta}; \quad (5)$$

$$\nu^*(\omega) = \nu_\infty + \frac{(\nu_0 - \nu_\infty)}{[1 + (i\omega\tau_\nu)^\alpha]^\beta}, \quad (6)$$

where E_0 and ν_0 are the low frequency values of the modulus and Poisson's ratio, E_∞ and ν_∞ are the high frequency values of the modulus and Poisson's ratio, α governs the width of the loss factor peak, β governs the asymmetry of the loss factor peak, and τ and τ_ν is the relaxation time of the complex modulus and complex Poisson's ratio, respectively. The formulation of Eqn. 6 follows the approach presented by Di Benedetto et al. (2007), where the 2S2P1D model was formulated to express the complex Poisson's ratio of asphalt concrete. Equation 6 has been applied to estimate the complex Poisson's ratio from modal testing of asphalt concrete in papers by Gudmarsson et al. (2014a; 2014b). The FRFs are not sensitive to values of E_0 and ν_0 within the range that is realistic for asphalt concrete. Therefore, the parameters E_0 and ν_0 have been assumed to 100 MPa and 0.5, respectively, which are typical values of asphalt concrete (Ullidtz et al. 2006; Di Benedetto et al. 2007; Gudmarsson et al. 2014a). Equation 5 and 6 are used to optimize the computed FRFs at each measurement temperature separately. The temperature dependency of asphalt concrete can, in addition to the frequency dependency, be accounted for by substituting the Williams-Landel-Ferry equation (see Eqn. 7) into the HN model. This enables an optimization of the FRFs at all temperatures simultaneously to obtain one set of parameter values that can describe all measured FRFs. $E^*(\omega, T)$ and $\nu^*(\omega, T)$ can be characterized through Eqns. 7, 8 and 9 accordingly,

$$\log \alpha_T(T) = \frac{-c_1(T - T_{ref})}{c_2 + T - T_{ref}}, \quad (7)$$

where T is the test temperature, T_{ref} is the reference temperature and c_1 and c_2 are material constants (Williams et al. 1955),

$$E^*(\omega, T) = E_\infty + \frac{(E_0 - E_\infty)}{\left[1 + (i\omega\alpha_T(T)\tau)^\alpha\right]^\beta}, \quad (8)$$

$$\nu^*(\omega, T) = \nu_\infty + \frac{(\nu_0 - \nu_\infty)}{\left[1 + (i\omega\alpha_T(T)\tau_\nu)^\alpha\right]^\beta}. \quad (9)$$

Through the use of shift factors there are seven parameters of the HN model (E_∞ , ν_∞ , α , β , τ , c_1 and c_2) that need to be estimated in the optimization of the computed FRFs. The optimization is performed by using COMSOL Multiphysics 4.3b to compute the FRFs and MATLAB to automatically minimize the difference between the measured and calculated FRFs. The *patternsearch* algorithm in MATLAB, which was used for this purpose, has been found to be efficient in finding the global minimum (Ren et al. 2011). The difference between the measured and theoretical FRFs are calculated over 40 frequencies for the longitudinal and flexural modes of vibration. Eqn. 10 presents the objective function used to minimize the difference between the theoretical and measured FRFs,

$$Error = \sum_{i=1}^N \left(\left| H_{MNorm_i} \right| \times \left| \frac{|H_{M_i}| - |H_{T_i}|}{|H_{M_i}|} \right| \right), \quad (10)$$

where H_{MNorm} is the normalized measured FRF used to weigh the frequencies around the resonances higher, H_M is the measured FRF, H_T is the theoretical FRF, N is the number of data points and i is the index of the data point.

Measurements by Gudmarsson et al. (2014a) of the flexural and longitudinal modes of vibration of a cylindrical specimen showed differences in the estimated loss moduli at higher temperatures between the two modes of vibration. Therefore, the longitudinal and flexural modes are estimated separately in this paper to identify possible differences between the mode types of the cylindrical specimens.

3 Results and discussion

An example of the fit of the optimized FEM computed FRFs to the measured FRFs is shown in Fig. 4, where measured and calculated FRFs are presented by normalizing the amplitudes over the peak values of the measured FRFs for each temperature. The amplitude is normalized to be able to show the fit for all different temperatures in one single figure. Figure 4 shows the fit for the GB3 (s.4) specimen over the frequency range covering the fundamental flexural mode of vibration. Note the increase of the width of the resonance peaks with increasing temperatures, which indicates the significant increase of the damping in the material.

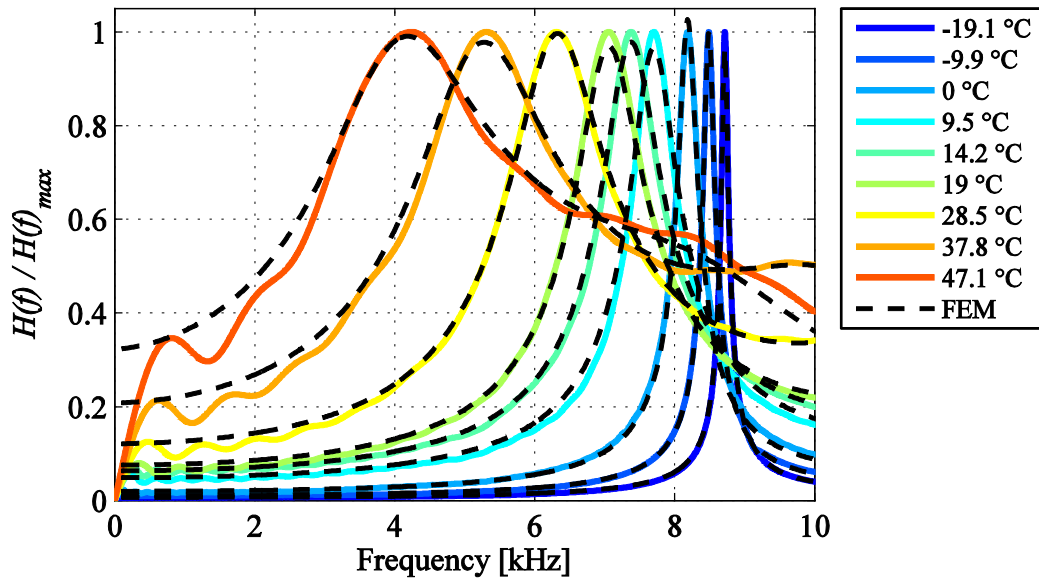


Fig. 4 Normalized measured (GB3 (s.4)) and finite element computed FRFs of the fundamental flexural mode of vibration

Table 4 presents the master curve parameter values of the HN model determined through the optimization of FRFs of the longitudinal and flexural mode types for the two mixes. Note that a unique value of the relaxation time (τ_v) of the complex Poisson's ratio has been applied to the longitudinal mode of vibration of GB3 (s.4). A unique value of the relaxation time for Poisson's ratio may in some cases improve the accuracy of the fit of the computed FRFs to the measurements. However, for the

three other measured FRFs a unique value of the relaxation time had a negligible effect to the fit of the FRFs. Therefore, the relaxation time of the complex modulus was also used for the Poisson's ratio to simplify the optimization of the FRFs. Table 5 presents the optimized master curve parameter values for the 2S2P1D model (Di Benedetto et al. 2007). The 2S2P1D parameter values are presented to facilitate further comparison of the modal test results to different test methods applying the 2S2P1D model to these mixture types. Similarly to the results presented in the paper by Gudmarsson et al. (2014a), the 2S2P1D model and the HN model resulted in similar E^* and ν^* master curves over the frequency range covered by the modal testing ($\sim 10^{-2}$ to 10^{12} Hz). Table 4 and 5 can be used to analyze and compare the modal testing results of the two models. However, the figures presented in this chapter show only the results of the HN model, since a comparison between the two models is not the focus of this paper.

TABLE 4. HN model parameter values of the FRF optimized master curves

Mix	Mode	E_0 [MPa]	E_∞ [MPa]	ν_0	ν_∞	α	β	τ [s]	τ_ν [s]	c_1	c_2
GB3	Long.	100	46650	0.5	0.225	0.476	0.224	1.150	34.47	16.1	97.0
GB3	Flex.	100	47951	0.5	0.325	0.563	0.212	0.288	0.288	15.9	109.1
GB5	Long.	100	50254	0.5	0.262	0.547	0.183	2.443	2.443	17.7	102.4
GB5	Flex.	100	50042	0.5	0.251	0.459	0.238	0.491	0.491	17.5	111.1

TABLE 5. 2S2P1D model parameter values of the FRF optimized master curves

Mix	Mode	E_0 [MPa]	E_∞ [MPa]	ν_0	ν_∞	δ	k	h	β	τ [s]	τ_ν [s]	c_1	c_2
GB3	Long.	100	45845	0.5	0.225	1.38	0.152	0.475	778	0.056	1.68	14.8	97.0
GB3	Flex.	100	47534	0.5	0.325	1.03	0.140	0.495	778	0.013	0.013	14.8	104.7
GB5	Long.	100	50254	0.5	0.262	0.98	0.112	0.380	22	0.070	0.070	17.7	102.4
GB5	Flex.	100	49800	0.5	0.251	1.03	0.130	0.440	75	0.029	0.029	18.2	117.1

Figure 5 shows the FRF optimized complex modulus master curves of the longitudinal and flexural mode types together with the longitudinal complex moduli characterized at each measurement temperature of GB3 (s.4). The results in Fig. 5a show that the flexural mode type give higher dynamic moduli at higher frequencies and lower moduli at lower frequencies. These results together with the higher phase angle in Fig. 5b and the higher loss moduli in Fig. 5c show that the flexural mode type exhibits a higher damping than the longitudinal mode type for this specimen. This difference between the mode types was also observed at higher temperatures by Gudmarsson et al. (2014a). The Cole-Cole diagram (Fig. 5c) show that the complex moduli estimated for each measurement temperature follow the master curve well. This indicates that the thermo-rheological simple assumption of the asphalt concrete is valid, which is a prerequisite to construct master curves (Nguyen et al. 2013a; Nguyen et al. 2013c).

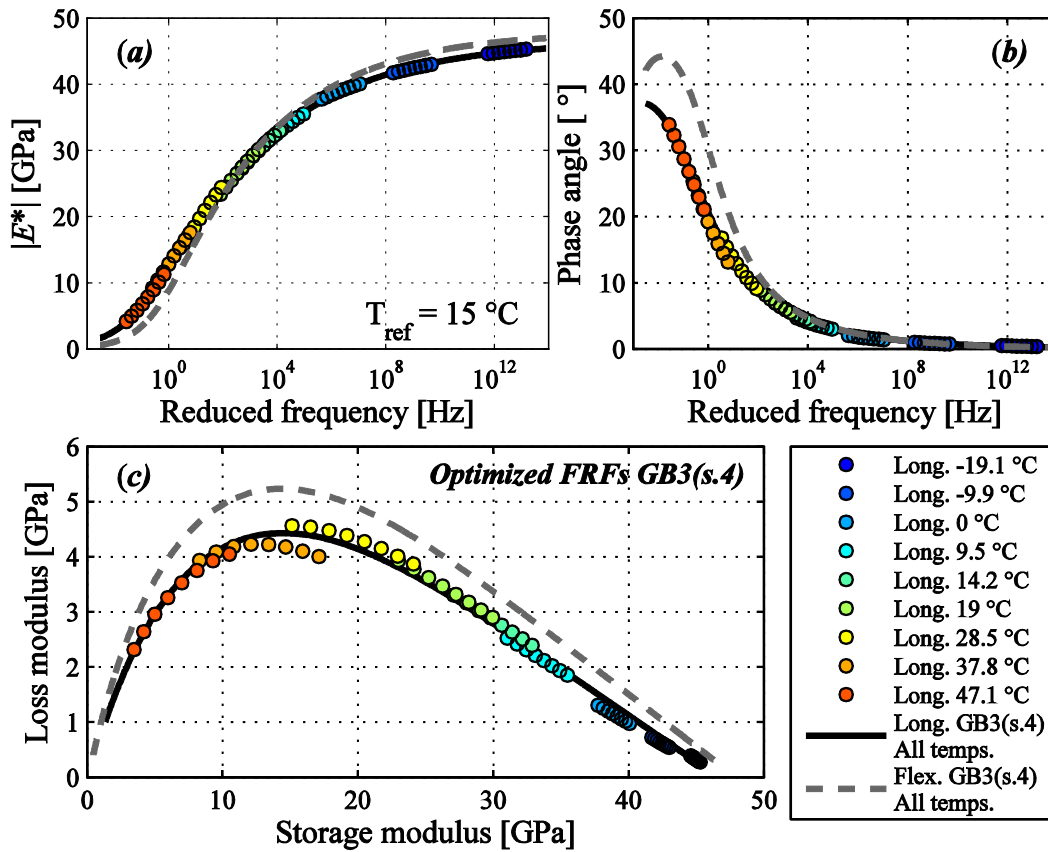


Fig. 5 GB3 (s.4) FRF optimized complex moduli master curves of the longitudinal and flexural modes of vibration showing the absolute value, $|E^*|$ (a), the phase angle (b), and loss and storage modulus (c)

The FRF optimized complex Poisson's ratio master curves of the longitudinal and flexural modes of vibration together with the longitudinal complex Poisson's ratio characterized at each measurements temperature of the GB3 mix are shown in Fig. 6. Figures 6a to 6c show a clear difference between Poisson's ratio of the flexural and longitudinal mode type for this specimen. The different longitudinal and flexural Poisson's ratios were necessary to obtain a good fit to the corresponding longitudinal and flexural measured FRFs. Note that the high frequency value of Poisson's ratio is determined with good accuracy based on the distance between the resonance peaks of the measured FRFs, while the low frequency Poisson's ratio is based on the estimated parameters of the HN model and the assumption of $\nu_0 = 0.5$.

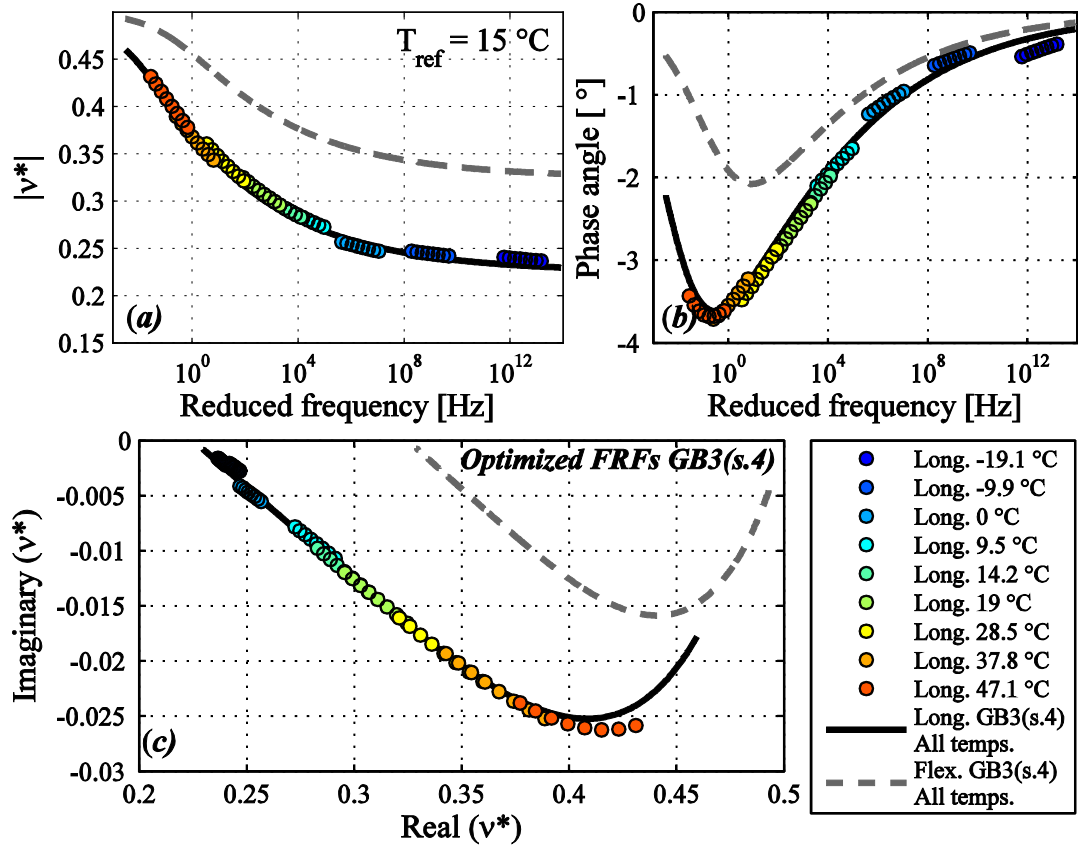


Fig. 6 GB3 (s.4) FRF optimized complex Poisson's ratio master curves of the longitudinal and flexural modes of vibration showing the absolute value, $|v^*|$ (a), the phase angle (b), and loss and storage modulus (c)

The effects of different Poisson's ratios to the FRFs are illustrated in Fig. 7, where the measured longitudinal and flexural FRFs at $-19.1\text{ }^\circ\text{C}$ are shown together with FEM computed FRFs using the Poisson's ratio of the longitudinal and flexural mode types. Figure 7a show the measured FRF of the longitudinal mode type and two FRFs that have been computed through the longitudinal and flexural determined complex Poisson's ratio. It is seen that the flexural values of Poisson's ratio gives a computed longitudinal FRF where the second resonance frequency is lower compared to the measured longitudinal FRF. Figure 7b show the same procedure for the flexural mode of vibration. Here it is seen that the use of the longitudinal value of Poisson's ratio gives a computed flexural FRF where the second resonance frequency is too high compared to the measurements. It can be seen in Figure 7 that a lower Poisson's ratio gives a larger distance between the resonance peaks, and vice versa. The influence of Poisson's ratio to the FRFs increases as the frequency increases.

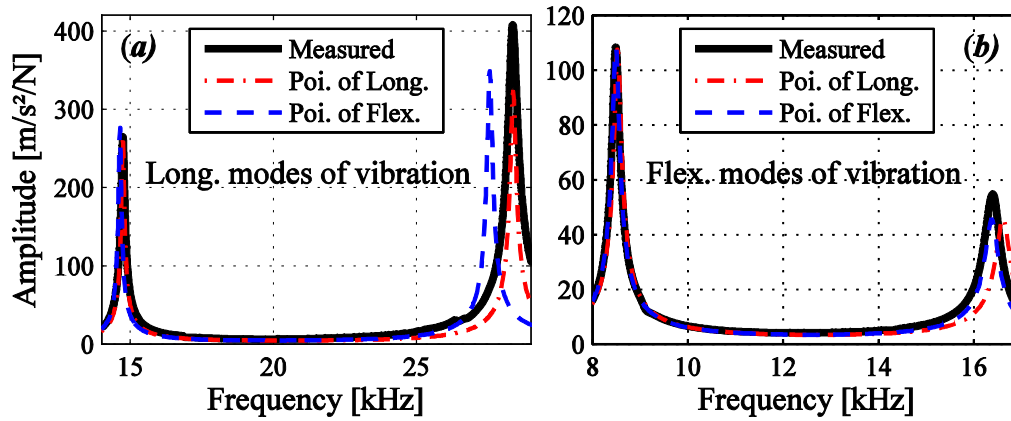


Fig. 7 Comparing FRFs calculated by using different Poisson's ratio to the measured FRFs of the longitudinal (a) and flexural (b) modes of vibration at -19.1 °C

The maximum strains at the fundamental resonance frequency of the longitudinal mode of vibration are shown for the different measurement temperatures in Fig. 8a. The strains have been approximated through the finite element method and the measured acceleration at each measurement temperature. The strains were derived from a point in the middle of the specimen (the node), which is the location of where the maximum strains occurs for the fundamental longitudinal mode of vibration. In addition to the temperature and frequency dependency, the strains in Fig. 8a are also a result of the magnitude of the applied force in the hammer impacts. Figure 8b show the strain normalized over the applied force to illustrate the effects of only the temperature and frequency on the strain level through modal testing.

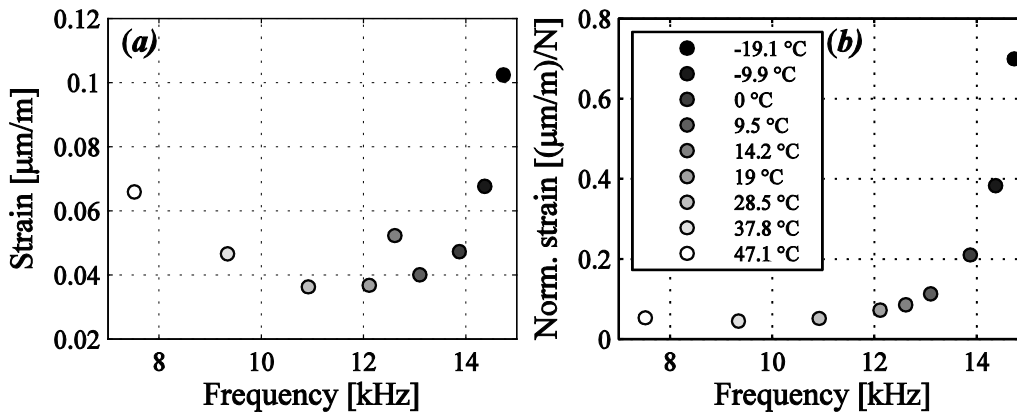


Fig. 8 The maximum strain levels at the fundamental resonance frequency of the longitudinal mode of vibration (GB3 (s.4))

Figure 9 present the FRF optimized complex moduli master curve of the longitudinal mode of vibration of the specimen GB3 (s.4) and the tension-compression measurement results of the asphalt concrete specimens of the same mix (GB3). The figure also shows the FRF optimized master curve of the specimen GB3 (s.3), which was determined and presented in Gudmarsson et al. (2014a). The two master curves determined through modal testing of the two specimens of the same mix but with different dimensions are nearly identical. Also, the tension-compression testing of

the three different specimens gave repetitive results of the complex moduli. The comparison between the FRF and the tension-compression determined complex moduli show that the low strain modal testing provides higher absolute values of the complex moduli. However, the differences between the methods reduces as the frequency increases which show that the material is less strain level dependent at higher values of the modulus.

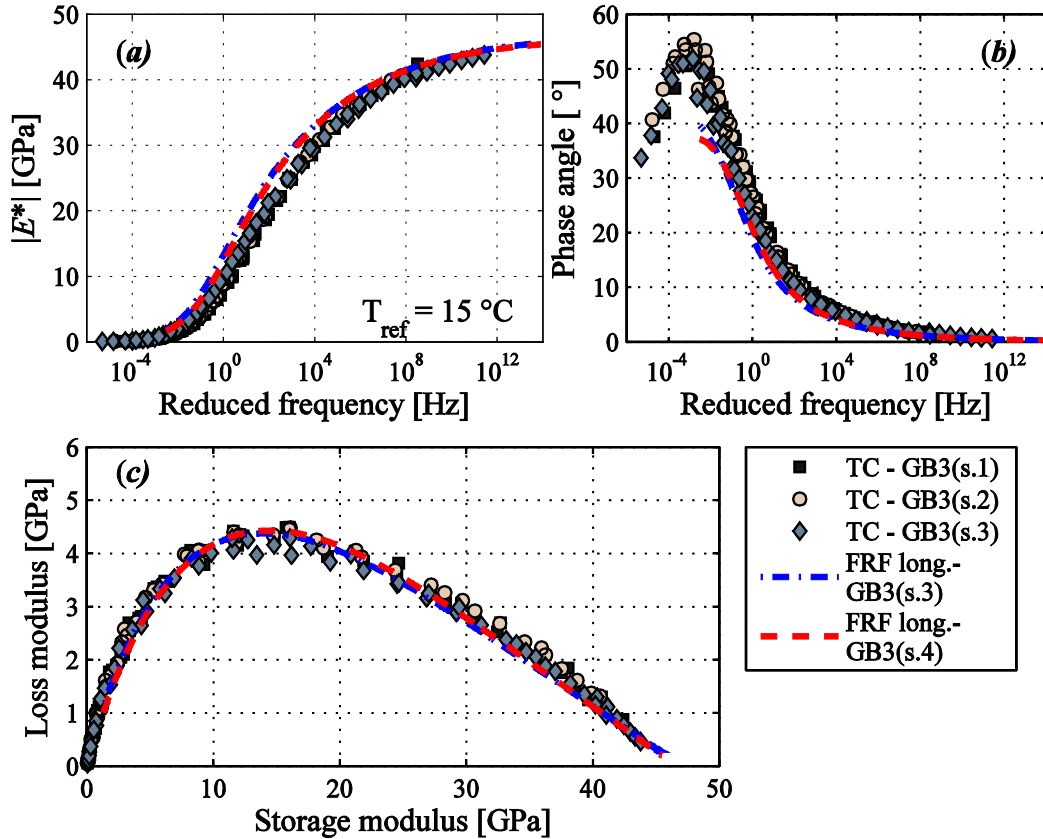


Fig. 9 Comparison of the complex modulus master curves determined through FRF and tension-compression testing of four different specimens showing the absolute value, $|E^*|$ (a), the phase angle (b), and loss and storage modulus (c)

Figure 10 presents the comparison of the tension-compression and FRF optimized complex Poisson's ratio of the longitudinal modes of vibration. The difference between the Poisson's ratios of the two specimens characterized through modal testing comes from that different amount of parameters in the applied HN model were optimized to match the theoretical and measured FRFs. The specimen GB3 (s.3) has been estimated using the same τ value for both the complex modulus and complex Poisson's ratio, while the specimen GB3 (s.4) has been estimated with a different value of τ for Poisson's ratio in the HN model. The latter approach slightly improved the fit of the computed FRF for the second longitudinal resonance frequency compared to using τ of the complex modulus for this specimen (GB3 (s.4)). It can also be seen that the modal testing determined Poisson's ratio of the specimen GB3 (s.4) agrees very well with two out of three presented tension-

compression results of Poisson's ratio. It is clear that the tension-compression determined Poisson's ratio of the specimen labeled TC - GB3 (s.3) differs from all other tension-compression and modal test results of the complex Poisson's ratio. This is a strong indication of that the tension-compression results of TC - GB3 (s.3) may not have been correctly measured. For example, a calculated FRF based on the tension-compression measured Poisson's ratio of TC - GB3 (s.3) results in a too large distance between the resonance peaks compared to the measured FRFs. Relating this to the previous results shown in Fig. 7, it means that the tension-compression determined Poisson's ratio of TC - GB3 (s.3) is too low. This is also what can be seen by comparing the tension-compression results to each other. It should be noted that small measurements errors in the conventional test have a relatively large effect on the Poisson's ratio. For example, an approximately $0.4 \mu\text{m}$ change of the specimen diameter corresponds to a change of Poisson's ratio with ~ 0.1 , which is about the difference shown in Figure 10a.

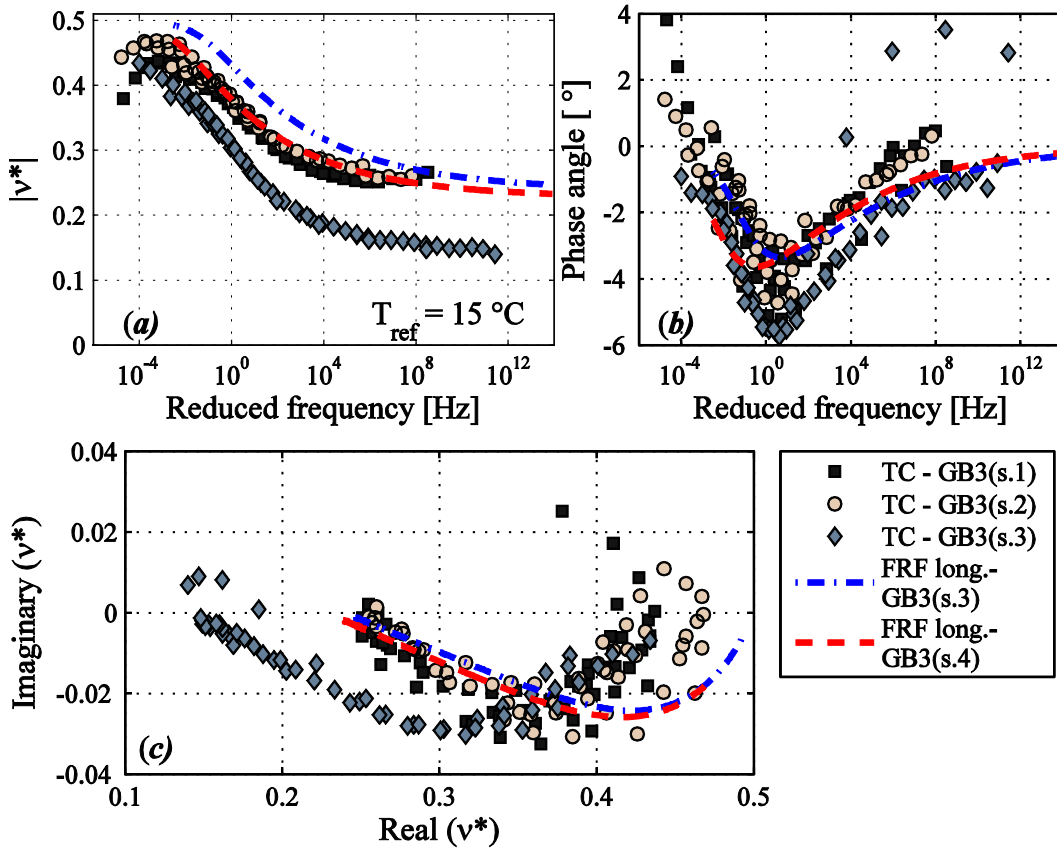


Fig. 10 Comparison of the complex Poisson's ratio master curves determined through FRF and tension-compression testing of four different specimens showing the absolute value, $|\nu^*|$ (a), the phase angle (b), and loss and storage modulus (c)

Results of the GB5[®] mix are shown in the final four figures of this paper. Figure 11 present the complex moduli master curves of the longitudinal and flexural mode types determined from the optimization of FRFs. The complex moduli estimated for each measurement temperature of the longitudinal modes of vibration are also presented. For this modal tested specimen (GB5 (s.4)) there are only small

differences between the complex moduli of the flexural and longitudinal modes of vibration. In all three subplots (Fig. 11a to 11c), the higher frequency range give almost identical results between the two modes of vibration, while smaller deviations in moduli and phase angle can be seen in the lower frequency range. The Cole-Cole diagram shows that the thermo-rheological simple assumption is valid also for this specimen.

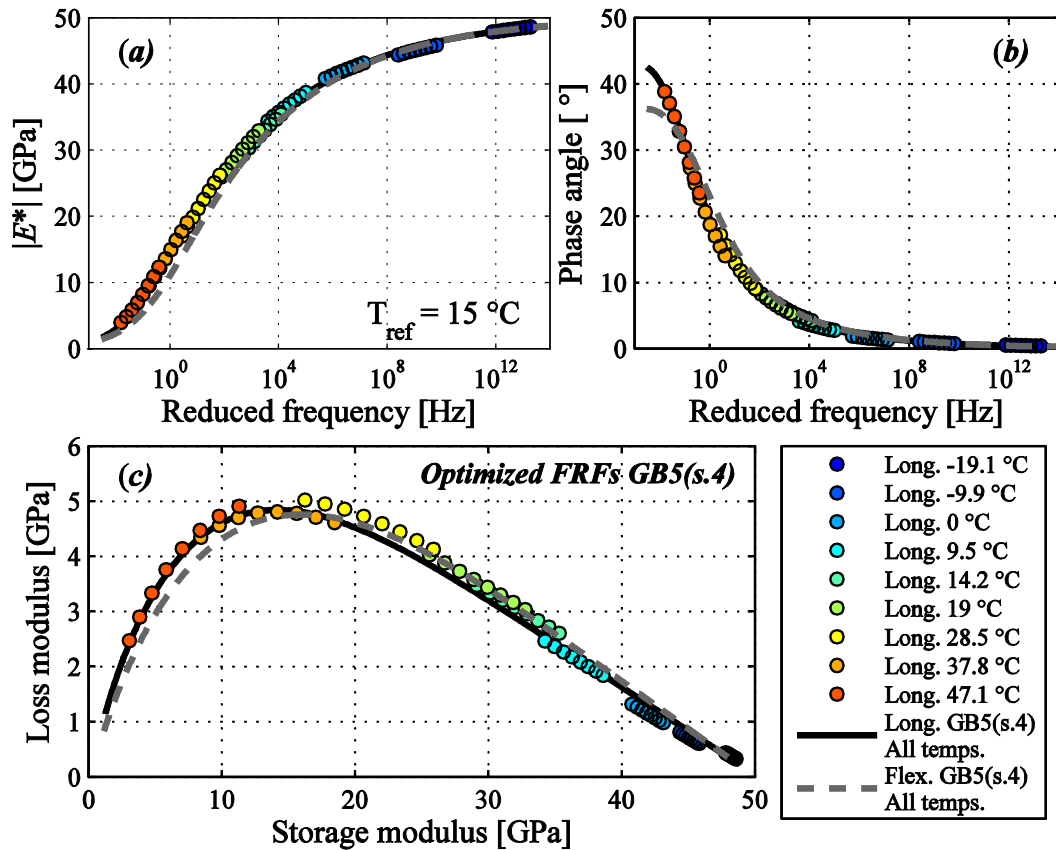


Fig. 11 GB5 (s.4) FRF optimized complex moduli master curves of the longitudinal and flexural modes of vibration showing the absolute value, $|E^*|$ (a), the phase angle (b), and loss and storage modulus (c)

Figure 12 presents the complex Poisson's ratio master curves of the longitudinal and flexural modes of vibration together with the longitudinal complex Poisson's ratio characterized at each measurements temperature. Similar to the complex moduli results, the values of complex Poisson's ratio for the two mode types are quite similar for this specimen (GB5 (s.4)).

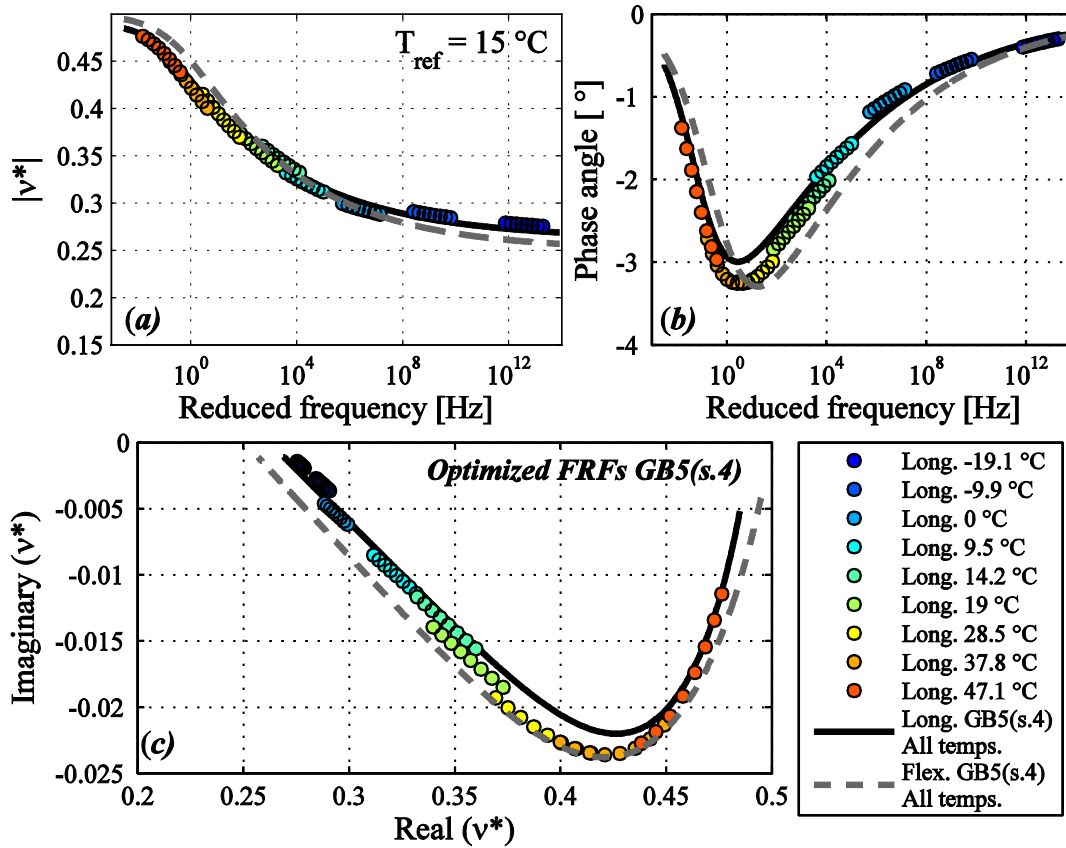


Fig. 12 GB5 (s.4) FRF optimized complex Poisson's ratio master curves of the longitudinal and flexural modes of vibration showing the absolute value, $|v^*|$ (a), the phase angle (b), and loss and storage modulus (c)

The comparison of the complex moduli between the cyclic tension-compression testing and the modal testing are presented in Fig. 13. The modal test determined complex moduli (FRF long. - GB5 (s.4)) gives a higher absolute value of the complex modulus which is precisely what has been seen in all of the other comparisons between the two test methods. The three tension-compression tested specimens show a good agreement between each other with a small exception of the measured phase angles at the lowest frequencies (see Fig. 13b).

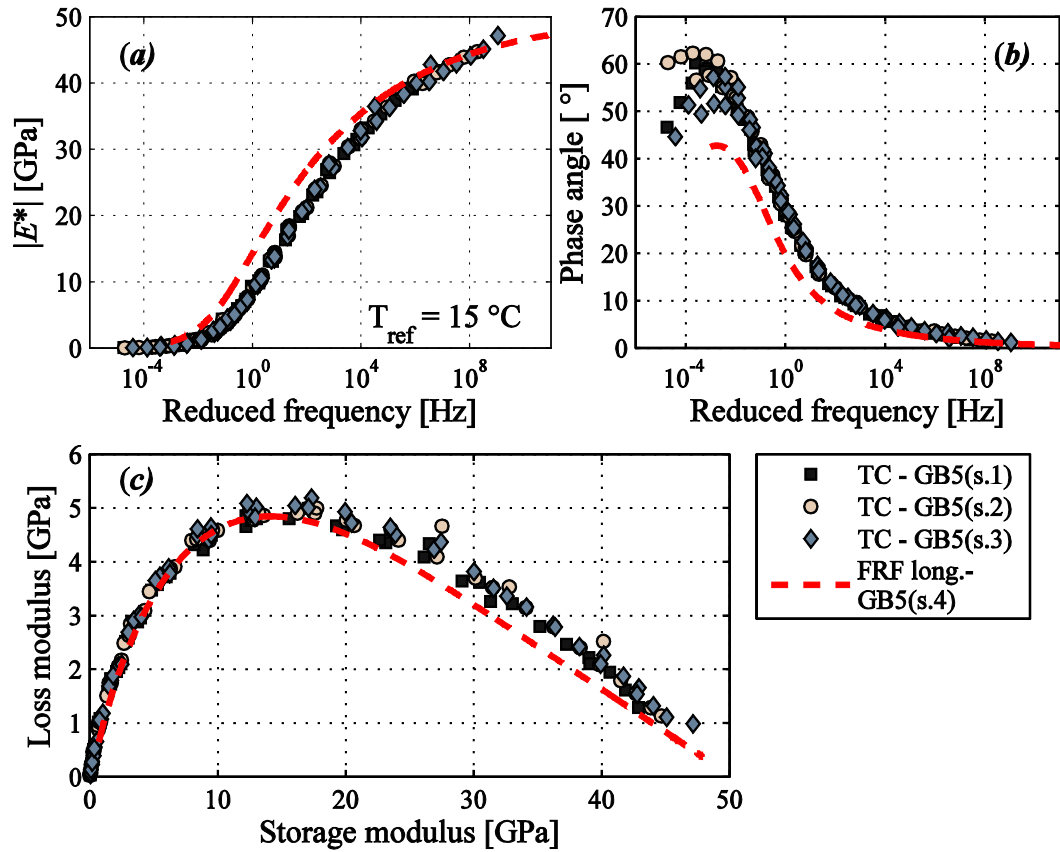


Fig. 13 Comparison of the complex modulus master curves determined through FRF and tension-compression testing of four different specimens showing the absolute value, $|E^*|$ (a), the phase angle (b), and loss and storage modulus (c)

Figure 14 shows the complex Poisson's ratio determined from the tension-compression and modal testing of the longitudinal modes of vibration. The modal testing resulted in a slightly higher absolute value of Poisson's ratio than the conventional cyclic testing at the high frequencies as shown in Fig. 14a. However, in general there is a fairly good agreement between the two test methods. The same subplot shows that there are differences between the three tension-compression tested specimens at low frequencies, where some conventional test results exceed Poisson's ratio of 0.5. The tension compression testing of the three specimens shows a general trend but at the same time there are several deviating measurements which are seen clearly in Fig. 14b and 14c. These results further indicate the complexity to accurately measure the complex Poisson's ratio of asphalt concrete.

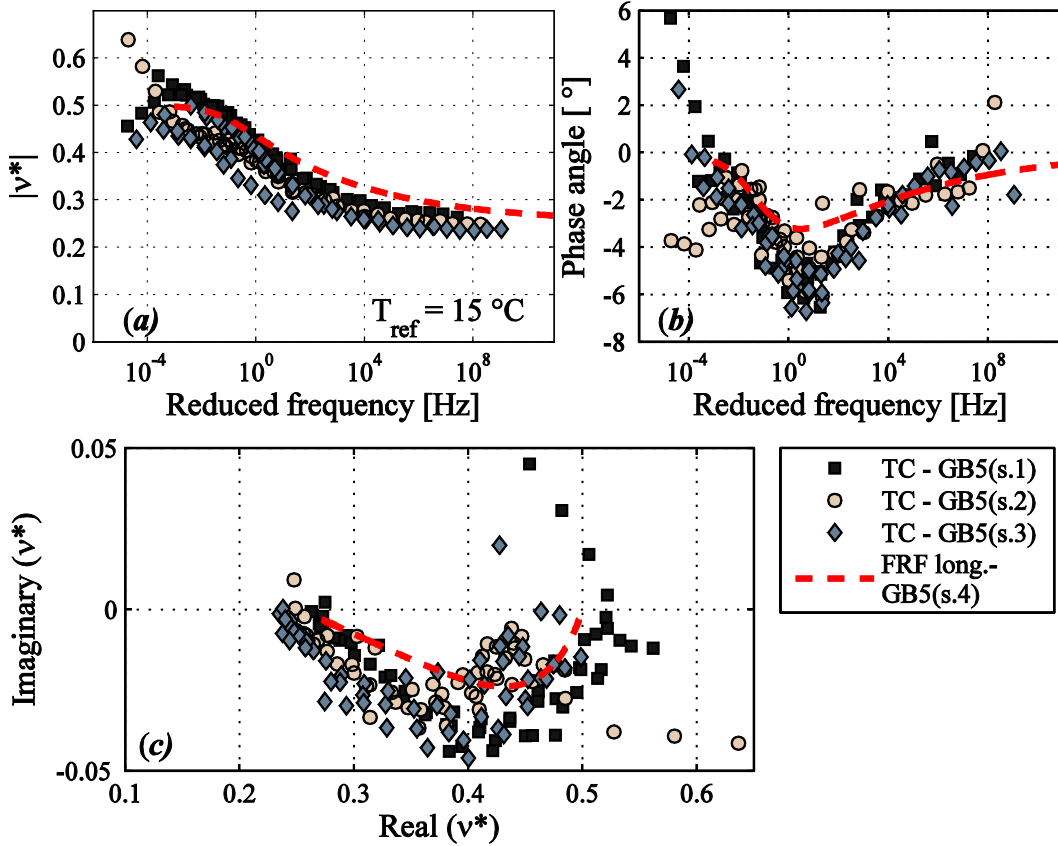


Fig. 14 Comparison of the complex Poisson's ratio master curves determined through FRF and tension-compression testing of four different specimens showing the absolute value, $|\nu^*|$ (a), the phase angle (b), and loss and storage modulus (c)

4 Conclusions

All three modal tested specimens (two different mixtures) have been shown to result in higher absolute values of the complex moduli and lower phase angles compared to the tension-compression testing. The comparison of the complex moduli performed in this paper strengthen previous results, shown in Gudmarsson et al. (2014a), of the strain level influence to the complex modulus master curve of asphalt concrete determined through modal and cyclic testing. Furthermore, it was seen that the different dimensions of the cylindrical specimens did not affect the modal test results.

The modal and tension-compression testing gives similar results of the complex Poisson's ratio, if the tension-compression complex Poisson's ratio results of the specimen labeled TC – GB3 (s.3) are disregarded. This indicates that in contrast to the complex moduli, the complex Poisson's ratio may be independent on the different strain levels in the studied strain range. An improvement of the fit of the FRFs may in some cases be possible by using a value of the relaxation time for Poisson's ratio different from the value used for the complex modulus. However, in most cases the optimization of the FRFs can be simplified by assuming the same relaxation time for the complex modulus and complex Poisson's ratio.

Differences between the flexural and longitudinal modes of vibration were seen for the GB3 (s.4) specimen, where the flexural modes of vibration resulted in higher loss moduli and higher Poisson's ratio. However, no clear differences of the damping (loss moduli and phase angle) between the two modes of vibration were seen for the GB5 (s.4) specimen. These results indicate that there are no systematic differences between the flexural and longitudinal modes of vibrations of asphalt concrete specimens.

Acknowledgements

The Swedish transport administration (Trafikverket) and the Swedish construction industry's organization (SBUF) are acknowledged for their financial support. Quang Tuan Nguyen and Nouffou Tapsoba are gratefully acknowledged for performing the tension-compression measurements. Simon Poguet at Eiffage Travaux Publics in Lyon is acknowledged for providing the specimens. A great appreciation is also given to the research group at Laboratoire Génie Civil et Bâtiment in ENTPE at the University of Lyon for all their help and hospitality.

References

- Airey, G. D., Rahimzadeh, B. (2004) "Combined bituminous binder and mixture linear rheological properties," *Constr. Build. Mater.*, Vol. 18, 535–548
- Bernard, S., Grimal, Q., Laugier, P. (2014). "Resonant ultrasound spectroscopy for viscoelastic characterization of anisotropic attenuative solid materials," *J. Acoust. Soc. Am.*, Vol. 135, Issue 5, 2601-2613.
- Di Benedetto, H., Delaporte, B., Sauzéat, C. (2007). "Three-Dimensional Linear Behavior of Bituminous Materials: Experiments and Modeling," *Int. J. Geomech.*, Vol. 7, No. 2, 149-157.
- Di Benedetto, H., Partl, M. N., Francken, L., De La Roche Saint André, C. (2001). "Stiffness testing for bituminous mixtures," *Mater. Struct.*, Vol. 34, pp. 66-70.
- Di Benedetto, H., Sauzéat, C., Sohm, J. (2009). "Stiffness of Bituminous Mixtures Using Ultrasonic Wave Propagation," *Road Materials and Pavement Design*, Vol. 10, No. 4, pp. 789-814.
- Doubbaneh, E. (1995). "Comportement mécanique des enrobés bitumineux des petites aux grandes déformations," Ph.D. dissertation, Institut National des Sciences Appliquées, ENTPE, Lyon.
- Falchetto, A.C., Marasteanu, M.O. (2011). "Physical hardening: from binders to mixtures," *Int. J. Roads Airports*, 1 (1), pp. 18–34

Gudmarsson, A., Ryden, N., Birgisson, B. (2012a). "Application of resonant acoustic spectroscopy to asphalt concrete beams for determination of the dynamic modulus," *Mater. Struct.*, Vol. 45, 1903-1913.

Gudmarsson, A., Ryden, N., Birgisson, B. (2012b). "Characterizing the low strain complex modulus of asphalt concrete specimens through optimization of frequency response functions," *J. Acoust. Soc. Am.*, Vol. 132, Issue 4, 2304-2312.

Gudmarsson, A., Ryden, N., Di Benedetto, H., Sauzéat, C., Tapsoba, N., Birgisson, B. (2014a), "Comparing linear viscoelastic properties of asphalt concrete measured by laboratory seismic and tension-compression tests, " *Journal of Nondestructive Evaluation*, Vol. 33, Issue 4, 571-582.

Gudmarsson, A., Ryden, N., Birgisson, B. (2014b), "Observed deviations from isotropic linear viscoelastic behaviour of asphalt concrete through modal testing," *Construction and Building Materials*, Vol. 66, 63-71.

Hartmann, B., Lee, G. F., and Lee, J. D. (1994). "Loss factor height and width limits for polymer relaxations," *J. Acoust. Soc. Am.* Vol. 95, 226–233.

Havriliak, S., and Negami, S. (1966). "A complex plane analysis of α -dispersions in some polymer systems," *J. Polym. Sci. C*, Vol. 14, 99–117.

Kweon, G., Kim, Y. R. (2006). "Determination of the Complex Modulus of Asphalt Concrete Using the Impact Resonance Test," *J. Transp.Res. Board*, Vol. 1970, 151-160.

Lacroix, A., Kim, Y. R., Far, M. S. S. (2009). "Constructing the Dynamic Modulus Mastercurve Using Impact Resonance Testing," *Assoc. Asph. Paving Technol.*, Vol. 78, 67-102.

Larcher, N., Takarli, M., Angellier, N., Petit, C., Sebbah, H. (2014). "Towards a viscoelastic mechanical characterization of asphalt materials by ultrasonic measurements," *Mater. Struct.*, DOI: 10.1617/s11527-013-0240-0.

Leisure, R. G., Willis, F. A. (1997). "Resonant ultrasound spectroscopy," *J. Phys.: Condens. Matter*, Vol. 9, 6001–6029.

Madigosky, W. M., Lee, G. F., and Niemiec, J. M. (2006). "A method for modeling polymer viscoelastic data and the temperature shift function," *J. Acoust. Soc. Am.*, Vol. 119, 3760–3765.

Migliori, A., Sarrao, J. L. (1997). *Resonant Ultrasound Spectroscopy – Applications to Physics, Materials Measurements and Nondestructive Evaluation* (Wiley – Interscience Publication, New York)

Mounier, D., Di Benedetto, H., Sauzéat, C., (2012). "Determination of bituminous mixtures linear properties using ultrasonic wave propagation," *Constr. Build. Mater.*, Vol. 36, 638-647.

Nazarian, S., Tandon, V., Yuan, D. (2005). "Mechanistic Quality Management of Hot Mix Asphalt Layers with Seismic Methods," *J. ASTM Int.*, Vol. 2(9).

Nguyen, Q. T., Di Benedetto, H., Sauzéat, C., (2013b). "Prediction of linear viscoelastic behaviour of asphalt mixes from binder properties and reversal," *Multi-Scale Model. & Charact. of Infrastruc. Mater.*, Kringos, N., Birgisson, B., Frost, D., Wang, L., (Eds.) Vol. 8, pp. 237-248.

Nguyen, Q. T., Di Benedetto, H., Sauzéat, C., (2014). "Linear and nonlinear viscoelastic behaviour of bituminous mixtures," *Mater. Struct.*, DOI: 10.1617/s11527-014-0316-5.

Nguyen, Q. T., Di Benedetto, H., Sauzéat, C., and Tapsoba, N. (2013a). "Time Temperature Superposition Principle Validation for Bituminous Mixes in the Linear and Nonlinear Domains." *J. Mater. Civ. Eng.*, 25(9), 1181–1188.

Nguyen M. L., Sauzéat C., Di Benedetto, H., Tapsoba, N. (2013c). "Validation of the time–temperature superposition principle for crack propagation in bituminous mixtures," *Mater. Struct.*, Vol. 46, Issue 7, pp 1075-1087.

Norambuena-Contreras, J., Castro-Fresno, D., Vega-Zamanillo, A., Celaya, M., Lombillo-Vozmediano, I., (2010). "Dynamic modulus of asphalt mixture by ultrasonic direct test," *NDT&E Int.*, Vol. 43, 629-634.

Olard, F. (2012). "GB5 mix design: high-performance and cost-effective asphalt concretes by use of gap-graded curves and SBS modified bitumens," *Road Materials and Pavement Design.*, DOI:10.1080/14680629.2012.657074.

Olard, F., Di Benedetto, H. (2003). "General "2S2P1D" Model and Relation Between the Linear Viscoelastic Behaviours of Bituminous Binders and Mixes," *Road Materials and Pavement Design.*, Vol. 4, No. 2, 185-224.

Ren, Z., Atalla, N., Ghinet, S. (2011). "Optimization Based Identification of the Dynamic Properties of Linearly Viscoelastic Materials Using Vibrating Beam Technique," *ASME J. Vib. Acoust.*, Vol. 133, Issue 4, 041012 1-12.

Ryden, N. (2011). "Resonant frequency testing of cylindrical asphalt samples," *Eur. J. Environ. Civ. Eng.*, Vol. 15, 587-600.

Ryden, N., Park, C.H. (2006). "Fast simulated annealing inversion of surface waves on pavement using phase-velocity spectra," *Geophysics.* Vol. 71, No. 4, R49-58.

Tiouajni, S., Di Benedetto, H., Sauzéat, C., Pouget, S. (2011). "Approximation of Linear Viscoelastic Model in the 3 Dimensional Case with Mechanical Analogues of Finite Size," *Road Materials and Pavement Design*, Volume 12, Issue 4, pp. 897-930.

Ullidtz P, Harvey J, Tsai B-W, Monismith C. (2006). "Calibration of CalME models using WesTrack performance data. Report UCPRC-RR-2006-14," Berkeley: Pavement Research Center, University of California.

Whitmoyer, S. L., Kim, Y. R. (1994), "Determining Asphalt Concrete Properties via the Impact Resonant Method," *J. Test. Eval.*, Vol. 22, No. 2, 139-148.

Williams, M. L., Landel, R. F., and Ferry, J. D. (1955). "The temperature dependence of relaxation mechanisms in amorphous polymers and other glass-forming liquids," *J. Am. Chem. Soc.*, Vol. 77, 3701.

Yusoff, N. I. Md., Shaw, M. T., and Airey, G. D. (2011). "Modelling the linear viscoelastic rheological properties of bituminous binders," *Constr. Build. Mater.* 25(5), 2171–2189

Zhao, Y., Liu, H., Bai, L., Tan, Y. (2013). "Characterization of Linear Viscoelastic Behavior of Asphalt Concrete Using Complex Modulus Model," *J. Mater. Civ. Eng.*, Vol. 25, No, 10, 1543-1548.

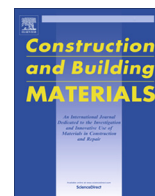
Paper V

Observed deviations from isotropic linear viscoelastic behavior of asphalt concrete through modal testing

ANDERS GUDMARSSON
NILS RYDEN
BJÖRN BIRGISSON

Published in
Construction and Building Materials 66
63–71





Observed deviations from isotropic linear viscoelastic behavior of asphalt concrete through modal testing



Anders Gudmarsson*, Nils Ryden, Björn Birgisson

Highway and Railway Engineering, KTH Royal Institute of Technology, Brinellvägen 23, 100 44 Stockholm, Sweden

HIGHLIGHTS

- Material properties of asphalt concrete were determined through modal testing.
- Isotropic linear relation between E^* , ν^* and G^* was observed above ~ 10 kHz at 0°C .
- Discrepancies were found from isotropic linear behavior below ~ 10 kHz at 0°C .
- G^* calculated from E^* and ν^* are overestimated at key frequencies and temperatures.

ARTICLE INFO

Article history:

Received 27 March 2014
Received in revised form 20 May 2014
Accepted 22 May 2014

Keywords:

Asphalt concrete
Complex modulus
Complex shear modulus
Complex Poisson's ratio
Modal testing
Frequency response functions

ABSTRACT

The complex Young's moduli, complex shear moduli and complex Poisson's ratio of a beam shaped asphalt concrete specimen have been characterized through low strain ($\sim 10^{-7}$) frequency response function measurements. The assumption of isotropic linear viscoelastic behavior has been applied and investigated. The results indicate that the asphalt concrete specimen agree with the isotropic linear viscoelastic assumption at low temperatures and high frequencies (>10 kHz at 0°C), but at higher temperatures and lower frequencies, discrepancies from isotropic linear behavior are shown. The dynamic shear moduli calculated from the estimated Young's moduli and Poisson's ratio of the asphalt concrete specimen are overestimated for frequencies and temperatures often applied to pavements.

© 2014 Elsevier Ltd. All rights reserved.

1. Introduction

The viscoelastic complex modulus of asphalt concrete is fundamental to modern pavement design due to the time and temperature dependency of bituminous materials. Methods to determine the complex modulus over a wide frequency and temperature range (i.e. master curve) are today based on predictive equations or mechanical laboratory testing [1–5]. The conventional cyclic loading tests of bituminous mixtures are expensive and complicated to perform while the predictive models are more economic but not as accurate as actual testing. New methods to measure the complex modulus of asphalt concrete through stress wave measurements are economic, accurate and open up the possibility of future nondestructive quality control of pavement materials [6–9].

In the field of pavement engineering, the complex Young's modulus (E^*) is often related to the complex shear modulus (G^*)

and complex Poisson's ratio (ν^*) according to isotropic linear viscoelastic theory. However, it has been shown in several papers that the relations of E^* , G^* and ν^* according to isotropic linear viscoelastic theory are not at all accurate for asphalt concrete [10–15]. It has instead been recommended to apply empirical formulations to relate E^* , G^* and ν^* [3,13]. The reason for the discrepancy from isotropic linear viscoelastic theory is not fully understood, even if anisotropy of the asphalt concrete has been believed to be one important reason [13,14,16]. At the same time, anisotropy has shown to have a minor influence to the small strain behavior as e.g. the dynamic modulus [2,17]. Di Benedetto et al. [16] concluded that the relation between E^* and G^* remains unknown for asphalt concrete and needs further studying.

In the field of geophysics it is well known that compression and shear waves exhibit different attenuation in saturated rocks and soils [18,19]. For these porous materials it has been necessary to apply the theory of linear poroelasticity to be able to predict the dynamic response. Different damping properties of compression and shear waves may also be the case of asphalt concrete, especially at higher temperatures, but this has not been thoroughly

* Corresponding author. Tel.: +46 733 84 85 76.
E-mail address: andgud@kth.se (A. Gudmarsson).

examined. On the other hand, it has been theoretically shown that the complex bulk moduli have a lower damping than the complex shear moduli for viscoelastic materials [20,21]. Furthermore, Pritz [22] showed that the bulk and shear loss factors are related through the dynamic Poisson's ratio for viscoelastic materials if the shear loss factor is lower than 0.3. It was also pointed out by Pritz [22,23] that the relation may be accurate enough for a higher shear loss factor. Measurements of asphalt concrete often results in loss factors above 0.3 for both E^* and G^* at high temperatures [5,9,24]. Possible differences between the loss factors of E^* and G^* of asphalt concrete could be a reason to discrepancies from isotropic linear viscoelastic theory [10,25].

Despite the uncertainties of the relation between the isotropic linear viscoelastic properties, there are few papers reporting measurements of E^* and G^* that have been performed on the same asphalt concrete specimens [10,11]. More common are measurements of E^* and G^* that have been performed to the same asphalt mixture but not on the same specimens cf. e.g. [13,14,26]. A probable reason for this are limitations of most of the conventional test methods to measure both E^* and G^* for the same specimen. In addition, the conventional test methods often introduces different boundary conditions and different types of set-up of the E^* and G^* measurements. Therefore, it is of high interest to further investigate the low strain E^* and G^* of asphalt concrete using nondestructive testing. Nondestructive stress wave measurements may enable the characterization of both E^* and G^* by measuring different modes of vibration of an asphalt concrete specimen.

Mounier et al. [27] performed ultrasonic testing to cylindrical asphalt concrete specimens where the propagation of compression and shear waves was measured. E^* and ν were determined through simplified approximate formulations for one loading frequency per temperature, but no results of G^* were presented. Other stress wave measurements performed to asphalt concrete has also been focused on only determining E^* , through either ultrasonic wave propagation measurements [25,28–31] or impact resonance testing [32–34]. In common for these tests is that simplified approximate relations have been used to determine one E^* per temperature (cf. e.g. ASTM C215 2008 [35]). Therefore, the frequency dependency of the asphalt concrete cannot be estimated through this approach. To characterize the frequency dependency of E^* through stress wave measurements, numerical methods (resonant acoustic spectroscopy) were applied by Ryden [36] and Gudmarsson et al. [8]. The combination of numerical computations and resonance frequency measurements allows the determination of the full elastic tensor of isotropic and anisotropic elastic materials, since the resonance frequencies of free solids depend on the mass, the dimensions and the elastic constants [6]. The application of resonant acoustic spectroscopy to the frequency dependent asphalt concrete enabled the determination of E^* at more than one resonance frequency. However, in order to determine master curves based only on stress wave measurements, it was also concluded that the measurements should not be limited to the discrete resonance frequencies. Frequency response functions (FRFs), i.e. the acceleration divided by the applied force in frequency domain, provide information of material properties over a wide frequency range including both resonance peaks and valleys in a frequency response curve. This allows material properties to be determined over a wide and fine sampled frequency range. Measurements of FRFs have been applied in other fields of engineering to estimate master curves, where properties of materials as e.g. metal polymer

sandwich [37], silicone rubber [38] and multi-layer beams of metal and viscoelastic material [39] have been characterized. Measurements of FRFs have also been applied to an asphalt concrete specimen where E^* was characterized over a wide frequency range [9]. This enabled the E^* master curve to be determined for the longitudinal modes of vibration by only applying modal testing to asphalt concrete. However, there have been no studies applying this method to characterize E^* , G^* and ν^* of asphalt concrete specimens.

In this paper, FRF measurements of the longitudinal, flexural and torsional modes of vibration are performed to characterize the low strain $E^*(T, f)$, $\nu^*(T, f)$ and $G^*(T, f)$ of a beam shaped asphalt concrete specimen. Theoretical FRFs are calculated numerically by the finite element method and optimized against measured FRFs to estimate the material properties of the asphalt concrete specimen. The results presented in this paper indicate that the calculated $G^*(T, f)$ from the estimated $E^*(T, f)$ and $\nu^*(T, f)$ are overestimated for the asphalt concrete specimen at important frequencies and temperatures.

2. Methodology

2.1. Materials and measurements

The asphalt concrete specimen used in these measurements has previously been tested in [8], where resonant acoustic spectroscopy was applied to derive the complex modulus from the discrete resonance frequencies. It has also been tested in [9], where the method of optimizing FRFs of asphalt concrete was developed and applied to characterize the complex modulus for the longitudinal modes of vibration over a wider frequency range. In this study, additional modes of vibration are measured to characterize and investigate the relation between E^* , G^* and ν^* of the beam shaped asphalt concrete specimen. The specimen consists of granite aggregates with the gradation according to Table 1 and Nynas binder with an original penetration grade of 70/100. The beam-shaped specimen has been sawn out from a roller compacted slab with the dimensions of 500 × 560 × 80. The length, width and height of the specimen are 382.00, 58.74 and 58.94 mm, respectively. The specimen has an air void content of 2.7% and the density is 2.359 g/cm³. The binder content of the asphalt concrete mixture is 6.3% by weight.

The specimen was placed on soft foam to provide free boundary conditions while exciting the flexural, longitudinal and torsional modes of vibration. An instrumented hammer (PCB model 086E80) was used to apply the load impulse and an accelerometer (PCB model 352B10) attached by wax was used to measure the response of the specimen. The light accelerometer (0.7 g) is assumed to not affect the measurements. The measurement devices were connected according the following scheme: hammer and accelerometer → signal conditioner (PCB model 480B21) → data acquisition device (NI USB-6251 M Series) → computer. The data from the hammer and the accelerometer were recorded with a sampling frequency of 500 kHz. Fig. 1 illustrates the locations of the hammer impacts and the placements of the accelerometer when measuring the flexural, longitudinal and torsional modes of vibration of the asphalt concrete beam. The accelerometer was placed on the opposite sides to the locations of the hammer impacts, which are marked in Fig. 1 for each mode of vibration. The strain levels were approximated for the fundamental resonance frequency where the highest strains occur. For the longitudinal modes of vibration the maximum strain has been approximated to the magnitude of 10^{-7} according to Eq. (1), where ε is the strain, $Y(f)$ is the measured acceleration and L is the length of the specimen [40,9]. Note that the highest acceleration at the fundamental resonance frequency (~ 17.5 m/s² at ~ 5200 Hz) was measured for the longitudinal modes of vibration.

$$\varepsilon = \frac{Y(f)}{4\pi L f^2} \quad (1)$$

The flexural, longitudinal and torsional modes of vibration were excited by five impacts each at seven temperatures between -30 and 30 °C, while the specimen was located inside the temperature chamber. The opening of the door to the temperature chamber is assumed to not affect the temperature of the specimen during the short time of the measurements (~ 10 – 20 s). The recorded load impulse and response of the specimen were used to calculate the FRFs according to Eq. (2), where the five measurements ($n = 5$) are averaged at each frequency. The coherence

Table 1
Gradation of the asphalt concrete mixture.

Sieve size (mm)	0.063	0.125	0.25	0.5	1	2	4	5.6	8	11.2	16	22.4
% Passing	8.9	12	16	21	28	39	50	58	70	81	98	100

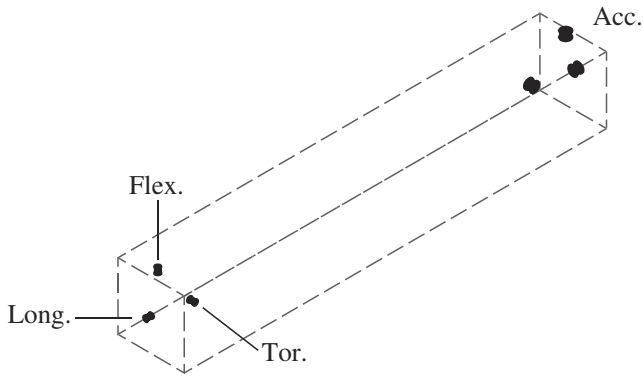


Fig. 1. Illustration of the locations of the hammer impacts and placements of the accelerometer for the flexural, longitudinal and torsional modes of vibration, respectively.

function is a quality estimator of FRFs showing differences of the phase in the complex domain for each frequency. A value of one of the coherence function means that the phase difference between the input and output is constant for the different impacts. The coherence function is calculated according to Eq. (3), where the averaging of the five measurements is performed, similar to the FRFs, in the complex domain at each frequency. Fig. 2 presents the measured response in time domain, the FRFs and the coherence functions of the flexural, longitudinal and torsional modes of vibration at 0 °C.

$$H(f) = \left(\frac{1}{n} \sum_{k=1}^n Y_k(f) \cdot X_k^*(f) \right) / \left(\frac{1}{n} \sum_{k=1}^n X_k(f) \cdot X_k^*(f) \right) \quad (2)$$

where $H(f)$ is the frequency response function, $Y(f)$ is the measured acceleration, $X(f)$ is the measured applied force and $X^*(f)$ is the complex conjugate of the applied force.

$$CF(f) = \left(\frac{1}{n} \sum_{k=1}^n X_k^*(f) \cdot Y_k(f) \right)^2 / \left[\left(\frac{1}{n} \sum_{k=1}^n X_k(f) \cdot X_k^*(f) \right) \cdot \left(\frac{1}{n} \sum_{k=1}^n Y_k(f) \cdot Y_k^*(f) \right) \right] \quad (3)$$

where $CF(f)$ is the coherence function, $X^*(f) \cdot Y(f)$ is the cross power spectrum, $X(f) \cdot X^*(f)$ is the auto power spectrum of the impulse and $Y(f) \cdot Y^*(f)$ is the auto power spectrum of the response.

2.2. Calculating theoretical frequency response functions

Fig. 3 presents the coordinate system and the applied mesh of the finite element model of the asphalt concrete specimen. The size of the mesh, consisting of maximum 2 cm tetrahedral elements with quadratic shape functions, has been determined through a convergence study of the torsional modes of vibration. The torsional modes of vibration at the low measurement temperatures were shown

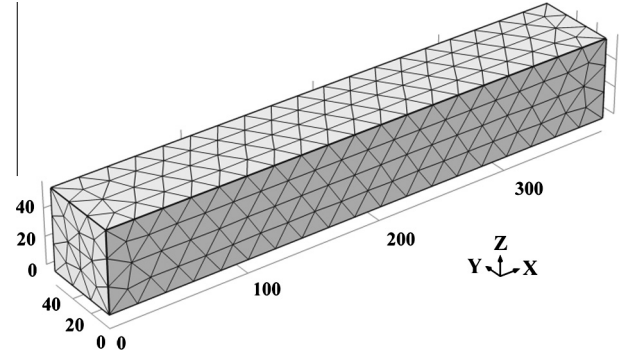


Fig. 3. The coordinates and the mesh of the modeled specimen [9].

to be most sensitive to the size of the mesh. Fig. 4 shows the convergence study at -30 °C. The point load (F_p) in the model was applied in the x , y and z coordinates (5, 58.74, 53.94) mm for the torsional mode, (5, 29.37, 58.94) mm for the flexural mode and (0, 29.37, 29.47) for the longitudinal mode. Similarly, the response was determined in the points (377, 0, 5), (377, 29.37, 58.94) and (382, 29.37, 29.47) for the torsional, flexural and longitudinal modes, respectively. These positions correspond to the actual points of the hammer impact and accelerometer placement during the measurements. The point load was applied between a frequency range of 100–20,000 Hz with the increment of 20 Hz.

Eq. (4) presents the three-dimensional equation of motion used to calculate the response of the finite element model in frequency domain due to the applied point load (1 N).

$$-\rho\omega^2 \mathbf{u} - \nabla \cdot \boldsymbol{\sigma} = F_p e^{i\phi} \quad (4)$$

where ρ is the density, ω is the angular frequency ($\omega = 2\pi f$), \mathbf{u} is the displacement vector, ∇ is the vector operator ($\nabla = [\partial/\partial X, \partial/\partial Y, \partial/\partial Z]$) and $\boldsymbol{\sigma}$ is the Cauchy stress tensor according to Eq. (5):

$$\boldsymbol{\sigma} = \mathbf{C} : \boldsymbol{\varepsilon}$$

$$\boldsymbol{\varepsilon} = \frac{1}{2} [(\nabla \mathbf{u})^T + \nabla \mathbf{u}]$$

$$\nabla \mathbf{u} = \begin{bmatrix} \frac{\partial u}{\partial X} & \frac{\partial u}{\partial Y} & \frac{\partial u}{\partial Z} \\ \frac{\partial v}{\partial X} & \frac{\partial v}{\partial Y} & \frac{\partial v}{\partial Z} \\ \frac{\partial w}{\partial X} & \frac{\partial w}{\partial Y} & \frac{\partial w}{\partial Z} \end{bmatrix} \quad (5)$$

where \mathbf{C} is the fourth-order stiffness tensor, $\boldsymbol{\varepsilon}$ the strain tensor, “:” is the double contraction operator, (X, Y, Z) are the constant material (reference) coordinates and (u, v, w) are the global Cartesian components of the displacement vector [41]. The asphalt concrete is assumed to be isotropic linear viscoelastic in the calculation of each mode

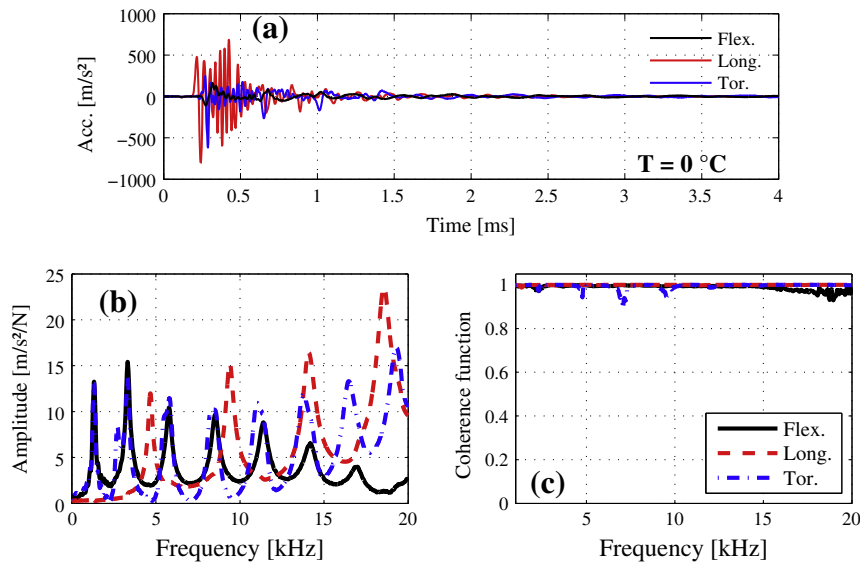


Fig. 2. The measured acceleration in time domain (a), measured FRFs (b) and the coherence functions (c) of the flexural, longitudinal and torsional modes of vibration at 0 °C.

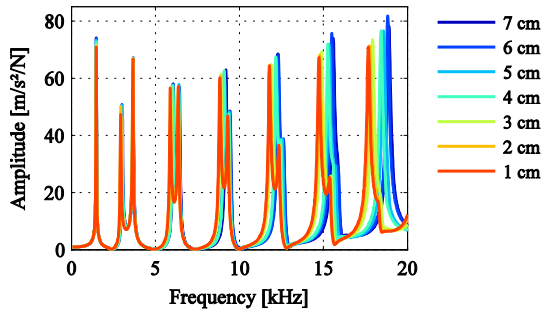


Fig. 4. Convergence study of the mesh size for the torsional modes of vibration at $-30\text{ }^{\circ}\text{C}$.

of vibration. The stiffness tensor has been built up by E^* and ν^* when calculating the response of the flexural and longitudinal modes of vibration and by E^* and G^* when calculating the torsional modes of vibration. The reason E^* and G^* are used for the torsional modes is because the torsional resonance frequencies are nearly independent of ν^* . This enables a characterization of G^* without any significant interference from possible values of E^* and ν^* .

E^* and G^* have been expressed by the Havriliak–Negami (HN) model according to Eqs. (6) and (7), respectively. The HN model is known to accurately characterize the behavior of viscoelastic materials [42–44]. The model has also been applied to both modal and conventional testing of asphalt concrete [9,45].

$$E^*(\omega) = E_{\infty} + \frac{(E_0 - E_{\infty})}{[1 + (i\omega\tau)^{\alpha}]^{\beta}} \quad (6)$$

$$G^*(\omega) = G_{\infty} + \frac{(G_0 - G_{\infty})}{[1 + (i\omega\tau_G)^{\alpha_G}]^{\beta_G}} \quad (7)$$

where E_0/G_0 is the static/low frequency modulus when $\omega \rightarrow 0$, E_{∞}/G_{∞} is the high frequency modulus when $\omega \rightarrow \infty$, α/α_G describes the frequency dependency, β/β_G governs the asymmetry of the loss factor peak, τ/τ_G is the relaxation time and $\omega = 2\pi f$ where f is the frequency (Hz).

The empirical HN model was also formulated to characterize a complex Poisson's ratio according to Eq. (8). Previously, the empirical relationship given by the NCHRP Guide for Mechanistic–Empirical Design [46] has been applied to estimate Poisson's ratio of asphalt concrete through FRF measurements [9]. This (NCHRP) relation is limited to real values of Poisson's ratio and cannot be used to estimate the loss factor/phase angle of Poisson's ratio. The modified formulation of the HN model enables the characterization of complex values. A similar approach has been applied successfully to Poisson's ratio measurements by e.g. Di Benedetto et al. [5].

$$\nu^*(\omega) = \nu_{\infty} + \frac{(\nu_0 - \nu_{\infty})}{[1 + (i\omega\tau)^{\alpha}]^{\beta}} \quad (8)$$

where ν_0 is the low frequency Poisson's ratio when $\omega \rightarrow 0$, ν_{∞} is the high frequency Poisson's ratio when $\omega \rightarrow \infty$.

FRFs of solids with arbitrary geometries can be calculated through the finite element method. Therefore, the method of optimizing calculated FRFs against measured FRFs to determine material properties can be applied to asphalt concrete specimens with any type of geometry.

2.3. Optimization of frequency response functions

Two approaches of optimizing the calculated FRFs have been applied in this paper. E^* , G^* and ν^* have been characterized for each measurement temperature through the optimization of FRFs when using Eqs. (6)–(8). Master curves of E^* , G^* and ν^* have also been estimated directly through the optimization of the FRFs by substituting shift factors into the HN model. This operation is based on the assumption that asphalt concrete is a thermo-rheological simple material [47]. Measurements performed at several temperatures over a limited frequency range can be expressed over much wider frequency range (reduced frequencies) at a specific reference temperature through this assumption. The shift factors are determined by the Williams–Landel–Ferry equation according to Eq. (9) [48]:

$$\log \alpha_T(T) = \frac{-c_1(T - T_{ref})}{c_2 + T - T_{ref}} \quad (9)$$

where $\alpha_T(T)$ is the shift factor, T the test temperature, T_{ref} the reference temperature and c_1 and c_2 are the material constants.

The shift factors multiplied with the frequencies are the reduced frequencies. Substituting the shift factors into the HN model gives the following equations, where the resulting reduced frequencies are multiplied with the only temperature dependent parameter (τ) in the HN model to account for the temperature dependency of the material properties [37,44].

$$E^*(\omega, T) = E_{\infty} + \frac{(E_0 - E_{\infty})}{[1 + (i\omega\alpha_T(T)\tau)^{\alpha}]^{\beta}} \quad (10)$$

$$G^*(\omega, T) = G_{\infty} + \frac{(G_0 - G_{\infty})}{[1 + (i\omega\alpha_T(T)\tau_G)^{\alpha_G}]^{\beta_G}} \quad (11)$$

$$\nu^*(\omega, T) = \nu_{\infty} + \frac{(\nu_0 - \nu_{\infty})}{[1 + (i\omega\alpha_T(T)\tau)^{\alpha}]^{\beta}} \quad (12)$$

The low frequency asymptotic parameters (E_0 , G_0 and ν_0) have no influence to the calculated FRFs for realistic values of asphalt concrete. These parameters have therefore been assumed to $E_0 = G_0 = 100$ MPa and $\nu_0 = 0.5$ based on test results reported in the literature [5,49]. The assumed values of the low frequency parameters were able to contribute to a good fit between the calculated and measured FRFs (see Fig. 5).

The optimization of the FRFs was performed by combining a finite element software with a software for numerical computations. The theoretical FRFs were calculated through the finite element method and the numerical computation software was applied to automatically minimize the difference between the measured and calculated FRFs. The parameters that were optimized for this purpose were in the case of the longitudinal and the flexural modes of vibration: E_{∞} , ν_{∞} , α , β , τ , c_1 and c_2 , and in the case of the torsional modes of vibration E_{∞} , ν_{∞} , α , β , τ , G_{∞} , α_G , β_G , τ_G , c_1 and c_2 . The parameters are not completely unique and the error can be minimized by several combinations. An algorithm that has been found efficient in finding the global minimum was used in the optimization procedure [9,37]. The error was calculated for 60 frequencies for the longitudinal modes of vibration and 80 frequencies for the flexural and torsional modes of vibration. The error between the FRFs was minimized through the following objective function, where normalized FRFs were used to weigh the frequencies around the resonances higher.

$$Error = \sum_{i=1}^N \left(|H_{MNorm,i}| \times \left| \frac{|H_{M,i}| - |H_{T,i}|}{|H_{M,i}|} \right| \right) \quad (13)$$

where H_{MNorm} is the normalized measured FRF, H_M is the measured FRF, H_T is the theoretical FRF, N is the number of data points and i is the index of the data point.

3. Results and discussion

Three different modes of vibration have been measured in this paper. The finite element method has been applied to calculate the theoretical response of each mode type based on the assumption of isotropic linear viscoelastic theory (see Eq. (14)). The longitudinal modes of vibration have provided a characterization of E^* and ν^* . The flexural modes have also provided E^* and ν^* , while the torsional modes of vibration have provided a characterization of E^* and G^* . All the three cases have been characterized independently of each other. Therefore, if isotropic linear viscoelastic theory is applicable to these measurement results, it should be possible to obtain the same results as characterized in the three different cases by calculating E^* , G^* and ν^* according to Eq. (14):

$$G^* = \frac{E^*}{2(1 + \nu^*)} \quad (14)$$

However, the results that are presented in this paragraph show that this is not the case of these measurements. The characterized E^* and ν^* that gives an optimum fit of the calculated FRFs to the longitudinal measurements give a G^* that does not match the torsional measurements very well. The same observation is also made from the flexural characterized E^* and ν^* . In the case of the torsional modes of vibration, G^* is characterized accurately since it is nearly independent of E^* or ν^* . An approximation of E^* can also be obtained from the torsional modes, since the flexural modes of vibration are also excited through the torsional measurements. However, the E^* characterized from the torsional modes does not give an optimum match to the FRFs of the flexural or longitudinal modes of vibration. Therefore, the torsional characterized E^* and the following ν^* (based on E^* and G^*) from the torsional modes are not considered to be the correct material properties. Instead, E^* and ν^* of the flexural and longitudinal mode types and G^* of the torsional modes of vibrations are considered to be the correct material properties. This conclusion is simply based on the fits of

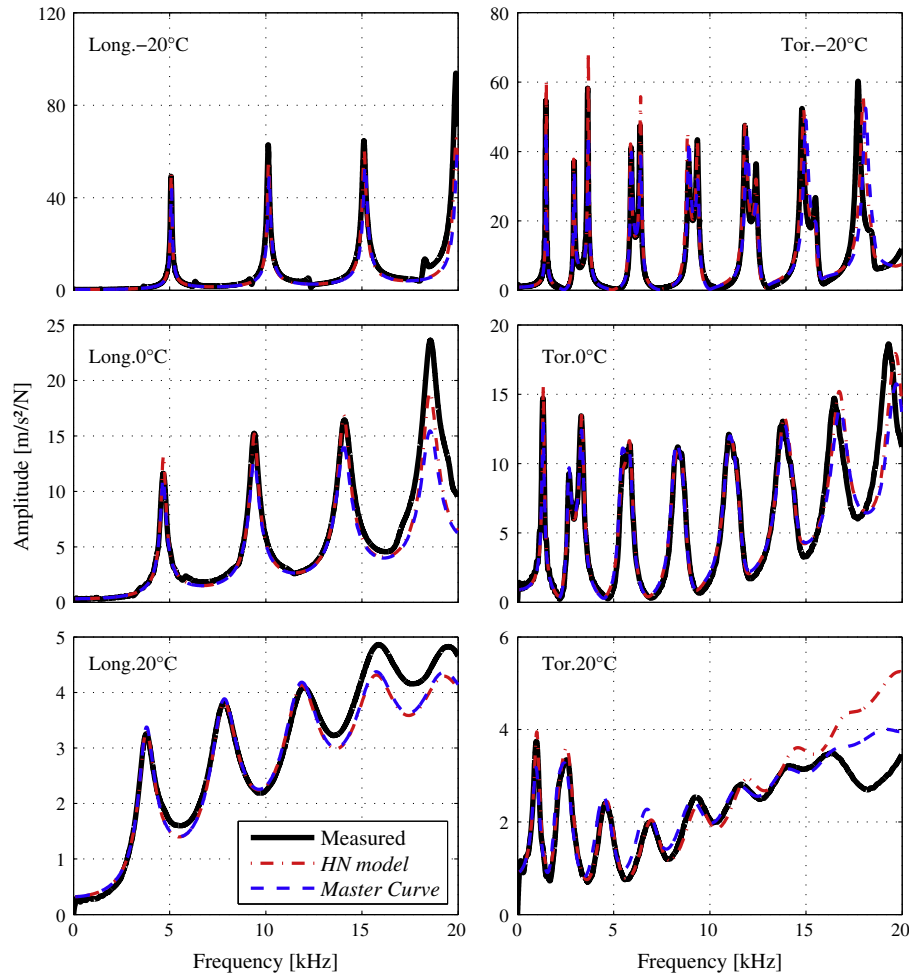


Fig. 5. Measured and calculated FRFs of the longitudinal and torsional modes of vibration at –20, 0 and 20 °C.

the calculated FRFs to the measured FRFs. It is emphasized that E^* , ν^* and G^* are considered correct only for the specific mode type that they have been characterized for. Figures of the flexural, longitudinal and torsional characterized E^* , ν^* and G^* are presented further into this section.

Other approaches have been considered in an attempt to obtain results which agree with isotropic linear viscoelastic theory. For example, by using G^* and ν^* to calculate the torsional modes of vibration, arbitrary values of ν^* can be used to characterize G^* . This G^* was thereafter used to characterize ν^* through optimization of the longitudinal and flexural modes of vibration. E^* was by this calculated from the characterized G^* and ν^* . This approach would give one set of E^* , G^* and ν^* for all modes of vibration. However, the attempt resulted in poor fits of the calculated FRFs to the measured FRFs. Therefore, it seems like the response of the three different modes of vibration cannot be linked together according to isotropic linear viscoelastic theory.

The best possible matches of the calculated to measured FRFs of the longitudinal and torsional modes of vibration are presented in Fig. 5. The measured FRFs at –20, 0 and 20 °C are presented together with two cases of optimized FRFs. The FRFs that have been optimized for each measurement temperature individually are labeled *HN model* in Fig. 4. Similarly, the FRFs that have been optimized against all measurement temperatures simultaneously are labeled *Master Curve*. In Fig. 5 it can be seen that the optimized master curves gives almost as good fit as the FRFs of each measurement temperature. The estimated parameters that provided the

best possible match of the master curves for each mode type are presented in Tables 2 and 3.

Figs. 6–9 consist of three subplots which all present information of the complex dynamic behavior of the specimen. Subplot *a* shows the absolute values of the complex modulus and subplot *b* presents the phase angle, which is related to the damping of the material. The phase angle (φ) is defined as $\varphi = \tan^{-1}(E''/E')$, where E'' is the imaginary part (loss moduli) of E^* and E' is the real part (storage moduli) of E^* . Subplot *c* is a Cole–Cole diagram presenting the loss and storage moduli. The Cole–Cole diagram is a good indication of the accuracy to the assumed thermo-rheological simple behavior of the specimen, since it is independent of the temperature and

Table 2

Estimated complex modulus (E^*) parameter values of the HN model, where $T_{ref} = 0$ °C, $c_1 = 16.30$ and $c_2 = 101.98$.

Mode type	E_0 (MPa)	E_∞ (MPa)	ν_0	ν_∞	α	β	τ (s)
Long.	100	38,380	0.5	0.247	0.536	0.241	3.605
Flex.	100	37,180	0.5	0.260	0.566	0.231	3.605

Table 3

Estimated complex shear modulus (G^*) parameter values of the HN model, where $T_{ref} = 0$ °C, $c_1 = 14.02$ and $c_2 = 120.02$.

Mode type	G_0 (MPa)	G_∞ (MPa)	α_G	β_G	τ_G (s)
Tor.	100	14,797	0.819	0.184	0.298

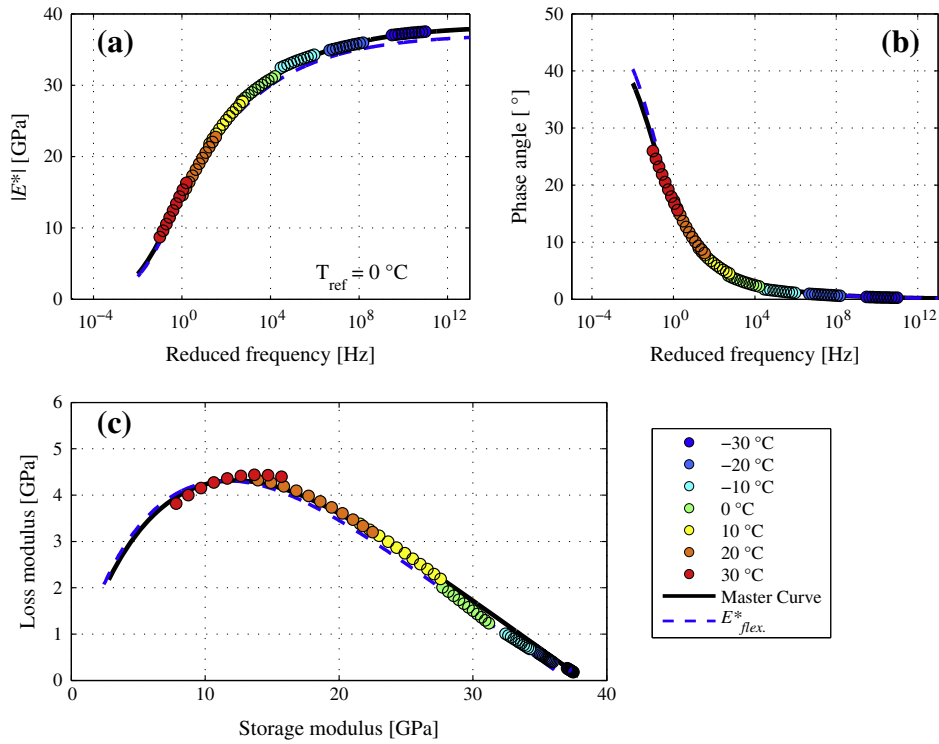


Fig. 6. The complex modulus (E^*) characterized at each measurement temperature for the longitudinal modes of vibration and the estimated master curves for the longitudinal and flexural modes.

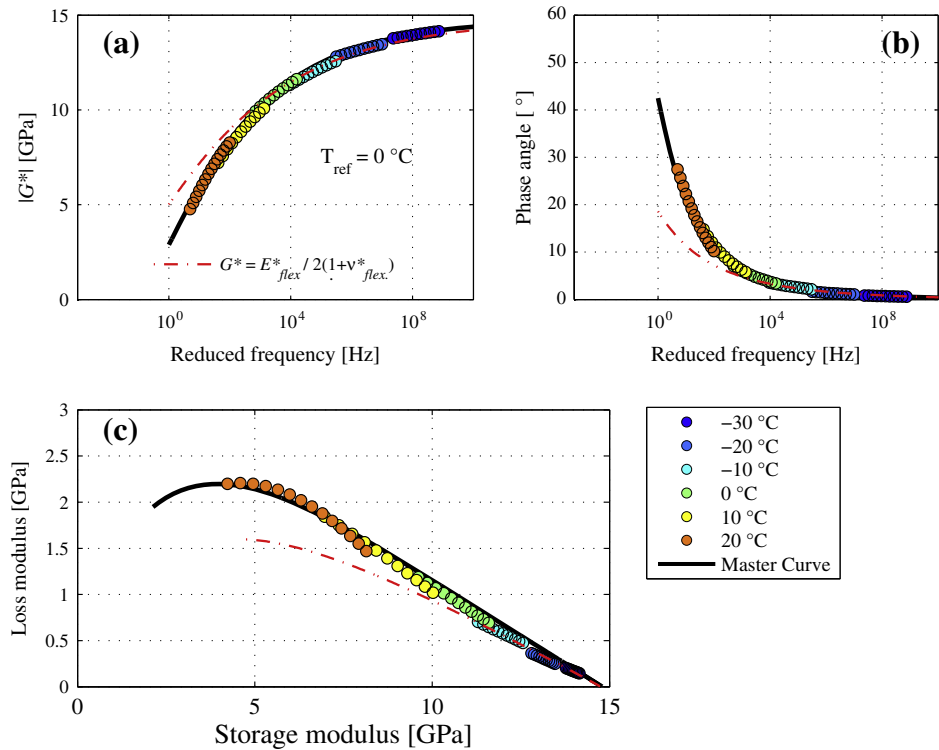


Fig. 7. The complex shear modulus (G^*) characterized at each measurement temperature for the torsional modes of vibration, the torsional estimated G^* master curve and the calculated G^* .

loading frequency. When the results from each measurement temperature follows a unique curve (i.e. master curve) this assumption is valid. Also, results from the low frequency and high temperature range are emphasized in the Cole–Cole diagram.

Fig. 6 presents values of E^* characterized at each measurement temperature of the longitudinal modes of vibration along with the master curves of the longitudinal and flexural mode type. The flexural and longitudinal master curve gives a similar E^* except for the

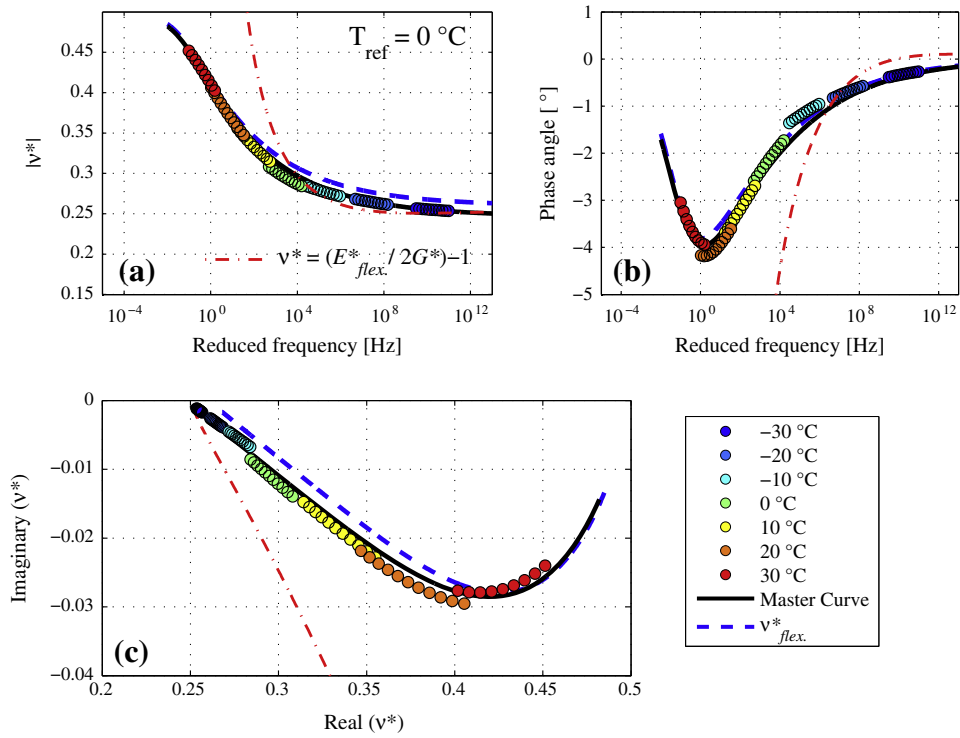


Fig. 8. Complex Poisson's ratio (ν^*) characterized at each measurement temperature for the longitudinal modes of vibration, the estimated ν^* master curves for the longitudinal and flexural modes and the calculated ν^* .

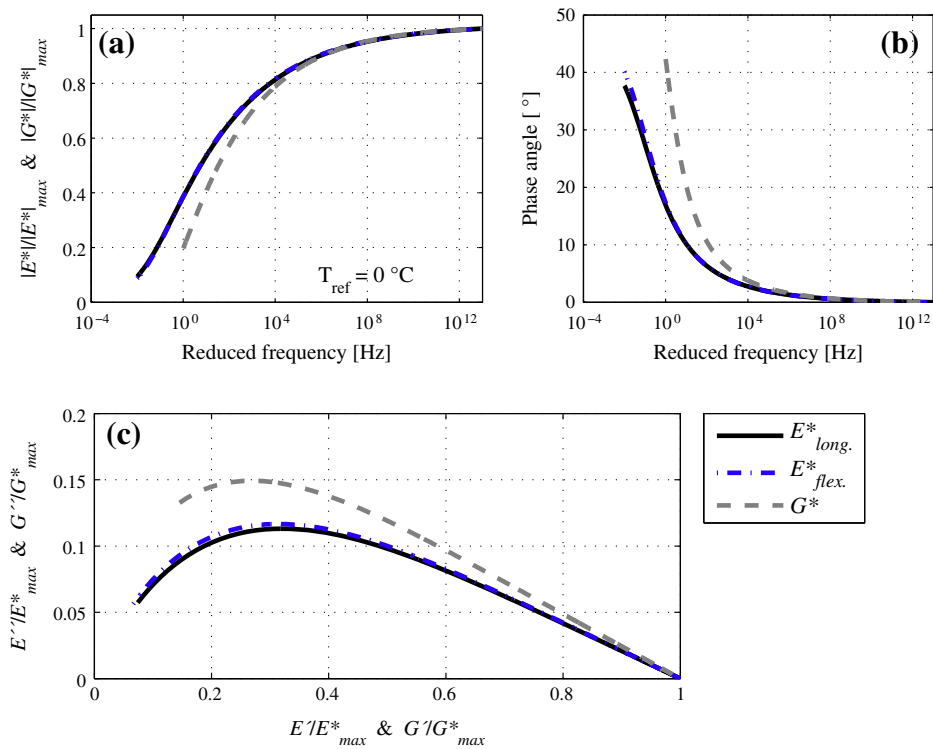


Fig. 9. The estimated normalized complex modulus master curves of the flexural, longitudinal and torsional modes of vibration.

higher frequencies where the flexural E^* is slightly lower than the longitudinal E^* . This difference may be related to the anisotropy of the specimen and e.g. Clec'h et al. [50] showed similar results from measurements performed in different directions of asphalt concrete specimens.

Fig. 7 shows the characterized G^* at each measurement temperature together with the optimized G^* master curve. Fig. 7 also presents a G^* calculated from the flexural characterized E^* and ν^* master curves according to Eq. (14). However, this calculated G^* provides finite element computed FRFs that gives a worse match

to the measured torsional FRFs compared to the FRFs of the characterized G^* . It can be seen in Fig. 7 that the calculated G^* has a lower phase angle and loss factor at lower frequencies compared to the characterized G^* . This shows that the calculated G^* gives an overestimation of the dynamic shear modulus at low frequencies and high temperatures. The discrepancy from the isotropic linear relationship becomes visible for frequencies lower than approximately 10 kHz at a reference temperature of 0 °C. These are normal temperatures and frequencies commonly applied to pavements. It should be pointed out that accurate values of G^* are as important as E^* to pavement design since the shear strain is often used to predict rutting and the tensile strain is used to predict fatigue cracking of pavements. The figure also indicates that the isotropic linear viscoelastic theory is accurate for higher frequencies (>10 kHz) and lower temperatures.

Fig. 8 presents ν^* characterized at each measurements temperature of the longitudinal modes of vibration together with the master curves of the longitudinal and flexural modes. The flexural and the longitudinal characterized ν^* show differences at high frequencies that may be linked to the same differences of the flexural and longitudinal E^* master curves. The results of the characterized ν^* (~0.25–0.5) are realistic values of asphalt concrete in comparison with other reported results [5]. Fig. 8 also shows a calculated ν^* according to isotropic linear viscoelastic theory. This ν^* have been calculated from the flexural characterized E^* master curve and the G^* master curve. The calculated ν^* results in values above 0.5 at lower frequencies (<10 kHz) and higher temperatures (>0 °C). Again at higher frequencies above ~10 kHz the isotropic linear assumption seems to give realistic values of $|\nu^*|$. The results are in agreement with earlier research showing high values of $|\nu^*|$ calculated from measured E^* and G^* at frequencies between ~10⁻² and 20 Hz [10,11,14,26].

Fig. 9 shows the normalized moduli characterized by the optimization of the flexural (E^*), longitudinal (E^*) and torsional (G^*) mode types. This figure shows a clear difference in phase angle and loss factor of E^* and G^* . Sousa and Monismith [10] showed that ν^* becomes larger than 0.5 as the difference in damping between axial and shear modes increases. The results presented here also indicate that a too large difference between the phase angle of E^* and G^* at frequencies lower than 10 kHz seems to be the reason to why Eq. (14) cannot be applied. However, the mechanisms of the asphalt concrete specimen causing the differences between the phase angle of E^* and G^* has not been investigated in this paper.

4. Conclusions

The results of the discrepancy from isotropic linear viscoelastic theory presented here confirm earlier measurements of E^* and G^* of asphalt concrete, where the calculated $|\nu^*|$ resulted in values above 0.5. Unlike some of the previous conventional testing of E^* and G^* performed to asphalt concrete, the FRF measurements does not introduce any differences in the test conditions between the E^* and G^* characterization. Therefore, the comparison can be focused only on different material behavior instead of accounting for possible interference from differences in the test equipment. In addition, the measurements are performed to the same specimen.

The results of the FRF measurements indicate that the asphalt concrete specimen exhibit different complex dynamic behavior for different modes of vibration. The differences in the damping properties between E^* and G^* at higher temperatures and lower frequencies may be the cause to the observed deviations from isotropic linear viscoelastic theory.

An overestimation of the dynamic shear modulus at high temperatures is made for the asphalt concrete specimen, if E^* and ν^* are used to calculate G^* according to isotropic linear viscoelastic

theory. This could have an important practical impact if this is also the case in pavements in the field, since models to predict rutting in pavement engineering are often based on a G^* that has been calculated from E^* and ν .

Acknowledgements

The Swedish transport administration (Trafikverket) and the Swedish construction industry's organization (SBUF) are acknowledged for their financial support.

References

- [1] Brown ER, Kandhal PS, Roberts FL, Kim YR, Lee DY, Kennedy TW. Hot mix asphalt materials, mixture design and construction. Maryland: NAPA Research and Education Foundation; 2009. ISBN:0-914313-02-1.
- [2] Kim YR, Seo Y, King M, Momen M. Dynamic modulus testing of asphalt concrete in indirect tension mode. J Transport Res Board 2004;1891:163–73.
- [3] Biswas K, Pellinen T. Practical methodology of determining the in situ dynamic (complex) moduli for engineering analysis. J Mater Civ Eng 2007;19(6):508–14.
- [4] Garcia G, Thompson MR. HMA dynamic modulus predictive models: a review. Research report FHWA-ICT-07-005. Illinois Center of Transportation; January 2007.
- [5] Di Benedetto H, Delaporte B, Sauzéat C. Three-dimensional linear behavior of bituminous materials: experiments and modeling. Int J Geomech 2007;7(2):149–57.
- [6] Migliori A, Sarrao JL. Resonant ultrasound spectroscopy – applications to physics, materials measurements and nondestructive evaluation. Wiley – Interscience Publication; 1997. ISBN:0-471-12360-9.
- [7] Ryden N, Park CH. Fast simulated annealing inversion of surface waves on pavement using phase-velocity spectra. Geophysics 2006;71(4):R49–58.
- [8] Gudmarsson A, Ryden N, Birgisson B. Application of resonant acoustic spectroscopy to asphalt concrete beams for determination of the dynamic modulus. Mater Struct 2012;45:1903–13.
- [9] Gudmarsson A, Ryden N, Birgisson B. Characterizing the low strain complex modulus of asphalt concrete specimens through optimization of frequency response functions. J Acoust Soc Am 2012;132(4):2304–12.
- [10] Sousa JB, Monismith CL. Dynamic properties of asphalt concrete. J Test Eval – JTEVA 1988;16(4):350–63.
- [11] Alavi SH, Monismith CL. Time and temperature properties of asphalt concrete mixtures tested as hollow cylinders and subjected to dynamic axial and shear loads. J AAPT 1994;63:152–81.
- [12] Masad E, Bahia H. Effect of loading configuration and material properties on nonlinear response of asphalt mixtures. J AAPT 2002;71:535–58.
- [13] Christensen Jr DW, Pellinen T, Bonaquist RF. Hirsch model for estimating the modulus of asphalt concrete. J AAPT 2003;72:97–121.
- [14] Saadeh S, Masad E, Stuart K, Abbas A, Papagiannakis T, Al-Khateeb G. Comparative analysis of axial and shear moduli of asphalt mixes. J AAPT 2003;72:122–53.
- [15] Abbas A, Papagiannakis A, Masad E. Linear and nonlinear viscoelastic analysis of the microstructure of asphalt concretes. J Mater Civ Eng 2004;16:133–9 [special issue: micromechanical characterization and constitutive modeling of asphalt mixes].
- [16] Di Benedetto H, Partl MN, Francken L, De La Roche C. Stiffness testing for bituminous mixtures. Mater Struct 2001;34:66–70.
- [17] Underwood S, Heidari HA, Guddati M, Kim YR. Experimental investigation of anisotropy in asphalt concrete. J Transport Res Board 2005;1929:238–47.
- [18] Johnston DH, Toksöz MN. Ultrasonic P and S wave attenuation in dry and saturated rocks under pressure. J Geophys Res 1980;85:925–36.
- [19] Zhubayev A, Ghose R. Contrasting behavior between dispersive seismic velocity and attenuation: advantages in subsoil characterization. J Acoust Soc Am 2012;131(2):EL 170–176.
- [20] Tschoegl NW. The phenomenological theory of linear viscoelastic behavior: an introduction. Berlin: Springer; 1989. <http://dx.doi.org/10.1007/978-3-642-73602-5>.
- [21] Theocaris PS. Interrelation between dynamic moduli and compliances in polymers. Kolloid Z Z Polym 1969;235(4):1182–8.
- [22] Pritz T. Relation of bulk to shear loss factor of solid viscoelastic materials. J Sound Vib 2009;324:514–9.
- [23] Pritz T. The Poisson's loss factor of solid viscoelastic materials. J Sound Vib 2007;306:790–802.
- [24] Olard F, Di Benedetto H. General “2S2P1D” model and relation between the linear viscoelastic behaviours of bituminous binders and mixes. RMPD 2003;4(2):185–224.
- [25] Pellinen T, Witczak M. Use of stiffness of hot-mix asphalt as a simple performance test. Transport Res Rec 1789 No. 02-2505 2002:80–90.
- [26] Witczak MW, Bonquist R, Von Quintus H, Kaloush K. Specimen geometry and aggregate size effects in uniaxial compression and constant height shear tests. J AAPT 2000;69:733–93.
- [27] Mounier D, Di Benedetto H, Sauzéat C. Determination of bituminous mixtures linear properties using ultrasonic wave propagation. Constr Build Mater 2012;36:638–47.

- [28] Hochuli AS, Sayir MB, Poulikakos LD, Partl MN. Measuring the complex modulus of asphalt mixtures by structural wave propagation. Clearwater Beach, FL: Association of Asphalt Paving Technologists (AAPT), March 19–21; 2001.
- [29] Nazarian S, Tandon V, Yuan D. Mechanistic quality management of hot mix asphalt layers with seismic methods. *J ASTM Int* 2005;2(9):88–99.
- [30] Di Benedetto H, Sauzéat C, Sohm J. Stiffness of bituminous mixtures using ultrasonic wave propagation. *RMPD* 2009;10(4):789–814.
- [31] Norambuena-Contreras J, Castro-Fresno D, Vega-Zamanillo A, Celaya M, Lombillo-Vozmediano I. Dynamic modulus of asphalt mixture by ultrasonic direct test. *NDT&E Int* 2010;43:629–34.
- [32] Whitmoyer SL, Kim YR. Determining asphalt concrete properties via the impact resonant method. *J Test Eval* 1994;22(2):139–48.
- [33] Kweon G, Kim YR. Determination of the complex modulus of asphalt concrete using the impact resonance test. *J Transport Res Board* 2006;1970:151–60.
- [34] Lacroix A, Kim YR, Far MSS. Constructing the dynamic modulus mastercurve using impact resonance testing. *Assoc Asph Paving Technol* 2009;78:67–102.
- [35] ASTM. C215-08. Standard test method for fundamental transverse, longitudinal, and torsional frequencies of concrete specimens. West Conshohocken, PA: American Society for Testing and Materials; 2008.
- [36] Ryden N. Resonant frequency testing of cylindrical asphalt samples. *Eur J Environ Civ Eng* 2011;15:587–600.
- [37] Ren Z, Atalla N, Ghinet S. Optimization based identification of the dynamic properties of linearly viscoelastic materials using vibrating beam technique. *ASME J Vib Acoust* 2011;133(4):041012 1–041012 12.
- [38] Rupitsch SJ, Ilg J, Sutor A, Lerch R, Döllinger M. Simulation based estimation of dynamic mechanical properties for viscoelastic materials used for vocal fold models. *J Sound Vib* 2011;330:4447–59.
- [39] Renault A, Jaouen L, Sgard F. Characterization of elastic parameters of acoustical porous materials from beam bending vibrations. *J Sound Vib* 2011;330:1950–63.
- [40] Pasqualini D. Intrinsic nonlinearity in geomaterials: elastic properties of rocks at low strain. In: Delsanto PP, editor. *Universality of nonclassical nonlinearity applications to non-destructive evaluations and ultrasonic*. New York: Springer Science and Business Media; 2006. p. 417–23.
- [41] Comsol Multiphysics 4.3b ©1998. Structural mechanics module user's guide; May 2013.
- [42] Havriliak S, Negami S. A complex plane analysis of α -dispersions in some polymer systems. *J Polym Sci C* 1966;14:99–117.
- [43] Hartmann B, Lee GF, Lee JD. Loss factor height and width limits for polymer relaxations. *J Acoust Soc Am* 1994;95:226–33.
- [44] Madigosky WM, Lee GF, Niemiec JM. A method for modeling polymer viscoelastic data and the temperature shift function. *J Acoust Soc Am* 2006;119:3760–5.
- [45] Zhao Y, Liu H, Bai L, Tan Y. Characterization of linear viscoelastic behavior of asphalt concrete using complex modulus model. *J Mater Civ Eng* 2013;25(10):1543–8.
- [46] Guide for Mechanistic-Empirical Design. Final report, Part 2. Design inputs. Material characterization. NCHRP; March 2004 [chapter 2].
- [47] Nguyen HM, Pouget S, Di Benedetto H, Sauzéat C. Time-temperature superposition principle for bituminous mixtures. *Eur J Environ Civ Eng* 2009;13(9):1095–107.
- [48] Williams ML, Landel RF, Ferry JD. The temperature dependence of relaxation mechanisms in amorphous polymers and other glass-forming liquids. *J Am Chem Soc* 1955;77:3701.
- [49] Ullidtz P, Harvey J, Tsai B-W, Monismith C. Calibration of CalME models using WesTrack performance data. Report UCPRC-RR-2006-14. Berkeley: Pavement Research Center, University of California; 2006.
- [50] Clec'h P, Sauzéat C, Di Benedetto H. Linear viscoelastic behaviour and anisotropy of bituminous mixture compacted with a French wheel compactor. *Paving Mater Pavement Anal* 2010;1:103–15. [http://dx.doi.org/10.1061/41104\(377\)14](http://dx.doi.org/10.1061/41104(377)14).

Paper VI

Non-Contact Excitation of Fundamental Resonance Frequencies of an Asphalt Concrete Specimen

ANDERS GUDMARSSON
NILS RYDEN
BJÖRN BIRGISSON

Accepted to

The 41st Annual Review of Progress in Quantitative Nondestructive
Evaluation, Boise, USA, AIP Conference Proceedings.

Non-Contact Excitation of Fundamental Resonance Frequencies of an Asphalt Concrete Specimen

Anders Gudmarsson^a, Nils Ryden^b, and Björn Birgisson^c

KTH Royal Institute of Technology, Highway and Railway Engineering, 100 44 Stockholm, Sweden.

^aCorresponding author: andgud@kth.se

^bnils.ryden@tg.lth.se

^bbjornbir@kth.se

Abstract. Impact hammer and non-contact speaker excitation were applied to an asphalt concrete, a PVC-U and a concrete specimen to measure the fundamental longitudinal resonance frequency at different strain levels. The impact and the non-contact excitation methods resulted in similar resonance frequencies for the undamaged asphalt concrete and for the PVC-U specimen. However, the two excitation approaches gave different results for the concrete specimen, which was shown to have a nonlinear response to increasing strain levels. A reduction and a following recovery of the resonance frequency of the asphalt concrete were shown after the specimen was exposed to a small amount of damage. However, no fast nonlinear dynamics were observed for the asphalt concrete through the speaker measurements.

INTRODUCTION

New nondestructive test methods are needed to characterize nonlinear properties of asphalt concrete such as slow dynamics, aging, damage and healing. Conventional complex modulus tests of asphalt concrete are performed at different temperatures and frequencies (~0.01 to 25 Hz) through cyclic loading at strain levels of about 50 microstrains. Below these strain levels the accuracy of the conventional cyclic loading is not satisfying to study the above mentioned nonlinear properties. Impact resonance and modal testing have shown to be economic and accurate alternatives to conventional tests to characterize the frequency and temperature dependent material properties of asphalt concrete at low strain levels [1-5]. Also, damage and healing was studied by applying impact resonance testing according to the concrete standard ASTM C215 to measure changes in the stiffness of asphalt concrete due to cyclic fatigue testing with rest periods [6]. However, manually applied impacts in modal testing often require an opening of the thermal chamber that can cause disturbances to the temperature. To study e.g. small changes of the fundamental resonance frequencies it is vital to limit any unwanted temperature variations in a thermal chamber since asphalt concrete is highly temperature dependent. Therefore, measurements requiring an opening of the thermal chamber are not optimal in this case, especially at low temperatures. Non-contact excitation of asphalt concrete makes it possible to eliminate any disturbances to the temperature by performing the measurements using automated excitation inside the thermal chamber. Thus, non-contact excitation may enable detailed measurements to investigate potential nonlinearities of asphalt concrete at strain levels lower than the possible measurement range of conventional test methods (i.e. $\sim 10^{-6}$).

Studying the dependency of resonance frequencies to strain amplitudes can give an indication and estimation of the nonlinearity of materials. This method, called nonlinear resonant ultrasound spectroscopy (NRUS), have been applied to other materials such as e.g. rocks, concrete, composites and damaged materials [7-9]. Different excitation techniques have also been used, where e.g. Leśnicki et al. [10] applied an impact hammer to excite resonance

frequencies to characterize damage in concrete. Van Den Abeele et al. [11] used a speaker to excite and measure the amplitude dependency of resonance frequencies of thin slate beams to detect damage. NRUS is based on the fact that nonlinear materials often experience a reduction of the modulus when it is disturbed by a mechanical force. This behavior which is called nonlinear fast dynamics is followed by slow dynamics where the material slowly returns to its initial equilibrium state. The nonlinear fast dynamics can be observed by e.g. increasing the excitation amplitude while measuring the resonance frequencies of a solid. A change of the resonance frequency with an increase or decrease in amplitude corresponds to a change of the wave speed and modulus. Slow dynamics can be monitored by measuring the recovery of resonance frequencies at very low amplitudes [12]. For undamaged materials the amplitude dependence are often weak while damaged materials most often show much stronger amplitude dependence [11]. These types of tests have not been presented for asphalt concrete and it is therefore not known if nonlinear fast and slow dynamics are sensitive damage indicators for asphalt concrete. Early indication of damage in asphalt concrete is important since fatigue failure of asphalt concrete is often caused by micro cracks that coalesce to macro cracks. It is plausible that nonlinear fast and slow dynamics may be observed for asphalt concrete by measuring resonance frequencies at different strain amplitudes.

In this study, a speaker is applied to excite the fundamental longitudinal resonance frequency of an asphalt concrete specimen at different fixed temperatures and amplitudes. The speaker measurements are also applied to concrete and PVC-U samples to investigate the repeatability and accuracy of the proposed test method.

METHODOLOGY

A concrete, PVC-U and an asphalt concrete specimen have been measured in this study. The concrete specimen has a diameter of 100 mm and a height 20 mm, the PVC has a diameter of 150 mm and a height of 40 mm and the asphalt concrete specimen has a diameter and height of 150.7 mm and 31.4 mm, respectively. The nominal aggregate size of the asphalt concrete specimen is 16 mm and it has a density of 2291 kg/m³. The asphalt mixture consists to 5.4 percent by weight of a polymer modified binder (45/80-55). The asphalt concrete specimen was tested at three different temperatures (0, -10 and -20 °C).

The test equipment used to excite and measure the resonance frequencies of the samples were: A speaker (Seas prestige 27TDFC/TV H1210), an amplifier (Marantz PM5004), a data acquisition device (NI USB-6251 M Series), a computer, a signal conditioner (PCB model 480B21), an impact hammer (PCB model 086E80) and an accelerometer (PCB model 352B10). The data acquisition toolbox in MATLAB was used to set-up the analog input and output channels of the data acquisition device and to run and record the measurements. The speaker was connected to an analog output channel of the data acquisition device via the amplifier. The accelerometer and the impact hammer were connected to analog input channels via the signal conditioner. The analog output and input were started simultaneously. Continuous sweeps with increasing frequency were performed by the speaker over a range of frequencies covering the fundamental longitudinal resonance frequency of the specimens (e.g. 5500 to 8500 Hz at -20 °C for the asphalt concrete). The sample rate of the speaker measurements were 100 kHz and the frequency sweep was applied during 10 seconds. This gives a frequency resolution of 0.003 Hz and approximate 0.035 to 0.055 Hz change in frequency from period to period over the applied frequency range in the case of the asphalt concrete at -20 °C. As a reference to the speaker measurements, an impact hammer was applied to perform resonance frequency measurements at each temperature using a sample rate of 500 kHz. The impact hammer excites the specimen over a range of frequencies which depend on the specific impact. The response to this impact is a transient vibration and the fast Fourier transform (FFT) has been applied to convert the responding amplitudes in time domain to corresponding amplitudes in frequency domain. In the case of the speaker excitation, the applied frequencies are defined beforehand and the amplitudes at each frequency are directly measured during the 10 seconds sweep. Figure 1 shows the set-up of the speaker, the specimen and the accelerometer attached by wax. Note that the samples were placed on soft foam for free boundary conditions. Figure 2 shows an example of the measured response of the asphalt concrete at -20 °C excited by a speaker frequency sweep, where the envelope of the response and a Savitzky-Golay filter were used to determine the amplitude [13]. The envelope of the response was determined through the Hilbert transform and the filter was applied to smooth the envelope and to reduce noise. The speaker was placed at a specific distance from the specimen for each measurement temperature. The distance was chosen so that resonance in the air gap between the speaker and specimen would not contaminate the measured fundamental resonance frequency of the specimen. Resonance in the air was expected and seen in the measurements when the distance between speaker and specimen was equal to approximately an even number of half wavelengths

(λ) in the air ($\lambda_{\text{air}}/2$, λ_{air} , $3\lambda_{\text{air}}/2$, etc.). The higher the temperature the more challenging it was to apply the speaker to excite the asphalt concrete specimen due to increased attenuation.

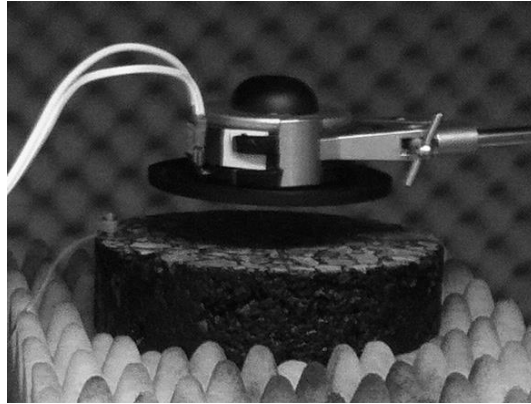


FIGURE 1. The test set-up showing the speaker attached above the sample for non-contact excitation.

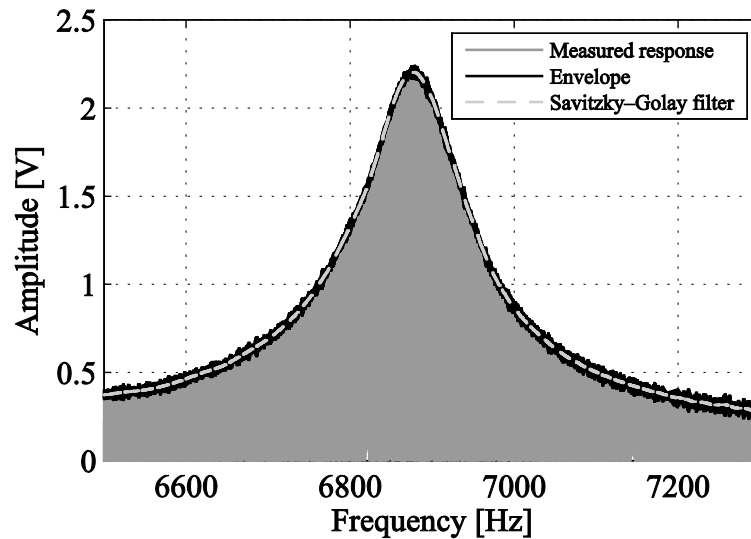


FIGURE 2. The measured response (positive amplitudes) at $-20\text{ }^{\circ}\text{C}$, the envelope of the response and the Savitzky-Golay filter to reduce noise.

RESULTS AND DISCUSSION

The measured fundamental longitudinal resonance frequency of the speaker and the impact hammer excitation of the asphalt concrete at different temperatures are presented in Fig. 3. The two excitation methods are shown to give the same resonance frequency at the two lowest temperatures, while the impact excitation resulted in a slightly lower resonance frequency than the speaker measurement at $0\text{ }^{\circ}\text{C}$. Although, it is not required to excite the asphalt concrete with the same amplitude (acceleration) for the two excitation methods, it is interesting that the speaker is capable to excite the asphalt concrete with similar magnitudes as the impact hammer. The results presented in Fig. 3 show that the speaker can be a promising non-contact approach to measure resonance frequencies of asphalt concrete specimens.

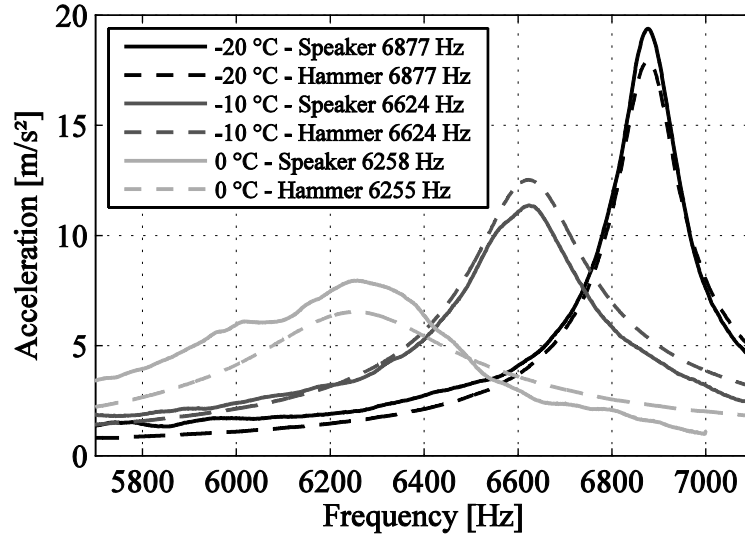


FIGURE 3. The fundamental longitudinal resonance frequency of the asphalt concrete specimen excited by a speaker and an impact hammer at different temperatures.

Figure 4 presents the fundamental longitudinal resonance frequency of the asphalt concrete at $-20\text{ }^{\circ}\text{C}$ excited by the speaker at different driving amplitudes. The results in Fig. 4 show that the resonance frequency is not depending on the strain amplitudes. Hence, there is no observed nonlinear behavior of the asphalt concrete at the strain levels generated by the speaker excitation. However, the non-existing resonance frequency shift does not necessarily mean that there is no nonlinearity in the material. A material can be nonlinear even though there is no shift in the resonance frequencies with different amplitudes. On the other hand, if there is a shift of the resonance peaks it is always an indication of nonlinearity [14]. The amplitude in Fig. 4 is close to the maximum vibration of the asphalt concrete that could be excited through the speaker measurements. The maximum amplitude corresponds to strain levels of approximately 0.26 micro-strains, where the volumetric strains have been estimated by finite element analysis of the asphalt concrete specimen using a similar approach as presented by Payan et al. [15]. It is possible that this amplitude may not be large enough to see nonlinear fast and slow dynamics effects of the asphalt concrete. However, it is also challenging to excite the asphalt concrete with larger vibrations through impact resonance tests [3].

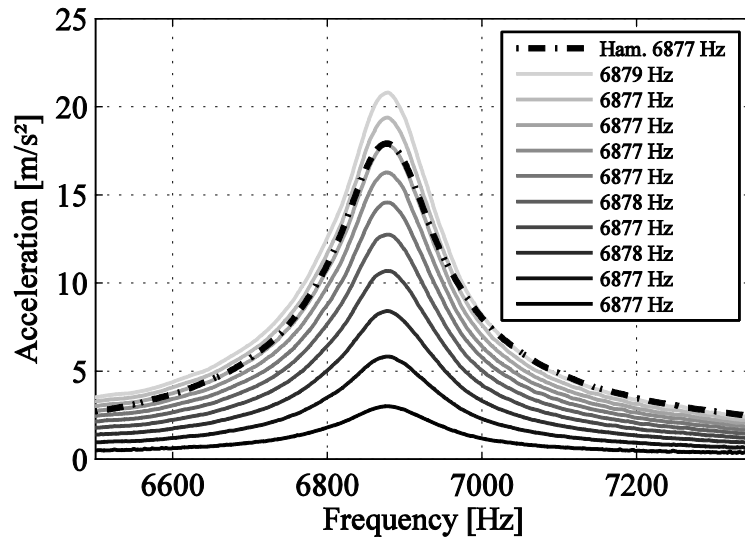


FIGURE 4. The fundamental longitudinal resonance frequency of the asphalt concrete specimen at $-20\text{ }^{\circ}\text{C}$ excited by a speaker at different amplitudes.

The speaker excitation was also performed to a PVC-U specimen that is known to be homogenous and linear. Figure 5 presents the fundamental longitudinal resonance frequency of the PVC-U specimen that has been excited at different amplitudes by both the speaker and the impact hammer. The hammer and the speaker excitation give, in similarity to the asphalt concrete specimen, similar results of the resonance frequency and, as expected for this linear material, neither of the two approaches show any amplitude dependency of the excited resonance frequency.

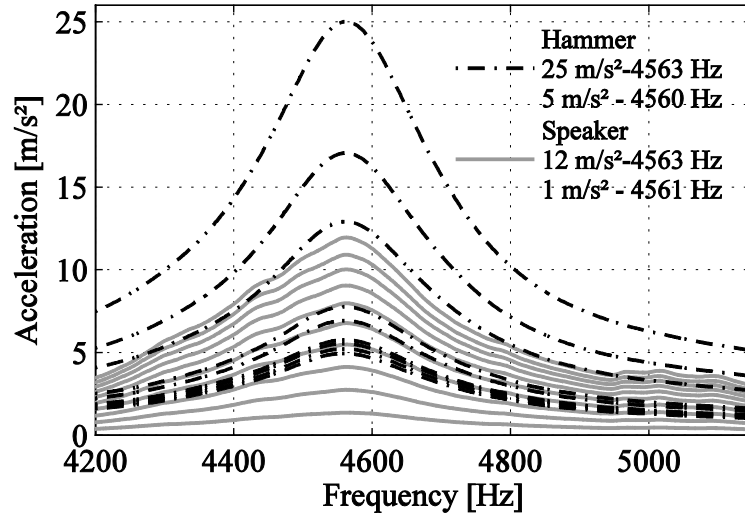


FIGURE 5. The fundamental longitudinal resonance frequency of a PVC specimen excited by a hammer and a speaker at different amplitudes.

The concrete specimen used in this study was known to be damaged to some extent without showing any visible damage. Therefore, the specimen was expected to have a nonlinear response to increasing strain amplitudes. Figure 6 presents the measured fundamental longitudinal resonance frequency excited by the speaker and the hammer at different amplitudes. In contrast to the asphalt concrete and the PVC-U specimen, the two excitation methods gave different results of the measured resonance frequency. The impact hammer gives consequently lower resonance frequency than the speaker excitation at comparable amplitude levels. The expected nonlinear response with a reducing resonance frequency to increasing amplitudes was also shown to be larger for the hammer excitation than the speaker excitation. The speaker measurements gave a small but still systematic reduction of the resonance frequency with increasing strain amplitudes.

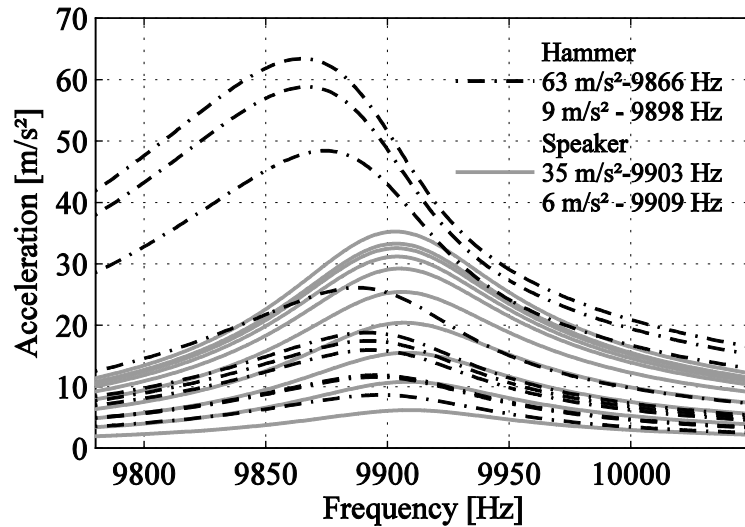


FIGURE 6. The fundamental longitudinal resonance frequency of a concrete specimen excited by a hammer and a speaker at different amplitudes.

A reason for these different results of the concrete specimen compared to the PVC-U specimen may be due to limitations of applying impact measurements to nonlinear materials. An impact gives very high amplitude in the early part of the responding transient time signal which rapidly decays with time. Due to the amplitude dependency, it may be variations of the resonance frequency within one signal for a nonlinear material where the high amplitude in the beginning probably gives a lower frequency than the low amplitude in the end of the signal [16-17]. However, the FFT is based on the average amplitude over time. The impact measured resonance frequencies of the concrete specimen may therefore not be completely correct. Furthermore, TenCate et al. [18] and Pasqualini et al. [19] have shown the existence of two strain regimes where a material below a certain strain threshold have a reversible strain amplitude dependency. Above this strain threshold memory effects of previously applied strain amplitudes affect the resonance frequency. It is reasonable to believe that the early time response due to an impact may exceed the amplitude of this threshold. If this is the case the resonance frequency will be lower than the resonance in the lower strain regime [19], which is also seen in Fig. 6. The averaging of the transient response due to the impact does not cause similar problems in the case of the linear PVC-U specimen, which have no significant amplitude dependency. The amplitude of the response from the speaker and hammer excitation is lower for the PVC-U and the asphalt concrete specimen in comparison to the concrete. The size, stiffness and damping of the solid are affecting the possibility to excite the specimens with large amplitudes.

To investigate the possibility to detect damage in the asphalt concrete several hard impacts with a ~0.055 kg hex key were applied to the specimen without introducing any visible damage [11]. Figure 7 shows the longitudinal resonance frequency excited by the hammer (black dash-dot line) and the speaker after the hard impacts were applied. The measured resonance frequency are here lower compared to the results from the undamaged state presented in Fig. 4, which indicate some degree of damage. Potential slow dynamics effects were investigated by first performing five low amplitude sweeps followed by one high amplitude sweep and finally five additional low amplitude sweeps (see Fig. 7). The first five sweeps should be performed at such low amplitude that the sample still respond linearly. The high amplitude sweep may disturb the specimen which would result in a lower resonance frequency and during the last low amplitude sweeps the resonance may return to the initial value. It is seen in Fig. 7 that there is no significant difference between the resonance frequency of the low and high amplitude speaker sweeps to the damaged asphalt concrete specimen. However, the hammer impact excitation results in a slightly lower resonance frequency compared to the speaker results. Considering the impact hammer and speaker results of the concrete this may be an indication of nonlinearity of the asphalt concrete, in addition to the drop in resonance frequency compared to Fig. 4.

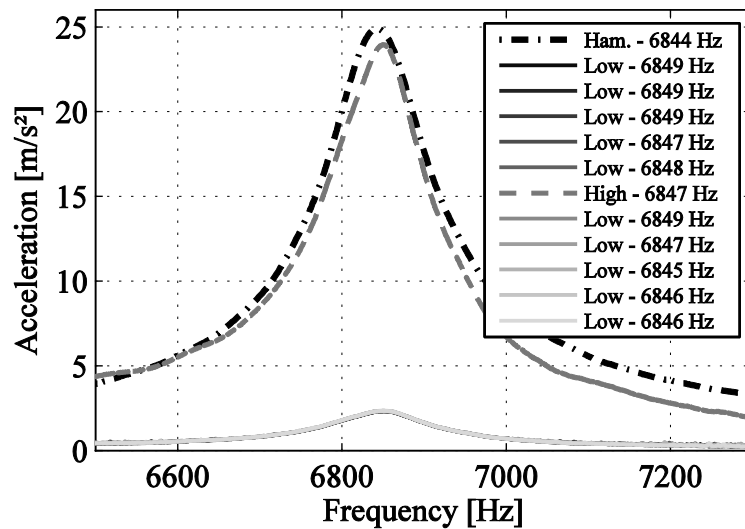


FIGURE 7. The fundamental longitudinal resonance frequency of a damaged asphalt concrete specimen at -20 °C excited by a speaker at ten low amplitudes, one high amplitude and a by a hammer.

Figure 8 shows the resonance frequencies of the damaged asphalt concrete specimen measured at different excitation amplitudes approximately two hours after the measurements presented in Fig. 7 were performed. Also in this case, there is no significant resonance frequency shift due to different excitation amplitudes. However, a recovery of the resonance frequency after the damaged was induced is indicated by comparing Fig. 7 and 8. The

measurements presented in Fig. 8 show in similarity to Fig. 7 that there is a small difference between the hammer and the speaker excited resonance frequency. Note that the impact hammer has not been applied to excite the asphalt concrete at different strain amplitudes due to the strong temperature dependency and the reasons stated in the introduction.

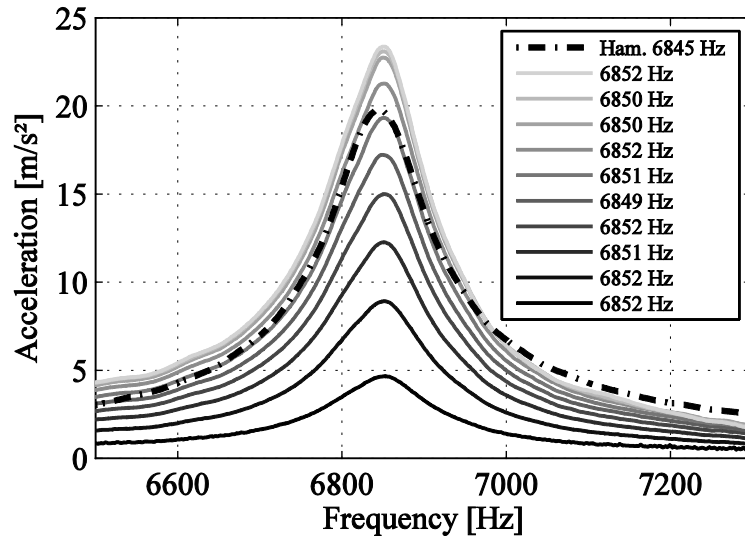


FIGURE 8. The fundamental longitudinal resonance frequency of a damaged asphalt concrete specimen at $-20\text{ }^{\circ}\text{C}$ excited by a speaker at different amplitudes.

Measurements of the recovery of the fundamental longitudinal resonance frequency are presented in Fig. 9 for a time span lasting over several days. A systematic recovery to the initial resonance frequency is observed with increasing time. The recovery may be due to healing of the asphalt concrete specimen or due to slow dynamics, where the recovery to the equilibrium state may last for days [20]. It is not possible to separate possible slow dynamics effects from the healing process in these measurements. Furthermore, thixotropy is another effect that should be mentioned when studying the recovery of asphalt concrete. A thixotropic material experiences a reduction of the viscosity when it's exposed to stress, which in turn would reduce the modulus and resonance frequencies of the material. This effect, which acts on the binder, is reversible and a recovery of the viscosity occurs when the material is at rest. However, thixotropy may not be of great importance in these measurements since these effects are more sensitive to shearing [21]. These results of the asphalt concrete measurements show similarities to results of measurements performed to rubber, which showed large slow dynamics effects while no fast nonlinear dynamics was present [22].

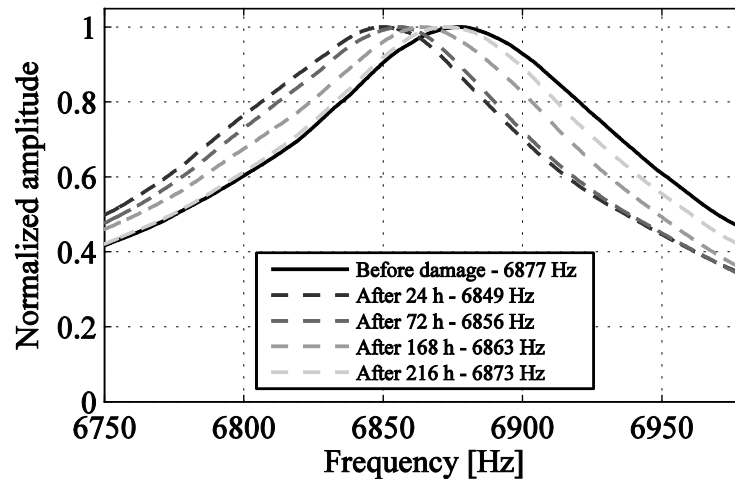


FIGURE 9. Recovery of the fundamental longitudinal resonance frequency of a damaged asphalt concrete specimen at $-20\text{ }^{\circ}\text{C}$.

CONCLUSIONS

A speaker can be used to excite the resonance frequencies of asphalt concrete specimens. Speaker excited resonance frequencies of the asphalt concrete specimen at 0, -10 and -20 °C agreed with the resonance frequencies excited by an impact hammer. Speaker and impact excited resonance frequencies at different strain amplitudes were also shown to give similar results for the PVC-U specimen. However, for the damaged concrete specimen the two excitation methods gave different results of the measured resonance frequencies. The concrete was also the only tested specimen that showed a systematic resonance frequency dependency to the strain amplitude. Damage in the asphalt concrete specimen was identified by a drop of the resonance frequency, but no nonlinear fast dynamics was observed. However, a recovery of the resonance frequency was measured over time for the damaged asphalt concrete specimen. This recovery may be due to healing or slow dynamics.

ACKNOWLEDGMENTS

The Swedish transport administration (Trafikverket) and the Swedish construction industry's organization (SBUF) are acknowledged for their financial support.

REFERENCES

1. N. Ryden, Eur. J. Environ. Civ. Eng. **15**(4), 587-600 (2011).
2. A. Gudmarsson, N. Ryden, B. Birgisson, Mater. Struct. **45**, 1903–1913 (2012).
3. A. Gudmarsson, N. Ryden, B. Birgisson, J. Acoust. Soc. Am. **132** (4), 2304–2312 (2012).
4. A. Gudmarsson, N. Ryden, H. Di Benedetto, C. Sauzéat, N. Tapsoba, B. Birgisson, J. Nondestruct. Eval. DOI: 10.1007/s10921-014-0253-9 (2014).
5. A. Gudmarsson, N. Ryden, B. Birgisson, Constr. Build. Mater. **66**, 63–71 (2014).
6. J. S. Daniel and Y. R. Kim, J. Mater. Civ. Eng. **13**, 434-440 (2001).
7. P. Johnson and A. Sutin, J. Acoust. Soc. Am. **117** (1), 124–130 (2005).
8. J. A. Ten Cate and T. J. Shankland, Geophys. Res. Lett. **23**(21), 3019-3022 (1996).
9. K. C. E. Haller and C. M. Hedberg, Phys. Rev. Lett. **100**(6), 068501(4) (2008).
10. K. J. Leśnicki, J.-Y. Kim, K. E. Kurtis and L. J. Jacobs, NDT&E Int. **44**, 721–727 (2011).
11. K. E.-A. Van Den Abeele, J. Carmeliet, J. A. Ten Cate and P. A. Johnson, Res. Nondestruct. Eval. **12**, 31–42 (2000).
12. P. A. Johnson, “Nonequilibrium Nonlinear-Dynamics in Solids: State of the Art,” in *Universality of Nonclassical Nonlinearity: Applications to Non-Destructive Evaluations and Ultrasonics*, edited by P. P. Delsanto (Springer Science and Business Media, New York, 2006), pp. 49-68.
13. A. Savitzky and M. J. E. Golay, Anal. Chem. **36**(8), 1627-1639 (1964).
14. P. A. Johnson, B. Zinsner and P. N. J. Rasolofosaon, J. Geophys. Res. **101**(B5), 11,553-11,564 (1996).
15. C. Payan, T.J. Ulrich, P. Y. Le Bas, T. Saleh, M. Guimaraes, J. Acoust. Soc. Am. **136** (2), 537-546 (2014).
16. K. Van Den Abeele, P. Y. Le Bas, B. Van Damme, T. Katkowski, J. Acoust. Soc. Am. **126** (3), 963-972 (2009).
17. J. N. Eiras, J. Monzó, J. Payá, T. Kundu, J. S. Popovics, J. Acoust. Soc. Am. **135** (2), EL82-87 (2014).
18. J. A. TenCate, D. Pasqualini, S. Habib, K. Heitmann, D. Higdon and P. A. Johnson, Phys. Rev. Lett. **93**(6), 065501 (2004).
19. D. Pasqualini, K. Heitmann, J. A. TenCate, S. Habib, D. Higdon and P. A. Johnson, J. Geophys. Res. **112**, B01204 (2007).
20. J. A. TenCate, E. Smith and R. A. Guyer, Phys. Rev. Lett. **85**(5), 1020-1023 (2000).
21. H. Di Benedetto, Q. T. Nguyen, C. Sauzéat, Road Mater. Pavement, **12**(1), 129-158 (2011).
22. K. C. E. Haller and C. M. Hedberg, “Three Nonlinear NDE Techniques On Three Diverse Objects,” in *Innovations in Nonlinear Acoustics: 17th International Symposium on Nonlinear Acoustics*, AIP Conference Proceedings 838, edited by A. A. Atchley *et al.* (American Institute of Physics, State College, Pennsylvania, 2006), pp. 87-90.